# Parameter Optimization of a Low Temperature Difference Gamma-Type Stirling Engine to Maximize Shaft Power

by

Calynn James Adam Stumpf

A thesis submitted on partial fulfillment of the requirements for the degree of

Master of Science

Department of Mechanical Engineering

University of Alberta

# Abstract

An investigation was performed with three main objectives. Determine the configuration and operating parameter of a low temperature difference Stirling engine (LTDSE) that would result in the maximum shaft power. Calculate the mean West number for LTDSEs and compare it to the mean West number for high temperature difference Stirling engines (HTDSEs). Validate the methods used to estimate the compression ratio of a Stirling engine.

Three different LTDSEs were developed: The Mark 1, Mark 2, used for initial development and the EP-1. The EP-1 used a bellows for its power piston and was the main engine investigated. A test rig was used that allowed for measurement of temperature, pressure, torque, engine speed, and crank shaft position. The LTDSEs were operated with a thermal source and sink temperature of 95 °C and 2 °C, respectfully, and were heated and cooled with two water flow loops. They used air as a working fluid and a constant buffer pressure of the atmosphere, which was equal to 92.5 kPa.

The compression ratio, phase angle, position of the thermal source heat exchanger, and power piston connection to the workspace was varied on the EP-1 to determine its maximum shaft power. A compression ratio of 1.206 ± 0.017, phase angle of 90 ± 1°, and the thermal source heat exchanger residing on top with the power piston connected to the expansions space resulted in the configuration that produced the maximum local shaft power. This was a shaft power of 6.58 ± 0.09 watts that occurred at an operating speed of 67.7 ± 0.3 rpm. A global maximum shaft power was not found due to limitations of the power piston. The West number for the configuration that produced the maximum local shaft power when using a power piston swept volume of 1835 ± 50ml was 0.238 ± 0.001.

The mean West number was calculated from 12 different LTDSEs that used air as the working fluid, the atmosphere as the buffer pressure, and a temperature difference less than 150 °C, and equaled 0.21. This was lower, but close to the mean West number for HTDSEs of 0.25. This suggests that the West number can be used for comparison of Stirling engine that operate at all temperature differences.

Three methods that estimated the compression ratio for Stirling engines were investigated. The compression ratios produced by these methods were compared to the compression ratio that produced the local maximum shaft power for the EP-1 of 1.206 ± 0.017. The three methods used were Kolin's compression ratio, Egas' ideal compression ratio, and Senft's optimum swept volume ratio. Using Kolin's method, a compression ratio of 1.085 was calculated by. If the experimental average temperature of the working fluid in the compression and expansion space of the EP-1 was used for Egas' method, a compression ratio of 1.156 was produced. If the thermal source and sink temperature was used for Egas' method, a compression ratio of 1.338 was calculated. Senft's method predicted the compression ratio closely when a mechanism effectiveness of 0.75 was used.

Based on the compression ratios used by the 12 experimental LTDSEs, a model was proposed to estimate the compression ratio that could produce the maximum shaft power. This model is applicable to LTDSEs that using air as a working fluid and a buffer pressure of atmospheric. The shaft power compression ratio was calculated from the temperature ratio of the thermal source and sink temperature. To further validate the model, more compression ratio optimization tests should be performed for various temperature ratios and LTDSEs.

# Preface

This thesis is an original work by Calynn Stumpf. Aspects of the research have been published in the following conference publications:

Conference Papers:

Speer, C.P., Michaud, J.P., Miller, D.A., Stumpf, C.J.A. and Nobes, D.S. (2017) Empirical Heat Transfer Correlations of Finned-Tube Heat Exchangers in Pulsatile Flow. World Academy of Science, Engineering and Technology, International Journal of Mechanical, Aerospace, Industrial, Mechatronic and Manufacturing Engineering, 11(6), 1150-1155.

Stumpf, C.J.A., Hunt, A.J. and Nobes, D.S. (2018) Effect of Scaling Up Low Temperature Differential Stirling Engines, 18th ISEC International Stirling Engine Conference, Tainan, Taiwan, Sept 19-21, 2018

Stumpf, C.J.A, Middleton, S. and Nobes, D.S. (2017) "Heat Transfer in Oscillating Fluid Flow Through Parallel Flat Plate Channel Heat Exchangers", Okanagan Fluid Dynamics Meeting, Kelowna, British Columbia, Canada, Aug 22-23, 2017

Speer, C.P., Michaud, J.P., Miller, D.A., Stumpf, C.J.A. and Nobes, D.S. (2017) 'Empirical heat transfer correlations of finned-tube heat exchangers in oscillating flow for low temperature Stirling engines', ICFMHTT 2017: 19th International Conference on Fluid Mechanics, Heat Transfer and Thermodynamics, Venice, Italy June, 21-22, 2017

Speer, C.P., Michaud, J.P., Miller, D.A., Stumpf, C.J.A. and Nobes, D.S. (2017) 'Modification of an ST05G-CNC Stirling Engine to Use a Low Temperature Heat Source', AIAA-2017-4793, 14th International Energy Conversion Engineering Conference, AIAA Propulsion and Energy Forum 2017, Atlanta, George, USA, July, 10-12. 2017

# Acknowledgements

The author gratefully acknowledges the support of his wife,

- Ashli MacDonald Stumpf

Supervisor,

- Dr. David Nobes

Lab mates (Team Stirling),

- Alex Hunt
- Jackson Kutzner
- Jason Michaud
- Steven Middleton
- David Miller
- Michael Nicol-Seto
- Connor Speer

Fellow academics, research groups, and co-op students.

- Dr. Jonathan Banks
- Nobes Research Group (ODL, RGL, DTECL)
- Co-op Students

And who all helped to make this project a success.

Financial support for this research was provided by the following funding bodies:

- Natural Sciences and Engineering Research Council (NSERC) of Canada
- Canadian Foundation of Innovation (CFI)
- Alberta Innovates Energy and Environment Solutions
- Terrapin Geothermics
- Future Energy Systems (FES)

# Table of Contents

# List of Tables

# List of Figures

# List of Symbols

## Roman Alphabet Symbols

| Variable | Description | Unit |
|---|---|---|
| $A_p$ | Cross sectional area of power piston | m |
| $B_n$ | Beale number | - |
| $c_p$ | Isobaric specific heat capacity | J / (kg*K) |
| $CR$ | Compression ratio | - |
| $CR_{exp}$ | Experimental compression ratio | - |
| $CR_{ideal}$ | Ideal compression ratio | - |
| $CR_{Kolin}$ | Kolin's compression ratio | - |
| $CR_{SP}$ | Shaft power compression ratio | - |
| $E$ | Mechanism effectiveness | - |
| $f$ | Engine frequency | Hz |
| $\dot{m}_w$ | Mass flow rate of water through the heat exchangers | kg/s |
| $m_{wf}$ | mass of the working fluid | kg |
| $P_{buf}$ | Buffer pressure | Pa |
| $P_c$ | Pressure of the compression space | Pa |
| $P_e$ | Pressure of the expansion space | Pa |
| $P_{ind}$ | Indicated power | W |
| $P_{max}$ | Minimum cycle pressure | Pa |
| $P_{rm}$ | Root mean cycle pressure | Pa |
| $P_{min}$ | Maximum cycle pressure | Pa |
| $P_{shaft}$ | Shaft power output | W |
| $P_{ws}$ | Pressure of the work space | Pa |
| $Q$ | Heat | J |
| $\dot{Q}$ | Heat transfer rate | W |
| $Q_{in}$ | Heat transferred into system | J |
| $\dot{Q}_{in}$ | Rate of heat transfer into system | W |
| $Q_{out}$ | Heat transferred out of system | J |
| $\dot{Q}_{out}$ | Rate of heat transfer out of system | W |
| $R$ | Ideal gas constant | J / (kg*K) |
| $r_1$ | Crank arm length | m |
| $r_2$ | Connecting rod length | m |

| | | |
|---|---|---|
| $r_3$ | Distance between the piston movement axis and crank arm rotation point | m |
| $r_{\bar{x}}$ | Random uncertainty | Dependent |
| $s_{\bar{x}}$ | Biased uncertainty | Dependent |
| $T$ | Temperature | K or °C |
| $T_C$ | Temperature of thermal sink | K or °C |
| $T_H$ | Temperature of thermal source | K or °C |
| $T_{he}$ | Temperature of the heater and expansion space | K or °C |
| $T_{kc}$ | Temperature of the cooler and compression space | K or °C |
| $T_{hxi}$ | Temperature of fluid at the heat exchanger inlet | K or °C |
| $T_{hxo}$ | Temperature of fluid at the heat exchanger outlet | K or °C |
| $u_{\bar{x}}$ | Combined standard uncertainty | Dependent |
| $V_c$ | Volume of the compression space | $m^3$ |
| $V_e$ | Volume of the expansion space | $m^3$ |
| $V_h$ | Volume of the heater space | $m^3$ |
| $V_k$ | Volume of the cooler space | $m^3$ |
| $V_{max}$ | Maximum engine volume | $m^3$ |
| $V_{min}$ | Minimum engine volume | $m^3$ |
| $V_p$ | Instantaneous volume of power piston | $m^3$ |
| $V_r$ | Volume of the regenerator space | $m^3$ |
| $V_{swd}$ | Volume swept by displacer piston | $m^3$ |
| $V_{swp}$ | Volume swept by power piston | $m^3$ |
| $V_{swt}$ | Volume swept by the displacer and power piston | $m^3$ |
| $V_{ws}$ | Volume of the work space | $m^3$ |
| $W_c$ | Compression work | J / cycle |
| $W_{cs}$ | Compression space work | J / cycle |
| $W_e$ | Expansion work | J / cycle |
| $W_{es}$ | Expansion space work | J / cycle |
| $W_{for}$ | Forced work | J / cycle |
| $W_{ind}$ | Indicated work | J / cycle |
| $W_n$ | West number | - |
| $W_{shaft}$ | Shaft work | J / cycle |
| $X$ | Constant used by Senft in the derivation of the Schmidt model | - |
| $x_p$ | the instantaneous position of the piston relative to the position of minimum volume | m |

| | | |
|---|---|---|
| $Y$ | Constant used by Senft in the derivation of the Schmidt model | - |

# Greek Alphabet Symbols

| Variable | Description | Unit |
|---|---|---|
| $\alpha$ | Phase angle between the displacer and power piston cranks arms | ° |
| $\Delta$ | Change in variable | - |
| $\eta_{th}$ | Thermal efficiency | % |
| $\theta$ | Angular measurement | radians or degrees |
| $\kappa$ | Swept volume ratio | - |
| $\tau$ | Ratio of the temperature in the expansion and compression space | - |
| $\tau_{shaft}$ | Shaft torque | Nm |
| $\varphi$ | Constant used by Senft in the derivation of the Schmidt model | - |
| $\chi$ | The ratio of the dead volume (heat exchangers, regenerator, clearance volumes, etc.) to the volume swept by the displacer piston | - |

# Chapter 1 Introduction and Literature Review

The following chapter contains a short section on the motivation for this research, followed by an overview of Stirling engines, and information about them that is pertinent to this research. The literature was reviewed with emphasis on the following topics: compression ratio optimization, phase angle optimization, heat exchanger position optimization, and low-temperature difference Stirling engines (LTDSE). The chapter ends with the thesis objective and structure.

## 1.1 Motivation

Modern society requires a significant amount of electricity to function. The generation of this electricity affects the climate of the earth due to the output of greenhouse gases from the burning of fossil fuels. Currently, the energy requirements of the world are massive, with 26 PWh of electricity being generated worldwide in 2017 [1]. Of this 26 PWh of electricity generated, 65% of the generation comes from oil, natural gas, and coal [1]. This use of fossil fuels creates carbon dioxide, which is a major contributor to climate change and global warming [2]. The energy requirements of society are projected to increase up to at least the year 2040 [3]. To combat climate change and global warming, while still providing for the world's energy demands, renewable electricity generation processes must be implemented in lieu of more traditional fossil fuel electricity generation processes.

A major problem with many renewable energy processes is that they are intermittent. Wind and solar electricity generation have been shown to have low capacity factors, 34.6% and 25.7% respectively in the US in 2017 [4]. Without energy storage methods, these processes have difficulty replacing conventional baseload energy generation processes that have higher capacity factors, such as natural gas, 51.3% , and coal, 53.7%, [5], [6]. When renewable energy is generated, the output is variable, and peak power output does not usually correspond to times of peak electricity demand [6]. There are some renewable energy generation processes that have more consistent power production with high capacity factors that can be used for baseload power production. These processes include nuclear, geothermal, and hydro, that have capacity factors of 92.2%, 43.1%, and 74.0% respectively.

In the transition to renewable electricity generation, the Canadian province of Alberta is phasing out coal power plants and plans to generate 30% of its electricity needs from renewables by 2030 [7]. This capacity of baseload electricity generation from coal power plants will need to be replaced. This could partially be accomplished by electricity generation from geothermal and waste heat electricity generation.

Alberta has been shown to have an extremely large geothermal potential of low-grade heat at or below a temperature of 150 °C [8]. This low-grade geothermal heat could be accessed through the

approximately 155,000 oil wells that are no longer producing oil in Alberta [9]. These wells could be retrofitted to produce geothermal heat electricity allowing these facilities to be repurposed.

Electricity can also be generated from waste heat from thermally intensive industrial processes. It has been shown that the Industrial Heartland of Edmonton and Strathcona have an estimated 293 MW of sensible heat available for conversion to electricity [10]. The steam assisted gravity drainage (SAGD) process used in the production of heavy bitumen in Alberta uses 408 PJ of heat energy to make steam each year [11]. There are also many other industrial processes that have waste heat streams and have invested heavily in calling technology that could be repurposed for electricity production.

Technologies that can produce electricity from a temperature difference include the organic Rankine cycle (ORC) [12], thermoelectric generators (TEG) [13], and Stirling engines [14]. There already exists commercial available options for all three listed technologies [12]–[14]. Only the ORC has a current commercially available options (i.e. the Power+ Generator 4200 by Electratherm) that can produce electricity off a temperature difference of less than 150 °C [12]. There currently exists a market for low-cost electricity generation from low grade heat. Stirling engines may be able to fill this void because of their inherent simplicity requires no pumps, valves or turbines unlike the organic Rankine cycle [15]. The TEGs are further simpler than the Stirling engine However, there maximum thermal efficiencies are dependent on both the materials used and the temperature of the thermal source and sink [16].

Since all heat engines operate off of a temperature difference between a thermal source and sink to produce power, if the thermal source temperature is fixed, then the lowest thermal sink temperature is desired. In most cases, the thermal sink used to reject heat is the ambient air. Alberta has a benefit of having a high latitude, which yields a calculated average yearlong air temperature of approximately 5 °C [17]. The opportunity to generate electricity by using low grade geothermal and waste heat has potential in Alberta.

## 1.2 The Ideal Stirling Cycle

The ideal Stirling cycle is a closed thermodynamic cycle [18]. This cycle requires four components which are listed below and visualized in Figure 1.1 [19], [20].

1. Work space: a sealed volume that has the ability to change its volume, with the volume change typically accomplished with a piston-cylinder system
2. Working fluid: a fluid, typically a gas, contained within the work space that can be heated, expanded, cooled, and compressed.
3. Thermal source: a heat source to provide heat to the working fluid.
4. Thermal sink: a heat sink to reject heat from the working fluid.

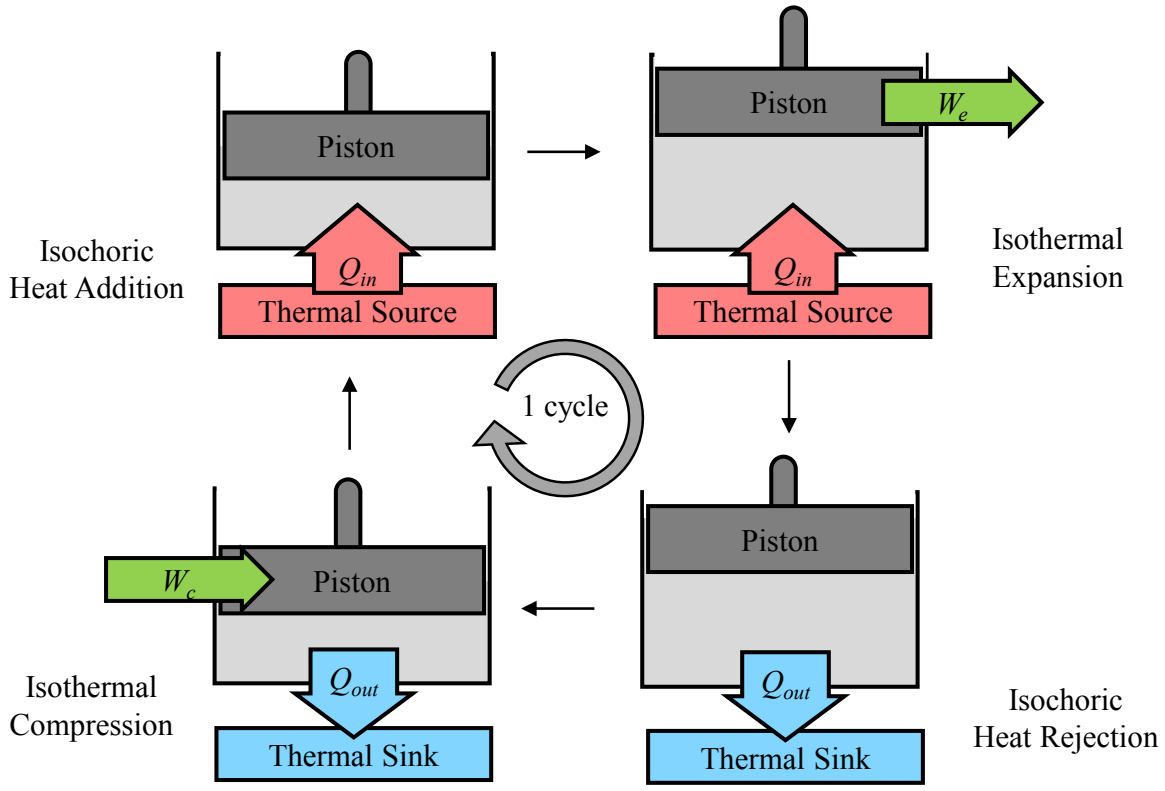


Figure 1.1 Schematic of the four thermodynamic processes that occur during the idealized Stirling cycle: isochoric heat addition, isothermal expansion, isochoric heat rejection, and isothermal compression.

Throughout one complete thermodynamic cycle, the working fluid contained inside the work space undergoes four sequential reversible thermodynamic processes [19], [21]. These processed are listed and explained below and are depicted in Figure 1.1.

### 1.2.1 Isochoric Heat Addition

During the isochoric heat addition thermodynamic process, the work space is held at its minimum volume, while heat in, $Q_{in}$, is added to the working fluid from the thermal source. The heat transferred into the working fluid from the thermal source increases the pressure of the work space, referred to as the working pressure, to its cycle maximum [19], [21].

### 1.2.2 Isothermal Expansion

During the isothermal expansion thermodynamic process, and expansions work, $W_e$, is done by the engine [20], [22]. The work space begins at its minimum volume, and then increases to its maximum volume. As the volume is increased the temperature of the working fluid stays constant at the temperature of the thermal source [19], [21].

### 1.2.3 Isochoric Heat Rejection

During the isochoric heat rejection thermodynamic process, the work space is held at its maximum volume, while heat out, $Q_{out}$, is rejected from the working fluid to the thermal sink during this constant volume process. The heat transferred from the working fluid to the thermal sink decreases the working pressure of the work space to its cycle minimum [19], [21].

### 1.2.4 Isothermal Compression

During the isothermal compression thermodynamic process, compression work, $W_c$, is done to the engine [20], [22]. The work space begins at its maximum volume, and then decreases to its minimum volume. As the volume decreases the temperature of the working fluid stays constant at the thermal sink's temperature [19], [21]

### 1.2.5 Indicator Diagram and Indicated Work

The most common method to visualize a thermodynamic cycle is with a pressure-volume (PV) diagram, which is commonly referred to as an indicator diagram [22]. As illustrated in Figure 1.2, when the four distinct thermodynamic processes are plotted using their change in both pressure and volume, the indicator diagram can be visualized. The area enclosed between the curves of the indicator diagram is equal to the indicated work per cycle [20].

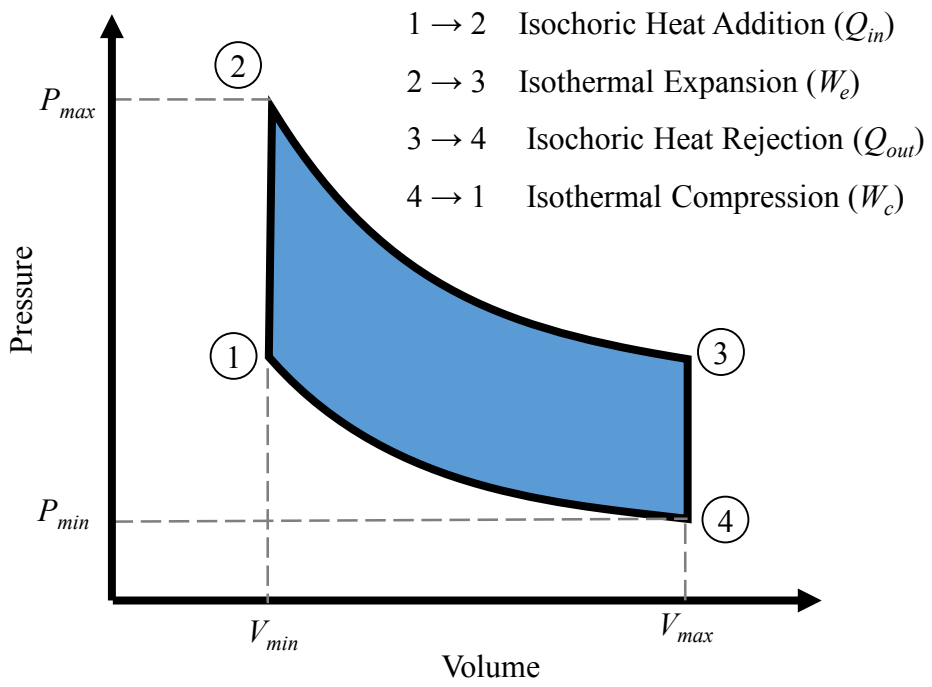


Figure 1.2 Indicator diagram of the idealized Stirling cycle.

The indicated work is determined by calculating the expansion and compression work [20]. Equation 1.1 is used to determine the expansion work, $W_e$. This integral determines the area directly underneath the pressure curve of the expansion process, $P_e(V)$, down to zero pressure from the engines minimum volume, $V_{min}$, to the maximum volume, $V_{max}$, as seen in Figure 1.3(a) [20]. Similarly, the compression work, $W_c$, is determined using Equation 1.2. This integral calculates the area directly underneath the pressure curve of the compression process, $P_c(V)$, down to zero pressure, and from the engine's maximum volume, $V_{max}$, to its minimum volume, $V_{min}$, which is showcased in Figure 1.3(b) [20]. Finally, Equation 1.3 shows that by adding the compression work

from the expansion work, the indicated work, $W_{ind}$, can be calculated [20]. The indicated work is illustrated in Figure 1.3(c) as the difference between the expansion and compression work [20].

$$W_e = \oint_{V_{min}}^{V_{max}} P_e(V_{ws})dV \tag{1.1}$$

$$W_c = \oint_{V_{max}}^{V_{min}} P_c(V_{ws})dV \tag{1.2}$$

$$W_{ind} = W_e + W_c \tag{1.3}$$

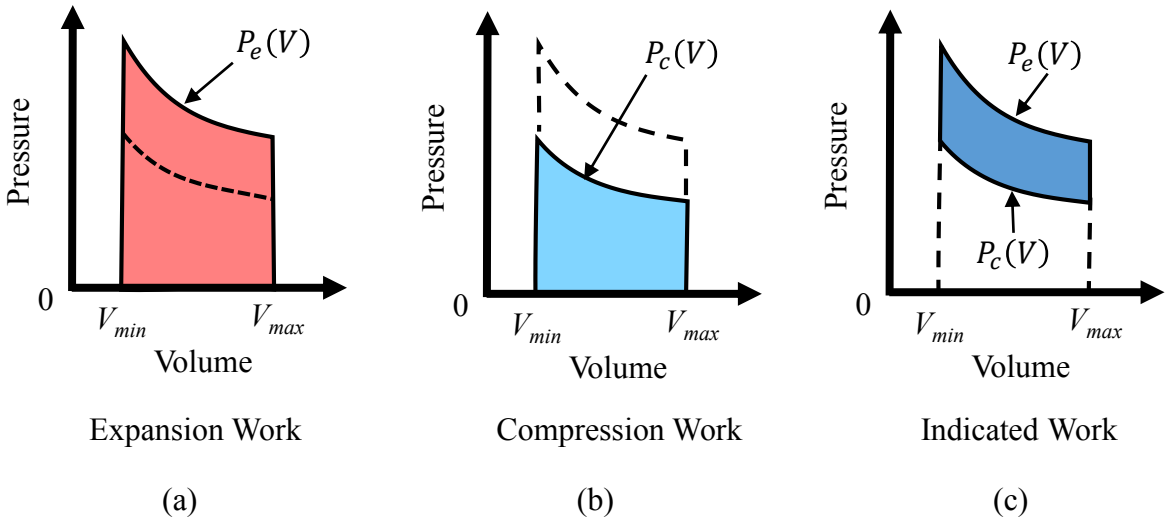


Figure 1.3 Schematic showing the areas of the indicator diagram that represent the (a) expansion work, (b) compression work, and (c) indicated work, modified from [20].

Since the four thermodynamic process showcased above are reversible, the ideal Stirling cycle's maximum efficiency is equal to the carnot efficiency [21]. Equation 1.4 showcases how the thermal efficiency, $\eta_{th}$, of the ideal Stirling engine is a function of the thermal sink temperature, $T_C$, and thermal source temperature, $T_H$ [21].

$$\eta_{th} = 1 - \frac{T_C}{T_H} \tag{1.4}$$

## 1.3 Application of the Ideal Stirling Cycle

For the Stirling cycle to be realized, additional components are required. The following explanation of the application of the ideal Stirling cycle will only be for a gamma-type Stirling engine with a discontinuous mechanism used to move the piston. This thesis will focus on the gamma-type Stirling engine as they are the most common Stirling engine used for low temperature differential (LTD) applications [23]. The following section provides an explanation of how a Stirling engine operates as defined by West [22]. The main components of a gamma-type Stirling are listed below and visualized in Figure 1.4.

1. A displacer piston and cylinder to transport the working fluid through the heat exchangers,
2. Heat exchangers to transfer heat from the thermal source to the working fluid and from the working fluid to the thermal sink,
3. A displacer piston and cylinder to transport the working fluid through the heat exchangers,
4. A regenerator to receive, store and return heat from/to the working fluid, and
5. A power piston and cylinder to change the volume of the engine.

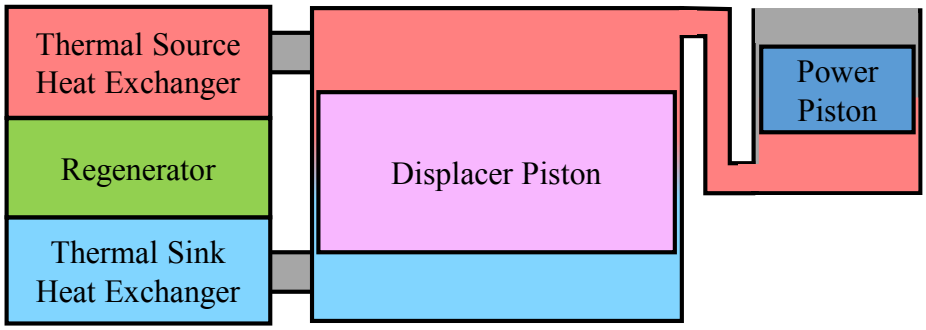


Figure 1.4 Schematic of the main components in a gamma-type Stirling engine.

### 1.3.1 Displacer Piston and Cylinder

The displacer piston system moves the working fluid throughout the work space, so that it can be heated and cooled by interacting with the heat exchangers and regenerator. Figure 1.5 shows a schematic of the displacer piston and cylinder and additional relevant components such as the flow duct, and a pressure gauge for the work space. An increase in the working pressure is represented by a clockwise rotation of the needle on the pressure gauge. The displacer piston can move from

top dead center (TDC) to bottom dead center (BDC) inside its cylinder. This movement of the displacer piston causes the working fluid in the displacer cylinder to travel through the flow duct to the other side of the displacer cylinder. Without any heat exchangers, this motion of the displacer piston does not affect the temperature of the working fluid and therefore the pressure of the working fluid remains constant. If frictional effects and other losses are ignored, no work occurs when the displacer piston is moved.

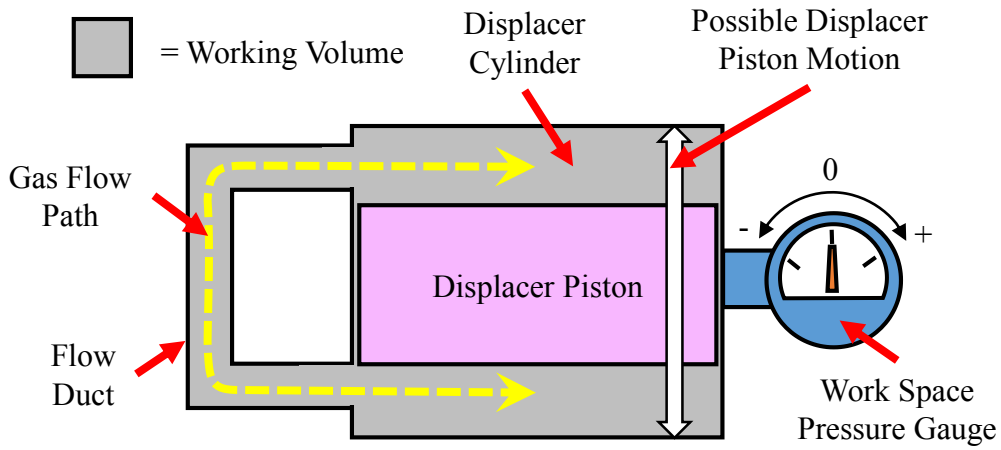


Figure 1.5 Schematic of the displacer piston system in a Stirling engine with the displacer piston located at mid-stroke inside the displacer cylinder modified from [15].

### 1.3.2 Heat Exchangers

Heat exchangers allow the working fluid to be heated from the thermal source and cooled by the thermal sink. Figure 1.6 illustrates that the work space contains the working fluid that has been heated by the thermal source heat exchanger is the expansion space, with the opposite case yielding the definition of the compression space. The heating and cooling of the working fluid corresponds to an increase or decrease in the working pressure displayed in Figure 1.7. When the displacer piston is moved to top dead center, the working fluid exits the thermal sink heat exchanger and fills the displacer cylinder with the cold working fluid. Since the work space primarily contains this cold working fluid, the pressure inside the work space decreases. This same process happens when the displacer piston is moved to bottom dead center, but now the working fluid is heated by the thermal source and therefore the work space pressure increases displacer in Figure 1.7.

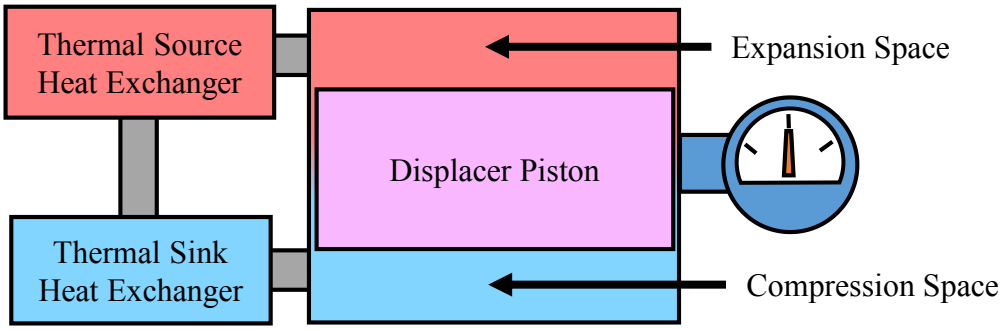


Figure 1.6 Schematic of the combination of the displacer piston and heat exchanger system that showcases the expansion space and compression space.

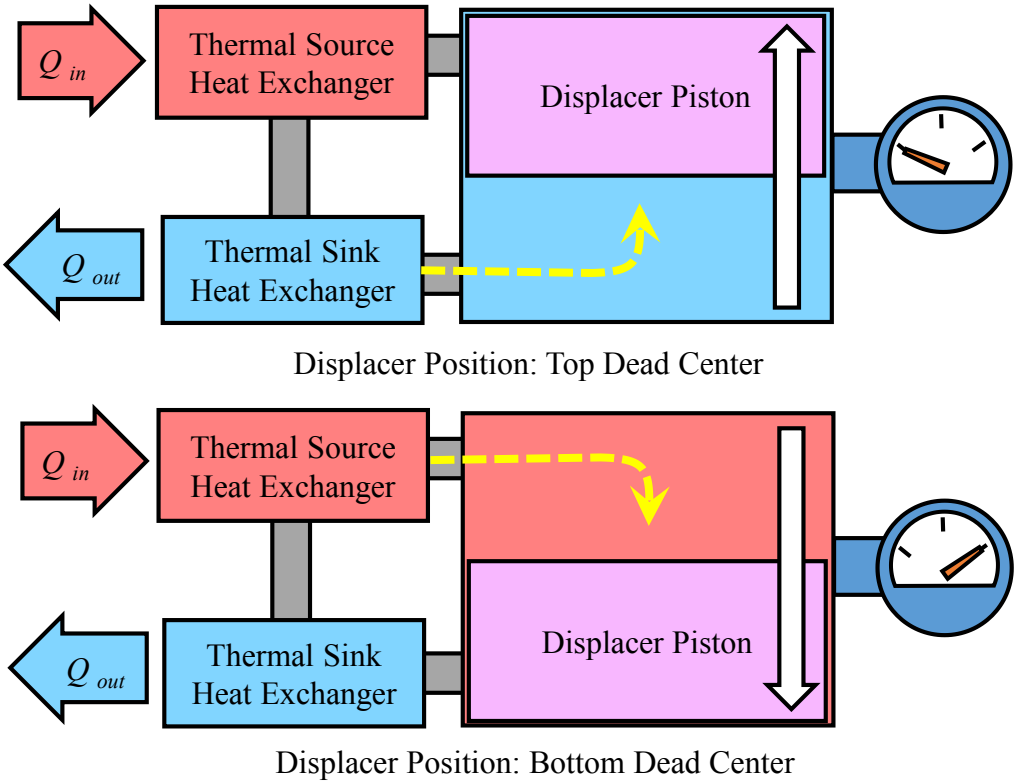


Figure 1.7 Schematic of the combination of the displacer piston and heat exchanger system that showcases how the working pressure of the work space changes when the displacer piston is moved.

### 1.3.3 Regenerator

When the displacer piston moves from bottom dead center to top dead center, the working fluid has to travel back through the same heat exchanger it just exited before it can travel through the other heat exchanger. In the case of the working fluid leaving the expansions space, the working fluid could be heated even more by the thermal source heat exchanger before it travels through the thermal sink heat exchanger to be cooled, with the opposite happening when the working fluid is exiting the compression space. This additional heating and cooling of the working fluid leads to a decrease in performance because of the increased thermal load imposed on the heat exchangers. To utilize this stored in the working fluid a regenerator can be implemented.

The regenerator is an additional heat exchanger and heat storage device in a Stirling engine. The location of the regenerator between the thermal source and sink heat exchangers is presented in Figure 1.8. In the case when the working fluid is exiting the expansion space, it travels through the thermal source heat exchanger and then through a regenerator before traveling through the thermal sink heat exchanger. Shown in Figure 1.8, as the working fluid travels through the regenerator it transfers heat to the regenerator; this pre-cools the working fluid before it travels through the thermal sink heat exchanger, this is referred to as hot blow [15]. The transferred heat is then stored in the regenerator. Cold blow then happens and the working fluid exits the compression space, and travels back through the thermal sink heat exchanger and then through the regenerator [15]. The heat stored in the regenerator is then transferred back into the working fluid and pre-heats the working fluid before it travels through the thermal source heat exchanger. The process is repeated throughout each engine cycle.

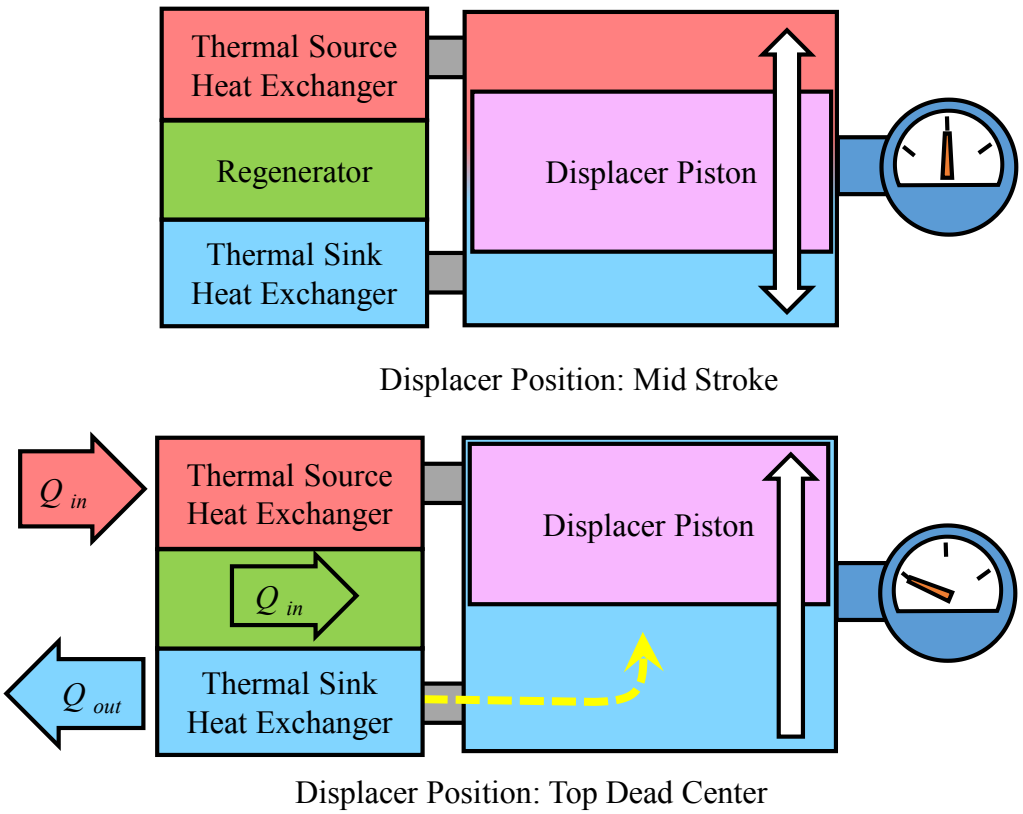


Figure 1.8 Schematic of how the regenerator system is able to transfer and store heat.

### 1.3.4 Power Piston

The power piston performs work in and out of the Stirling engine. This is done by the power piston changing the volume of the work space. Figure 1.9 shows that when the working pressure increases, due to the working fluid being heat, the power piston system increases the work space and expansion work occurs. Compression work occurs for the opposite case as presented in Figure 1.10. In the idealized Stirling cycle, the motion of both the power and displacer pistons sequential and independent of one another. This motion of each piston throughout a cycle can be seen in Figure 1.11. This figure showcases the phase offset of movement of the displacer piston relative to the power piston by a quarter of a cycle.

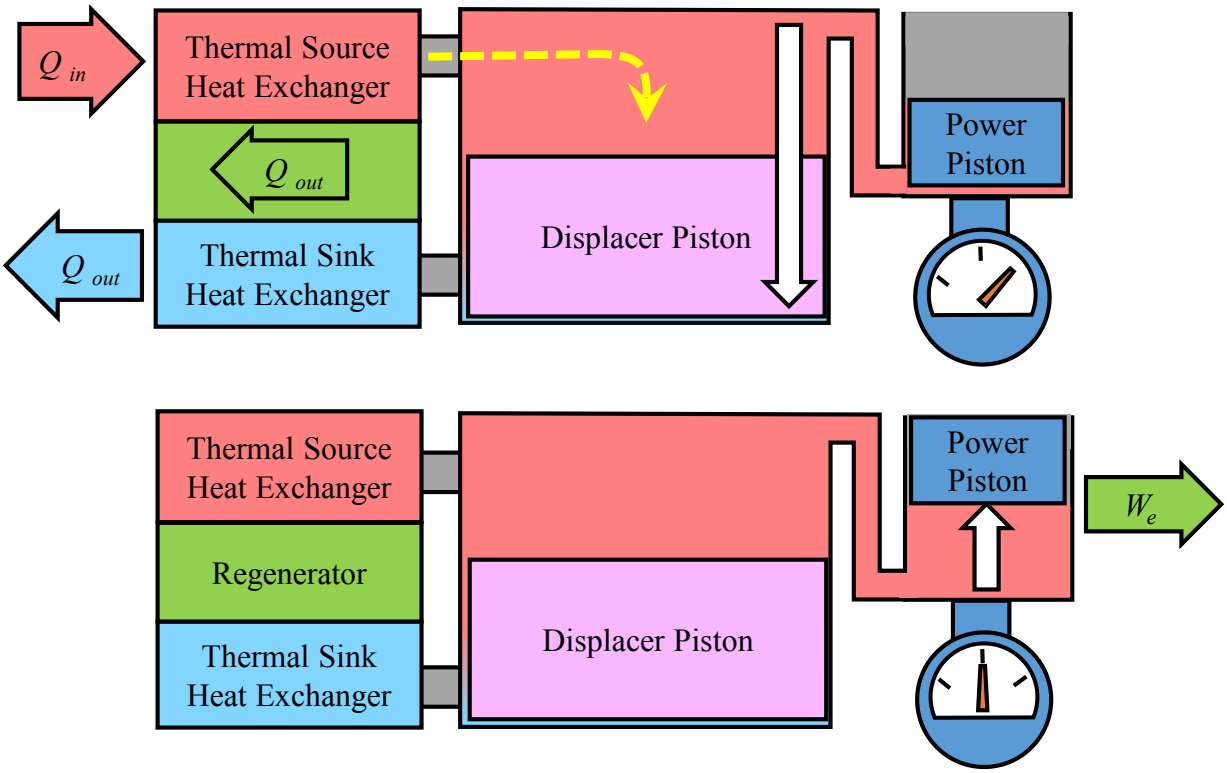


Figure 1.9 Schematic of how the power piston system is able to change the volume of the work space when the working fluid is heated.

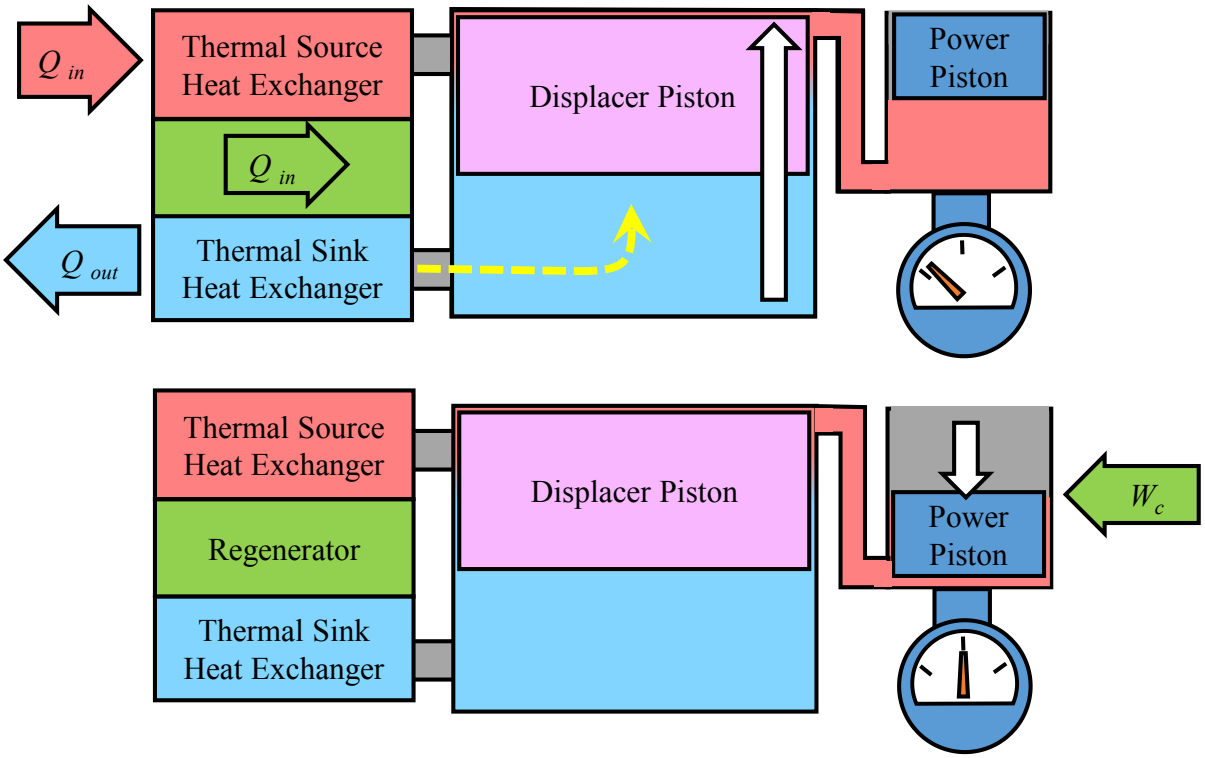


Figure 1.10 Schematic of how the power piston system is able to change the volume of the work space when the working fluid is cooled.

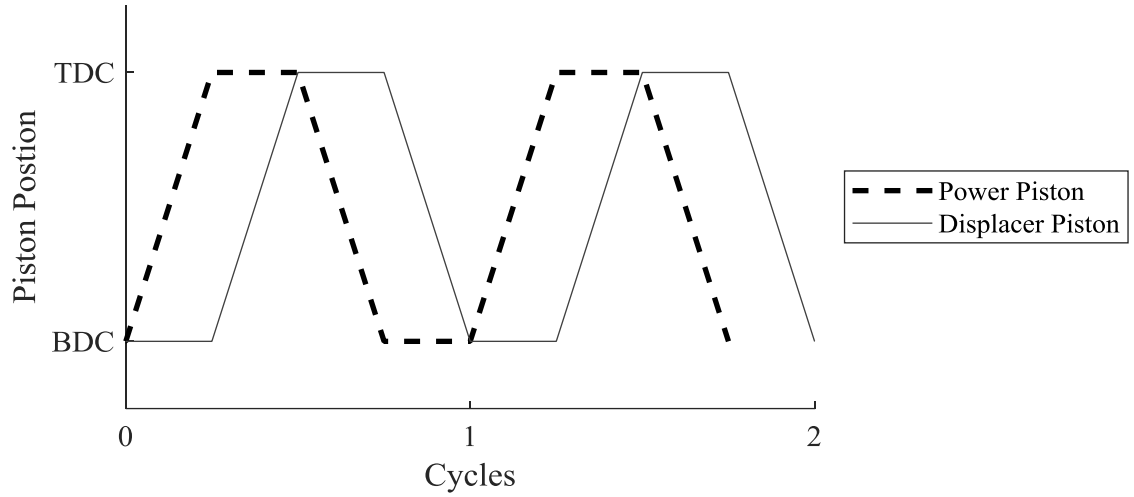

Figure 1.11 Motion of the displacer and power piston movement in an ideal Stirling cycle.

## 1.4 Stirling Engine Types

There exists a number of types of Stirling engines based on the arrangement and size of the displacer and power pistons. Of these are three main engines types termed: alphas, betas, and gammas [19]. Beta-types are nearly identical to gamma-types except that the displacer and power piston share the same cylinder [19]. Alpha-types use two piston, both of which transport the working fluid through the heat exchangers and change the work space volume [19]. A schematic of the alpha and beta Stirling engines is presented in Figure 1.12(a) and Figure 1.12(b). A summary of some the types of Stirling engine can be seen below, with an emphasis on the different types of gamma-types shown.

1. Gamma (Power piston and displacer piston each have separate cylinders)
    a. Kinematic (Kinematically coupled power and displacer piston)[21]
    b. Ringbom (Kinematic power piston, and free displacer piston) [20]
    c. Martini (Kinematic displacer piston and free power piston) [24]
    d. Free Piston (Free power and displacer piston) [21]
    e. Liquid Piston (Fluid power and displacer piston) [25]
2. Beta (Power piston and displacer piston both share the same cylinder)
3. Alpha (Two pistons two separate cylinders and seals)

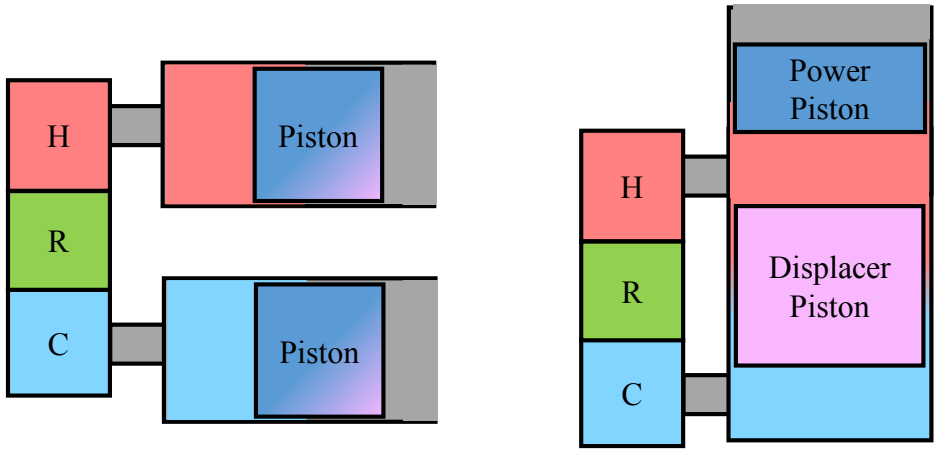


(a) (b)

Figure 1.12 Two types of Stirling engines (a) alpha and (b) beta.

## 1.5 The Practical Stirling Cycle

The practical case of the Stirling cycle for a kinematic gamma-type Stirling engine sees the motion of the displacer and power piston kinematically linked to one another [19]. Each piston is typically driven with a slider-crank mechanism, which produces a continuous, near sinusoidal motion of the pistons [19], as illustrated in Figure 1.13. The slider-crank mechanisms for each piston are then linked together by using the same crankshaft [19]. To produce the constant rotational motion of the engine, a quarter cycle lag of the power piston's motion relative to the displacer piston is imposed, and is termed the phase angle [22] of the engine.

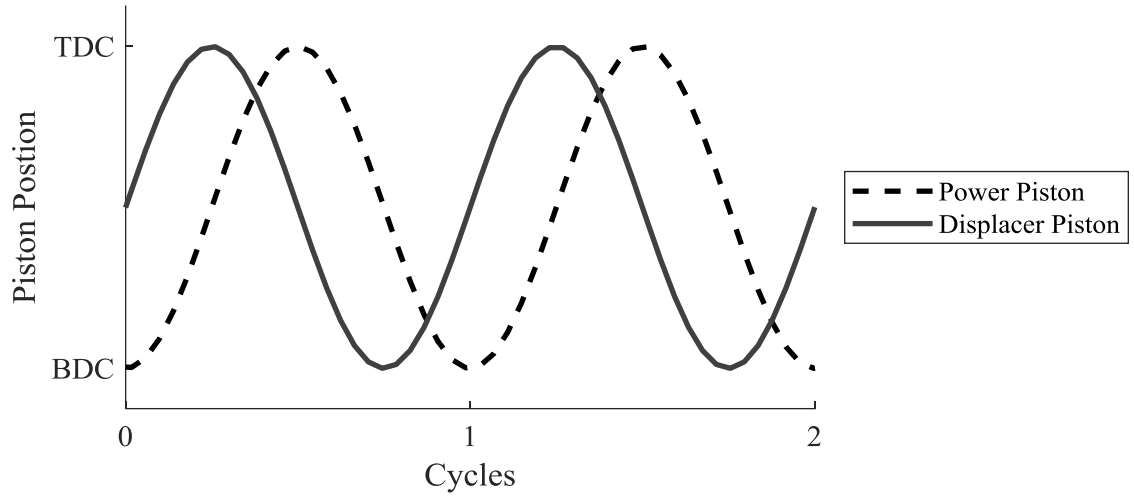


Figure 1.13 Motion of the displacer and power piston movement in the practical Stirling cycle.

### 1.5.1 Phase Angle

The phase angle is the motion lag of the power piston relative to the power piston [22]. Depending on the location of the heat exchangers relative to the power piston, the displacer piston will either lead or lag the power piston, this results in which direction the Stirling engines spin. Figure 1.14 shows that when the displacer piston is at BDC, and the working fluid primarily resides in the expansion space, with the power piston residing at mid-stroke. Figure 1.14 further displays that as the power piston continues to increase the volume of the engine, it causes the displacer piston to move upward, and when the power piston is at the end of its stroke the displacer piston will be at

its mid stroke. This means that the thermodynamic processes now overlap one another which leads to changes in the shape of the indicator diagram [21].

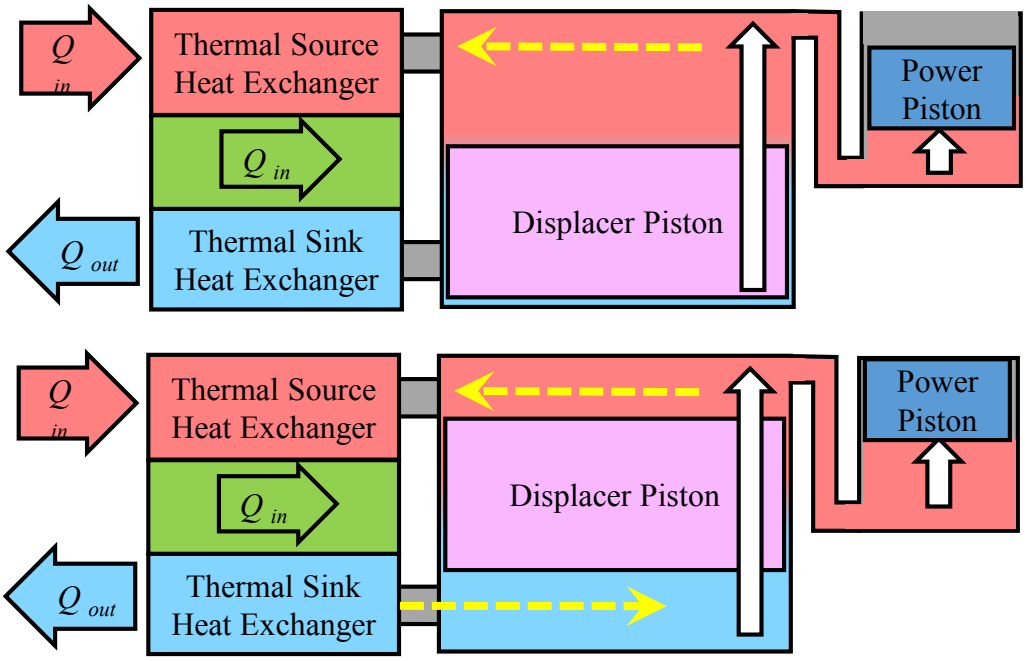


Figure 1.14 Schematic of how the continuous motion of the practical Stirling cycle causes thermodynamic processes to overlap.

### 1.5.2 The Practical Indicator Diagram

The practical Stirling cycle is continuous, and the thermodynamic processes overlap one another, such as expansion and cooling, and compression and heating as depicted in Figure 1.15 [21]. The practical Stirling cycle changes the shape of the indicator diagram compared to the ideal Stirling cycle [22]. Figure 1.16 shows how the shape of the indicator diagrams becomes rounded for the practical case. The mathematical description of indicated work and the engine efficiency presented earlier stays the same for the practical indicator diagram[20].

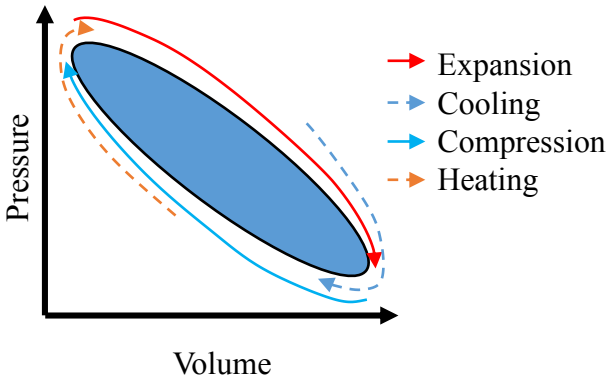


Figure 1.15 Overlapping of thermodynamic process in the practical Stirling cycle.

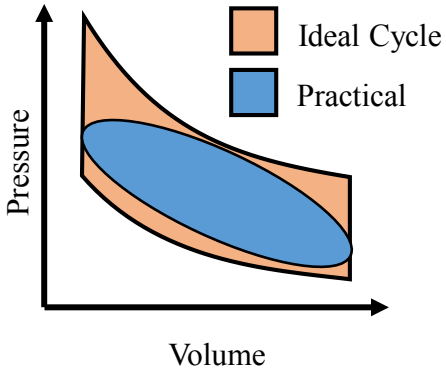


Figure 1.16 Comparison of the indicator diagrams of the ideal Stirling cycle and the actual Stirling cycle.

## 1.6 Stirling Engine Operating Parameters

There exists many different parameters of a Stirling engine that can be changed to optimize its performance [20], [26], [27]. These parameters can be specific to the overall engine or individual components as showcased in Figure 1.17. Only the compression ratio, phase angle, and power piston location will be covered in greater detail in the following section as they are the focus of this thesis. These parameters are were chosen because they strongly influence the initial design of the Stirling engine in deciding on the basic size and scale of major components.

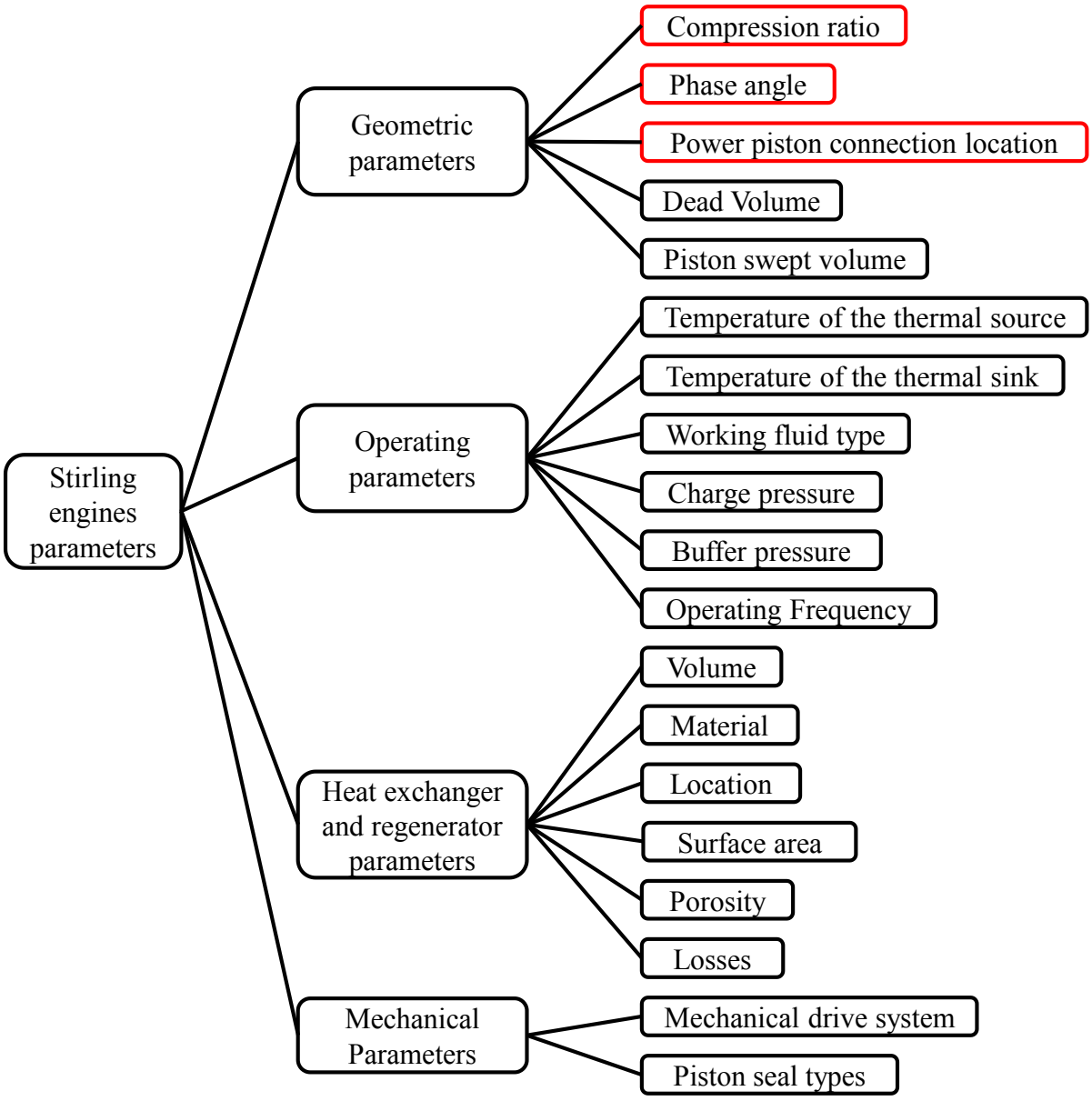


Figure 1.17 Parameters of a Stirling engine that can change its performance modified from [26]

### 1.6.1 Compression Ratio

The compression ratio (*CR*) of a Stirling engine is the ratio of the maximum and minimum engine volume [19]. The compression ratio of a Stirling is governed by the volume swept by displacer and power piston, and the dead volume of the engine. Dead volume corresponds to any volume of the Stirling engine that is not swept by either piston. This volumes can include: heat exchangers, regenerators, flow ducts, and clearance volumes [28]. The compression ratio can be calculated from the maximum engine volume, $V_{max}$, and the minimum engine volume, $V_{min}$, shown in Equation 1.5 [19]. Methods to estimate the optimal compression ratio are provided in Chapter 2.

$$CR = \frac{V_{max}}{V_{min}} \tag{1.5}$$

### 1.6.2 Phase Angle

For a gamma-type Stirling engine, a phase angle value of 90° produces the maximum possible indicated work [19]. However, a small increase in the theoretical shaft work can sometimes been seen for phase angles less than 90° for Stirling engines with a low-temperature difference because of the effects of forced work [20]. The theoretical performance gain from optimizing the phase angle is usually small compared to the performance gain from compression ratio optimization [20].

### 1.6.3 Power Piston Location

In this thesis, the power piston location in a Stirling engine will refer to where the power piston is located relative to each heat exchanger. The power piston can either be connected so it interacts with the hot gas in the expansion space, or the cold gas in the compression space. Through analytical means, Kentfield [27] showed that having the power piston connected to the expansion space yielded a larger amount of specific work than when the power piston was connected to the compression space. The increase in specific work was a function of the temperature ratio between the thermal source and sink, with the increase in specific work being small for small temperature ratios.

## 1.7 Energy Transfer throughout the Practical Stirling Cycle

Throughout the Stirling cycle the transfer of energy in the engine is dependent on the indicator diagram, buffer pressure, and mechanical losses of the engine [20]. Energy can be both transferred out of and into the Stirling engine through the cycle [20]. Understanding mechanical interactions and energy transfers are critical to the design of Stirling engines. The following section will provide an overview of the energy transfers throughout the Stirling cycle as described by Senft [20]. Figure 1.17 showcases these energy transfers.

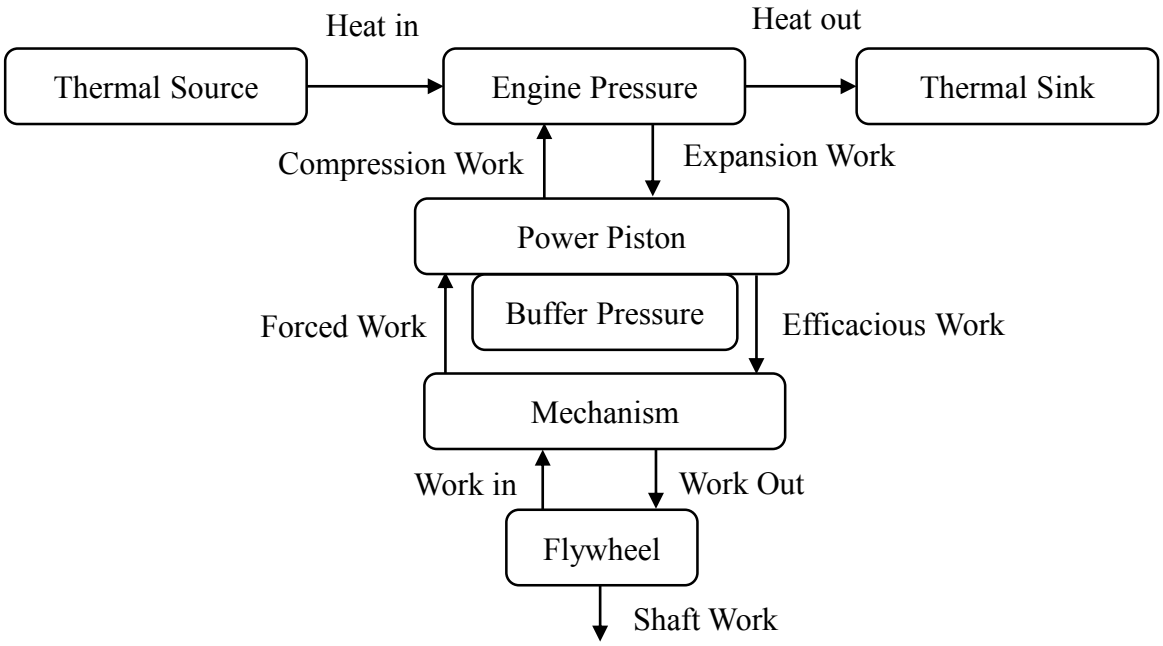


Figure 1.18 Block diagram of the showcasing the energy transfers that occur in a Stirling engine throughout its cycle, modified from [20].

### 1.7.1 Buffer Pressure

The buffer pressure is the pressure that acts external on the Stirling engine. This buffer pressure is a property of the buffer space. The buffer space is the volume external to the Stirling engine, being either a finite vessel or a practically infinite volume such as the atmosphere.

The buffer pressure has a significant impact on the energy transfer in the Stirling cycle. It changes the areas of the cycle when work can be stored as rotational energy in the flywheel, and when

energy must be removed from the flywheel and returned to the engine. With atmospheric buffer spaces, the buffer pressure is nearly constant throughout the cycle and is typically equal to the mean pressure of the cycle as depicted in Figure 1.18(a). However, with internally charged Stirling engines, the buffer space usually takes the form of a finite volume pressure vessel. Since the volume is finite, a change in the work space also produces the opposite change in the buffer space volume, which changes its pressure. Therefore, the buffer pressure is a function of the work space which is shown in Figure 1.18(b).

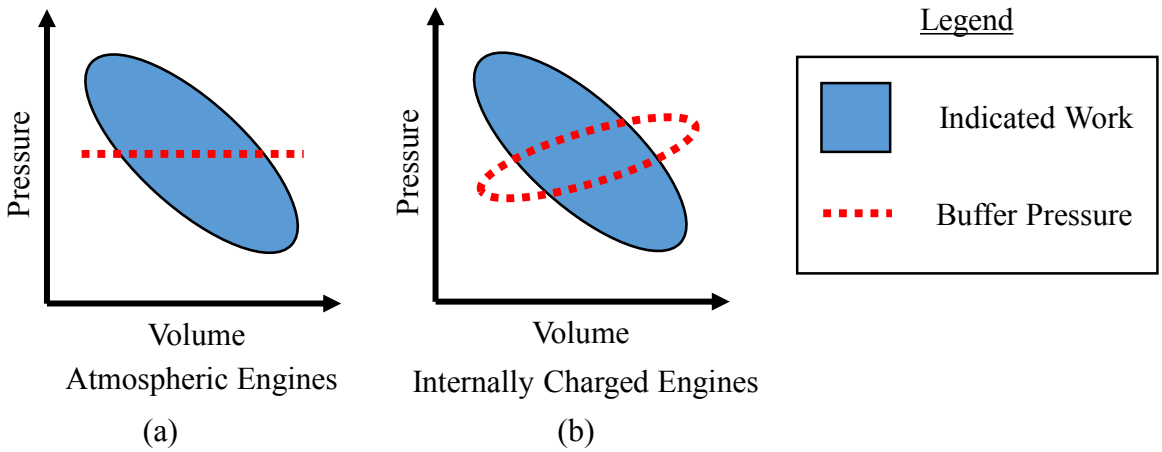


Figure 1.19 Schematic showing the typical buffer pressure profiles for (a) an atmospheric Stirling engine and (b) an internally charged Stirling engine.

### 1.7.2 Efficacious and Forced Work

During parts of the cycle where the working pressure is greater than the buffer pressure and the work space is increasing, efficacious expansion work, as termed by Senft[20], occurs. Similarly, where the working pressure is less than the buffer pressure and the work space is decreasing work, efficacious compression work occurs. Figure 1.19(b) displays the areas of efficacious expansion and compression work as compared to the typical area of indicated work in Figure 1.19(a). Throughout parts of the cycle where the working pressure is greater than the buffer pressure and the work space is decreasing, forced compression work occurs; likewise, where the working pressure is less than the buffer pressure and the work space is increasing, expansion forced work occurs as shown in Figure 1.19(c). By knowing the buffer pressure profile, the areas of efficacious and forced work can be determined.

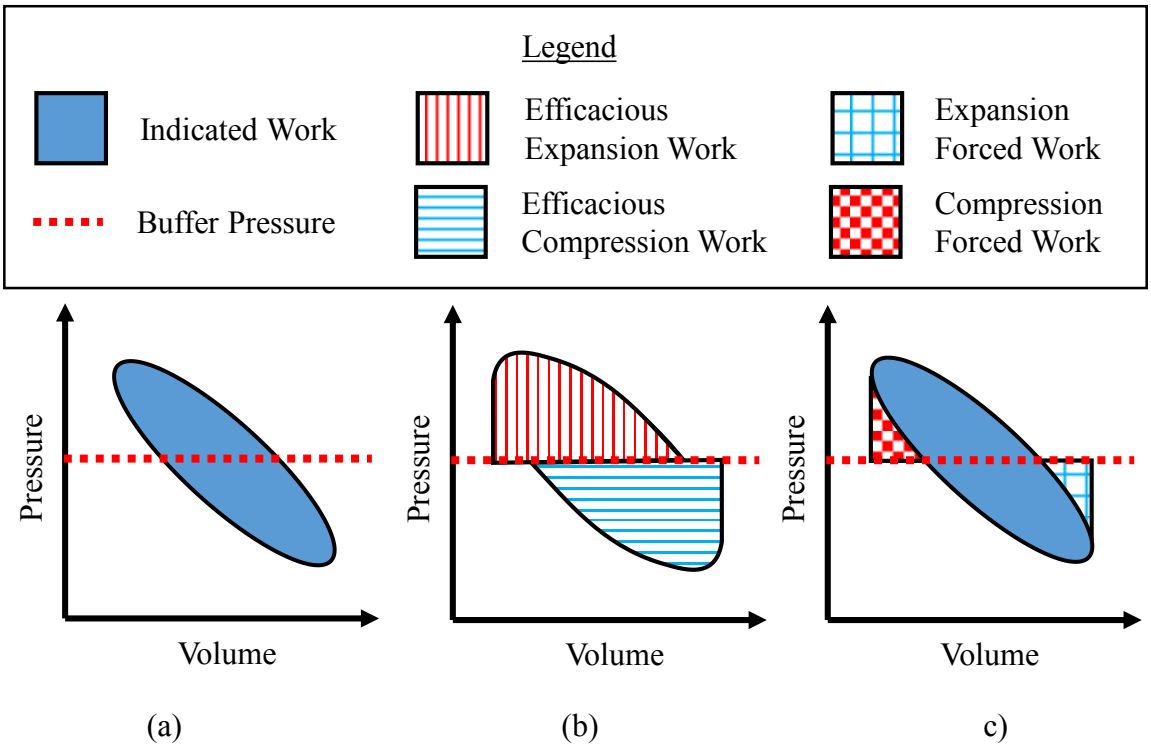


Figure 1.20 Schematic showing the different types of work that occur during the Stirling cycle based on the indicator diagram and buffer pressure profile.

### 1.7.3 Mechanism Effectiveness

The mechanism effectiveness is the instantaneous mechanical efficiency of a kinematic heat engine mechanism. By applying a differential pressure to the power piston face, a torque can be measured on the crankshaft. In an ideal case, the torque measured on the crankshaft would be equal to the force applied at the power piston multiplied by the moment arm. However, in the actual case, the force multiplied by the moment arm is greater than the torque measured at the crankshaft. This ratio of the actual torque and the ideal torque is termed the mechanism effectiveness. This loss in torque is caused by mechanical friction losses in the mechanism such as bearing, piston seals, etc.

### 1.7.4 Work Out, Work In

Work out, is work that is transferred to the flywheel during and is based on the mechanism effectiveness and efficacious work. Efficacious work has to travel through the mechanism, and therefore has a loss associated with it, before it can either be stored in the flywheel.

Work in, is work that is transferred from the flywheel back to the Stirling engine, and is based on the mechanism effectiveness and the forced work. During periods of forced work, a work input is required for the cycle to continue. This work input comes from the stored energy in the flywheel and is transmitted back through the mechanism and again suffers a loss due to the mechanism effectiveness.

### 1.7.5 Shaft Work

Shaft work is the work that leaves the Stirling engine. It is a function of both the work in and out of the flywheel. If more shaft work is extracted from the engine then the requirements of the work in, the cycle will stop operation.

## 1.8 Stirling Engine Performance Characterization

The performance of a Stirling engines can be characterized with direct output comparisons and non-dimensional correlations. Direct output comparisons such as indicated and shaft power are useful when Stirling engines are to be directly compared [22]. Non-dimensional correlations such as the Beale and West numbers are useful if Stirling engines that use different geometries, sizes, and temperatures differences are to be compared and are presented in Chapter 2 [22].

### 1.8.1 Indicated Power

The indicated power is an output of the Stirling engine cycle that can be used to characterize its thermodynamic performance [22]. Equation 1.6 shows that indicated power, $P_{ind}$, is equal to the indicated work, $W_{ind}$, multiplied with the engine operating frequency $f$. In general, a larger indicated power usually equates to a better performing or geometrically larger Stirling engine [22]. It may also correlate to a Stirling engine that operates with a higher frequency or a larger temperature difference between the thermal source and sink [22]. Using the indicated power for performance characterization is not accurate because it does not represent the power that can be extracted from the shaft of the Stirling engine due to neglecting mechanical losses[20].

$$P_{ind} = W_{ind} \times f \tag{1.6}$$

### 1.8.2 Shaft Power

The shaft power is the most practical method to directly characterize the performance of a Stirling engine [22]. Shaft power, $P_{shaft}$, is the product of the shaft work, $W_{shaft}$, and the engine's loaded operating frequency $f$ as displayed in Equation 1.7 [22]. The shaft work, $W_{shaft}$, can be determined directly from the average shaft torque output, $\tau_{shaft}$, and the distance it acts through in one cycle (two pi radians) as shown in Equation 1.8. Also, if torque cannot be measured directly, an indirect method to determine the shaft work by using the fundamental efficiency theorem can be used[20]. This is done by loading the engine and determining the experimental indicator diagram. Equation 1.9 then uses the indicated work, $W_{ind}$, and forced work $W_{for}$, and coupling them with the

engine's and mechanism effectiveness *E* as seen in. The accuracy of this approach is dependent on the accuracy of the mechanism effectiveness[20].

$$P_{shaft} = W_{shaft} \times f \tag{1.7}$$

$$W_{shaft} = \tau_{shaft} \times 2\pi \tag{1.8}$$

$$W_{shaft} = (W_{ind} \times E - \left(\frac{1}{E} - E\right) \times W_{for}) \tag{1.9}$$

## 1.9 Low-Temperature Difference Stirling Engines

The literature was reviewed for gamma-type LTDSE with the focus on the following categories:

- History
- Implementation in geothermal and waste heat applications
- Experimental engines

For this thesis, the definition of a LTDSE will be a Stirling engine that operates with a temperature difference of the source and sink of equal to or less than 150 °C.

### 1.9.1 The Drive to Operate at a Lower Temperature Difference

The journey to reduce the temperature difference that a Stirling engine could operate off was led by Kolin [29] and Senft [29]. In 1980, Kolin [29] showcased a gamma-type Stirling engine that could run off a temperature difference of 44 °C. From 1980 to 1991 this temperature difference was driven even lower and the record of the engine to operate off the lowest temperature difference passed between Senft [29] and Kolin [29]. Finally, in 1991, Senft [29] was able to produce an engine that ran off a temperature difference of 0.5 °C. All the LTDSEs developed by Senft [29] and Kolin [29] were gamma-type, and used flat plate heat exchangers.

### 1.9.2 Geothermal and Low-Grade Waste Heat applications

Power generation from a Stirling engine using geothermal heat was explored. No cases were found that had implemented a Stirling engine system. Instead, suggestions were made that a Stirling engine system could be used, and in some cases the theoretical output of the Stirling engine system was compared to other geothermal power generation processes [30]–[36].

Power generation from a Stirling engine using low-grade waste heat (temperature <150 °C) was explored. Like the geothermal cases, theoretical implementations have also been explored for low-grade waste heat applications [37]–[39]. There has been one implementation of a commercially available Stirling system for low-grade waste heat recovery, the ThermoHeart by Cool energy [40]. This engine can operate with a thermal source temperature of 150-400 °C with a thermal sink of 20 °C that has an output electrical power from 7 to 25 kW.

### 1.9.3 Experimental Engines

When the literature was reviewed for experimental engines, the goal was to find LTDSEs that could be compared to the experimental results in this thesis. This comparison required that the following operating parameters be known:

- Thermal source and sink temperature,
- Buffer Pressure
- Shaft power,
- Operating speed, and
- Power piston swept volume
- Compression ratio or engine volumes.

Six gamma-type LTDSEs were found that had the required properties for comparison. Their operating parameters that produced the maximum shaft power, and their design characteristics are summarized in Table 1.1 and Table 1.2.

A Ringbom LTDSE was designed, built, and tested by Senft [41]. Two working fluid fluids were tested, air and helium. Using helium as the working fluid, a nearly three times increase in shaft power was observed for the same operating speed when compared to air as the working fluid.

Iwamoto [42] performed experiments on a large scale LTDSE. The engine used scotch yoke mechanism for the displacer and power piston. The entire drive mechanism was contained inside a buffer space, and the engine and buffer space could be pressurized.

A LTDSE engine that used two power piston was tested by Kongtragool [43]. It was heated with a halogen lamp. The intensity of the lamp was varied by changing the distance between it and the displacer cylinder of the engine.

Tavakolpour [44] tested a LDTSE that coupled two engines together. The swept volume ratio used by the engine was determined by performing an optimization of the Schmidt model with finite heat transfer to find the swept volume ratio that produced the maximum dimensionless work. The phase angle used by the engine was chosen by using a computer program to find the theoretical maximum indicated work by varying the phase angle.

Kongtragool [45] tested a LTDSE with four power piston that was heated with four tungsten halogen lamps. Various intensity of the lamps were tested. Four power pistons were used because it was easier to manufacturer four smaller power pistons rather than one large one. The regenerator was built into the displacer piston. The maximum lamp intensity tested corresponded to the maximum shaft power.

Cinar [46] tested a LTDSE at various thermal source temperatures — (320, 300, 280, 160, 140 °C), and with two different displacer pistons, aluminum and MDF wood. Over the tested thermal source temperatures and displacer piston types, the maximum shaft power was produced with a thermal source temperature of 160 °C and the MDF displacer piston.

Table 1.1 Literature LTDSE's maximum shaft power and operating parameters.

| Name and Ref | $T_H$ (°C) | $T_C$ (°C) | Working Fluid | Buffer Pressure | Phase Angle (°) | Shaft Power (W) | Speed (rpm) |
|---|---|---|---|---|---|---|---|
| Ringbom [41] | 90 | 10 | Air, Helium | Atmospheric | NA | 0.69 | 113 |
| 300 Watt [42], [47], [48] | 130 | 15 | Air | Atmospheric = 0.1 MPa | 90 | 146 | 143 |
| Two Piston [43] | 163 | 34 | Air | non-pressurized | 90 | 1.69 | 52.1 |
| Two Engine [44] | 110 | 25 | Air | Atmospheric* | 90 | 0.27 | 14 |
| Four Piston [45] | 166 | 34 | Air | Atmospheric | 90 | 6.1 | 20 |
| MDF Displacer [49] | 160 | 25 | Air | Atmospheric | 90 | 3.1 | 214 |

*Assumed to be atmospheric based on the design

Table 1.2 Design characteristics of Literature LTDSE's.

| Name and Ref | Thermal Source | Thermal Sink | Heat Exchanger Type | Power Piston Space Location | Power Piston Swept Volume ($m^3$) | Regenerator |
|---|---|---|---|---|---|---|
| Ringbom [41] | Water | Water | Flat Plate | N/A | 0.00015 | None |
| 300 Watt [42], [47], [48] | Water | Water | Finned Tube | Compression | 0.025133 | Stacked mesh |
| Two Piston [43] | One Halogen Lamp | Water | Flat Plate | Compression | 0.000894 | Holes in Displacer |
| Two Engine [44] | Sun | Water | Flat Plate | Compression | 0.001168 | None |
| Four Piston [45] | Four Halogen Lamps | Water | Flat Plate | Compression | 0.007392 | Holes in Displacer |
| MDF Displacer [49] | Gas Burner | Water | Flat Plate | Compression | 0.000154 | Holes in Displacer |

Other LTDSEs were found in the literature, however they did not provide all the required information necessary for comparison. These other engines included small or "toy sized" and solar heated LTDSE.

All the LTDSEs described are gamma-type. Researchers at Saitima University optimized the performance of the 10 Watt engine by varying the temperature difference and compression ratio [50]. The compression ratio was varied to determine the maximum shaft power output for three thermal source temperatures—130 °C, 110 °C and 80 °C. The compression ratio that produced the maximum shaft power was found to change based on the temperature of thermal source.

Several small or "toy sized" gamma-type LTDSE have been investigated. Lemaire [51] investigated if Stirling engines could be miniaturized to power electronics. Aragon-Gonzalez [52] measured the shaft power and efficiencies of a Ringbom Stirling engine at four temperatures differences — (16,18,20,22 °C). Kwankaomeng [53] investigated making a Stirling engine able to run with a temperature difference less than 10 °C. Kato [54], [55] compared the indicator diagrams

between the use of flat plate and channel heat exchangers in a LTDSE with a 5 times increase in indicated power seen for the channel based heat exchanger. Li [56]compared simulation results with experimental results for various losses in a LTDSE.

Investigation into LTDSE using a non-concentrated solar source has also been explored. Kongtragool [57] correlated the direct normal intensity of sunlight with power output of a Stirling engine. Boutammachte [58] compared the performance of two solar Stirling engines — SSM III and SSM IV. The SSM IV used a cam mechanism to produce near discontinuous motion for the displacer piston which resulted in an increase in the indicated work. Hassani [59] varied the phase angle (30° to 140°) and found an indicated power maximum for a phase angle of 90°, and also varied the compression ratio (1.039,1.045 and1.057) and found an increase in the indicated work for larger compression ratio, but shaft power was not measured. Jokar [60] used a solar gamma Stirling engine with a liquid power piston with a displacer piston that was driven by an electric motor.

Based on the literature reviewed, there currently exists limited knowledge on compression ratio choice and optimization, power piston location, and optimal phase angle of the LTDSE. Important questions that remain unanswered include: How is the compression ratio chosen? What is the compression ratio that will produce the maximum shaft power? Does the location of the power piston change the performance? Will using a phase angle of 90° produce the maximum shaft power? Answering these questions may assist in the future designs of LTDSE.

## 1.10 Thesis Objectives and Structure

The objective of this thesis is to determine the operating parameters of a LTDSE that will produce the maximum shaft power, and to investigate the validity of methods used to estimate the compression ratio. The LTDSE tested will use the following operating parameters:

- Thermal source temperature of 95 °C,
- Thermal sink temperature of 2 °C,
- Working fluid of air, and
- Buffer pressure equal to atmospheric pressure and air

The manipulated operating parameters used to produce the maximum shaft power will be:

- Compression ratio,
- Location of heat exchangers relative to the power piston, and
- Phase angle.

The engine's performance will then be compared to other experimental LTDSEs and thermodynamic models that use similar operating parameters. The West number calculated from various LTDSE will be used to determine the mean West number for LTDSE and how it compares to the mean West number for HTDSEs.

The structure of this thesis will be as follows:

Chapter 2 will showcase the thermodynamic modelling techniques used to compare the performance of Stirling engines and for analytically estimating their performance. It will also showcase methods used to estimate the compression ratio and swept volume ratio to use for a certain operational temperature difference.

Chapter 3 will provide a breakdown of the equipment, data acquisition (DAQ) devices, experimental procedures, data processing techniques, and the uncertainty analysis used.

Chapter 4 will describe three different LTDSE (Mark 1, Mark 2, and EP-1), and showcase their development, performance evaluation (Mark 1 and 2 only), and lessons learned.

Chapter 5 will provide experimental results that show the optimization process for the EP-1 to produce the maximum shaft power by varying the compression ratio, phase angle, and heat exchanger and power piston position. It will also compare the maximum performance of the EP-1 to other experimental engines.

Chapter 6 will investigate the validity of methods used to estimate the optimal compression ratio.

Chapter 7 will provide conclusions on the work completed and suggest any future work required.

# Chapter 2 Stirling Engine Modelling

The following chapter overviews thermodynamic modeling used to predict the performance of a Stirling engine. The models that are explained in detail include the Beale number [61], West number [62], Isothermal model [18], Schmidt model [20], and the fundamental efficiency theorem [20]. The second half of this chapter contains models used to estimate the compression ratio and swept volume ratio of a Stirling engine. These models are Kolin's compression ratio, Egas' ideal compression ratio, and Senft's optimum swept volume ratio. Finally, the chapter ends with the investigation of compression ratios used by experimental LTSDSEs.

## 2.1 Thermodynamic Modelling

To predict the thermodynamic cycle of a Stirling engine, several different models can be used. These thermodynamic models vary in complexity and assumptions, and are described by their order, with the range of orders being from first to third [63]. First order models are typically used to give a rough order of magnitude for the performance of the Stirling engine and use correlations or assume an ideal case with no losses [63]. First order models include the Beale number [61], West Number [62], and the Schmidt model [63]. Second order models assume a simplified engine cycle such as the isothermal model, adiabatic, or semi-adiabatic model, and then subtract losses from the engine cycle independently [63]. Third order models involve one dimensional discretization of the engine into control volumes, usually called nodes, and then applying one-dimensional conservation laws and solving systems of equations to determine the thermodynamic cycle [63]. The following section will only go into detail for the Beale number, West number, isothermal model, and Schmidt model.

### 2.1.1 Beale Number

The Beale number is a non-dimensional performance characterization parameter typically used for high temperature Stirling engines [22]. The Beale number is determined from the shaft power $P_{shaft}$ in units of Watts, absolute root mean pressure, $P_{rm,}$ in units of Pascals, engine operating frequency, $f$, in units of Hz, and the total volume change of the engine — which corresponds the volume swept by the power piston for gamma-type Stirling engines —, $V_{swp,}$ in cubic meters as seen in Equation 2.1 [22]. A typical Beale number for a high temperature Stirling engine that uses a thermal source temperature of 500 °C or greater is 0.15 [22].

$$B_n = \frac{P_{shaft}}{P_{rm} \times f \times V_{swp}} \tag{2.1}$$

### 2.1.2 West Number

To compare the performance of Stirling engines that operate at different source and sink temperatures the West number is used [22]. Equation 2.2 shows that the West number is calculated by adding a temperature correction factor to the Beale number. This temperature correction factor is the ratio of the addition of the temperature of the thermal source, $T_H$, and sink, $T_{C,}$ over the

difference between the thermal source and sink temperatures [22]. The typical value of the West number is 0.25, and is based off the mean value determined from many experimental high temperature difference Stirling engines (HTDSEs) [22].

$$W_n = \frac{P_{shaft}}{P_{mean} \times f \times V_{swp}} \times \frac{(T_H + T_C)}{(T_H - T_C)} = B_n \times \frac{(T_H + T_C)}{(T_H - T_C)} \quad 2.2$$

### 2.1.3 Isothermal Model

The isothermal model is a thermodynamic model used to predict the performance of a Stirling engine. In Figure 2.1, the spatial temperature profile of the working fluid throughout the five different volumes in the Stirling engine is shown. These volumes are the expansion space, heater, regenerator, cooler, and compression space. The following section will showcase the governing equations as derived by Urieli and Berchowitz [18]. The assumptions that the isothermal model makes are listed below [18].

1. The working fluid equates to the temperature of the heat exchanger instantaneously upon entering it
2. The heat exchangers and regenerator have insignificant flow friction
3. Infinite heat transfer occurs within the expansion and compression space to keep the working fluid at the temperature of the thermal source or sink
4. The work space does not leak and therefore the mass of the working fluid is constant
5. The working fluid has a constant specific heat
6. The ideal gas law applies to the working fluid
7. There is no spatial change in pressure throughout the engine
8. Engine pressure is only a function of crank angle
9. The model runs at a cyclical steady state
10. The kinetic and potential energies of the working fluid are ignored

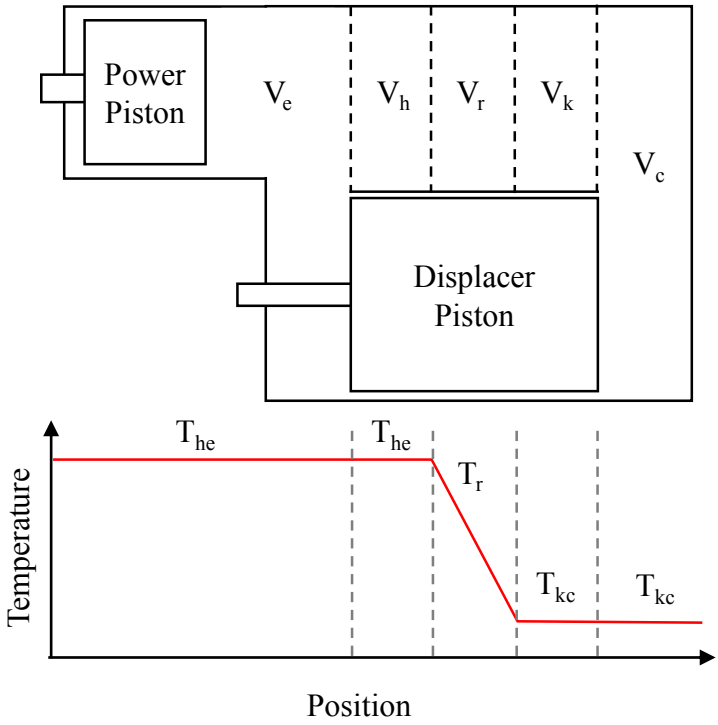


Figure 2.1 Temperatures of the working fluid in certain section of a Stirling engine for the isothermal mode modified from [15].

The pressure inside the Stirling engine is determined using the ideal gas law and conservation of mass and energy. The mass of working fluid, $m_{wf}$, must initially be chosen, and the corresponding ideal gas constant of the working fluid, $R$, used. To produce an indicator diagram with the close to the minimum amount of forced work the mass of gas should be chosen so that the mean pressure produced by the cycle is equal to the expected mean pressure of the buffer space [20]. The temperature of the heater and expansion space, $T_{he}$, and the cooler and compression space, $T_{kc}$, can be chosen to be any value, but are typically the temperature of the thermal source and sink. If the goal is to compare the isothermal model to experimental performance the experimental gas temperatures measured in the expansion and compression space are used. The volume of the heater, cooler, and regenerator are, $V_k$, $V_r$, $V_h$, respectively, and correspond to optional independent sub volumes of the work space. Finally, the volume of the expansion space, $V_e(\Theta)$, and the compression space, $V_c(\Theta)$, as function of the angular crankshaft position are chosen. All these values can be combined to determine the instantaneous pressure of the work space as seen in Equation 2.3.

$$P_{ws}(\theta) = m_{wf} \times R \times \left( \frac{V_c(\theta)}{T_{kc}} + \frac{V_k}{T_{kc}} + \frac{V_r \times \ln(\frac{T_{he}}{T_{kc}})}{T_{he} - T_{kc}} + \frac{V_h}{T_{he}} + \frac{V_e(\theta)}{T_{he}} \right)^{-1} \quad 2.3$$

Equation 2.4 and 2.5 show that the change in volume of the expansion space and compression space are used to calculate the expansion space and compression space indicated work, $W_{es}$ and $W_{cs}$. Additionally, they show that the expansion space work is equal to the heat into the cycle, $Q_{in}$, and likewise the compression space work, $Q_{out}$, equal to the heat out of the engine.

$$Q_{in} = W_{es} = \oint P_{ws}(\theta) \times (\frac{dV_e}{d\theta}) d\theta \quad 2.4$$

$$Q_{out} = W_{cs} = \oint P_{ws}(\theta) \times (\frac{dV_c}{d\theta}) d\theta \quad 2.5$$

The expansion space and compression space indicated work, $W_{es}$, and $W_{cs}$, are added to get the indicated work, $W_{ind}$, of the engine as seen in Equation 2.6. Equation 2.6 also shows that if the volume variations of the work space, $V_{ws}$, is known, the indicated work can be calculated directly using:

$$W_{ind} = W_{es} + W_{cs} = \oint P_{ws}(\theta) \times (\frac{dV_{ws}}{d\theta}) d\theta \quad 2.6$$

The thermal efficiency of the cycle, $\eta_{th}$, is equal to the Carnot efficiency of the cycle based on the temperature of the expansions and compression space used, and can also be determined from the indicated work and the heat input to the cycle as:

$$\eta_{th} = \frac{W_{ind}}{Q_{in}} = 1 - \frac{T_C}{T_H} \quad 2.7$$

### 2.1.4 Schmidt Model

The Schmidt model takes the isothermal model and applies sinusoidal motion to both the displacer and power piston. This sinusoidal motion can produce a numeric closed form solution of the indicator diagram as described by Gustav Schmidt in 1871 [20]. The governing equations of the Schmidt model shown below were derived by Senft [20].

To simplify the equations for instantaneous pressure and volume, and indicated work, Senft created three constants, *X*, *Y*, and, $\varphi$ [20]. Equation 2.8 shows that, *X*, is dependent on three additional constants.

$\kappa$ = the ratio of the power piston swept volume to the displacer piston volume, i.e. the swept volume ratio

$\tau$ = the ratio of the temperature in the expansion and compression space

$\alpha$ = the phase angle between the displacer and power piston cranks arms

$$X = \sqrt{\kappa^2 - 2 \times \kappa \times (1 - \tau) \times \cos(\alpha) + (1 - \tau)\text{^}2} \quad 2.8$$

*Y*, is calculated with Equation 2.9. *Y* is yet again dependent on other constants.

$\chi$ = the ratio of the dead volume (heat exchangers, regenerator, clearance volumes, etc.) to the volume swept by the displacer piston

$$Y = 1 + \tau + \kappa + \frac{4\tau\chi}{1 + \tau} \quad 2.9$$

The final constant, $\varphi$, is derived in Equation 2.10.

$$\varphi = \cos^{-1}\left(\frac{\kappa - (1 - \tau) \times \cos(\alpha)}{X}\right) \quad 2.10$$

Equation 2.11 is used to calculate the instantaneous pressure, $P_{ws}$. This equation is dependent on the constants described above and in the previous isothermal model section, which are: *Y, X*, $\varphi$, $m_{wf}$, $R$, and $T_{CC}$. It is also dependent on the volume swept by the displacer piston, $V_{swd}$, and the instantaneous angular position of the piston crankshaft, $\theta$.

$$P_{ws}(\theta) = \frac{2m_{wf}RT_{kc}}{V_{swd} \times (Y + X\cos(\theta - \varphi))} \quad 2.11$$

Senft [20] calculates the root mean pressure, $P_{rm}$, to simplify the equations for instantaneous pressure further. Calculating the root mean pressure, $P_{rm}$, is useful because it provides a value for the buffer pressure that is close to the optimal value that minimizes forced work[20].

By analyzing Equation 2.11, it can be seen that the maximum cycle pressure, $P_{max}$, corresponds to the point where the cosine function is at its maximum. This is shown in Equation 2.12. A similar analysis can be applied to determine the minimum cycle pressure $P_{min}$, by making that cosine function produces its minimum value shown in Equation 2.13. Finally, with the maximum and minimum cycle pressure, $P_{max}$, and $P_{min}$ being known, Equation 2.14 can be used to determine the root mean pressure, $P_{rm}$.

$$P_{max} = \frac{2m_{wf}RT_{kc}}{V_{swd} \times (Y + X)} \quad 2.12$$

$$P_{min} = \frac{2m_{wf}RT_{kc}}{V_{swd} \times (Y - X)} \quad 2.13$$

$$P_{rm} = \sqrt{P_{max}P_{min}} \quad 2.14$$

Equation 2.15 shows the simplified equation for the instantaneous pressure, $P_{ws}$. This equation is dependent on the constants described above, *Y, X*, and $\varphi$. It is also dependent on the root mean pressure, $P_{rm}$, and the instantaneous angular position of the piston crankshaft, $\theta$.

$$P_{ws}(\theta) = P_{rm}\frac{\sqrt{Y^2 + X^2}}{Y + X\cos(\theta - \varphi)} \quad 2.15$$

The instantaneous engine volume, $V_{ws}$, is solved for using Equation 2.16. It uses the following constants previously discussed, $\kappa$, and, $\chi$. It is also dependent on the total volume swept by the displacer and power piston, $V_{swt}$, and the instantaneous angular position of the piston crankshaft, $\theta$.

$$V_{ws}(\theta) = \frac{V_{swt}}{\kappa + 1}(1 + \frac{\kappa}{2}(+\cos(\theta)) + \chi) \quad 2.16$$

Finally, the closed form indicated work, $W_{ind}$, can be determined in Equation 2.17.

$$W_{ind} = \frac{V_{swt}P_{rm}}{\kappa + 1}\frac{\pi(1 - \tau)\kappa\sin(\alpha)}{\sqrt{Y^2 - X^2} + Y} \quad 2.17$$

### 2.1.5 Fundamental Efficiency Theorem

The fundamental efficiency theorem links the indicated work, forced work, and mechanism effectiveness to determine the theoretical shaft work output of a Stirling engine [20]. Equation 2.18 shows that the shaft work, $W_{shaft}$, can be calculated if the indicated work, $W_{ind}$, and forced work, $W_{for}$, are known, along with the mechanism effectiveness $E$ being estimated and assumed constant [20]. Likewise, the constant mechanism effectiveness can be calculated if the indicated work, forced work, and shaft work are known as seen in Equation 2.19. Appendix D contains the code that's couples the Schmidt model and the fundamental efficiency theorem

$$W_{shaft} = W_{ind} \times E - \left(\frac{1}{E} - E\right) \times W_{for} \quad 2.18$$

$$E = \frac{W_{shaft} + \sqrt{4W_{for}^2 + 4W_{ind} \times W_{for} + W_{shaft}^2}}{2W_{for} + 2W_{ind}} \quad 2.19$$

## 2.2 Estimating the Optimal Compression Ratio

Several methods exist to estimate the compression ratio to use for LTDSE. The following sections showcases these literature methods.

### 2.2.1 Kolin's Compression Ratio

Kolin's compression ratio ($CR_{Kolin}$), estimates the compression ratio of a LTDSE based on the temperature of the thermal source, $T_H$, and sink, $T_C$ [29]. This compression ratio correlation was developed empirically from data for various LTDSEs. Kolin [29] states that this mathematical relation should be considered as an average rule, and that the compression ratio should be varied according to the operating conditions used. This ratio can be expressed as:

$$CR_{Kolin} = 1 + \frac{T_H - T_C}{1100} \tag{2.20}$$

### 2.2.2 Egas' Ideal Compression Ratio

Egas' ideal compression ratio ($CR_{ideal}$) estimates a maximum compression ratio where no forced work occurs by using the ideal gas law [64]. Two different states of the ideal gas law are required to determine the ideal compression ratio. The first state determines the maximum volume of the work space, $V_{max}$. This state requires the working pressure to equal the buffer pressure, $P_{buf}$, while the working fluid temperature is equal to the temperature of the thermal source, $T_H$, presented in Equation 2.21. The second state determines the minimum volume of the work space, $V_{min}$. Equation 2.22 depicts this second state where the working pressure to equal the buffer pressure, $P_{buf}$, when the working fluid's temperature is equal to the temperature of the thermal sink, $T_C$. Since the mass, $m_{wf}$, and ideal gas constant, $R$, of the working fluid are constant, Equation 2.21 and 2.22 can be combined to determine the ideal compression ratio seen in Equation 2.23. This equation shows that the ideal compression ratio is equal to, and only dependent on, the ratio of the temperature of the thermal source and sink [64]. Egas [64] suggests that the ideal compression ratio represents the maximum compression ratio for an ideal Stirling engine with the following properties:

- Has a working fluid throughout the Stirling engines equates to the temperature of the thermal source and sink.
- Is a reversible system, where the work space that can be held at is maximum or minimum until the working fluid temperature has reached steady state.
- Is a thermodynamic cycle where no forced work occurs.

$$\frac{V_{max}}{T_H} = \frac{m_{wf}R}{P_{buf}} \quad 2.21$$

$$\frac{V_{min}}{T_C} = \frac{m_{wf}R}{P_{buf}} \quad 2.22$$

$$CR_{ideal} = \frac{V_{max}}{V_{min}} = \frac{T_H}{T_C} \quad 2.23$$

For a gamma-type Stirling engine, the method described above would results in an engine where the pressure swing caused by the displacer piston is equal to the pressure swing caused by the power piston. This method can be validated by determining the pressure change of the workspace caused by each piston independently.

Egas [64] studied how the compression ratio of experimental, high-temperature Stirling engines compared to Kolin's compression ratio. He showed that all the experimental compression ratios were below the ideal compression ratio, and that they resided both above and below the corresponding compression ratio calculated using Kolin's method [64].

### 2.2.3 Senft's Optimum Swept Volume Ratio

Senft [20] presented a method to determine the optimum swept volume ratio to produce the maximum theoretical shaft work. This is accomplished by varying the swept volume ratio in the Schmidt model to determine the indicator diagram so that indicated work and forced work can be determined [20]. The fundamental efficiency theorem can then be used to find the maximum shaft work for a specific compression ratio and mechanism effectiveness, *E*, by combining the indicated work and forced work with the varying the mechanism effectiveness, *E* [20]. Since the Schmidt model is based off the isothermal model, the temperatures of the working fluid will be equal to the thermal source and sink temperature used. In Figure 2.2, this process is visualized for a variable

compression ratio, instead of the swept volume ratio. It shows that for each mechanism effectiveness, a maximum shaft work can be found by varying the compression ratio. This proposed method could be applied to higher order thermodynamic model that are able to produce an indicator diagram. These models could provide better results if they are also able to the predict operating speed so that the maximum shaft power could be determined, and if they can estimate heat transfer between the working fluid and the thermal source and sink so that the working fluid temperatures are closer to the real-world case.

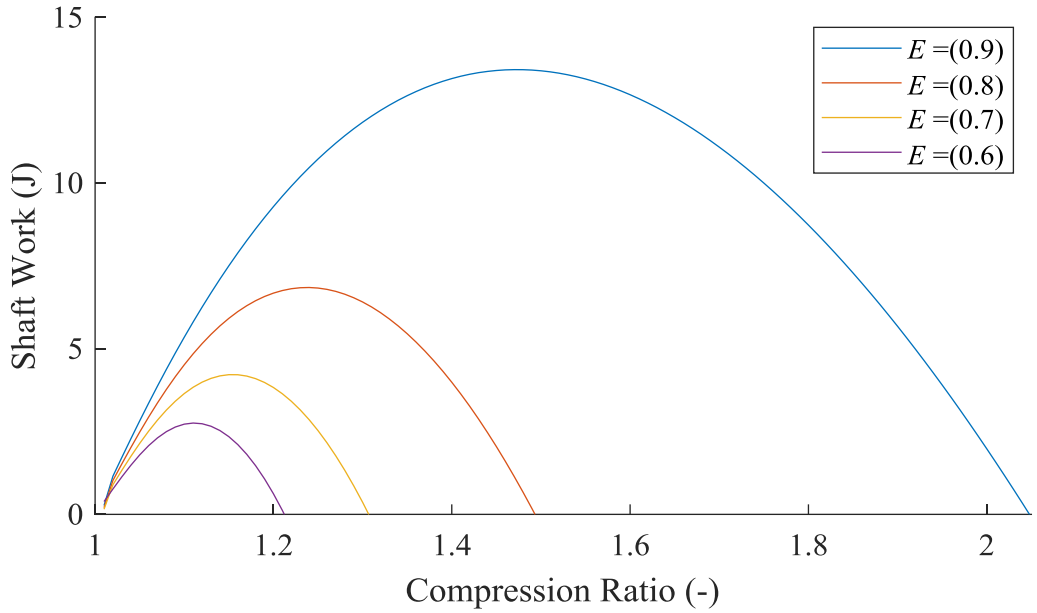


Figure 2.2 Optimization of the shaft work by varying the compression ratio in the Schmidt model and varying the mechanism effectiveness in the fundamental efficiency theorem. The Schmidt model used a thermal source temperature of 95 °C and a thermal sink temperature of 2 °C with a dead volume ratio of 1, a displace piston swept volume of 0.0059m$^3$ and a phase angle of 90°.

## 2.3 Conclusions

Different modeling methods used for Stirling engine were investigated. Unlike the Beale number, the West number allows for performance comparison of Stirling engines that operate at any temperature difference. Therefore, in Chapter 5, it will be used for performance comparison of the tested LTSDSEs in this thesis to other experimental LTDSEs. The mean West number calculated from LTDSE could also be compared to the mean value of 0.25 for HTDSEs. The Schmidt model is a thermodynamic model that is based off the isothermal model but makes the assumption of sinusoidal volume variations. The Schmidt model is a closed form solution that can directly calculate the indicated work. The indicator diagram produced by this model can be coupled with

the fundamental efficiency theorem to estimate the shaft work if a mechanism effectiveness is known or assumed.

Approaches used to estimate the compression ratio and swept volume ratio were reviewed. Kolin's compression ratio and Egas' ideal compression ratio only required the temperature of the thermal source and sink to be calculated. Senft's optimum swept volume ratio requires several operating parameters of an engine to be known before it can be calculated. The validity of all these approaches on how close the estimated compression ratio they produce is to the experimental compression ratio that produces the maximum shaft power will be investigated in Chapter 6.

# Chapter 3 Equipment, Experimental Setup and Procedure.

The following chapter starts with an overview of three different kinematic gamma-type LTDSEs developed: Mark 1, Mark 2, and EP-1. Other equipment used by the LTDSEs such as the heating and cooling system, and motoring system are described. The data acquisition (DAQ) instruments used to measure temperature, pressure, torque, and position and speed of the crank shaft is presented. This includes the specifications, DAQ equipment and calibration procedures of the instruments. The experimental procedures used for engine operation and data gathering is listed. The methods used for processing the data is described. The approaches used to calculate the uncertainty of measurements made by the instruments and for calculated values is shown. Finally, the chapter ends with a justification for when the engine has reached steady state operation so that measurement can be taken.

## 3.1 LTDSE Overview

Over the course of this project, three different kinematic gamma-type LTDSEs were developed: Mark 1, Mark 2, and EP-1. These engines are briefly introduced below. Their development, and final configuration description, is presented in Chapter 4.

The first kinematic gamma-type LTDSE that was designed, manufactured, and experimentally tested, was the Mark 1. It was able to run; however, no power measurements were able to be recorded due to the low shaft power. Since the Mark 1 was a proof of concept, the analysis of its performance was strictly qualitative, not quantitative, and no physical measurements (temperature, pressure, etc.) were recorded. Several lessons were learned from the Mark 1 based on its design, the manufacturing process, and the steps required for it to operate.

The Mark 2 was the second engine that was designed, manufactured, and experimentally tested. The design used several of the lessons learned from the Mark 1. The Mark 2 was able to run, however, due to the limits of the measurement devices used, coupled with its low shaft power it was decided that a larger engine would be required. The performance analysis of the Mark 2 was quantitative with pressure, temperature, shaft power, and several other measurements being recorded.

The EP-1 was the third and last engine that was designed, manufactured, and experimentally tested. The EP-1 will be the main focus of this thesis. The following sections will highlight the equipment, experimental procedures, data processing methods, uncertainty analysis, and steady state measurement justification used by it.

## 3.2 Equipment

### 3.2.1 Heating and Cooling Systems

Two recirculating water loops were used to heat and cool the LTDSEs. Each loop consisted of a water bath, the hoses used to transport the water, and the heat exchangers of the specific LTDSE. Using a fluid, specifically water, to heat and cool the heat exchangers was chosen for the reasons listed below.

1. It would stay in the liquid phase between the desired testing temperature bounds and at the atmospheric pressure tested. At the testing location, Canada, Alberta, Edmonton, with an elevation of 668 m, water would boil at 97.8 °C [65], and freeze at 0 °C [66].
2. It had limited safety risks associated with it and was abundantly available.
3. In a field application of a LTDSE system, the geothermal brine used for heating the engines would pass its heat through a heat exchanger to a clean fluid, such as water. This water would then be circulated through the engine's heat exchangers. A similar process, using a fluid flow loop, would be used to reject heat to the environment.
4. The temperature of the water at the inlet and outlet of the heat exchangers, along with the mass flow rate of the water through them, could be measured so that the rate of heat transfer could be determined. This in turn could be used to determine the thermal efficiency of the engine.

The heated water loop was fed by a 13-liter rapid-cool circulating bath (KH-12101-41, Cole-Parmer Canada Company), while the cooled water loop was fed by a 28.4-liter refrigerated bath (KH-12111-21, Cole-Parmer Canada Company). The specifications for these water baths are presented in Table 3.1. Each bath contained a suction pump that was used to circulate the water through its flow loop. The flow rate of these pumps could be adjusted using the onboard controller; however, they were always operated at the maximum flow rate permitted. The temperature of the water was set using an onboard controller and measured using a built-in platinum resistance temperature detector (RTD). These two systems provided a feedback control system which heated or cooled the fluid accordingly to reach the desired set point temperature. The water baths used a proportional–integral–derivative (PID) controller for the feedback control system.

Table 3.1 Heating and cooling water baths specifications.

| Model No. | Bath Capacity (liter) | Temperature Range (°C) | Pump Flow Rate (l/min) | Heating Capacity (W) | Cooling Capacity |
|---|---|---|---|---|---|
| KH-12111-21 | 28.4 | -25 to 150 | 8 to 18 | 1000 | 260 W @ -20 °C<br>700 W @ 20 °C |
| KH-12101-41 | 13 | -45 to 200 | 8 to 18 | 1000 | 825W @ 0 °C<br>900W @ 20 °C |

If both baths were turned on at the same time, they would both reach their respective temperatures at approximately the same time. This was not the case if the baths were switched. If the KH-12111-21 was used as a heater, the time taken to reach the desired temperature of 95 °C was double than that of the KH-12101-41, as would be expected from the larger bath capacity.

To reduce heat lost to the ambient air, parts of the heating and cooling system were insulated. The tubes used to transport the water to the LTDSEs were insulated using hose insulation. The top surfaces of each water bath were also insulated using expanded polystyrene (EPS).

### 3.2.2 Motoring Systems

To determine the pressure fluctuations caused by the displacer and power piston systems of the EP-1 independently, an electric motor was used. The electric motor was a software-controlled stepper motor (Clearpath CPM-MCVC-3441S-RLN, Teknic). The electric motor could have its operating frequency programmed, and therefore a range of controlled operating speeds could be tested. Figure 3.1 shows how the electric motor was used to drive the displacer system of the EP-1. This approach allowed the engine to be run in a controlled fashion and allow data to be collected. The data collected could then be used to validate Egas' ideal compression ratio.

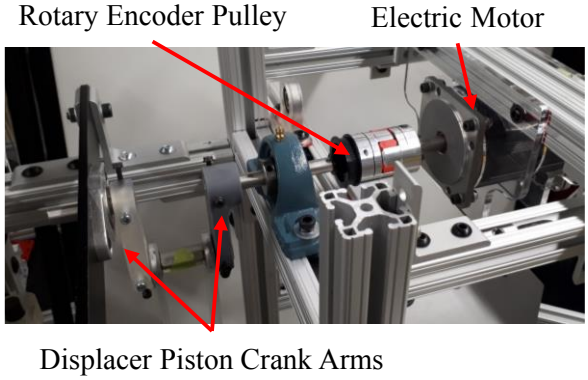


Figure 3.1 Image of the motoring system used by the EP-1.

## 3.3 Data Acquisition Equipment

### 3.3.1 Overview

A performance evaluation of a Stirling engine requires several outputs to be recorded:

- Working fluid temperature in compression, $T_c$, and expansion space, $T_e$,
- Heat source and sink temperature, $T_H$, and, $T_C$,
- Heat source mass flow rate, $\dot{m}_w$,
- Crankshaft position, $\Theta$,
- Engine operating frequency, $f$,
- Work space pressure, $P_{ws}$,
- Buffer space pressure, $P_{bs}$, and
- Shaft torque, $\tau_{shaft}$.

The instruments and data acquisition (DAQ) equipment used by the LTDSEs are presented in a block diagram in Figure 3.2, and will be discussed in the following sections. The methods used to calculate the standard uncertainty of each instrument are provided later in the chapter and sample calculations for each instrument are located in Appendix A.

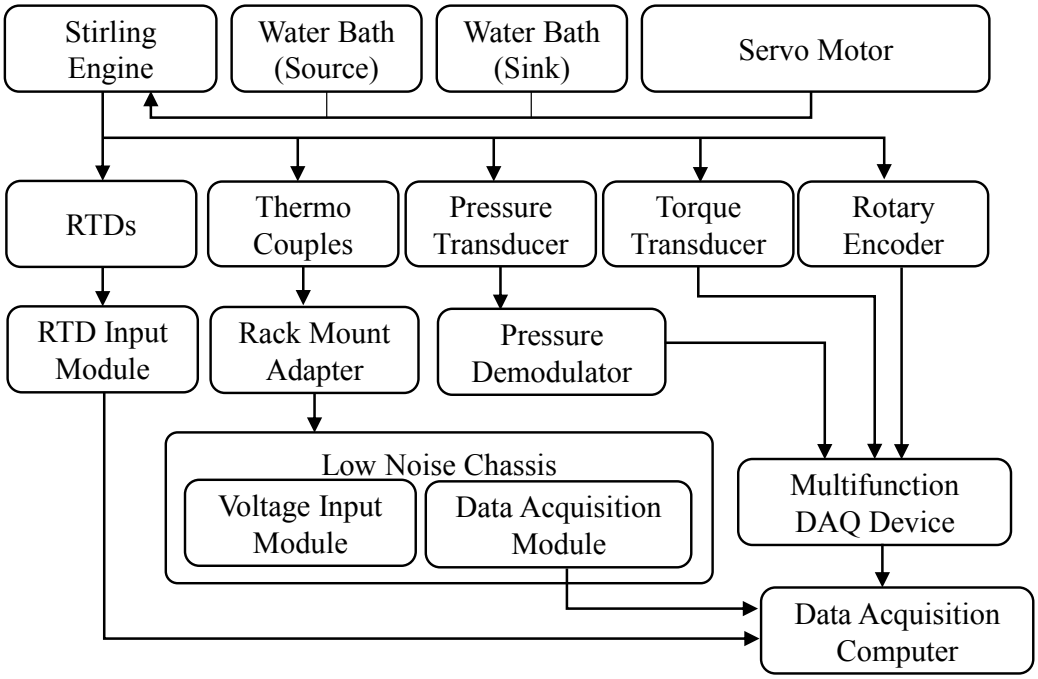


Figure 3.2 Block diagram of the equipment and instruments used.

### 3.3.2 Temperature Measurement

#### 3.3.2.1 Thermocouples

Thermocouples were used to measure the temperature of the working fluid. The temperature of the working fluid in the compression and expansion space can be used to determine the performance of the heat exchangers and regenerators. They can also be used to compare the experimental performance to the predicted performance from a thermodynamic model.

The thermocouple used was a Type T unsheathed thermocouple (TTSS-116E-6, Omega Engineering Inc.). This thermocouple was used because the temperature to be measured fell within its operating range, it was unsheathed, and it had a very small sensing mass with a diameter of 0.75mm. The size of the sensing mass is displayed in Figure 3.3. Even though the sensing mass of the thermocouple was quite small, it did not allow for the measurement of instantaneous temperature of the working fluid, and instead provided the mean temperature of the location measured. However, some fluctuations in the temperature measured were seen during engine operation as shown in Figure 3.4. A summary of the relevant specifications of the thermocouple is tabulated in Table 3.2.

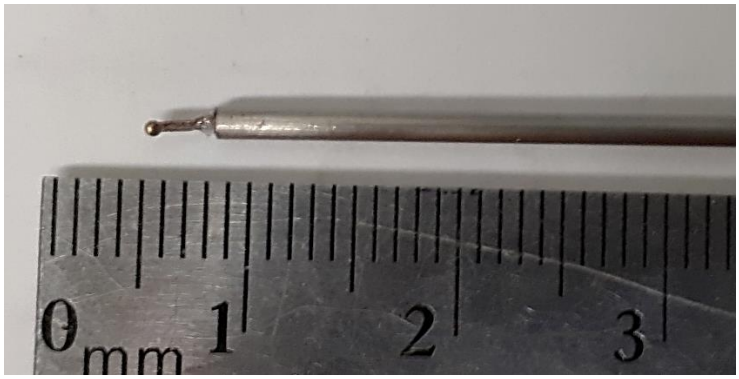


Figure 3.3 Image showing the size of the sensing mass for the Type-T thermocouples used.

Table 3.2 Thermocouple specifications.

| Operating Range | Resolution | Standard Uncertainty | Response time |
|---|---|---|---|
| -200 to 350 °C | 0.1 °C | ±1.9 °C | Not Measured |

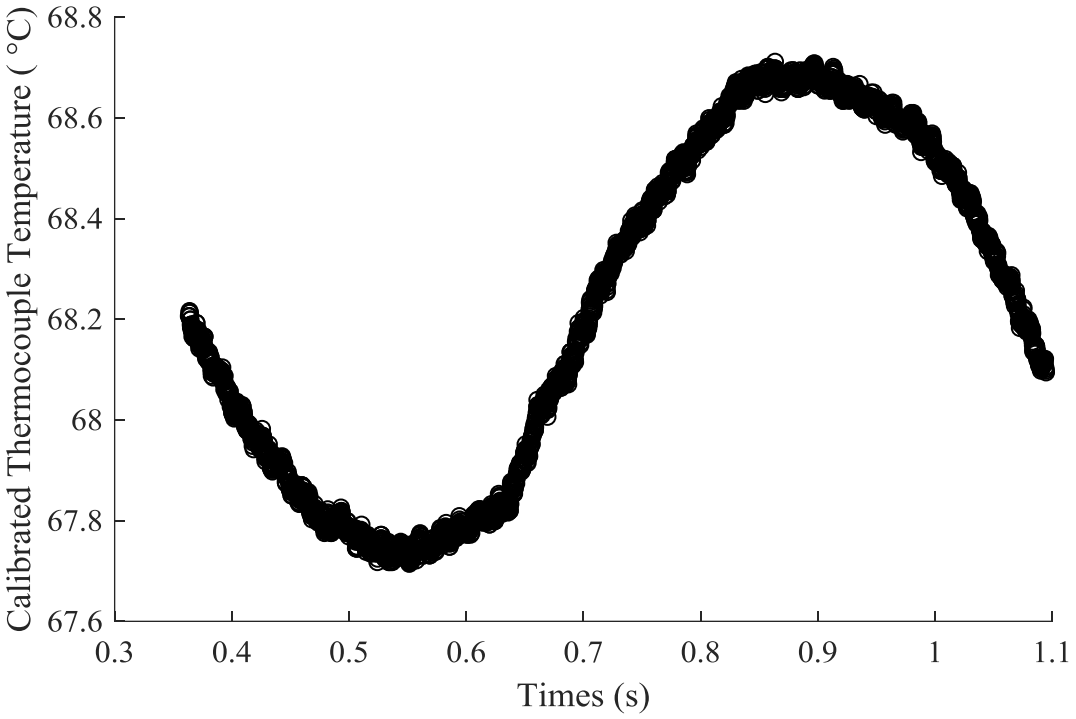


Figure 3.4 Operational temperature fluctuations of the working fluid in the expansion space of the EP-1 over one cycle.

To change the voltage produced by the thermocouple into a measurable value, several DAQ devices were used. First, the thermocouples were plugged into a rack mount adapter (TC 2095, National Instruments Inc.). The voltage signal was then sent to the voltage input module (SCXI-1102B, National Instruments Inc.) that resided inside a low noise chassis (SCXI-1000, National Instruments Inc.). The voltage was then converted from an analog signal into a digital signal using an analog to digital converter (SCXI-1600, National Instruments Inc.). This analog to digital converter (ADC) also resided in the low noise chassis. Finally, the digital signal was sent to the DAQ computer where is was sampled by the DAQ software. The thermocouples were sampled at a rate of 5000 Hz. The DAQ software used converted the thermocouple voltage into temperature data. This temperature data was then calibrated.

The thermocouples were calibrated using the water baths described earlier, and a mercury thermometer (1005-3S, Ertco). The thermometer was first checked to see if it was calibrated by recording the temperature of an ice bath. This resulted in a measured temperature of 0 °C, and

calibration of the thermocouples proceeded. The thermocouples and thermometer were linked together so that there was limited spatial variation in temperature measurement location. They were then placed in water baths of varying temperatures and allowed to equilibrate to the temperature of the bath for 3 minutes. The thermocouple temperature was then sampled using the DAQ software, while simultaneously, the temperature of the thermometer was recorded visually. The sampled thermocouple data was then was averaged. A linear fit was applied for the average thermocouple temperature and the thermometer temperature shown in Figure 3.5. With the standard uncertainty of thermocouple system applied the thermocouple temperature, all error bars fall within the linear fit. Based on this, and the thermocouple specifications sheet also predicting a linear response [67], a linear fit was used to calibrate the thermocouples. Using the recorded thermometer temperature as the desired values, a linear fit using the thermocouple temperature as the input was performed. Figure 3.6 shows the difference between the calibrated thermocouple temperature and the thermometer temperature. The range of the calibrated thermocouple temperature when the standard uncertainty is applied includes the point of zero difference.

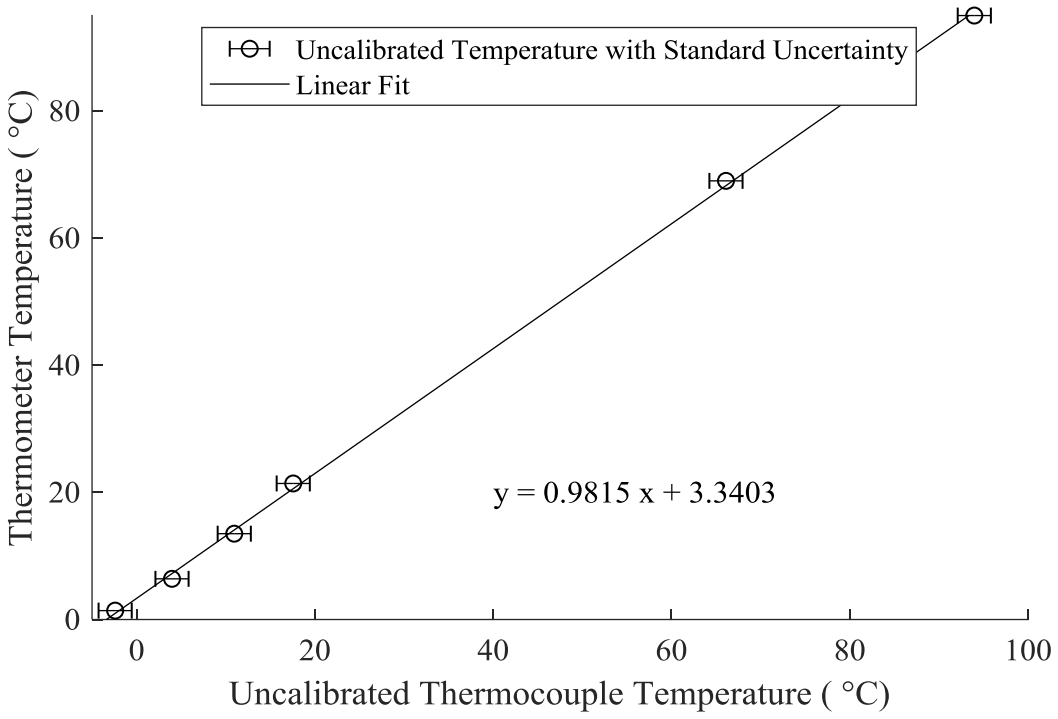


Figure 3.5 Uncalibrated thermocouple temperatures for various thermometer temperatures.

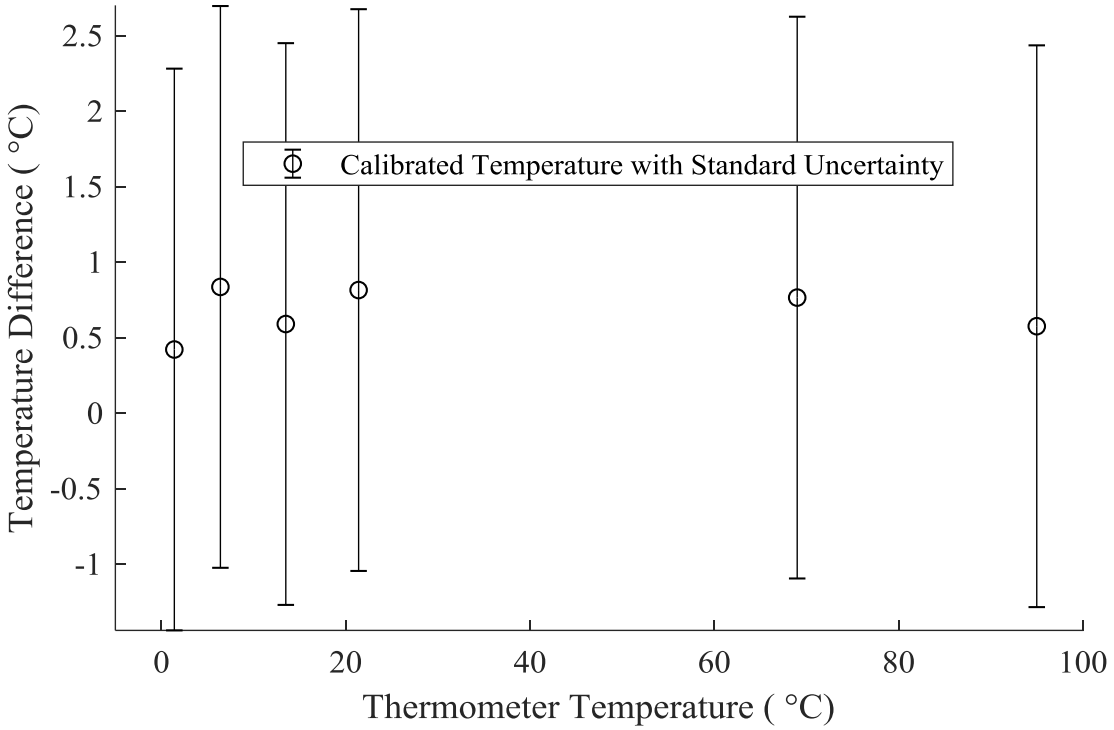


Figure 3.6 Temperature difference between the calibrated thermocouple and the thermometer

#### 3.3.2.2 Resistance Temperature Detectors

Resistance temperatures detectors (RTDs) were used to measure the temperature of the water at the inlet and outlet of the heat exchangers. By measuring this, the rate of heat transfer into and out of the engine can be determined when combined with the mass flow rate of fluid through the heat exchangers. This heat transfer rate can then be combined with the shaft power to determine the thermal efficiency of the engine.

The RTDs used were high-accuracy fluid immersion RTDs (RTD-810, Omega Engineering Inc.). They were used because, like the thermocouples, the temperatures to be measured fell within their operating range. Since the RTDs were grounded, any grounding issues with measuring an electrically conductive liquid were eliminated. The time constant of the RTD was not measured. Having a small-time constant was not important since the goal was to determine the temperature difference between the inlet and outlet of the heat exchangers at steady state operation. Figure 3.7

shows the operational steady state temperature of the water inlet and outlet of the thermal sink heat exchanger of the EP-1.Table 3.3 summarizes the pertinent specifications of the RTDs used.

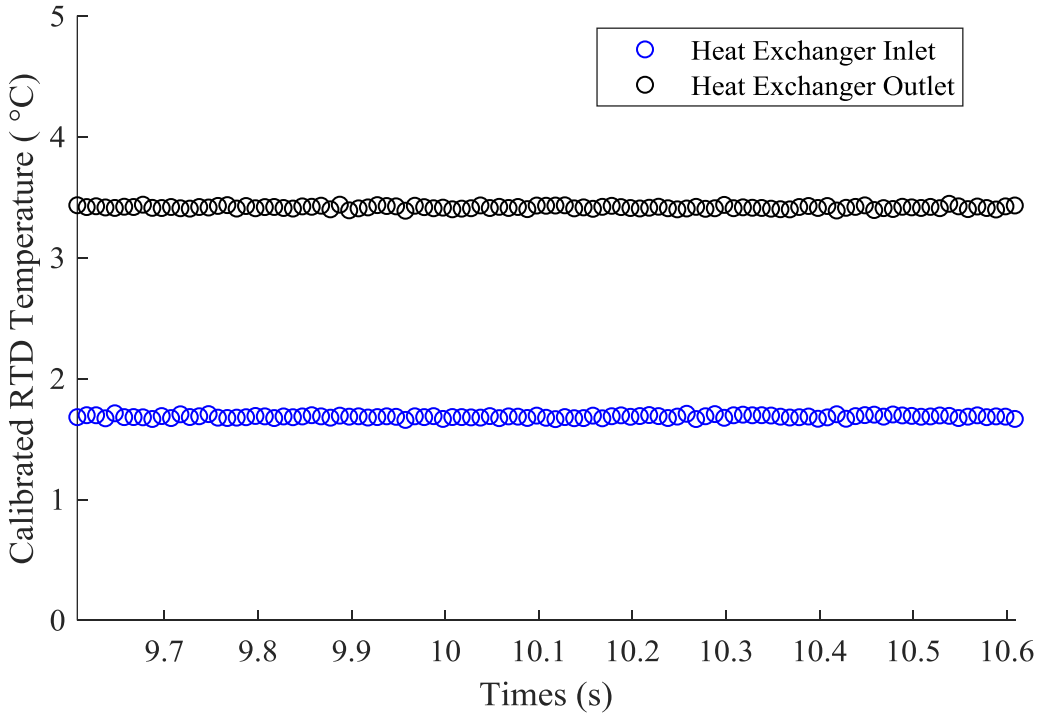


Figure 3.7 Temperature of the fluid entering and exiting the EP-1's thermal sink heat exchanger, while the EP-1 is running at 68 rpm.

Table 3.3 RTD specifications.

| Operating Range | Resolution | Standard Uncertainty | Response time |
|---|---|---|---|
| -200 to 750 °C | 0.01 °C | ±0.62 °C | Not Measured |

To record the temperature of the RTD, DAQ systems were used. The RTDs were wired to an ADC DAQ module (NI 9217, National Instruments Inc.). The digital signal output from the ADC was then sent to the DAQ computer where it was sampled by the DAQ software. The RTDs were sampled at a rate of 100 Hz. Like the thermocouples, the DAQ software already converted the RTD voltage to a corresponding temperature, and this temperature data was then calibrated.

The RTDs were calibrated using the same method as the thermocouples. Figure 3.8 shows the average sampled RTD temperatures for the corresponding recorded thermometer temperature. A linear fit of the data was applied. With the standard uncertainty applied, all the temperatures

measured by the RTDs fell within the linear fitted curve. Therefore, like the thermocouples, a linear fit was applied to calibrate the RTDs. The associated measurement difference between the calibrated RTD temperature and the measured thermometer temperature is shown in Figure 3.9. This figure shows that the range produced by the standard uncertainty includes the point of zero difference.

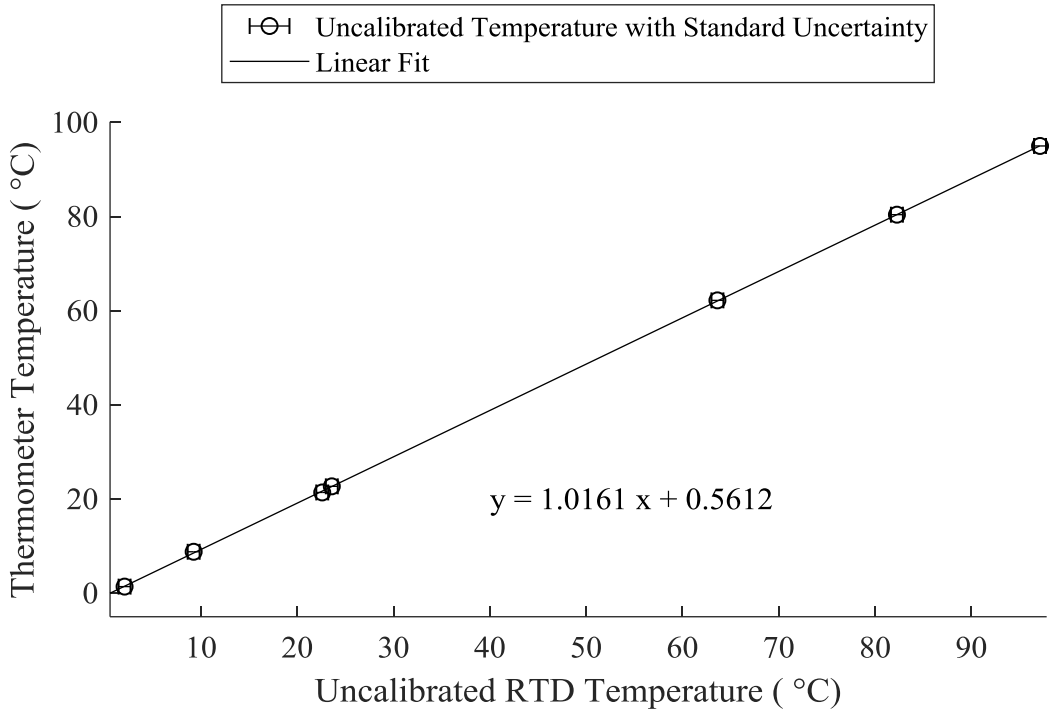


Figure 3.8 Uncalibrated RTD temperatures for various thermometer temperatures.

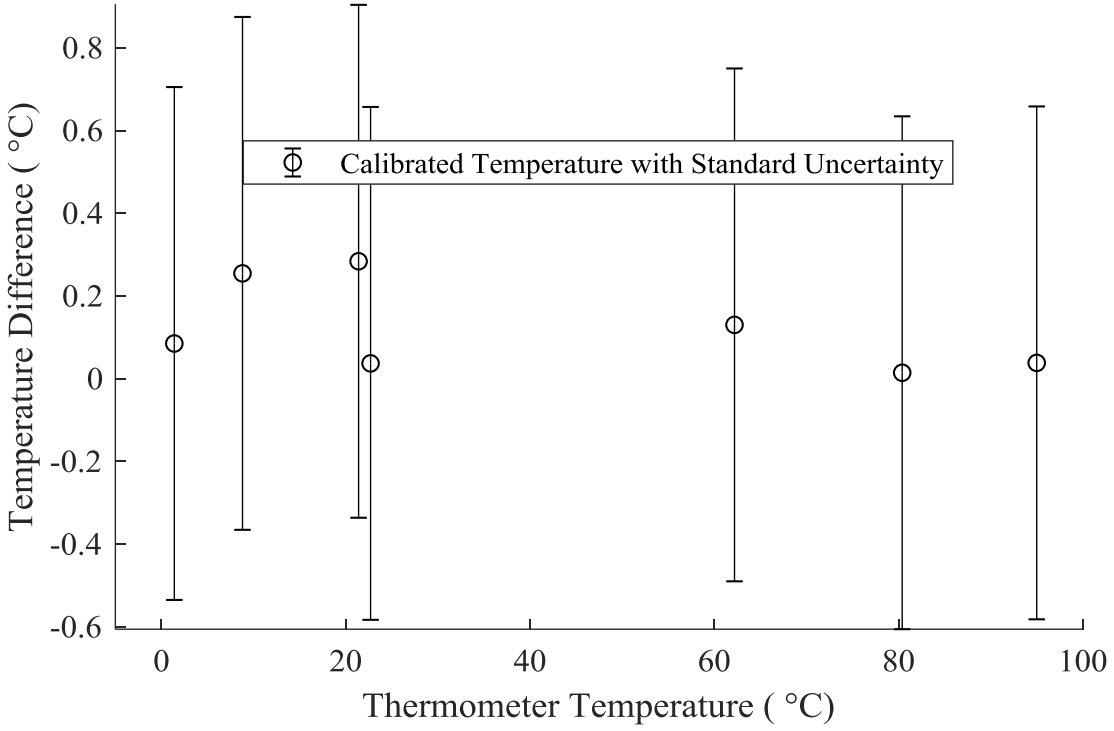


Figure 3.9 Temperature difference between the calibrated RTDs and the thermometer.

### 3.3.3 Mass Flow Rate Measurement

The mass flow rate of the heating flow loop was measured. Using Equation 3.1, the mass flow rate of the water through the heat exchanger, $\dot{m}_w$, can be coupled with the temperature of the water at the inlet and outlet of the heat exchanger, $T_{hxi}$, and $T_{hxo}$, and the Isobaric specific heat capacity of water, $c_p$, to determine the rate of heat transfer into the engine, $\dot{Q}_{in}$. The shaft power, $P_{shaft}$, can be divided by the rate of heat transfer rate into the engine, $\dot{Q}_{in}$, to determine the thermal efficiency of the engine, $\eta_{th}$, as seen in Equation 3.2.

$$\dot{Q_{in}} = \dot{m}_w \times c_p \times (T_{hxi} - T_{hxo}) \quad 3.1$$

$$\eta_{th} = \frac{P_{shaft}}{\dot{Q_{in}}} \quad 3.2$$

The flow loop was decoupled so that the inlet back into the water bath was instead allowed to drain into a bucket. The water bath's pump was then turned on, and the water was allowed to flow from the water bath, through hosing, through the heat exchanger, and through the rest of the hosing and

then into the bucket. The flow loop was run for approximately 30 seconds. The actual time of when the flow loop was turned on and off was recorded with a cellphone stopwatch. The mass of water transferred into the bucket was measured with a weight scale (Ohaus B50AS). This test was repeated five times to determine the mass flow as shown in Table 3.4. The average flow rate was determined to be 0.0316 kg/s with a standard deviation of 0.0011kg/s.

Table 3.4 Mass flow rate determinatiuon for heating flow loop.

| Time (s) | Mass (kg) | Initial Mass (kg) | Delta Mass (kg) | Mass Flow Rate (kg/s) |
|---|---|---|---|---|
| 30.15 | 1.976 | 0.731 | 1.245 | 0.0413 |
| 30.3 | 2.05 | 0.734 | 1.316 | 0.0434 |
| 29.87 | 2.033 | 0.732 | 1.301 | 0.0436 |
| 29.89 | 2.051 | 0.733 | 1.318 | 0.0441 |
| 29.91 | 2.031 | 0.732 | 1.299 | 0.0434 |

### 3.3.4 Position and Speed Measurement

A rotary encoder was used to measure the crankshafts' angular position, and the operating frequency of the engine. With the instantaneous angular position of the crankshaft known, the volume variations of power piston assembly could be calculated. This could then be coupled with the cyclical pressure change of the workspace to determine the indicator diagram. The time required to complete one revolution of the crank shaft can be determined and therefore the engine's operating frequency can be calculated. The operating frequency can be combined with the shaft torque to determine the shaft power of the engine.

An incremental optical rotary encoder (15S-19M1-0500NV1ROC-F03-S1, Encoder Products Company) was used. An optical encoder works by shining a light through slots in a disk. This light is then detected by a photodiode [68]. The rotary encoder used had three analog voltage outputs, an A, B, and Z channel. Each channel output either: zero volts when no light was detected by the photodiode, or a five-volt output when photodiode detected light. The A and B channel each had a resolution of 500 pulses per revolution. There is a phase offset between these two channels so the direction of rotation of the encoder could be determined. The Z channel had one pulse per revolution. The Z channel is used as a reference channel to determine when one complete revolution of the encoder had occurred. Only the A and Z output were used, as rotation direction was determined visually. A typical output of the rotary encoders' A and Z channel is shown in

Figure 3.10. It shows the voltage change when the A and Z channel go over a pulse and that the pulses occur simultaneously.

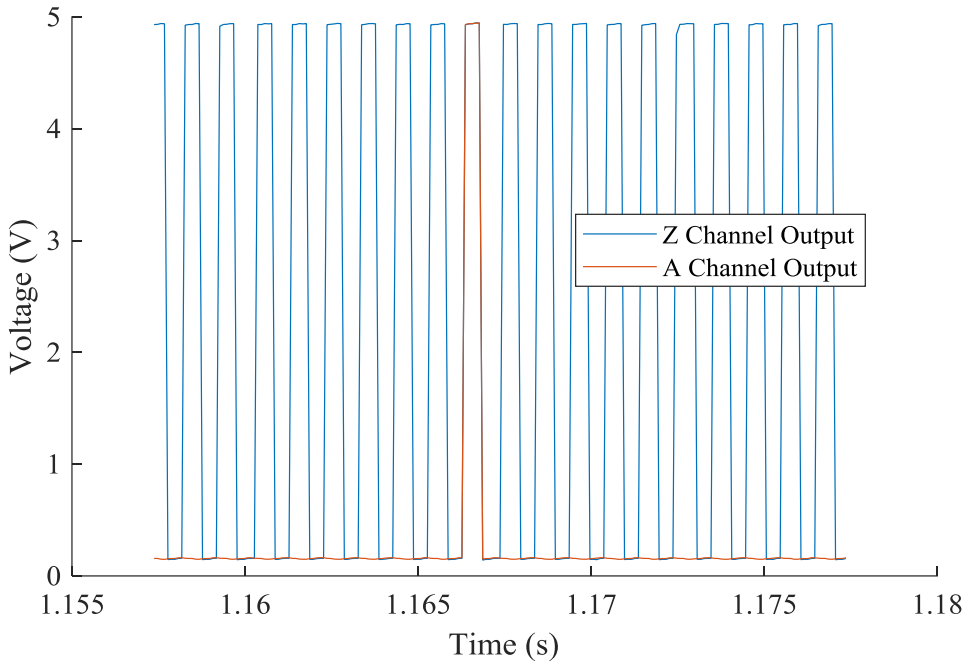


Figure 3.10 Rotary encoder voltage output while the engine is operating.

To collect the rotary encoder's analog outputs an analog input to a DAQ systems were used. The rotary encoder was wired directly to the ADC DAQ module (NI USB-6211, National Instruments Inc.). The digital signal was then sampled by the DAQ software.

The sampling rate of the rotary encoder was based off the operating frequency of the engine. To capture all the on and off pulses of the A channel of the rotary encoder, it had to be sampled at least 2000 times the engine's frequency. These values were calculated from the sampling rate theorem [69]. As both the zero and five-volt outputs needed to be recorded, 1000 points needed to be sampled per revolution. To avoid aliasing of the data, the sample rate should be greater than twice the maximum frequency measured [69]; therefore, a minimum sampling rate of 2000 times the engine's frequency was calculated. However, since the engine may not run at a constant speed, the sampling rate was increased even further to 4000 times the operating frequency. This accounted for the potential of the engine's speed to vary significantly through the cycle.

Calibration of the rotary encoder relied on the initial alignment of the Z pulse with a specific position of the engine's crank arm. This location corresponded to the point of maximum volume of the engine. The rotary encoder was connected to the crankshaft with two toothed pulleys of the same diameter and a timing belt as shown in Figure 3.11. This was done to make sure once the Z pulse was aligned it could not become unaligned.

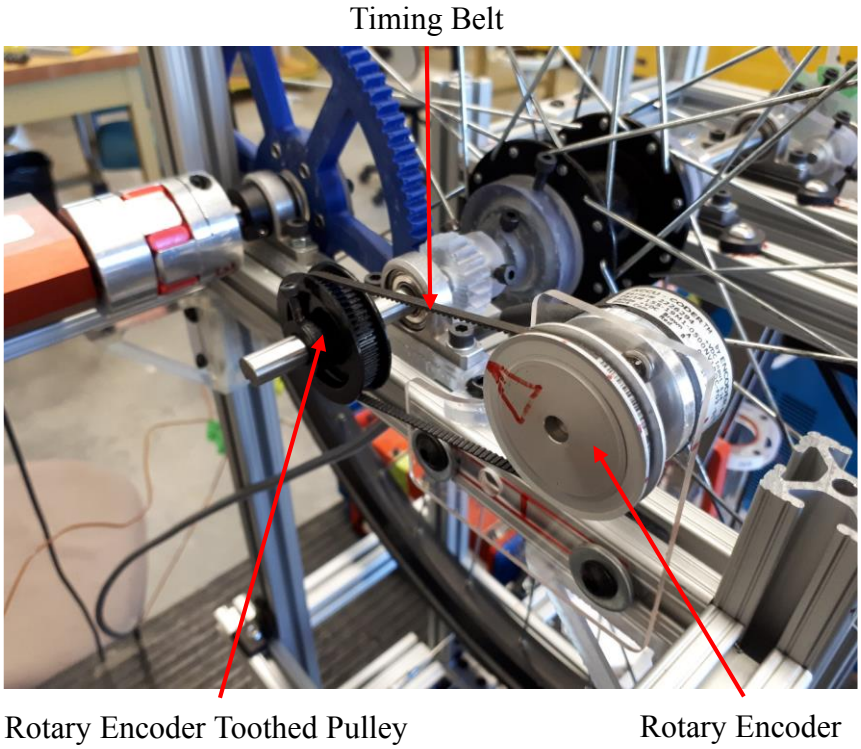


Figure 3.11 Rotary encoder connection for the Mark 2.

## 3.3.5 Pressure Measurement

### 3.3.5.1 Work Space Pressure

The pressure of the work space was measured with a pressure transducer. By measuring the work space pressure, the cyclical pressure change throughout the engine cycle could be determined. This could be combined with the cyclical volume variations to produce the indicator diagram.

A variable reluctance differential pressure transducer (Validyne DP15-50, Validyne Engineering) was used with an 86.0 kPa (12.5 PSI) diaphragm. The pressure transducer and the specific diaphragm were chosen as they were already existing laboratory equipment. The desired pressure

to be measured fell within the operating range of the diaphragm. The response time was important to measure the varying pressure change of the engine. The response time of the transducer was deemed to be fast enough to measure the cyclical pressure change. This was because the engine maximum operating frequency was slow ( ≈ 2.5 Hz) compared to the flat response time of the transducer of ≈70 Hz, when a tube length of 5cm was used [70]. The instantaneous pressure measured throughout one engine cycle is presented in Figure 3.12 .The specifications of the pressure transducer used is summarized in Table 3.5.

Table 3.5 Pressure transducer specifications.

| Operating Range | Resolution | Standard Uncertainty | Response time |
|---|---|---|---|
| -86 to 86 kPa | 0.1 kPa [70] | ±0.4 kPa | 3.6 ms [70] |

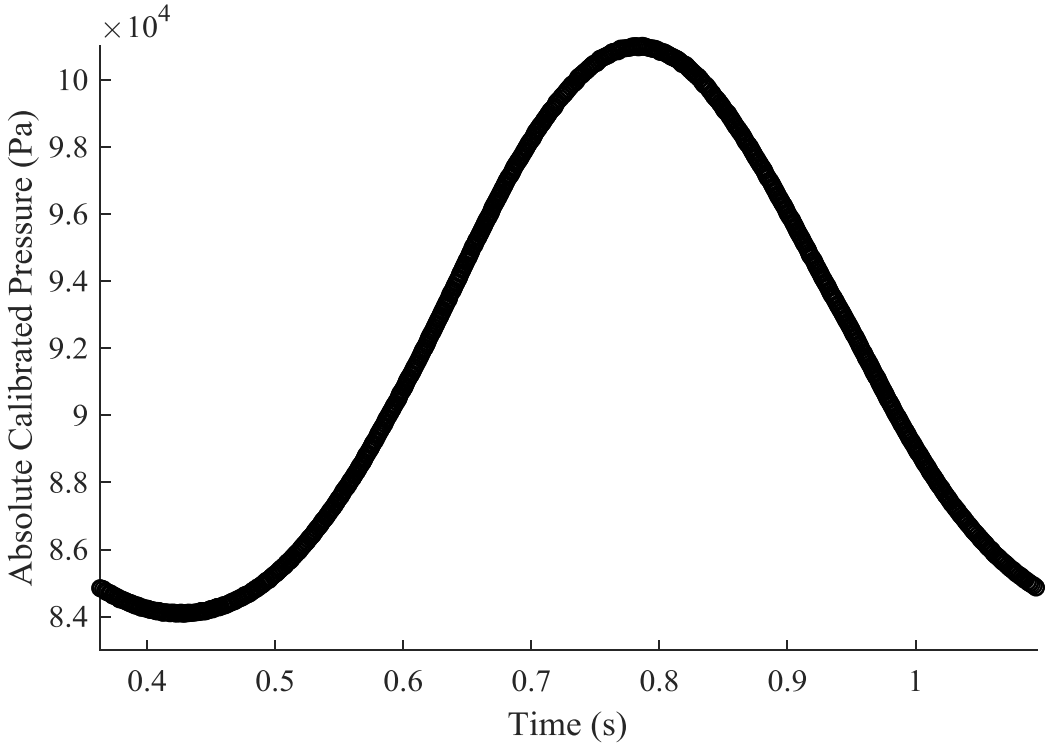


Figure 3.12 Cyclical pressure fluctuations of the EP-1.

DAQ modules were used to measure the voltage output of the pressure transducer. The pressure transducer was first connected to a pressure demodulator (CD280-DUAL, Validyne Engineering). Next, the analog voltage signal from the pressure demodulator was sent to an ADC DAQ module

(NI USB-6211, National Instruments Inc.). Finally, the digital voltage signal was recorded by the DAQ software on the DAQ computer. Because of the DAQ software used, the sampling frequency of the pressure transducer was equal to the sampling frequency of the torque transducer and rotary encoder. The digital voltage was converted into pressure values when the data was processed, but first the voltage had to be calibrated.

The pressure transducer was calibrated using a portable pressure calibrator (DPI 603, Druck). The calibrator had a built-in pump that was used to produce various different pressures for the transducer. First, with no pressure applied to the transducer, the pressure demodulator's zero value was tuned so that a corresponding zero voltage was output from it. Next, a pressure of 68.9 kPa (10 PSI) was applied to the transducer using the calibrator's pump, and the demodulator's span was tuned to produce an output of ten volts. After the zero and span of the demodulator was set, the calibrator's pump was used to cycle the pressure of the transducer for various values between 0 and 68.9 kPa. Using the DAQ software the voltage of the transducer was sampled while the corresponding pressure value was visually recorded from the calibrator's onscreen display for each tested point. The transducer voltage sampled were then averaged and converted into Pascals assuming a linear relationship of one volt to 6.8 kPa (1 PSI). The average pressure of the transducer was then compared to the recorded pressure of the calibrator shown in Figure 3.13. The assumption of a linear relationship between transducer voltage and calibrator pressure was shown in to be valid. This is because when using the standard uncertainty for the sampled pressure values, the range produced includes the linear fit line. Figure 3.14 depicts the difference between the transducer's pressure and the recorded calibrator pressure. Yet again, the range of measured values with the standard uncertainty includes the point of zero difference for all pressures measured.

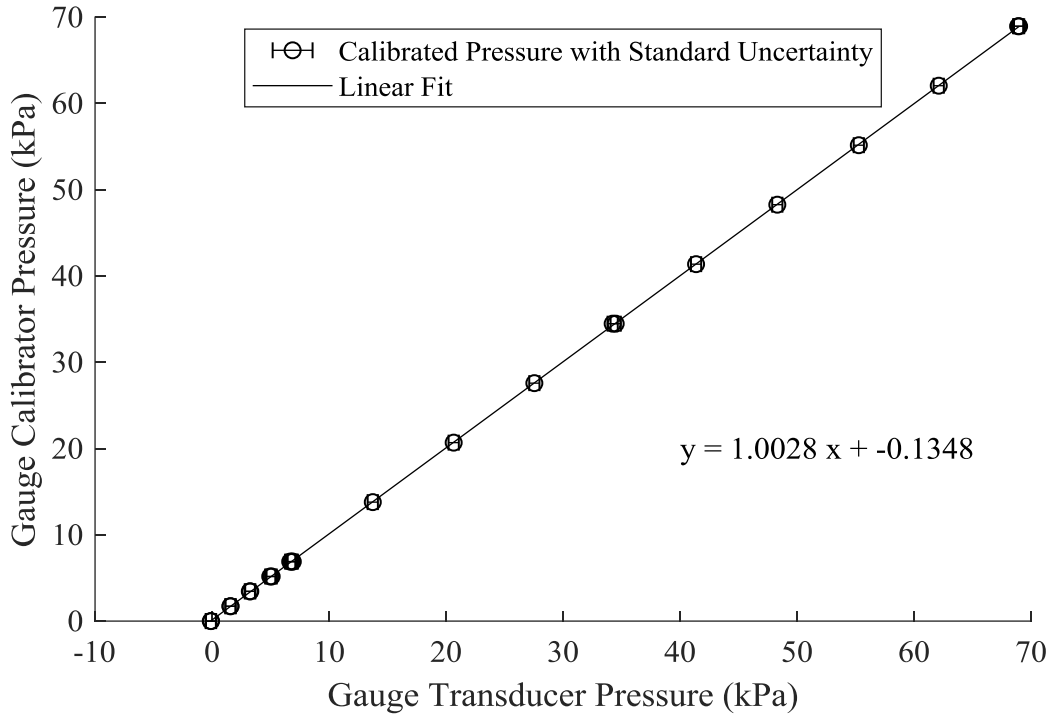


Figure 3.13 Transducer voltage output for given calibrator pressures.

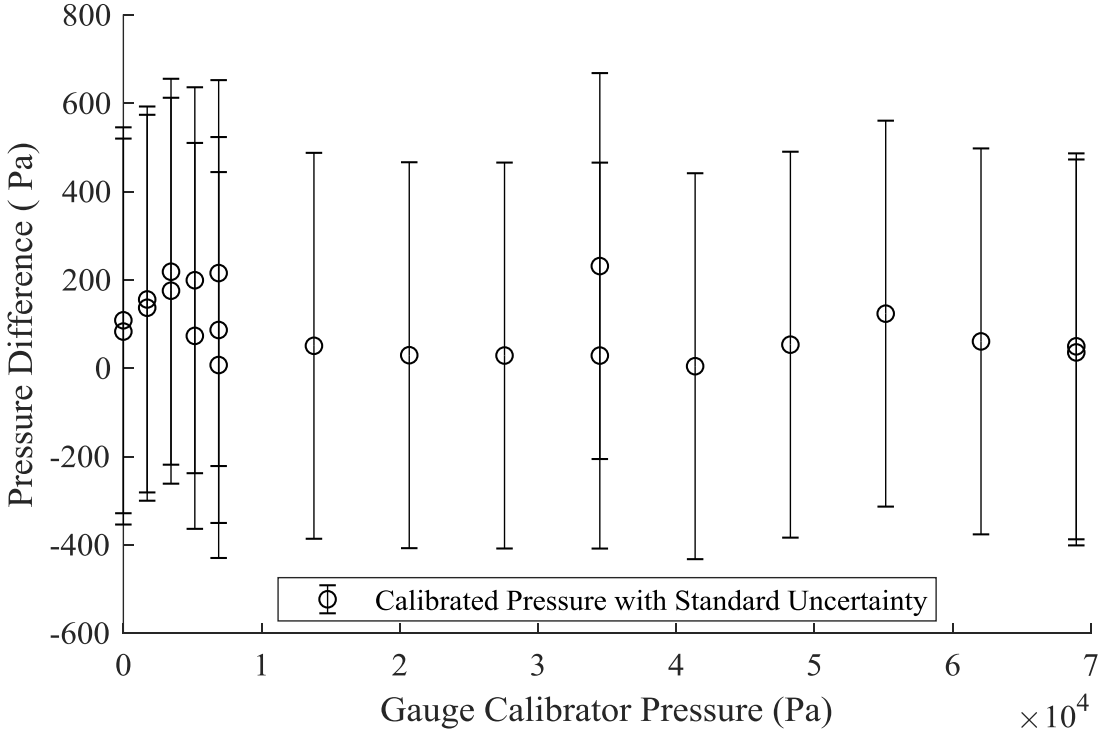


Figure 3.14 Pressure difference between the calibrated pressure transducer and the pressure calibrator.

#### 3.3.5.2 Atmospheric Pressure

Since the pressure transducer used to measure the work space was a differential pressure transducer, only the gauge pressure was measured. To determine the absolute pressure, the atmospheric pressure had to be measured. This was done with a barometer built into a cell phone (Galaxy A5 2018, Samsung). The cellphone barometer was calibrated with a mercury barometer (University of Alberta Department of Mechanical Engineering's standard mercury barometer). The model number of the barometer could not be found. The atmospheric pressure was recorded for the cellphone and the barometer, and then the barometer measurement was corrected for temperature and latitude. These measurements are tabulated in Table 3.6. The tables used for this correction of temperature and latitude are available in Appendix C. A linear fit was used to for calibration of the cellphone pressure.

Table 3.6 Barometer pressure and corresponding cellphone barometric pressure.

| Cellphone Measurement (kPa) | Barometer Measurement (mmHg) | Corrected Barometer Measurement (kPa) |
|---|---|---|
| 93.642 | 706.0 | 93.86 |
| 91.375 | 689.4 | 91.65 |

### 3.3.6 Torque Measurement

The torque produced by the engine's crankshaft when it was loaded was measured. By determining the crankshaft torque and combining it with the operating frequency, the shaft power can be calculated.

Two non-contact rotary torque sensors (TRS600, Futek Advanced Sensor Technology Inc.) were used. The relevant specifications of the sensors are listed in Table 3.7. They were both the same model, but had different measurement ranges of 10 Nm, and 1 Nm. The 10 Nm sensor was initially used, but due to the small torques required to stall the engines, less than 1.5 Nm, the 1 Nm sensor was installed instead. This was primarily done to reduce the uncertainty in the torque measurement. The instantaneous torque produced by the sensor was not of importance as the torque data sampled was averaged over each cycle. However, the instantaneous torque could be measured as shown in Figure 3.15. With a maximum operating speed of 12,000 rpm [71] possible, the response time of the torque sensor was largely ignored.

Table 3.7 Torque transducer specifications.

| Model Number | Operating Range | Resolution | Standard Uncertainty | Response time |
|---|---|---|---|---|
| TRS600 | -1 to 1 Nm | 0.001 Nm | ±0.006 Nm | Not Measured |
| TRS600 | -10 to 10 Nm | 0.010 Nm | ±0.06 Nm | Not Measured |

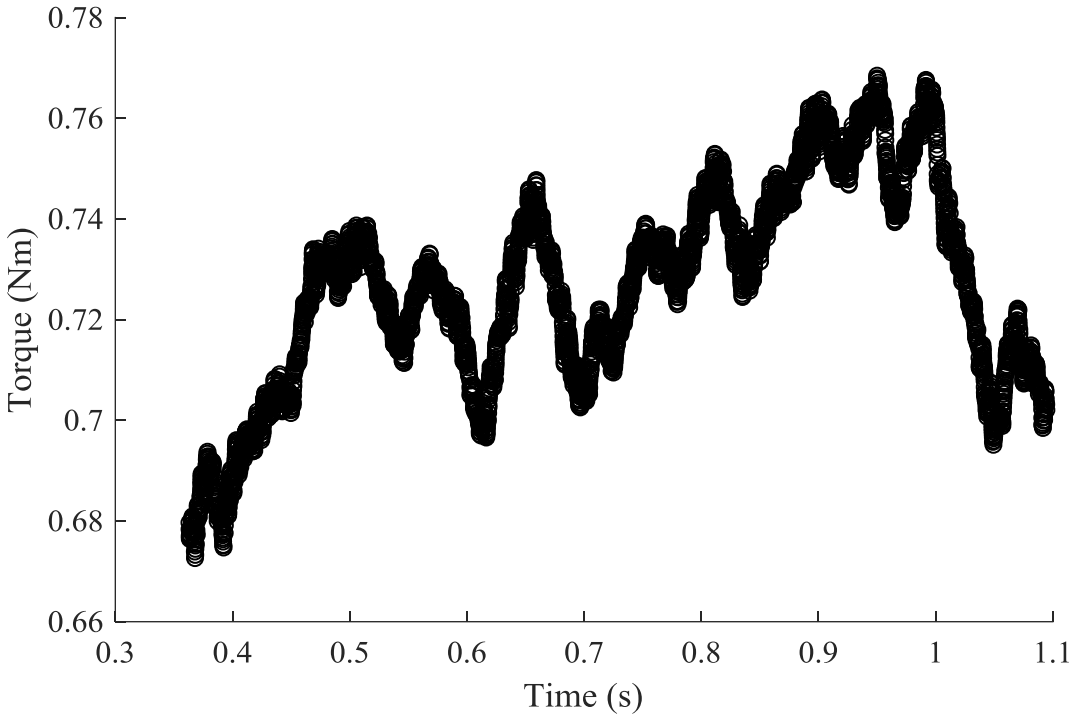


Figure 3.15 Torque sensor output for one cycle of the EP-1 when it is loaded during operation.

To acquire the output voltage of the sensor, DAQ systems were used. The sensor was wired to the same ADC DAQ module (NI USB-6211, National Instruments Inc.) used by the pressure transducer and rotary encoder. The digital voltage output was then recorded by the DAQ computer and software. The torque sensor was sampled at the same rate as the rotary encoder and pressure transducer as discussed above.

The torque sensor came calibrated from the factory. This consisted of a six-point calibration in both rotation directions. The applied torque and voltage output from this calibration was used to

produce a linear fit to convert experimental output voltages to experimental output torques. The calibration sheet is provided in the Appendix C.

### 3.3.7 Data Acquisition Software

The DAQ software used to record data from the instruments described in the previous sections was developed in-house written in a commercial package (LabWindows CVI, National Instruments). The software can present a live data output for almost all the instruments. Using the rotary encoder, the live operating speed can be displayed. Data is recorded by the software and stored into text files where it can then be processed using a separate software. In Figure 3.16, an image of the DAQ software interface is presented.

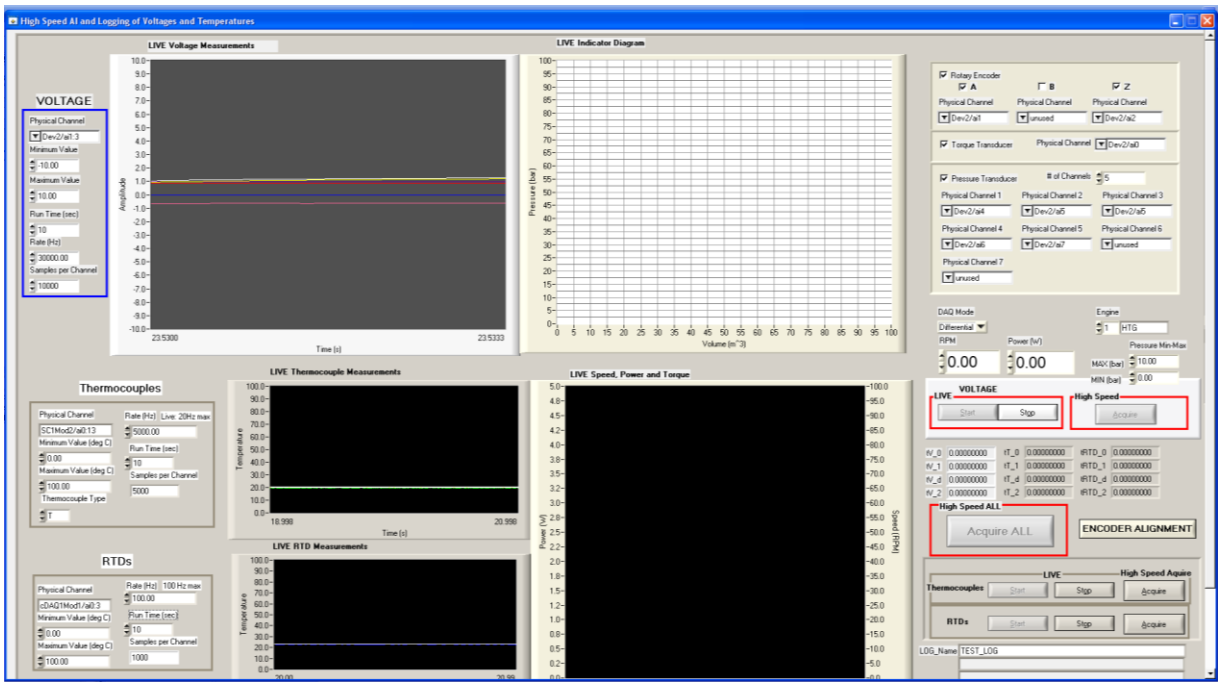


Figure 3.16 Image of the interface used by the DAQ software.

When data is sampled by the DAQ software, three log files of raw data are produced, one for each group of instruments, as shown in Table 3.8. For each group a sampling time and frequency can be chosen. Figure 3.17 shows the RTD log file produced by the software that contains the start and end time of sampling, along with the temperature data sampled. The log files produced by the DAQ software are text files (.txt).

Table 3.8 Groups of instruments sampled together by the DAQ software.

| Group | Instruments Sampled |
|---|---|
| 1 | Thermocouples |
| 2 | RTDS |
| 3 | Pressure Transducer, Rotary Encoder, and Torque Transducer. |

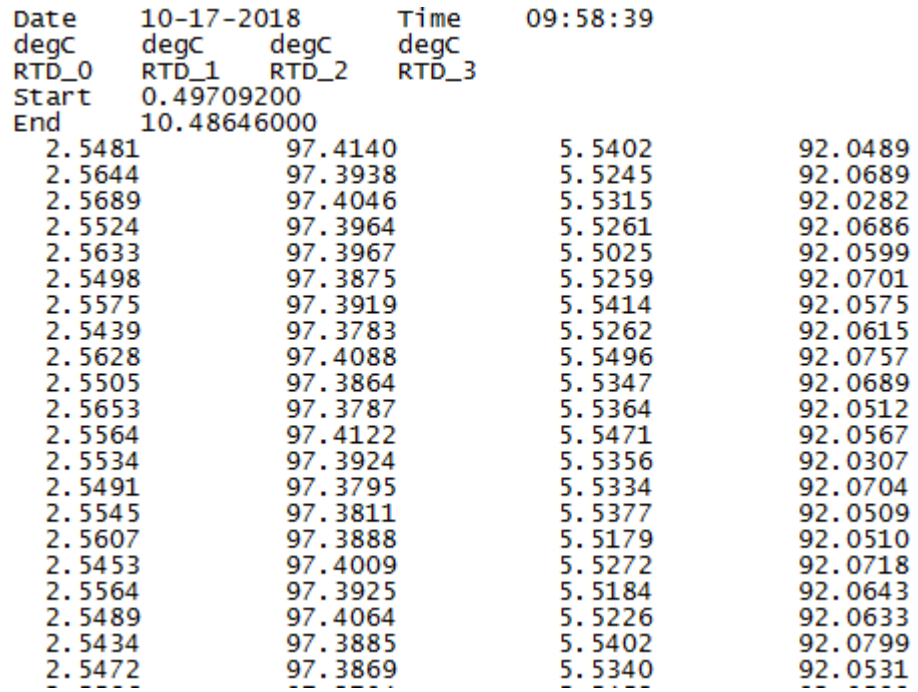

```
Date     10-17-2018       Time     09:58:39
degC     degC     degC     degC
RTD_0    RTD_1    RTD_2    RTD_3
Start    0.49709200
End      10.48646000
  2.5481           97.4140           5.5402           92.0489
  2.5644           97.3938           5.5245           92.0689
  2.5689           97.4046           5.5315           92.0282
  2.5524           97.3964           5.5261           92.0686
  2.5633           97.3967           5.5025           92.0599
  2.5498           97.3875           5.5259           92.0701
  2.5575           97.3919           5.5414           92.0575
  2.5439           97.3783           5.5262           92.0615
  2.5628           97.4088           5.5496           92.0757
  2.5505           97.3864           5.5347           92.0689
  2.5653           97.3787           5.5364           92.0512
  2.5564           97.4122           5.5471           92.0567
  2.5534           97.3924           5.5356           92.0307
  2.5491           97.3795           5.5334           92.0704
  2.5545           97.3811           5.5377           92.0509
  2.5607           97.3888           5.5179           92.0510
  2.5453           97.4009           5.5272           92.0718
  2.5564           97.3925           5.5184           92.0643
  2.5489           97.4064           5.5226           92.0633
  2.5434           97.3885           5.5402           92.0799
  2.5472           97.3869           5.5340           92.0531
```

Figure 3.17 Image of the log file produced when the DAQ software is used to sample the RTDs.

## 3.4 Data Processing

The experimental data captured by the DAQ software and stored into log files was imported and processed using custom code (MATLAB, The Mathworks, Inc.). The raw data log files were first imported and saved in raw data .mat files, the binary data container format used by the software [46]. These raw data .mat files were then calibrated and processed, and a new .mat file was produced. This was done because the process to convert the raw data log files into .mat files took significantly more time than to process and calibrate the data. If a different method to process the data, or new calibration data was acquired, the existing raw data .mat file could be quickly and easily modified to create a new processed and calibrated .mat file. The following sections will show examples of how some of the raw data was processed.

### 3.4.1 Calculation of Theta

Voltage data from group 3 was trimmed down so only an integer number of cycles was captured. The Z channel of the rotary encoder was used to find the start of the first complete cycle, and the end of the last complete cycle. This was completed by finding the first and last five-volt Z pulse in the log file.

With the Z pulses acting as an indicator of when a rotation of the crankshaft was complete, the angle of the crankshaft, theta, could be calculated. The A channel was used to determine the increment of the crankshaft from the on and off pulses. These 500 increments were then converted into the angular position of the crankshaft, theta. The process was repeated for each complete rotation of the crankshaft.

### 3.4.2 Calculation of Constant Engine Volumes

To determine the minimum work space volume of the tested LTDSEs, their solid models were used. This was done using two methods. Method one added the void volume of each component together for engines that had several parts that connected to each other, like in the Mark 2. The other method, method two, was used for the Mark 1 and EP-1, where most of the internal components resided inside a common engine body. Method two calculated the engine bodies' total void volume, and then subtracted the volume of components that were added internally.

The validity of the approaches previously descripted depend on how close the manufactured part's dimensions were to the solid model's dimensions. 3D printing was used to produce most of the parts for the three engines tested. The two printers used were a fused filament fabrication (FFF) printer (Ultimaker 2+, Ultimaker B.V.), and a stereolithography (SLA) printer (Form 2, Formlabs Inc.). A detailed description of these two printers is presented in Chapter 4. The SLA printer was able to produce parts with very small dimensional inaccuracies (<0.15mm) in all three axes of the print, while the FFF printer was able to produce small inaccuracies in the Z direction of the printed parts (<0.2mm), however the *x* and *y* axis produced inaccuracies of up to 1% in the part size. Therefore a 2% uncertainty was provided for the calculations of the volumes and areas using the solid models of parts printed using the FFF printer. While parts made using the SLA printer were assumed to have a negligible uncertainty associated with them.

### 3.4.3 Calculation of Variable Engine Volumes

The volume variations of each engine were determined from the drive mechanism that they used. Both the Mark 2 and EP-1 used a slider-crank mechanism to produce the motion of the displacer and power pistons. A schematic of a typical slider-crank mechanism is shown in Figure 3.18. In the figure, the crank arm length, connecting rod length, and distance between the piston movement axis and crank arm rotation point are $r_2$, $r_3$, and $r_1$, respectively. The instantaneous angle of the crank arm, $\theta_1$, was combined with the mechanism dimensions to calculate the instantaneous position of the piston relative to the position of minimum volume, $x_p$, using Equation 3.3 [72].

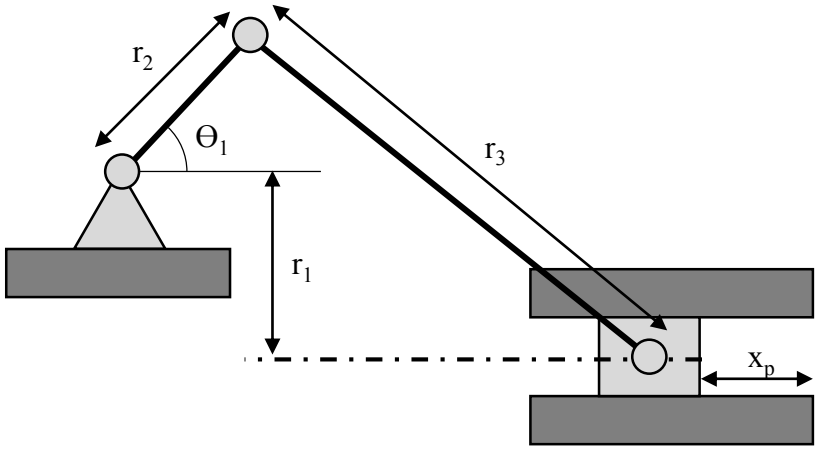


Figure 3.18 Schematic of a slider-crank mechanism modified from [72].

$$x_p(\theta) = (r_2 + r_3) - ((r_2\cos(\theta_1) - r_3 cos\left(\pi - \sin^{-1}\left(\frac{-r_1 + r_2\sin(\theta_1)}{r_3}\right)\right)) \quad 3.3$$

In a typical piston-cylinder system, the instantaneous piston position, $x_p$, can then be coupled with the cross-section area of the piston, $A_p$, to determine the volume variations of the piston-cylinder system, $V_p$ as shown in Equation 3.4.

$$V_p(\theta) = A_p x_p(\theta) \quad 3.4$$

### 3.4.4 Calculation of Working Fluid Mass

To compare the experimentally determined indicator diagram to the Schmidt model's indicator diagram, the approximate mass of working fluid had to be determined. The mean cycle pressure of the experimental indicator diagram could be used to estimate the mass of gas required. The Schmidt model would calculate an initial mass of gas based on the experimental determined mean cycle pressure using the ideal gas law. The mass of gas was then iteratively changed so that the mean cycle pressure of the Schmidt model was equal to the mean cycle pressure of the experimental engine.

### 3.4.5 Calculation of Indicated Work and Forced Work

The volume variations of the engine determined from the crank shaft position can be combined with the cycle pressure to produce the indicator diagram. The area enclosed by the indicator diagram, the indicated work, was calculated using an inbuilt function (function *polyarea,* MATLAB)

With the indicator diagram determined, and the buffer pressure measured and assumed constant, the amount of forced work could be calculated. This was done using the definition of forced work. Forced work occurs when the pressure difference across the power piston, caused by the working pressure and buffer pressure, has the opposite direction of the volume change vector [73]. Based on this definition, a Riemann's sum coupled with an IF statement can be used to determine the

amount of forced work that occurs during a cycle. The experimental indicator diagram showing the indicated work, forced work and buffer pressure is illustrated in Figure 3.18.

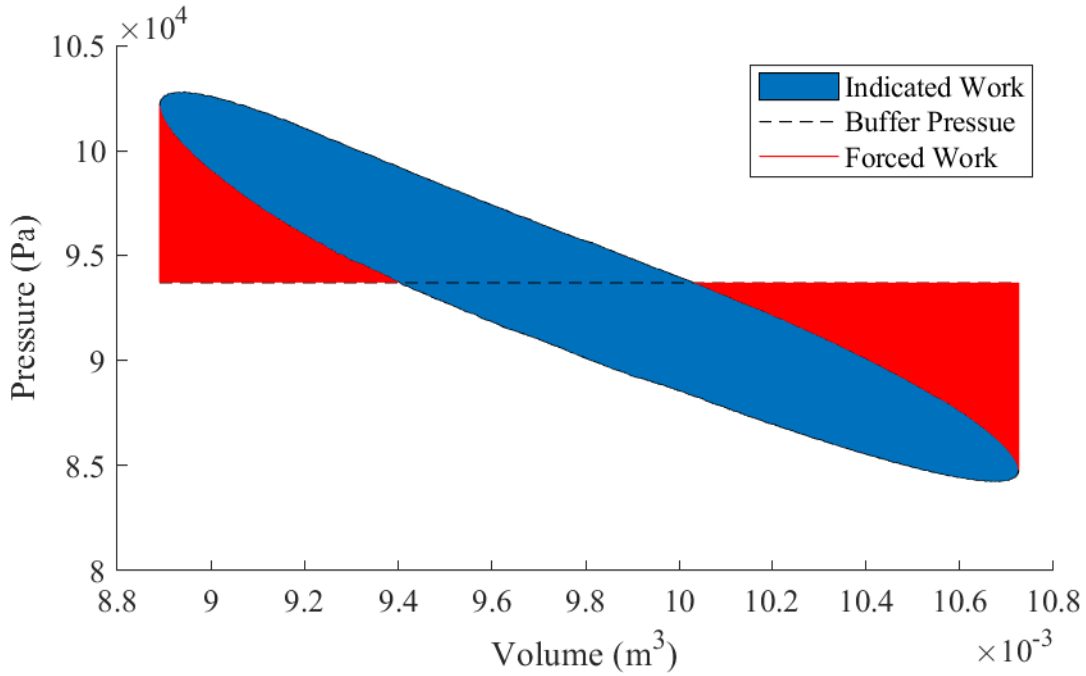


Figure 3.19 Experimental indicator diagram.

## 3.5 Experimental Uncertainty

For each measurement device and output variable calculated, a standard uncertainty in the measurement or value was calculated. The standard uncertainty was calculated directly for measurement devices, while the propagation of uncertainty method was used to determine the standard uncertainty for output variables [69]. If the standard uncertainty could not be calculated directly using the propagation of uncertainty method, the "worst-case" method was used [74]. This method was used to determine the standard uncertainty in the cases of indicated work, forced work, and mechanism effectiveness. All standard uncertainties that will remain constant are tabulated in Table 3.9. Sample calculations for the constant and variable standard uncertainties are provided in the Appendix A and B.

Table 3.9 Constant standard uncertainties for the EP-1.

| Equipment / Output Variable | Standard Uncertainty | Uncertainty Notes |
|---|---|---|
| Thermocouple Type T (TTSS-116E-6, Omega Engineering Inc.) | ± 1.86 °C | Calibration |
| RTD (RTD-810, Omega Engineering Inc.) | ± 0.62 °C | Calibration |
| Weight Scale (Ohaus B50AS) | ± 0.017 kg | Calibration |
| Rotary Encoder (15S-19M1-0500NV1ROC-F03-S1, Encoder Products Company) | ± 1° | Position Calibration |
| Rotary Encoder (15S-19M1-0500NV1ROC-F03-S1, Encoder Products Company) | ±0.005 % | Frequency |
| Pressure Transducer (Validyne DP15-50, Validyne Engineering) | ± 0.44 kPa | Calibration |
| Atmospheric Pressure (Galaxy A5 2018, Samsung) | ± 0.10 kPa | Calibration |
| Torque Transducer (TRS600, Futek Advanced Sensor Technology Inc.) | ± 0.006 Nm | Calibration |
| Linear Dimensions (x, y) - 3D Printing (Ultimaker 2+) | ± 1 % | Calibration No Calculation |
| Linear Dimensions - 3D Printing (Form 2) | 0.15 mm | Calibration No Calculation |

### 3.5.1 Calculation of Standard Uncertainty for Measurement Devices

To calculate the standard uncertainty of a measurement device, the sources of systematic and random error were required [69]. The typical sources of errors and their respective types used in the following uncertainty analysis are tabulated in Table 3.10.

Table 3.10 Error sources and types used to calculate the standard uncertainty.

| Error Source | Error Type | Ref |
|---|---|---|
| Instrument error stated by manufacturer | Systematic | [69] |
| DAQ module error stated by manufacturer | Systematic | [69] |
| Calibration device resolution | Systematic | [69] |
| Spatial variation of measurement | Systematic | [69] |
| Time constant | Systematic | [69] |
| Noise and quantization | Random | [69] |

The root of the sum of squares (RSS) method was used to calculate the total systematic uncertainty, $s_{\bar{x}}$, and the random uncertainty, $r_{\bar{x}}$, as displayed in Equation 3.5 and 3.6 [69]. After these two values are calculated, they are combined together using RSS to determine the combined standard uncertainty, $u_{\bar{x}}$, as depicted in Equation 3.6 [69].

$$s_{\bar{X}} = \left( \sum_{k=1}^{K} \left( s_{\bar{X}_k} \right)^2 \right)^{\frac{1}{2}} \quad 3.5$$

$$r_{\bar{X}} = \left( \sum_{k=1}^{K} \left( r_{\bar{X}_k} \right)^2 \right)^{\frac{1}{2}} \quad 3.6$$

$$u_{\bar{X}} = \sqrt{(s_{\bar{X}})^2 + (r_{\bar{X}})^2} \quad 3.7$$

### 3.5.2 Calculation of Standard Uncertainty for Output Variables

The standard uncertainty of the output variables was calculated from the standard uncertainty of the measurement devices. The method used was the propagation of uncertainty [69], [75], [76]. This method involves taking the partial derivative with respective to each independent variable and combining it with that variable's standard uncertainty. To showcase this, an arbitrary function, $F_X$, shown in Equation 3.8 has the propagation of uncertainty applied to it shown in Equation 3.9

[75]. If the measurement of the variables are independent of one another, then the trailing term Equation 3.9., the covariance, is assumed to be zero, and the standard uncertainty is calculated using Equation 3.10 [75].

$$F_X = f(A, B \dots) \tag{3.8}$$

$$u_{\overline{F_X}} = \sqrt{\left(\frac{\partial F_X}{\partial A}\right)^2 (u_{\bar{A}})^2 + \left(\frac{\partial F_X}{\partial B}\right)^2 (u_{\bar{B}})^2 + \cdots \left(\frac{\partial F_X}{\partial A}\right)\left(\frac{\partial F_X}{\partial B}\right)(u_{\bar{A}\bar{B}})^2 \dots} \tag{3.9}$$

$$u_{\overline{F_X}} = \sqrt{\left(\frac{\partial F_X}{\partial A}\right)^2 (u_{\bar{A}})^2 + \left(\frac{\partial F_X}{\partial B}\right)^2 (u_{\bar{B}})^2 + \cdots} \tag{3.10}$$

Most output variables were calculated using a combination of multiplication, division, subtraction or addition. This allowed the equations to calculate the standard uncertainty to be simplified [76]. If an arbitrary output variable, $F_X$, as shown in Equation 3.11, is calculated only using addition or subtraction, then the standard uncertainty is calculated using Equation 3.12 [76].

$$F_X = A + B - C \tag{3.11}$$

$$u_{\overline{F_X}} = \sqrt{(u_{\bar{A}})^2 + (u_{\bar{B}})^2 + (u_{\bar{C}})^2} \tag{3.12}$$

If an arbitrary output variable, $F_X$, as shown in Equation 3.13, is calculated only using multiplication or division, then the standard uncertainty is calculated using Equation 3.14 [76].

$$F_X = \frac{AB}{C} \tag{3.13}$$

$$\frac{u_{\overline{F_X}}}{F_X} = \sqrt{\left(\frac{u_{\bar{A}}}{A}\right)^2 + \left(\frac{u_{\bar{B}}}{B}\right)^2 + \left(\frac{u_{\bar{C}}}{C}\right)^2} \tag{3.14}$$

### 3.5.3 Calculation of Standard Uncertainty for "Worst-Case" Method

The worst-case method [74] was used to calculate the standard uncertainty for some values. These values included integral dependent values, and values that were derived from complex equations. The uncertainties calculated this way include the indicated work, forced work, compression ratio, West number, and mechanism effectiveness.

To determine the uncertainty in the indicated work, the indicator diagram with the largest indicated work was determined. Figure 3.20 shows how the standard uncertainty in the work space pressure was added to the work space pressure from the minimum volume to the maximum volume and subtracted from the maximum volume to the minimum volume. The standard uncertainty in the volume was added to the cycle volume from the maximum pressure to the minimum pressure and subtracted from the minimum pressure to the maximum pressure as depicted in Figure 3.21. The combination of both of these methods is shown in Figure 3.22. The difference between the maximum indicated work and mean indicated work was equal to the standard uncertainty in the indicated work. A similar method was used to determine the forced work standard uncertainty.

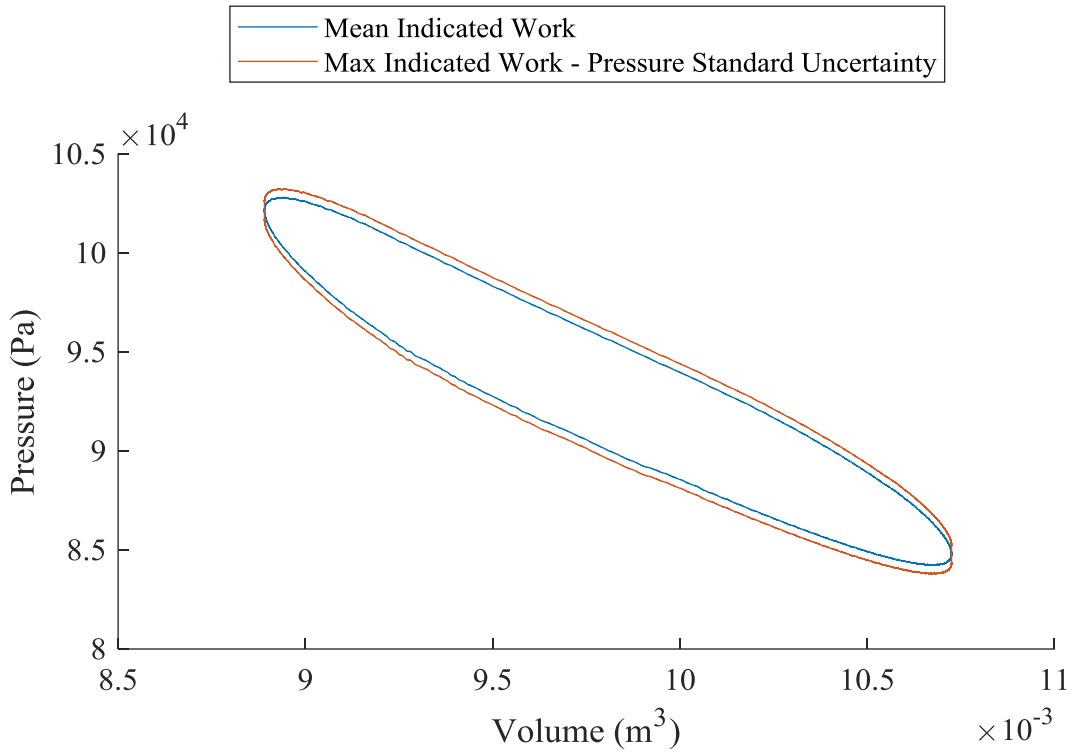


Figure 3.20 Change in the size of the indicator when the standard uncertainty in pressure is applied.

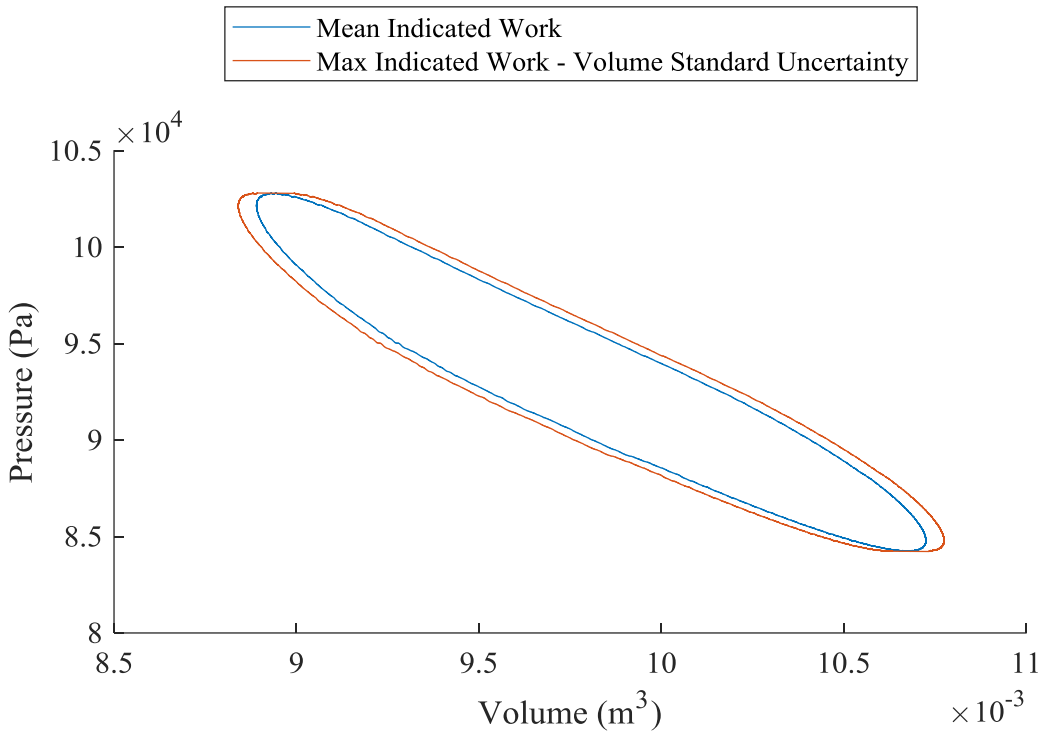


Figure 3.21 Change in the size of the indicator when the standard uncertainty in volume is applied.

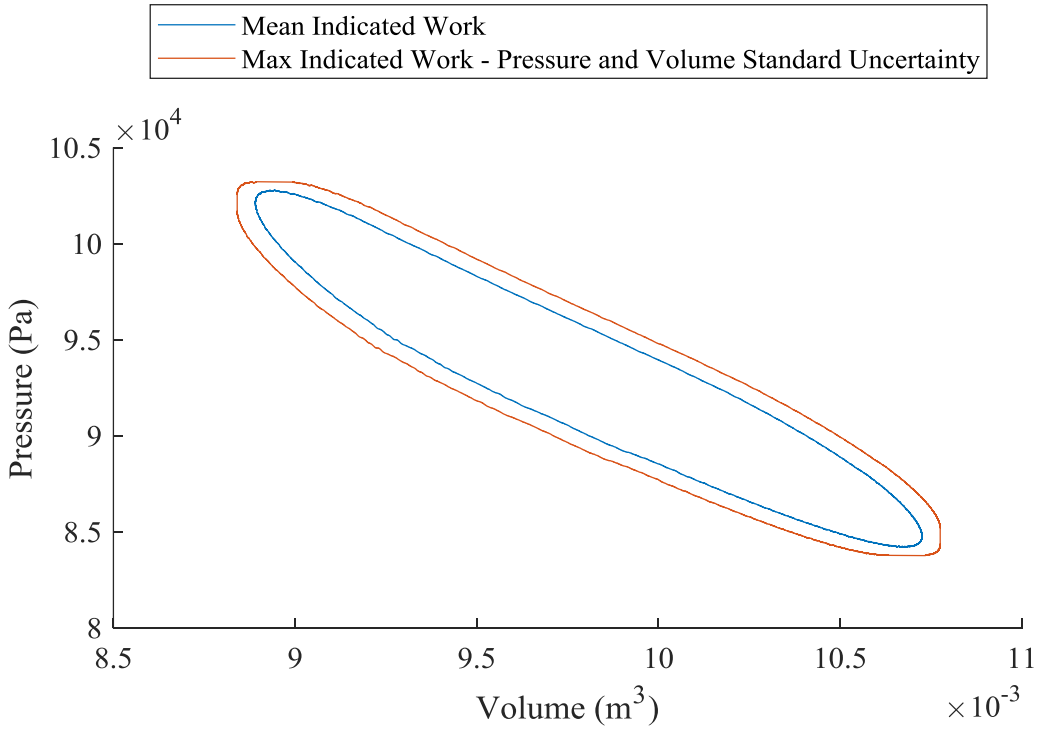


Figure 3.22 Change in the size of the indicator when the standard uncertainty in pressure and volume is applied.

Two different uncertainties were calculated for the compression ratio, the relative and absolute uncertainty. Throughout the compression ratio tests, the minimum volume of the engine would not change. Only the power piston swept volume would change. Therefore, the tested compression ratios could be compared relative to one another with a reduced uncertainty. This uncertainty only included the uncertainty in the instantaneous power piston volume. After the relative compression ratio that produced the maximum shaft power is found, then the absolute uncertainty will be applied to it. The absolute uncertainty in the compression ratio is calculated with both the uncertainty in instantaneous power piston volume and the minimum engine volume.

An existing solver, Worst-Case Propagation of Uncertainty [77], was used to calculate the standard uncertainty in the mechanism effectiveness. This was done instead of using the propagation of uncertainty method because of the complexity of the equation. To calculate the uncertainty if the mechanism effectiveness, the methods listed above were first used to calculate the standard uncertainty in the indicated work, forced work, and shaft work. These uncertainties, along with the mean values were then input into the solver to determine the mean value of the mechanism effectiveness and its associated standard uncertainty.

## 3.6 Experimental Procedures

The following section will describe the procedures required to operate and test the Stirling engines. These processes are important to follow so that results are repeatable. They are also important so that no injuries occur doing operation to the operator, or damage to the engine.

### 3.6.1 Warm Up Procedure

1. Check the area around the engine to ensure it is tidy and free of tripping hazards.
2. Plug the water baths into two separate circuits so that they do not trip the breakers.
3. Close the valves on the water baths so water cannot circulate through the heat exchangers.
4. Turn on the water baths so they can begin heating and cooling to the desired temperatures. They will take approximately 90 minutes to reach temperature. The larger volume water bath should be used for cooling.
5. Turn on all DAQ equipment so that it can warm up and reach an operational state.
    a. DAQ Computer
    b. DAQ Modules
    c. Power supply for rotary encoder and torque transducer
6. Check various engine components for secureness.
7. Once the water baths are close to reaching the desired temperatures slowly open valves to let the water flow through the heat exchangers.
8. Once values are fully open, check for leaks at all tubing connection points.
9. Once the water baths have reached their desired temperature, check to see if the DAQ software is working properly by taking some sample data and checking if it is outputting correctly.

### 3.6.2 Changing Engine Configuration Procedure

1. Make sure that the engine seal plug is removed so that the work space of the engine is open to atmosphere.
2. Modify engine to the desired configuration (compression ratio, phase angle, power piston, displacer piston, heat exchanger position, etc.)
3. Make sure all critical components are secured.

4. Check to make sure that the engine can complete a few rotations by slowly spinning the engine through a few revolutions.

### 3.6.3 Engine Start Procedure

1. Bring the power piston to the position of mid stroke. Mid stroke provides the mass of working fluid contained in the work space that closely approximates that calculated in the model.
2. Replace in the engine seal plug.
3. Using the engine flywheel, spin in the correct direction based on the location of the heat exchangers relative to the power piston. The engine may be difficult to initially turn; however, it may take off spinning quickly so caution is recommended.
4. The engine will begin spinning.
5. Let the engine run for at least two minutes so that the mass of the working fluid can equalize. The temperature of the hot water bath may drop.
6. Load the engine slightly to reduce the engine operating speed and therefore the rate of heat transfer into the engine.
7. Wait until both water baths have returned to their set point temperature.

### 3.6.4 Engine Stop Procedure

1. Remove engine seal plug.
2. Wait for engine to stop. The leak should be large enough for engine to stop operation after a few revolutions.

### 3.6.5 Shaft Power Measurement Procedure

1. Modify engine to desired configuration.
2. Get engine to start operating, by following engine start procedure.
3. Incrementally apply the desired load to the engine by:
    a. Adding a fraction of the desired load. Add in quarters of the desired load.
    b. Waiting for the engine to reach steady state speed based on the DAQ software live view.
    c. Repeating until desired load is applied.

4. Wait two minutes or until the engine has reached a steady state operating speed.
5. Sample instruments using DAQ software.
6. Repeat for all desired loads.
7. Repeat for all desired configurations.

### 3.6.6 Motoring Testing Procedure

1. Modify engine to desired configuration.
2. Put in engine seal plug when:
    a. If power piston system is being controlled by the motor, plug engine when power piston is at mid stroke.
    b. If displacer piston system is being controlled by the motor, plug engine when displacer piston is at mid stroke.
3. Use electric motor control software to control electric motor speed.
4. Let the engine run for at least two minutes so that the mass of the working fluid can equalize.
5. Sample instruments using DAQ software.
6. Repeat for all desired speeds.
7. Repeat for all desired configurations.

### 3.6.7 Cool Down Procedure

1. Make sure engine has stopped running.
2. Make sure engine seal plug is removed.
3. Turn off water baths and close valve.
4. Drain water from engine's heat exchangers.
5. Turn off all DAQ equipment.

## 3.7 Transient to Steady State Justification

### 3.7.1 Engine Startup

To determine when data should be sampled, tests were performed to showcase the transition from transient to steady state operation of the EP-1. Recording data at steady state allowed for the best-case possible to produce repeatability of results.

The first test was to see if, and when, the mean cycle pressure would reach steady state. Since none of the engines are hermetically sealed, the mean cycle pressure of the engine should eventually reach a relative constant value. The change in the mean cycle pressure is largely dependent on the mass of the working fluid. As the engine's working pressure varies cyclically, extra air is drawn into the engine when the working pressure is below atmospheric pressure, and air is expelled when the working pressure is above the atmospheric pressure. Eventually, these leak rates should equate to one another and the mean cycle pressure should reach a constant value.

Figure 3.23 shows the change in the mean pressure of the engine during the first two minutes of operation. To determine the mean cycle pressure, the sampled pressure data could not be used, and instead had to be determined from a curve fitted to the pressure data. This was required because the engine speed could vary throughout the cycle. If the engine speed varied, then the pressure data throughout one cycle would not be uniformly distributed per crank angle. For example, if the engine ran slower during a section of the cycle, then more pressure data would be sampled per crank angle during this section. This would create a biased in the mean cycle pressure because of the higher number of amount of data points during this section. To eliminate this, a curve was fitted to the pressure data. This curve would be continuous, which would therefore eliminate any biases when the mean cycle pressure was calculated. The mean cycle pressure quickly changes during the first ten seconds of operation before slowly changing for the duration of the test. A steady state mean cycle pressure did not occur during the two minutes of the test; however, the rate of change of the mean cycle pressure was reduced.

The water baths used to heat and cool the water in the flow loops were not able to provide, or reject, enough heat to keep the inlet temperature of heat exchanger constant. Figure 3.24 shows

the change in the temperature of the water at the inlet and outlet of the thermal sink heat exchanger for the two-minute transient to steady state test. This figure shows that the temperature of the outlet changes quickly initially, before reaching a constant value. This showcases that the cooling rate of the thermal sink water bath is able to keep up with the engines heat rejection rate. Similar observations can be seen for the thermal source heat exchangers inlet and outlet temperature in Figure 3.25. However, unlike the thermal sink, the thermal source's inlet temperature continues to drop. This demonstrates that the heating rate of the thermal source water bath is no able to keep up with the engines heat input rate requirements.

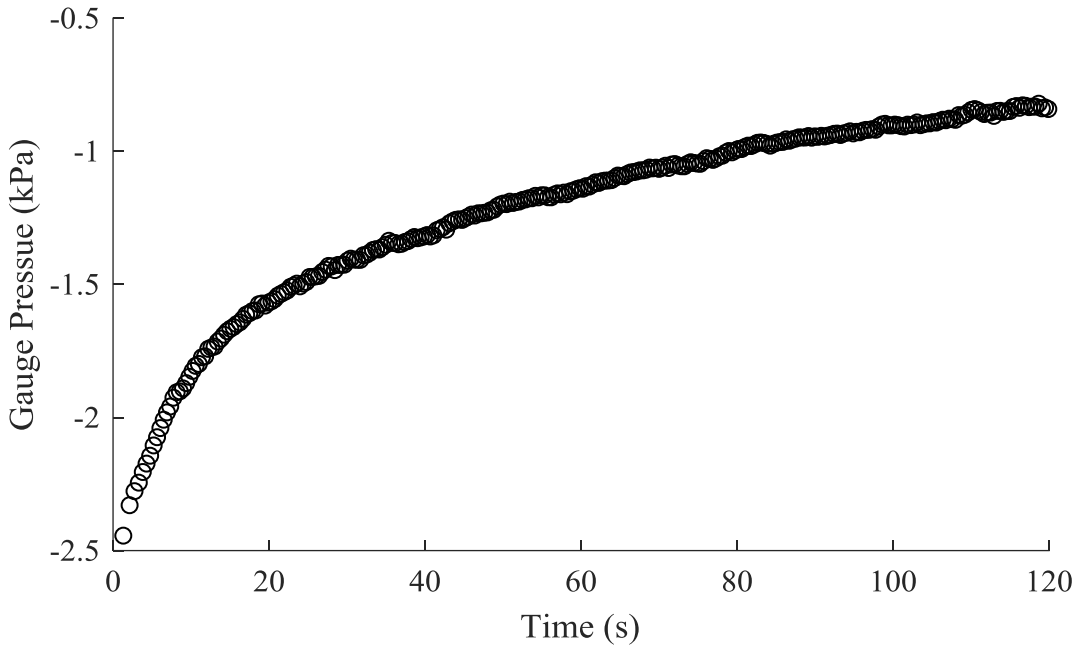


Figure 3.23 Transient test of the change in the mean cycle pressure of the EP-1 as it is started and run for two minutes. Engine configuration: Compression Ratio (CR) = 1.17, Phase Angle (α) = 90°, Engine Load = Unloaded, Hot Heat Exchanger Position = Top, and Regenerator = Slotted.

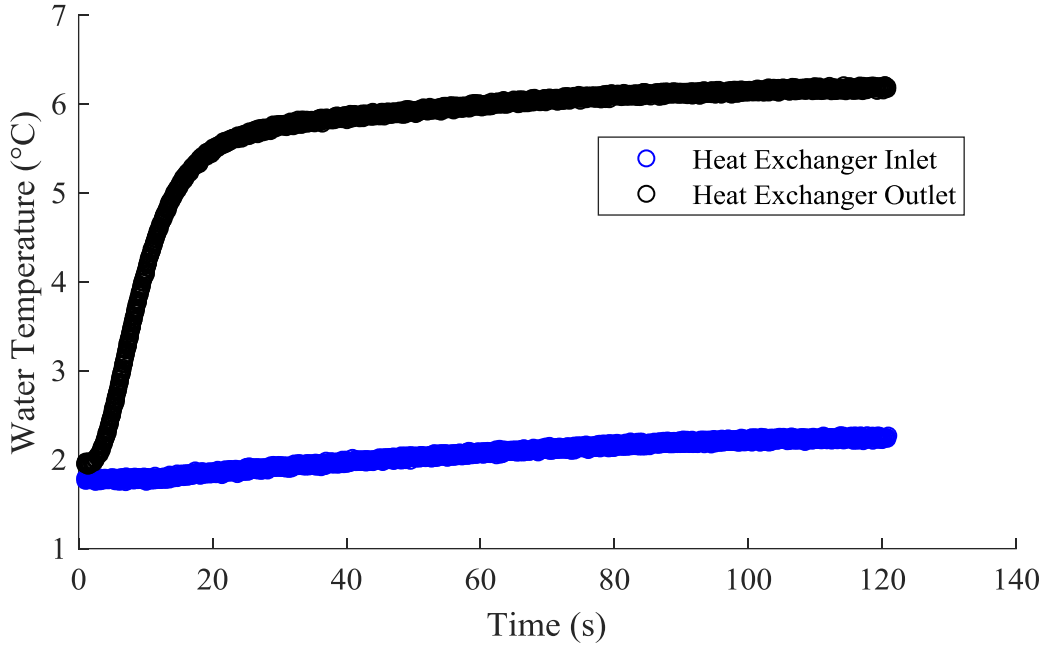


Figure 3.24 Transient test of the change in temperature of the thermal sink fluid at the inlet and outlet of the heat exchanger of the EP-1 as it is started is run for two minutes. Engine configuration: Compression Ratio (CR) = 1.17, Phase Angle (α) = 90°, Engine Load = Unloaded, Hot Heat Exchanger Position = Top, and Regenerator = Slotted.

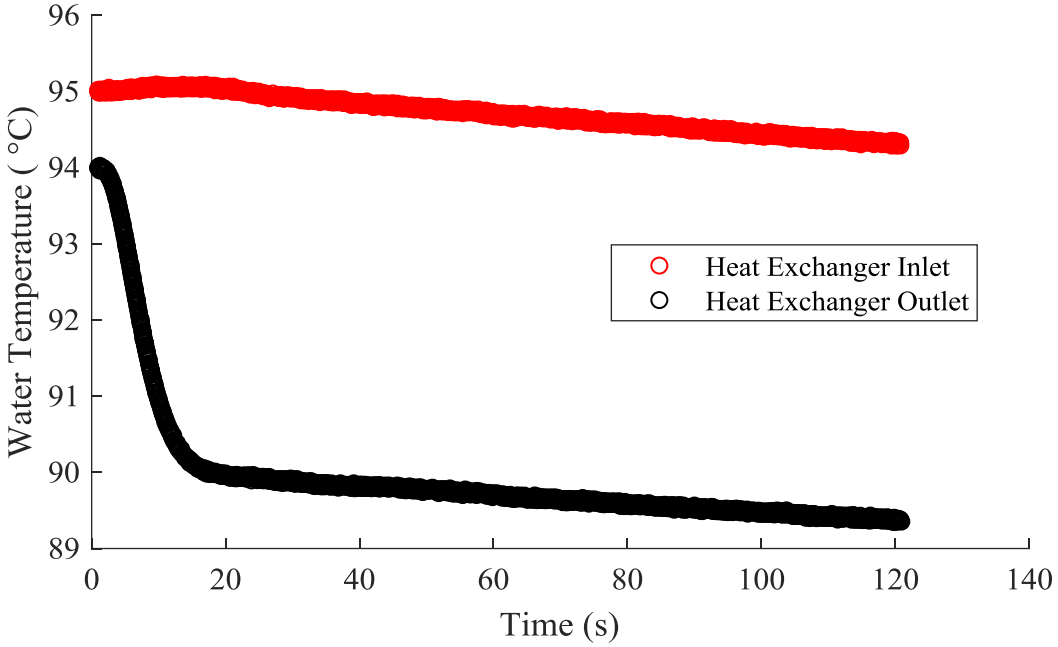


Figure 3.25 Transient test of the change in temperature of the thermal source fluid at the inlet and outlet of the heat exchanger of the EP-1 as it is started is run for two minutes. Engine configuration: Compression Ratio (CR) = 1.17, Phase Angle (α) = 90°, Engine Load = Unloaded, Hot Heat Exchanger Position = Top, and Regenerator = Slotted.

With the information of the change in the mean cycle pressure and the thermal source inlet temperature, when the engine was first started, it was allowed to run for five minutes before data was sampled for processing. During these five minutes, a load was applied to the engine to reduce the operating speed so that the temperatures of the water baths stayed constant.

The temperature of the working fluid in the expansion and compression space throughout the transient to steady state was investigated. Figure 3.26 shows the temperature of the working fluid in the compression space, while the temperature in the expansion space is shown in Figure 3.27. Both these figures show that the working fluid temperature changes initially before reaching a steady state fluctuation. The figures appear to show a lot of noise in the temperature measurement. This is not noise but is instead the cyclical temperature fluctuations. These cyclical temperature fluctuations are shown for the last two cycles of the test in the compression space in Figure 3.28 and the expansion space in Figure 3.29.

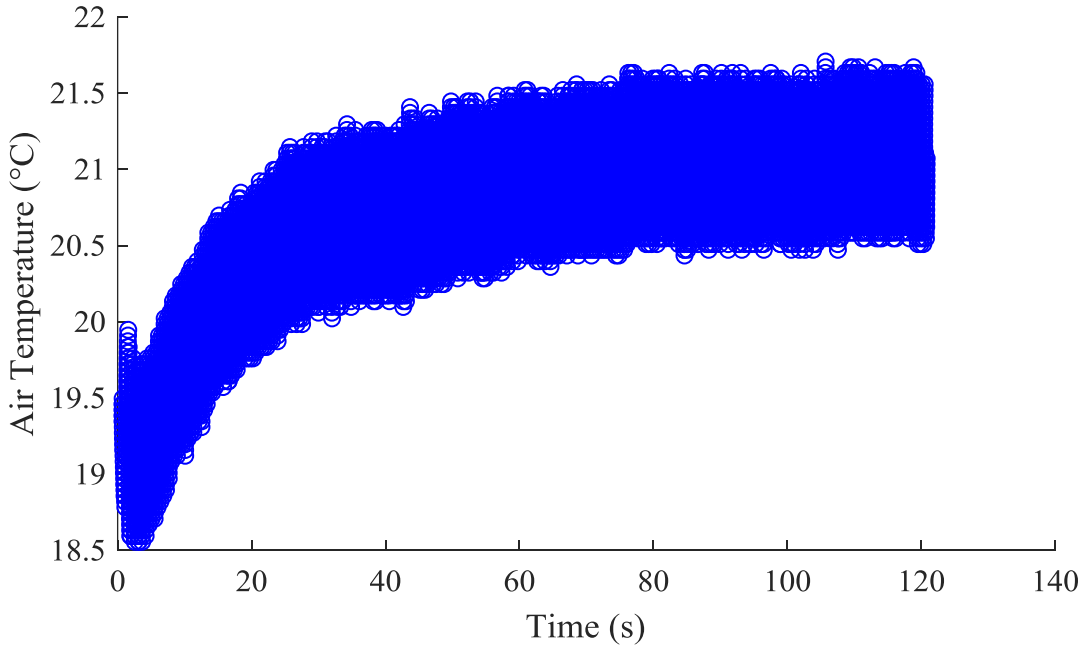


Figure 3.26 Transient test of the change in temperature of the working fluid in the expansion space of the EP-1 as it is started is run for two minutes after a load change Engine configuration: Compression Ratio (CR) = 1.17, Phase Angle (α) = 90°, Engine Load = Unloaded, Hot Heat Exchanger Position = Top, and Regenerator = Slotted.

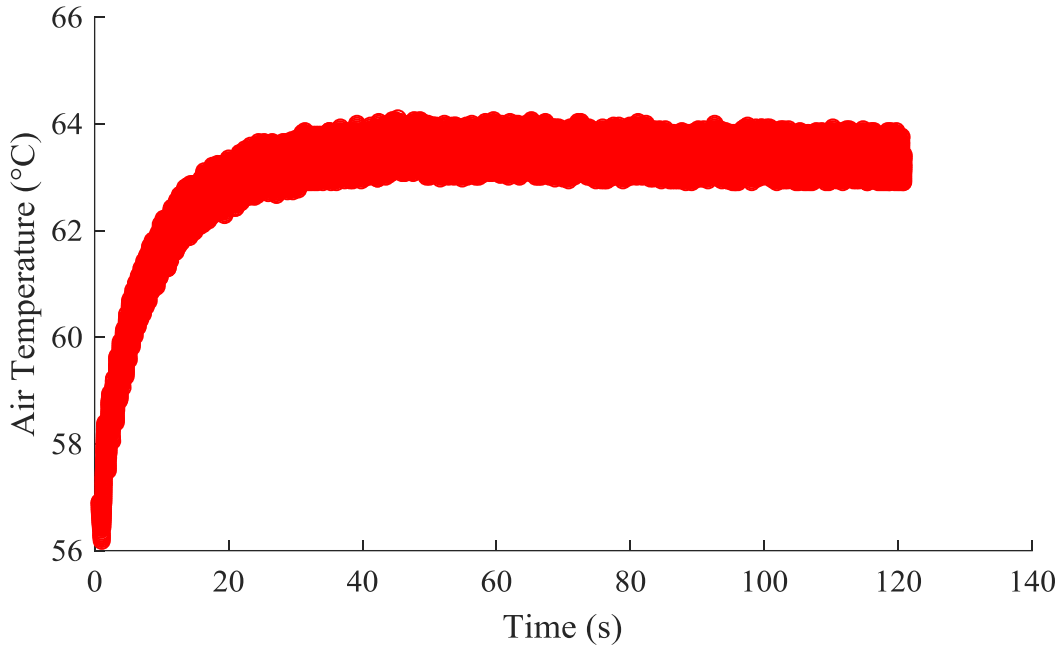


Figure 3.27 Transient test of the change in temperature of the working fluid in the compression space of the EP-1 as it is started is run for two minutes after a load change Engine configuration: Compression Ratio (CR) = 1.17, Phase Angle (α) = 90°, Engine Load = Unloaded, Hot Heat Exchanger Position = Top, and Regenerator = Slotted.

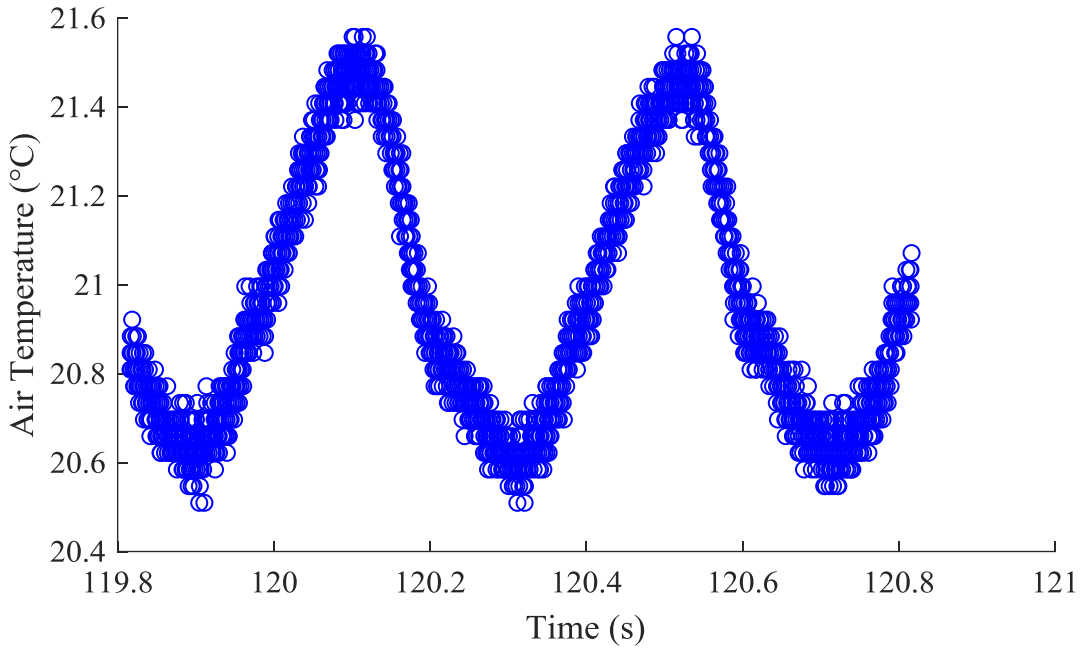


Figure 3.28 Compression space working fluid temperature fluctuations.

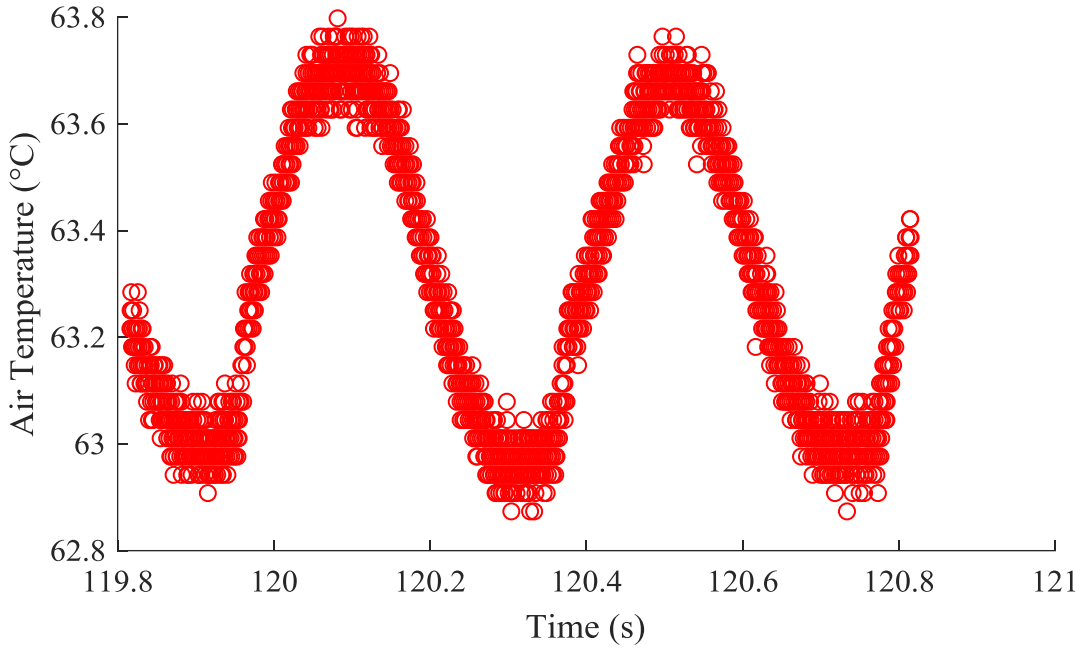


Figure 3.29 Expansion space working fluid temperature fluctuations.

Finally, the operating speed is examined. The operating speed was also found to increase dramatically, before plateauing, and very slowly decreasing over the duration of the test. This change in the operating speed is shown in Figure 3.30. This could be caused by the change in the mean cycle pressure or the change in the inlet temperature of the heating and cooling fluid or other factors.

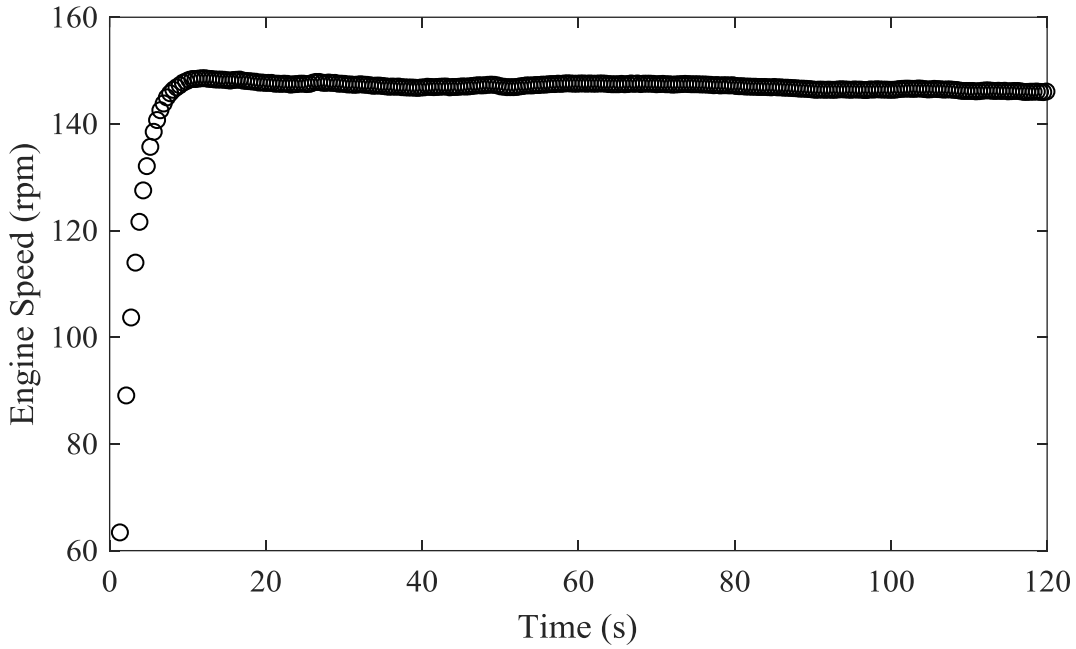


Figure 3.30 Transient test of the change in the engine speed of the EP-1 as it is started and ran for two minutes. Engine configuration: Compression Ratio (CR) = 1.17, Phase Angle (α) = 90°, Engine Load = Unloaded, Hot Heat Exchanger Position = Top, and Regenerator = Slotted.

### 3.7.2 Engine Load Change

The steady state operation of the engine is also desired when the loading condition on the engine is changed. When the load on the engine was changed the speed of the engine and the mean cycle pressure would change. This change in the mean cycle pressure when the load is changed is showcased in Figure 3.31.When the engine was loaded, measurements were made after two minutes of operation to allow for the mean cycle pressure to reach a steady state value.

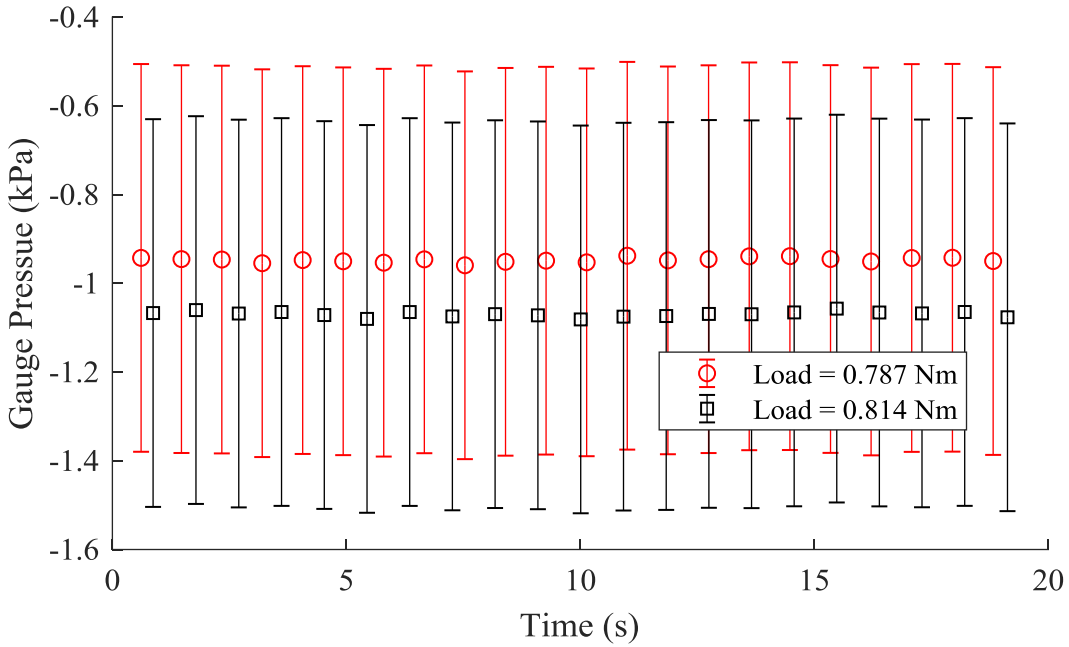


Figure 3.31 Change in the mean cycle pressure between two different loaded states.

# Chapter 4 Experimental Engines

This chapter covers the development of the following three kinematic gamma-type LTDSEs: Mark 1, Mark 2 and EP-1. A summary of the operating parameters, manufacturing techniques, and materials used is presented. To finish, a thorough description of the final configuration of each engine is provided, along with lessons learned from each engine. The Mark 1 and 2 sections also contain a brief look at how each engine performed.

## 4.1 Operating Parameters

All three engines shared six operating parameters that influenced their designs. These parameters are tabulated in Table 4.1 and the reasons behind each value are described below, except for the fluid based heating and cooling method which was previously described in Chapter 2.

Table 4.1 Operating parameters of the three tested engines.

| Property | Value and Units |
|---|---|
| Temperature of the Thermal Source | 95 °C |
| Temperature of the Thermal Sink | 2 °C |
| Heating and Cooling Method | Liquid |
| Working Fluid | Atmospheric Air |
| Buffer Pressure | Atmospheric Pressure ≈ 93.5 kPa [17]. |
| Charge Pressure | Atmospheric, 0 gauge |

The 95 °C temperature of the thermal source and 2 °C temperature of the thermal sink was criteria used to define the overall limits of the investigation. The thermal source temperature was chosen to replicate the temperature of a geothermal brine that could be found in Alberta [8]. While the thermal sink temperature was chosen because in a field application of a Stirling system, the ambient air would act as the thermal sink, and the average ambient air temperature in Alberta is approximately 5 °C as calculated from the Canadian Climate Normals 1981-2010 Station Data for Edmonton [17].

Air was chosen as the working fluid because it had limited safety risks associated with it and was abundantly available. This was also done so that the working space and buffer space would use the same gas. With the same gas in each space, there would be no contamination problems of the working fluid if there were any leaks of the Stirling engines. The three engines were chosen not to be pressurized relative to atmospheric pressure and used atmospheric pressure as the buffer pressure. This allowed for the engines to not be hermetically sealed. The atmospheric pressure could stay fairly constant over small periods of time, which would provide constant testing conditions [78]. Finally, the working fluid of air, the buffer pressure equal to atmospheric, and no charge pressure were chosen because other LTDSEs typically use these parameters, and it made potential comparison to these engines easier [23].

## 4.2 Manufacturing and Materials

To manufacture and modify the three LTDSEs, several different manufacturing techniques and materials were used. The most common manufacturing technique used was 3D printing, and the most common material type used was plastic. This section will overview why certain 3D printers and printing materials were used, and why other materials, both plastics and metals, were used in the manufacturing process. This section will also act to reduce repeat explanations in the following sections where the engines are described.

### 4.2.1 3D Printing

Two different 3D printers were used for manufacturing the LTDSEs: the Ultimaker 2+ [Ultimaker B.V.], and the Form 2 [Formlabs, Inc.]. These two printers each have specific advantages and disadvantages based on the fundamental printing technologies used, material compatibility and cost, and size of parts they are able to produce.

#### 4.2.1.1 Ultimaker 2+

The Ultimaker 2+ is a 3D printer that uses fused filament fabrication (FFF). A FFF 3D printer consists of several components listed below [79].

1. Plastic filament: the material used to create the part.
2. Nozzle and heating element: used to heat the plastic filament so that a continuous bead of plastic can be extruded through the nozzle onto a build platform or existing plastic.
3. Mechanical movement system: used to move the nozzle around the area of the build platform, and to raise and lower the build platform.
4. Build platform: used to secure the printing part throughout the 3D printing process.

To reduce print time, and material used, FFF usually do not produce parts that are 100% solid [80]. Instead they rely on printing a shell of the part and an infill to this shell the produces an internal support structure of a density less than 100%. The quality of the finished part is based on the nozzle size and the layer height chosen. In general, FFF 3D printers, and the materials they use, are inexpensive relative to other 3D printing technologies. They produce parts that are less dimensionally accurate and have a lower resolution surface when compared to other printing technologies; however, they are able to produce parts quickly.

Parts created by FFF 3D printers can have imperfections and voids in the shell, and are usually not water or air tight [80]. To make them water and air tight, post processing is required. This can be done by coating the part in a paint or epoxy to fill these imperfections and voids and create a continuous barrier. If acrylonitrile butadiene styrene (ABS) material is used, acetone smoothing can be used [80]. Acetone smoothing temporarily melts some of the external shell, so that the material can flow and fill the imperfections and voids before it solidifies once the acetone evaporates.

The Ultimaker 2+'s build volume governed the size of both the Mark 1 and Mark 2. The build volume, along with other specifications of the Ultimaker 2+, and the specifications used are highlighted in Table 4.2.

Table 4.2 Specifications of 3D printers used.

| Printer | Build Volume (mm) | Resolution (mm) | Layer Height (mm) | Material | Reference |
|---|---|---|---|---|---|
| Ultimaker 2+ | 223 × 223 × 205 | 0.25, 0.4, 0.6, 0.8[1] | 0.12, 0.2[1], 0.4 | ABS[1],PLA, CPE+, etc. | [81] |
| Form 2 | 145 × 145 × 175 | 0.14[1] | 0.025, 0.5, 0.1[1] | Standard Clear[1], Standard Grey[1] High Temperature[1] | [82] |

[1]Materials and specifications primarily used

#### 4.2.1.2 Form 2

The Form 2 is a 3D printer that use stereolithography (SLA). The parts a SLA printer uses are summarized below [80]:

1. Photo cured plastic resin: the material used to create the part.
2. Laser: used to cure the resin to the build platform or existing cured resin.
3. Mechanical movement system: used to move the laser around the area of the build platform, and to raise and lower the build platform.
4. Build platform: which acts as a base to secure a part throughout the 3D printing process.

SLA 3D printers produce parts that are 100% solid [80]. The quality of the finished part is based on the size of the laser spot and the layer height used. In general SLA 3D printers, and the material they use, are expensive relative to FFF printing [80]. They produce parts of high dimensional

accuracy when compared to other printing technologies; however, the rate of part production is slow.

Since the parts produced are 100% solid, they require no post processing to be air and water tight, but, post processing is required for other reasons [80]. Throughout the printing process the part is continually submerged in a bath of resin; therefore, the finished part will be covered in uncured resin. To dissolve any uncured resin, the part is placed into a high purity isopropanol bath. For the part to achieve the desired material properties it must be post cured with a combination of ultraviolet (UV) light and heat.

The Form 2's build volume provided a size constraint for the final power piston system used for the EP-1. Table 4.2 shows the build volume, along with the other specifications of the Form 2, and the specifications used.

### 4.2.2 Materials

#### 4.2.2.1 Ultimaker 2+ Materials

There exist many different plastic filament types that can be used for FFF 3D printers. The primary filament used for manufacturing was ABS. ABS was used because of its high heat deflection temperature, ease of machining, and options available for post processing [80]. ABS was initially found to be difficult to print due to its high coefficient of thermal expansion causing warping of the part as it cooled [80]. This was addressed by using a special adhesive surface, (BuildTak, Ideal Jacobs Corp), for the build platform, and by enclosing the build volume with insulation to raise its temperature so that the part cooled more evenly. PLA was also used initially on the Mark 1, but due to its difficulty in machining, and low heat deflection temperature it was not used on either the Mark 2 or EP-1 [80]. A summary of the relevant material properties of ABS and PLA can be seen in Table 4.3.

#### 4.2.2.2 Form 2 Materials

There are several different resins available for the Form 2; but only the standard clear and grey, and high temperature resins were used. The standard resin was used to make structural parts such as crank arms and mounting brackets. High temperature resin was used in parts that experienced high thermal loads and were only loaded in compression, due to the brittleness of the material. A

summary of the relevant material properties of both the standard and high temperature resins can be seen in Table 4.3.

#### 4.2.2.3 Other Plastics

Three main plastics were also used in the construction of all three engines: acrylic, polycarbonate (PC) and expanded polystyrene (EPS). Acrylic parts were used where large plate assemblies were required, as the material came in large sheets and could be easily cut into shapes using a laser cutter (VLS3.5, Versalaser). PC was used in areas that required its flexibility, transparency, and ability to resist thermal loads [83], [84]. All three engines used expanded polystyrene (EPS) for their displacer pistons. This was because of its low thermal conductivity, which reduced thermal short-circuiting through the displacer piston. It was also used because of its low density, which reduced the mass of the displacer piston, and its ability to withstand thermal loads[83], [84]. A summary of the relevant material properties of acrylic, PC, and EPS can be seen in Table 4.3.

Table 4.3 Material properties of plastics used.

| Printer | Material | Deflection Temperature at 0.46 MPa (°C) | Ultimate Tensile Strength (MPa) | Reference |
|---|---|---|---|---|
| Form 2 | Standard | 73.1[1] | 65[1] | [85] |
| Form 2 | High Temperature | 289[1] | 51[1] | [85] |
| Ultimaker | ABS | 98 | 40 | [83], [84] |
| Ultimaker | PLA | 49 | 26 | [86] |
| - | EPS | 95 | 40 | [83], [84] |
| - | PC | 140 | 70 | [83], [84] |
| - | Acrylic | 95 | 70 | [83], [84] |

[1]Materials properties are only valid if proper post processing steps have been applied

#### 4.2.2.4 Metals

The two main metals used for the heat exchangers were aluminum and copper. These two metals were used because of their high thermal conductivity and ability to resist corrosion, displayed in Table 4.4.

Table 4.4 Material properties of metals used.

| Material | Thermal Conductivity (W/m-K) | Corrosion Resistant | Reference |
|---|---|---|---|
| Aluminum | 289 | Yes | [87] |
| Copper | 398 | Yes | [88] |

## 4.3 Engine Description: Mark 1

### 4.3.1 Engine Development and Description

The Mark 1 is a kinematic gamma-type LTDSE that was designed as a proof of concept. Some aspects of the Mark 1's design were based around an existing 3D printed "toy-sized" gamma-type LTDSE. These included the compression ratio, the displacer cylinder sleeve, and the regenerator channel [89]. All 3D printed parts of the Mark 1 were made on the Ultimaker 2+ using either ABS or PLA. The final configuration of the Mark 1 is shown in Figure 4.1, and presents the main systems that will be described in detail in the following sections. A drawing package for the Mark 1 is included in the Appendix E.

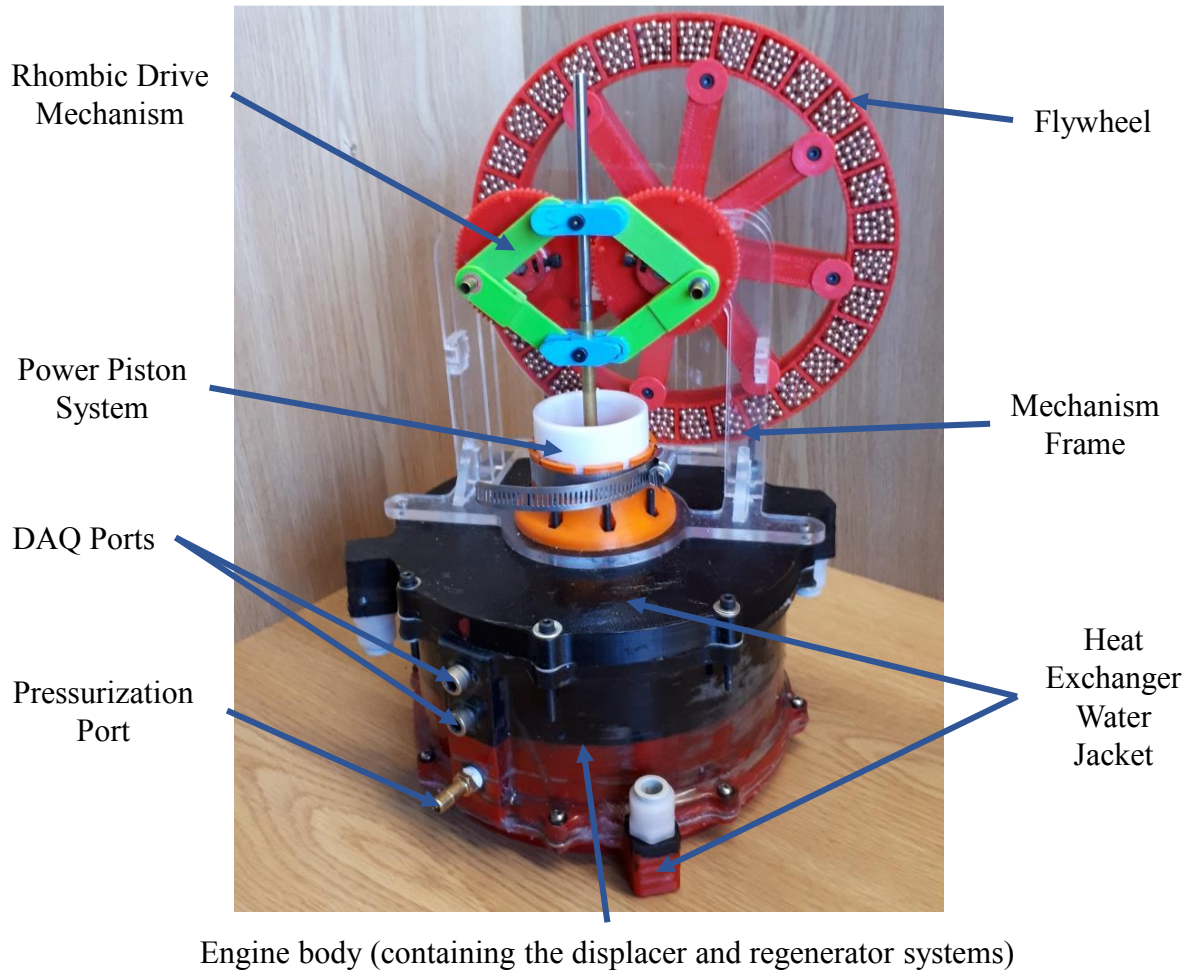


Figure 4.1 Image of the final configuration of the Mark 1.

#### 4.3.1.1 Power Piston System

The Mark 1 uses a custom-made piston-cylinder set for its power piston system. The system consists of a 3D printed power piston that resides in a Delrin cylinder. The power piston system has a bore diameter of 0.05 cm, a stroke of 4.5 cm, and a swept volume of 86 $cm^3$ that results in a compression ratio of 1.06.

The power piston uses an adjustable O-ring seal to contain the working fluid inside the engine. The seal can be modified to find a balance between sealing capability and friction. This is accomplished by changing how much the O-ring is compressed between the main body of the power piston and the clamping flange with four adjustment bolts. Figure 4.2 shows these components and how they interact.

Due to the rhombic drive mechanism used, the power piston rod is hollow and resides in a hole that goes through the center of power piston as shown in Figure 4.2. This is required because the displacer piston rod has to travel up and down through the hollow power piston rod during operation of the engine.

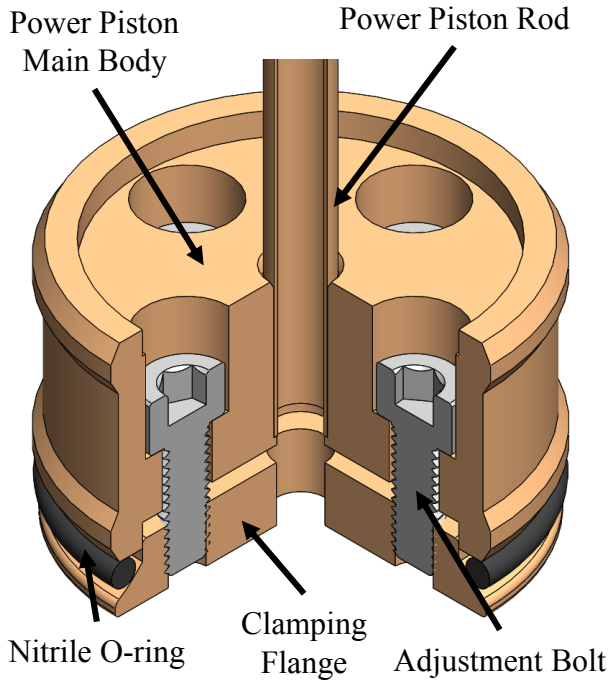


Figure 4.2 Section view of a solid model of the Mark 1's power piston.


Figure 4.3 Image of the Mark 1's power piston system.

The Delrin cylinder that was used for the power piston system was purchased, and no additional manufacturing was performed to adjust its bore, or finish of the bore. This was done because of the inherent low friction [90] of the Delrin, along with the smooth surface finish, and dimensional accuracy of the cylinder. The Delrin cylinder was secured to the top heat exchanger water jacket with a cylinder support mount. Figure 4.3 shows the main components of the manufactured power piston system and how the cylinder is secured to the top heat exchanger water jacket.

#### 4.3.1.2 Displacer Piston System

Like the power piston system, the displacer piston system used for the Mark 1 also consisted of a custom-made piston-cylinder set. The engine body housed a removable displacer cylinder that the displacer piston ran through. The displacer piston system has a bore diameter of 17.8 cm, a stroke of 4.45 cm, and a swept volume of 1110 $cm^3$.

The displacer piston consisted of a 3D printed support frame that secured the displacer rod and was used to hold the two EPS discs. To reduce the dead volume, and to reduce heat loss from the cylinder sleeve wall and the working fluid, the displacer piston had a thickness equal to its stroke of 4.45 cm. The displacer piston did not use a formal seal and simply relied on a close fit between the EPS discs of the displacer piston and the displacer cylinder sleeve. Figure 4.4 shows the arrangement components in the half-section view of the assembly.

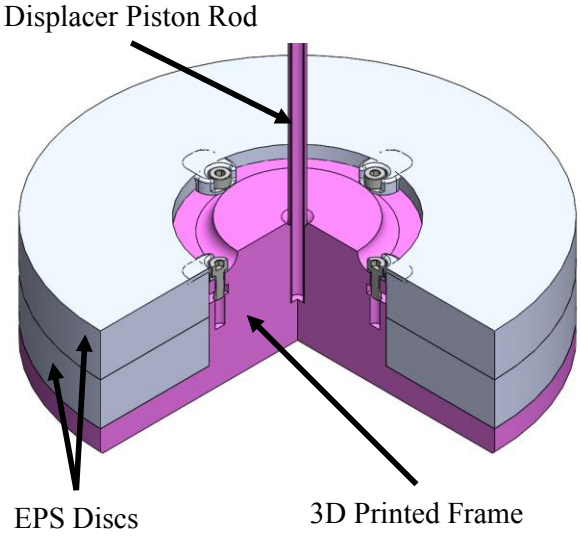


Figure 4.4 Section view of the solid model of the displacer piston used by the Mark 1.

The engine body acted as the main support structure for the Mark 2. The work space was created by connecting both heat exchangers, which acted as end caps, to the engine body. The engine body contained two DAQ ports that could be used for temperature and pressure measurement, and a pressurization port that was used to test the sealing capabilities of the engine.

The displacer cylinder frame was 3D printed and was housed inside the engine body. The bottom of the displacer cylinder rested on internal tabs inside the engine body so that the working fluid could travel through the annulus created by the displacer cylinder and the engine body. This is depicted in Figure 4.5. The displacer cylinder could not move in the engine body because of the tight concentric fit between the displacer cylinder and the engine body, and because it was clamped between the internal tabs and the top flat plate heat exchanger shown in Figure 4.5. If the top heat exchanger was removed, the displacer cylinder could be removed from the engine body.

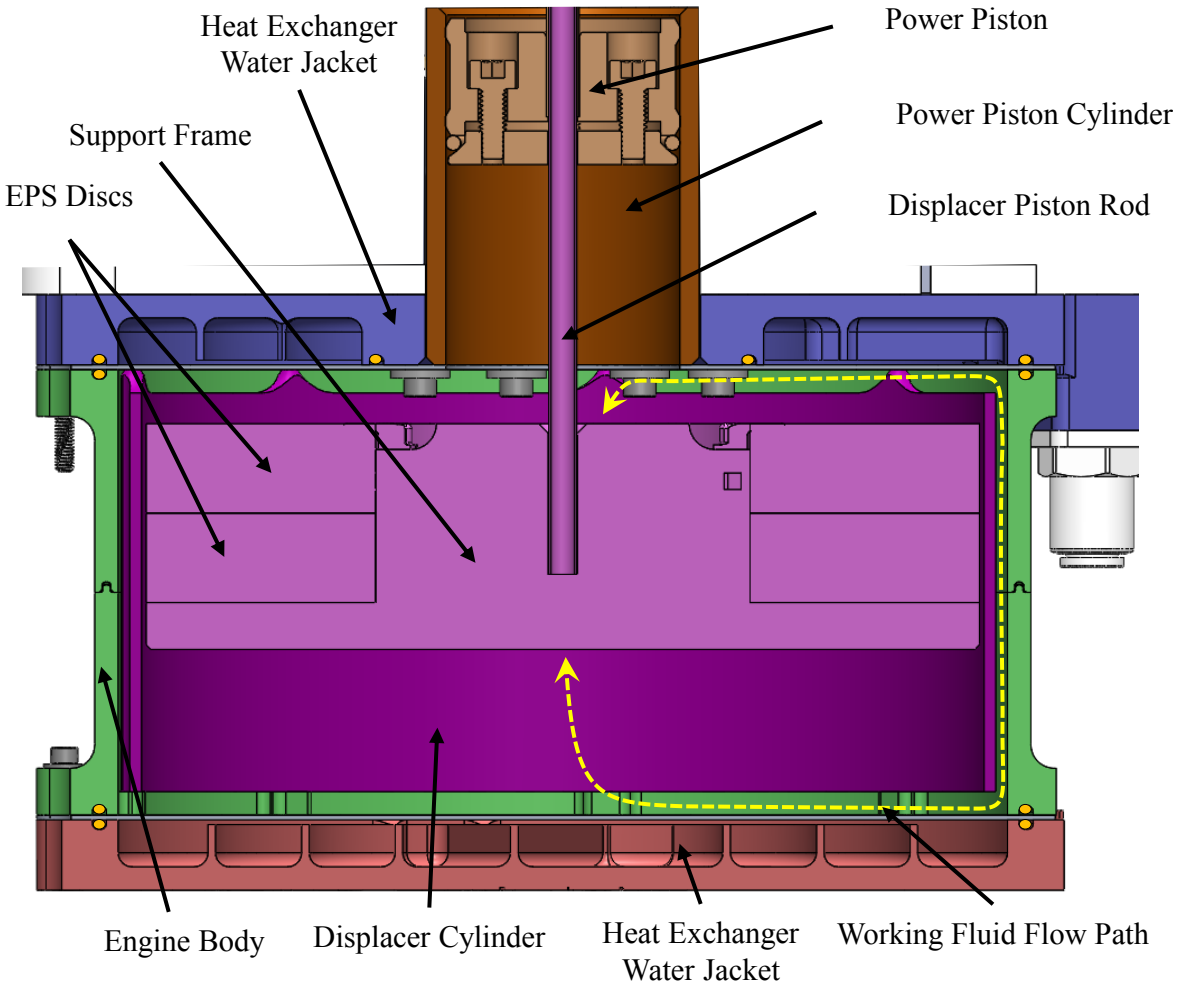


Figure 4.5 Section view of the Mark 1's solid model that shows its internal systems.

Figure 4.6 shows how the displacer piston rod travels through the hollow power piston rod. This interface between the two rods required a sealing mechanism, since a close fit did not provide a good enough seal. The sealing mechanism used was a rubber diaphragm that was secured to both piston rods as shown in Figure 4.7.

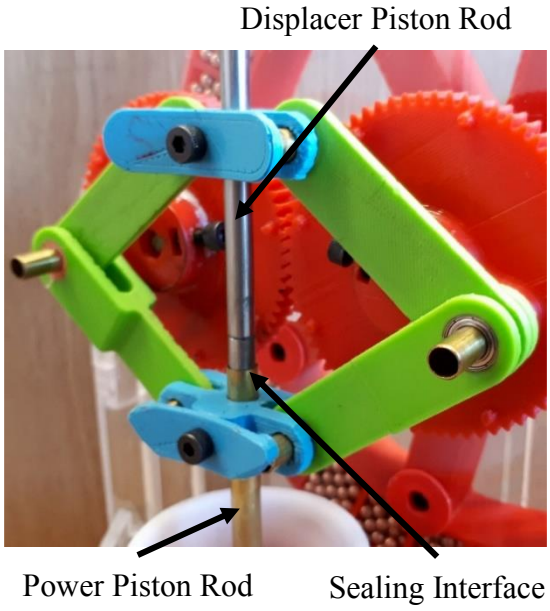


Figure 4.6 Image of the connection between the power piston rod and displacer piston rod on the Mark 1.

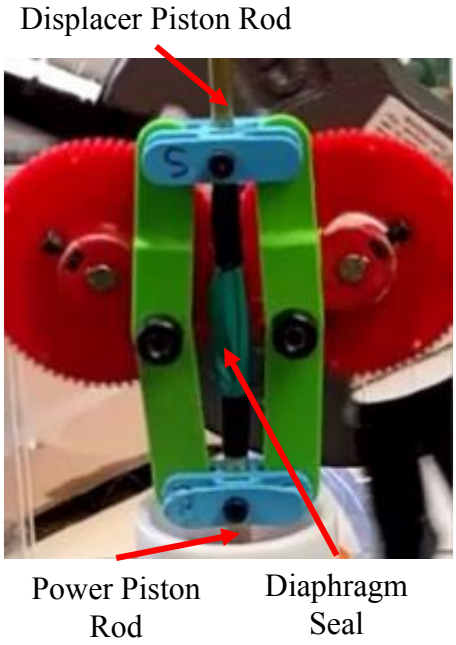


Figure 4.7 Image of the rubber diaphragm seal used for the displacer piston rod power piston rod interface.

#### 4.3.1.3 Heat Exchangers

The heat exchanger system used by the Mark 1 consisted of flat plate heat exchangers. Flat plate heat exchangers were chosen because of the small pressure loss and dead volume associated with them. The flat plates were made from aluminum. The thickness of the plate (1 mm) was chosen to reduce conduction losses through the plate, and to provide enough structural support to resist the pressure across it.

The construction of each heat exchanger consisted of the flat plate and the water jacket. Each plate was clamped between the engine body and the heat exchanger water jacket as seen in Figure 4.10 with one O-ring sealing the water in, and another sealing the working fluid. Due to the area requirements of the power piston-cylinder, the heat exchangers did not have the same surface area. The bottom heat exchanger has a surface area of 280 $cm^2$ while the top heat exchanger has a surface

area of 260 $cm^2$. The water used to directly heat and cool the flat plates flowed through the water jackets. Figure 4.8, and Figure 4.9, show flow the diverters that were used to direct the water through the water jackets.

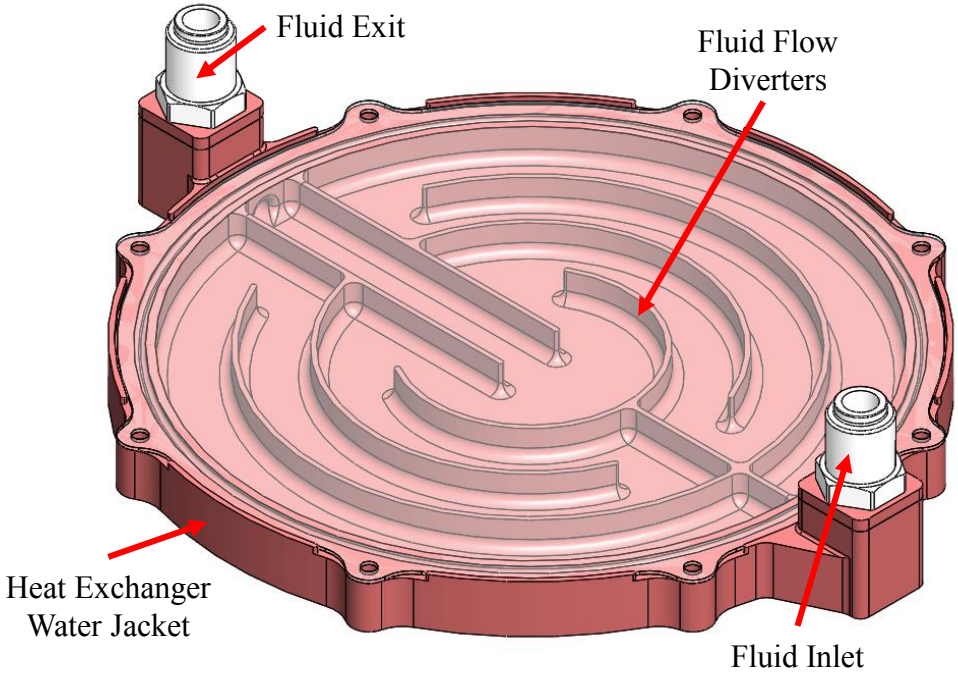


Figure 4.8 A solid model of bottom heat exchanger with the metal flat plate semitransparent to showcase the flow diverters underneath.

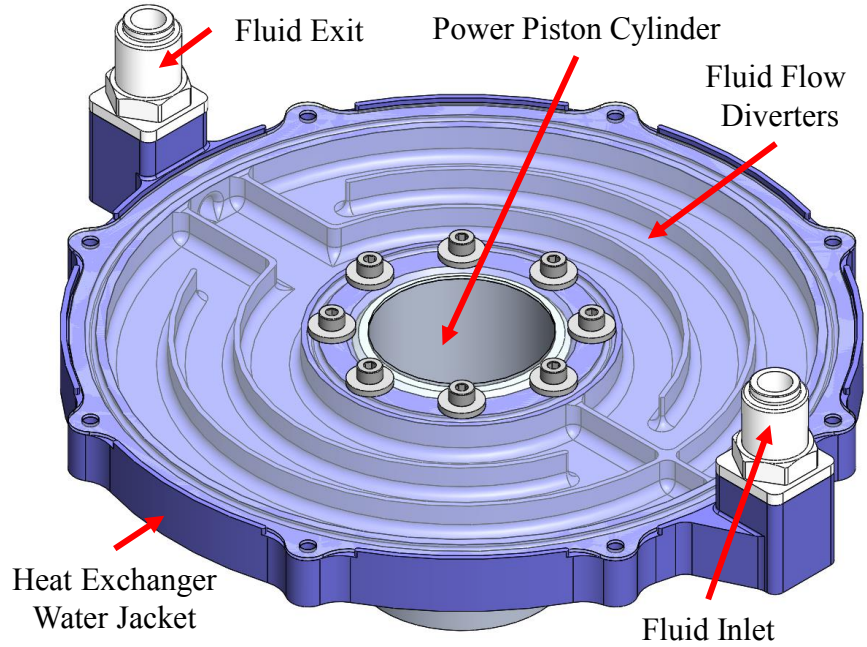


Figure 4.9 A solid model of the Mark 1's top heat exchanger with the power piston-cylinder with the metal flat plate semitransparent to showcase the flow diverters underneath.

#### 4.3.1.4 Regenerator

The regenerator volume of the Mark 1 was the annulus created by the engine body and displacer cylinder. The regenerator was designed to test different regenerator materials. Figure 4.10 shows how the regenerator volume was created by the engine body and displacer cylinder.

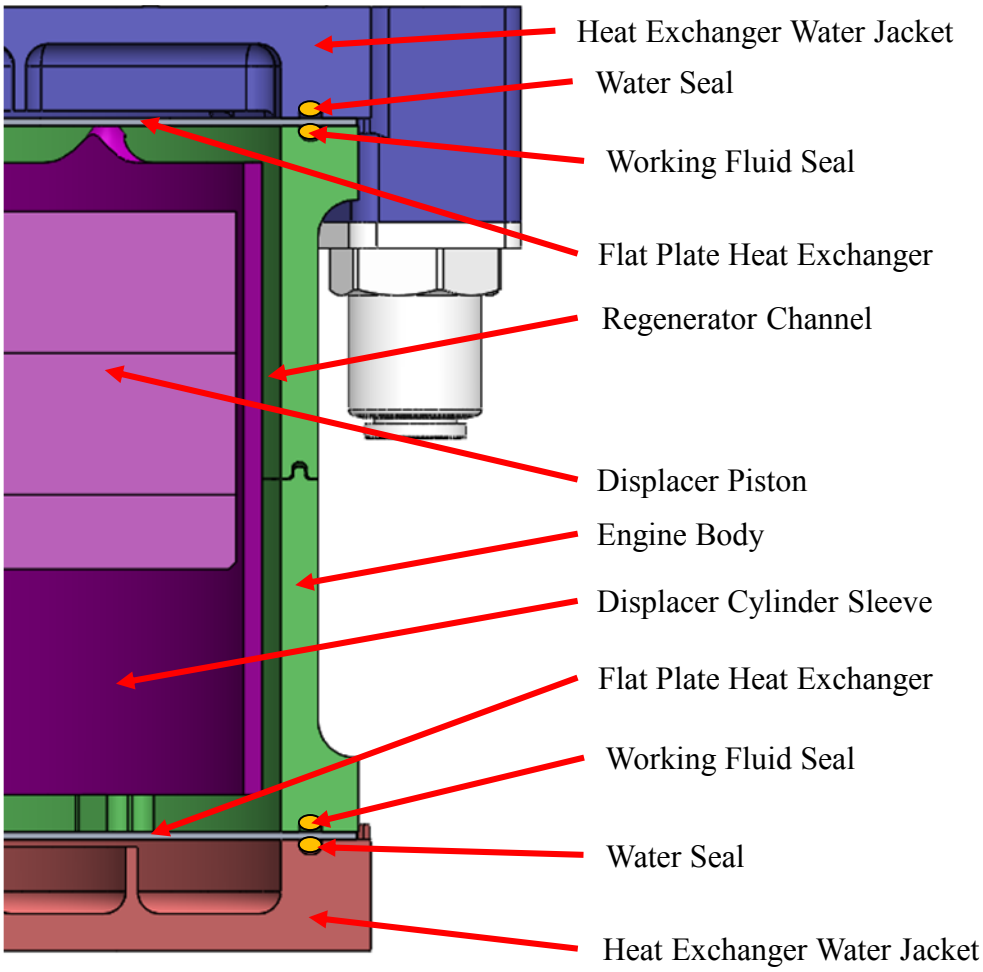


Figure 4.10 A section view of a solid model of the Mark 1 showcasing the regenerator channel, and the displacer piston and heat exchanger components.

#### 4.3.1.5 Drive Mechanism and Frame.

A rhombic drive mechanism was used for the Mark 1. It was chosen because it could be dynamically balanced and showed potential in the literature [18]. The rhombic drive mechanism linked the motion of the power and displacer piston together through a series of linkages and gears as seen in Figure 4.11. The dimensions of the mechanism were determined using equations from the literature [91]. The nature of the rhombic drive fixed the value of the power piston's stroke and phase angle, so only one compression ratio and phase angle could be tested.

In Figure 4.12, the original flywheel, a 5 lb. weight with addition sockets, is shown. The sockets were added to increase the moment of inertia of the flywheel and off-weight it. The flywheel shown in Figure 4.1 and Figure 4.11 was later developed but was never tested because development of the Mark 2 had begun.

The mechanism frame was made from acrylic. Due to the constraints of the rhombic drive, the frame only had to support the two shafts from the rhombic drive mechanism and flywheel. The mechanism frame was designed so that the power and displacer piston were concentric in their respective cylinders.

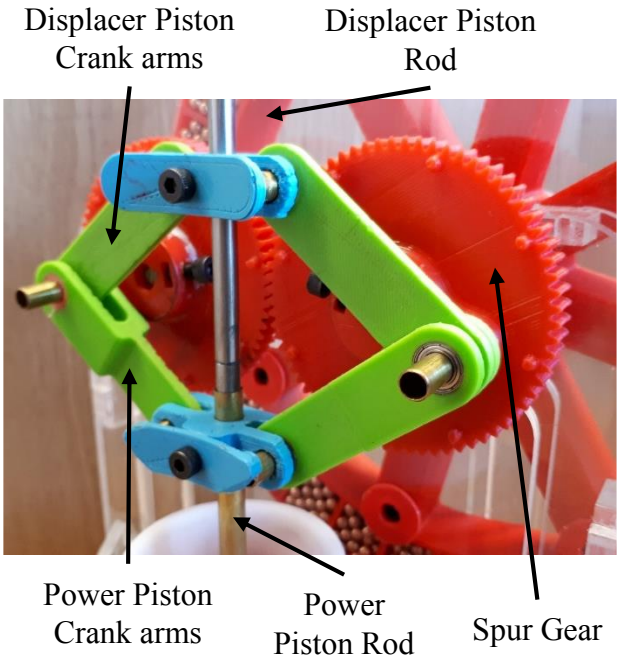


Figure 4.11 Image of the rhombic drive mechanism used to provide motion for the power piston and displacer piston of the Mark 1.

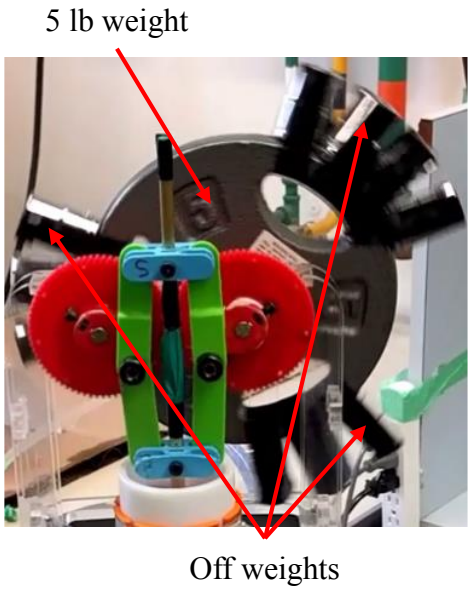


Figure 4.12 Image of the off weighted flywheel.

#### 4.3.1.6 Component Summary

A summary of the dimensions and systems used for the Mark 1 is shown in Table 4.5.

Table 4.5 Component summary of the Mark 1.

| Engine Name | Mark 1 |
|---|---|
| Engine Type | Gamma |
| Drive Mechanism | Rhombic drive, |
| Displacer Piston System | Piston-cylinder Set |
| Displacer Piston Dimensions | Bore = 0.178 m<br>Stroke = 0.0445 m<br>Swept Volume= 0.00111 $m^3$ |
| Power Piston System | Piston-cylinder Set |
| Power Piston Dimensions | Bore = 0.05 m<br>Stroke = 0.0439 m<br>Swept Volume= 0.000086 $m^3$ |
| Compression Ratio (Maximum) | 1.06 |
| Heat Exchanger Type | Flat Plate |
| Heat Exchanger Material | Aluminum |
| Heat Exchanger Volume | $\approx 0$ $m^3$ |
| Heat Exchanger Surface Area | Top = 0.026 $m^2$<br>Bottom = 0.028 $m^2$ |
| Regenerator Volume | 0.00014 $m^3$ |
| Regenerator Notes | None used |
| Flywheel Moment of Inertia | None calculated |

### 4.3.2 Lessons Learned

Many lessons were learned from the Mark 1. These lessons were learned from the manufacturing process, developing strategies to start the engine, and from trying to optimize the performance as discussed below.

#### 4.3.2.1 Manufacturing

- When using a rhombic mechanism, it is crucial that the dimensions of it are chosen correctly. This is so that the crank arms of the power and displacer piston are never parallel to one another. This is important because if they are parallel to one another, the system has some clearance in it and the piston will be able to move out of alignment in their respected cylinder. This increases friction and may cause the engine to stop running.
- Internal threads can be printed by Ultimaker 2+. However, they were quickly worn down from the repeated insertion and removal of metal bolts. Captive metal nuts glued into the component make provide a more robust solution.

#### 4.3.2.2 Operation

- The displacer piston should be as light as possible to prevent dynamic balancing issues, and to reduce the work required to lift it.
- The displacer piston should be able to fall under its own weight when fully connected to the mechanism (seals, bearings, etc.). This provides a simple test to determine if the system is aligned. It also determines if the frictional loads are small. This is because if the mass of the displacer piston is small, it will only be able to fall if the frictional loads are also small.
- The engine should feel ‘bouncy’ when it is fully sealed. When moved from maximum volume to minimum volume it should stay pressurized for at least five seconds. This is carried out to test how much the engine leaks, as it was found that the engine could only run with a very small leak. Ross [92] introduced this term “bouncy” and corresponding five second test.
- The engine could only run when the flywheel was off-weighted, this was suspected to be caused by the work required to lift the displacer piston and power piston.
- The frictional losses in all components should be reduced to the minimum value possible.

#### 4.3.2.3 Optimization

- The engine was tested with various different regenerators but could only run with no regenerator material in the regenerator volume. This was most likely a result of the increased pressure drop caused by, for example, the inclusion of a steel wool regenerator material.
- The engine could not operate when the displacer cylinder was removed, with the engine body acting as the displacer cylinder. This could have been caused by the increase in dead volume, or the reduction in speed of the fluid exiting the regenerator. This speed reduction could have affected the convective heat transfer coefficient of the working fluid when it interacted with the flat plate heat exchangers.

## 4.4 Engine Description: Mark 2

### 4.4.1 Engine Development and Description

The Mark 2 is a kinematic gamma-type LTDSE, and its design was focused on modularity. To test different configurations, the heat exchangers, regenerator, and the power piston system could be removed and changed. The drive mechanism was designed to allow the phase angle and the compression ratio to be changed. All 3D printed parts of the Mark 2 were made from either the Ultimaker 2+ or Form 2. The final configuration of the Mark 2 is displayed in Figure 4.13. This figure showcases the main systems that will be described further in the following sections. A drawing package for the Mark 2 is included in the Appendix E.

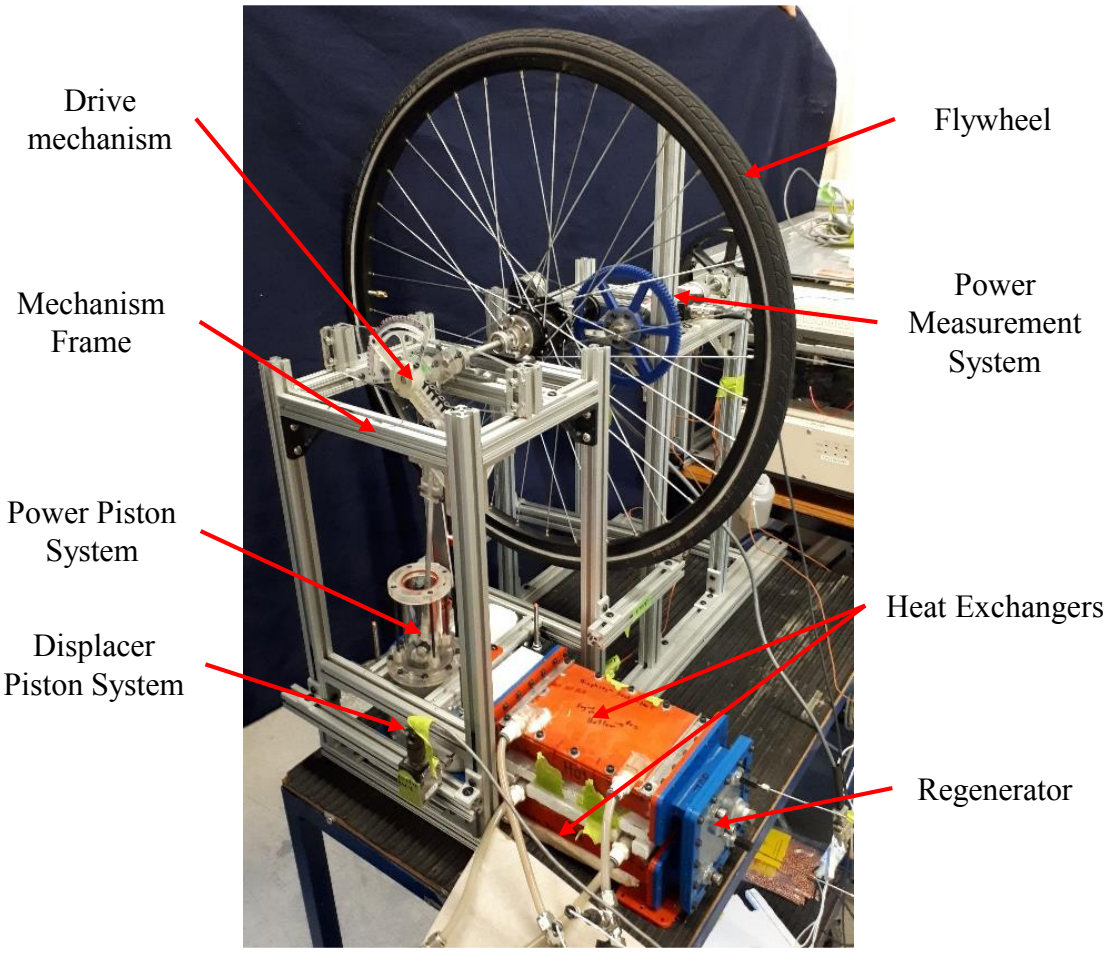


Figure 4.13 Image of final configuration of the Mark 2.

#### 4.4.1.1 Power Piston System

The Mark 2 went through several power piston sealing iterations: a rolling diaphragm, O-ring, and finally a precision glass cylinder with graphite piston. This section will only focus on the precision glass cylinder with graphite piston. The reason being that it was only power piston system that allowed the engine to operate.

The Mark 2 used a commercially available piston-cylinder set for its power piston system. The piston-cylinder set consist of a graphite piston and a glass cylinder made by Airpot Corp [93]. A set was chosen that had a 12.7 cm stroke, a piston diameter of 4.445 cm (the maximum piston diameter available), and a maximum swept volume of 197 $cm^3$. The set was chosen because it produced a large range of testable compression ratios (1 to 1.10), while not requiring a drive mechanism with extremely long crank arms and connecting rods. It was also chosen due to its ability to produce a very good seal while having a very low friction load associated with it. Figure 4.14 shows how the power piston system was attached to the top end cap of the displacer piston system using a 3D printed housing. The graphite piston was connected onto the connecting rod with a 3D printed frame and ball end joint presented in Figure 4.15.

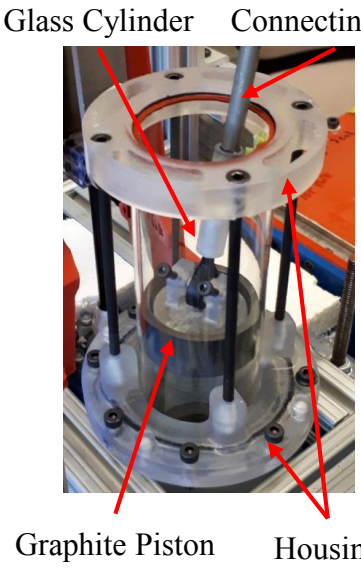


Figure 4.14 Image of the power piston assembly used by the Mark 2.

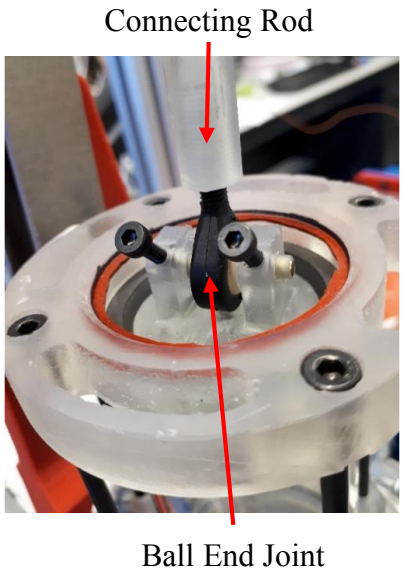


Figure 4.15 Image of the power piston ball end joint connection.

#### 4.4.1.2 Displacer Piston System

The displacer piston system used for the Mark 2 was a custom-made piston-cylinder set. The displacer piston system consisted of a purchased polycarbonate cylinder, a custom-made 3D printed displacer piston, and two 3D printed ends caps that secured the cylinder. The displacer system had a bore diameter of 19.47cm, a stroke of 5.35cm, and a swept volume of 1590 $cm^3$.

As a result of the success of the Mark 1's displacer piston, the Mark 2 used a similar design. The main change made was the addition of a formal piston seal. A low friction polymer lip seal made from a thin plastic sheet was clamped between two EPS discs. An internal 3D printed core was used to secure the two EPS discs, and as a mount for the displacer piston rod displayed in Figure 4.16. The displacer piston had a thickness of 4.8cm.

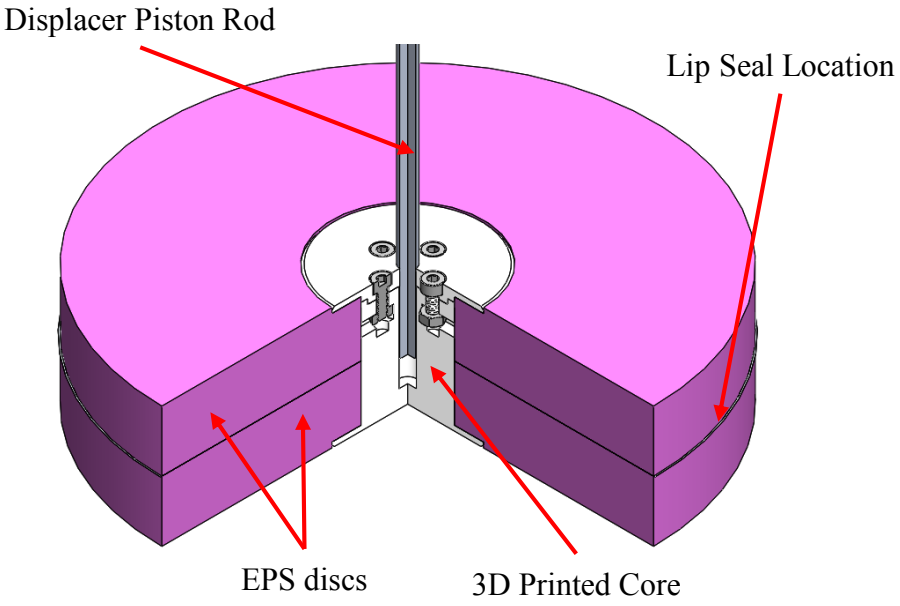


Figure 4.16 A section view of a solid model of the displacer piston.

A stock polycarbonate tube was chosen for the displacer cylinder. It was clamped between two 3D printed end caps. The polycarbonate tube was transparent and allowed the inside of the engine to be viewed as seen in Figure 4.17.

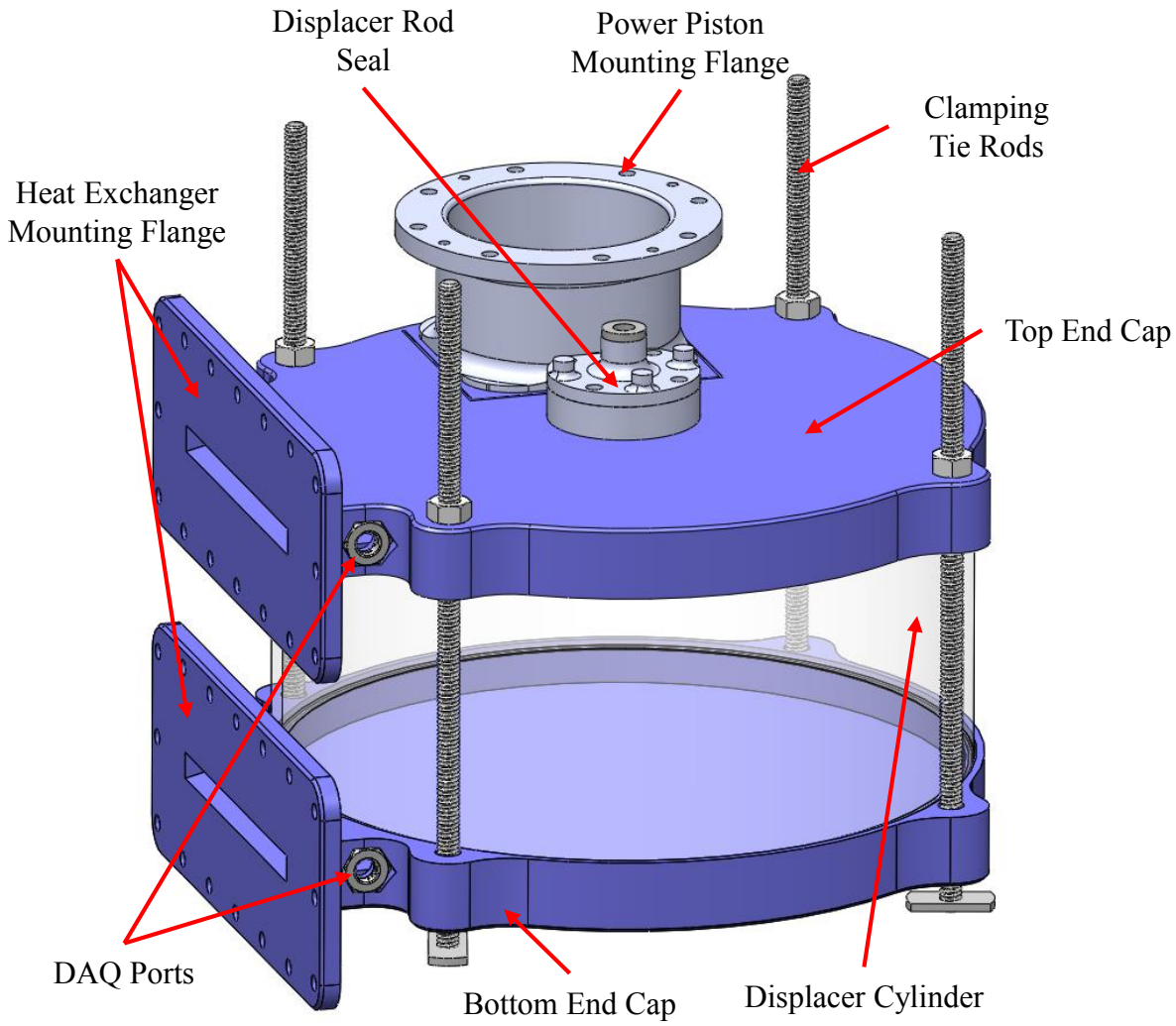


Figure 4.17 A solid model of how the displacer cylinder and end caps are assembled together.

The end caps were designed so that they could clamp the displacer cylinder using tie rods. Both end caps used an O-ring where the end cap and the displacer cylinder meet, which was compressed when the tie rods were tightened. The bottom end cap has a modular end flange for a heat exchanger to be mounted to, along with two DAQ ports for thermocouples or pressure transducers. The top end cap uses the same end flange and DAQ ports seen on the bottom flange, and also has a flange to hold the power piston system and a flange for the displacer rod seal. Figure 4.17 depicts how the caps and displacer cylinder are connected.

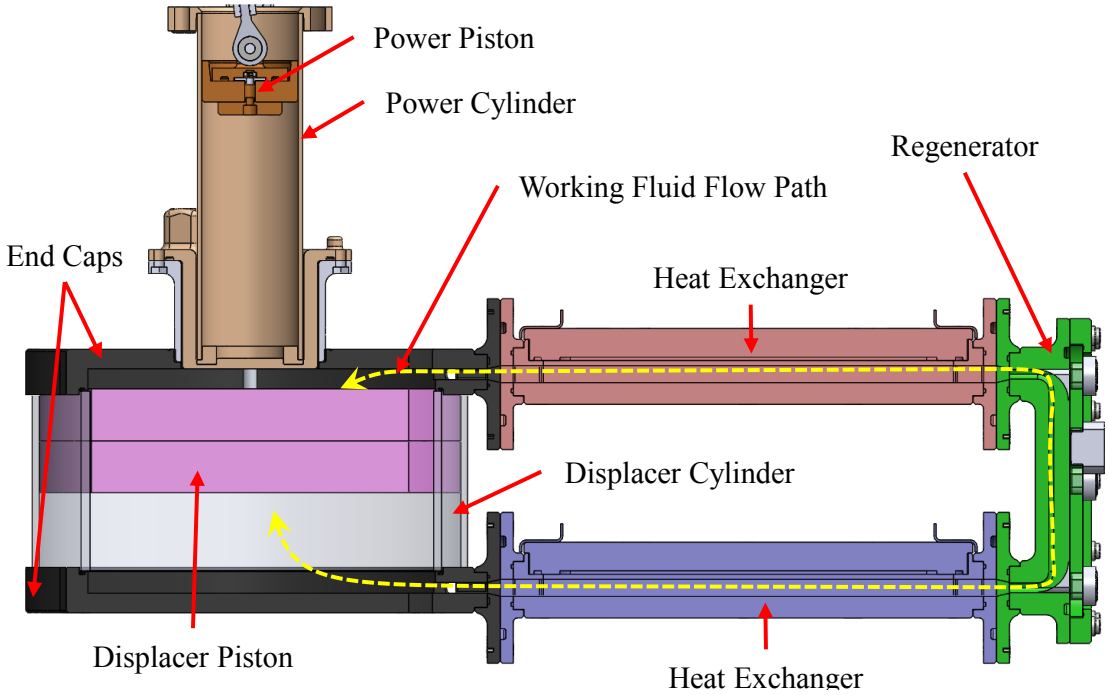


Figure 4.18 Section view of the Mark 2's solid model that shows its internal systems.

The displacer piston rod seal flange was designed to test multiple seals. It accomplished this using a mounting flange that allowed for different rod seals to be mounted easily, and coaxially with a PTFE busing shown in Figure 4.19.The displacer piston rod was supported with the rod support tower as seen in Figure 4.20.

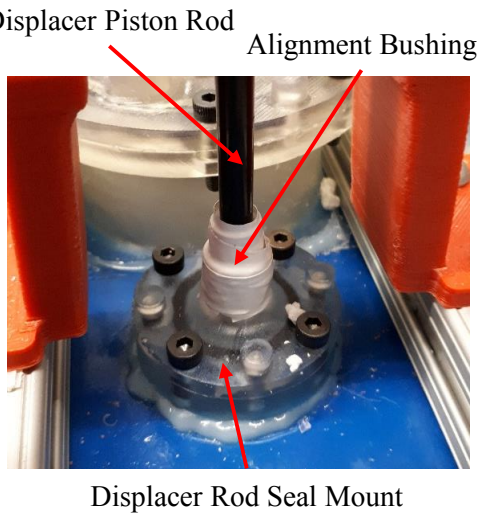


Figure 4.19 Image of the displacer piston rod seal system.

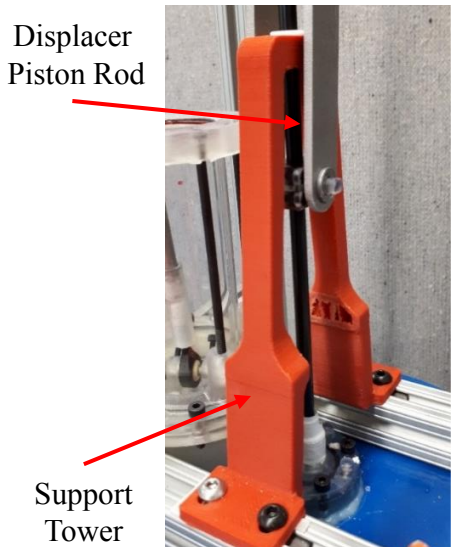


Figure 4.20 Image of the displacer piston rod support tower.

#### 4.4.1.3 Heat Exchangers

The Mark 2 used two types of heat exchangers throughout its development: a flat plate duct, and an extruded aluminum heat sink. This section will only focus on the extruded aluminum heat sink, as the flat plate duct resulted in very poor performance where shaft power could not be measured.

The final heat exchanger system used on the Mark 1 was an extruded aluminum heat sink. It was chosen due to the material properties, low cost, simple geometry, size, and surface area. The surface area of the heat sink in contact with the working fluid is 1300 $cm^2$. Figure 4.21 shows extruded aluminum heat sink used.

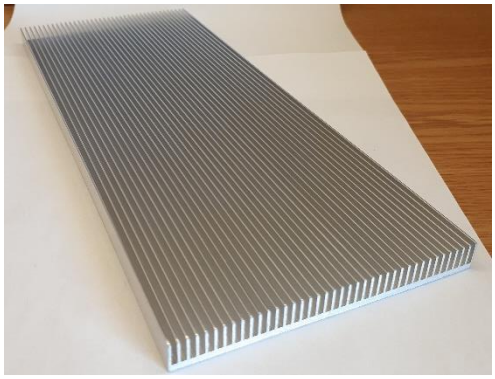

Figure 4.21 Image of the extruded aluminum heat sink used for the heat exchanger on the Mark 2.

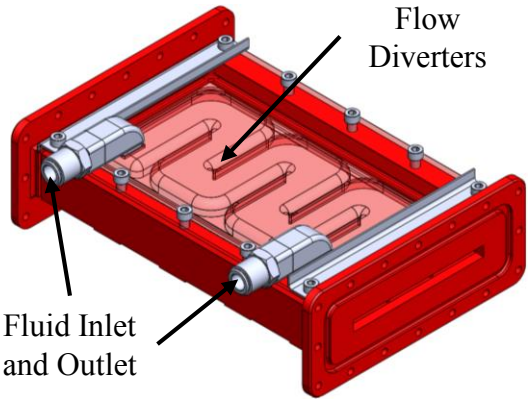


Figure 4.22 Solid model of Mark 2's heat exchanger showing the fluid flow path created by the flow diverters.

The heat exchanger assembly consisted of three main parts, the main body with two mounting flanges, the heat sink, and the water jacket. Figure 4.23 shows an exploded assembly view of these three parts. The enclosure allowed the working fluid to travel through the finned section of the heat sink and made each finned section into a duct depicted in Figure 4.24. Similar to the Mark 1, the heat sink used a water jacket with flow diverters to contain and direct the water used for heating and cooling through the heat exchanger. Figure 4.22 shows the flow diverters and the path they created between the fluid inlet and outlet. A separate seal was used for the working fluid and the heating and cooling fluid. These separate seals, along with the cavity that contained the heating and cooling fluid, are shown in Figure 4.24.

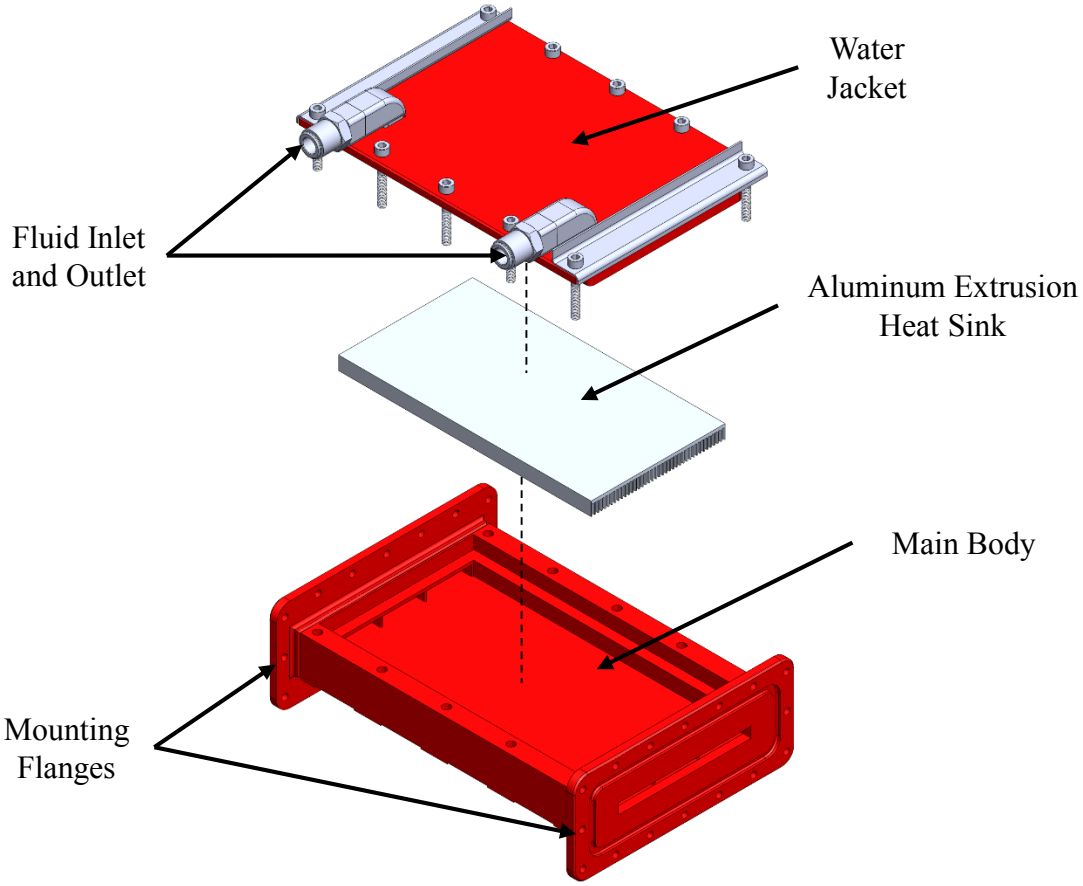


Figure 4.23 Exploded view of the solid model of the Mark 2's heat exchanger assembly.

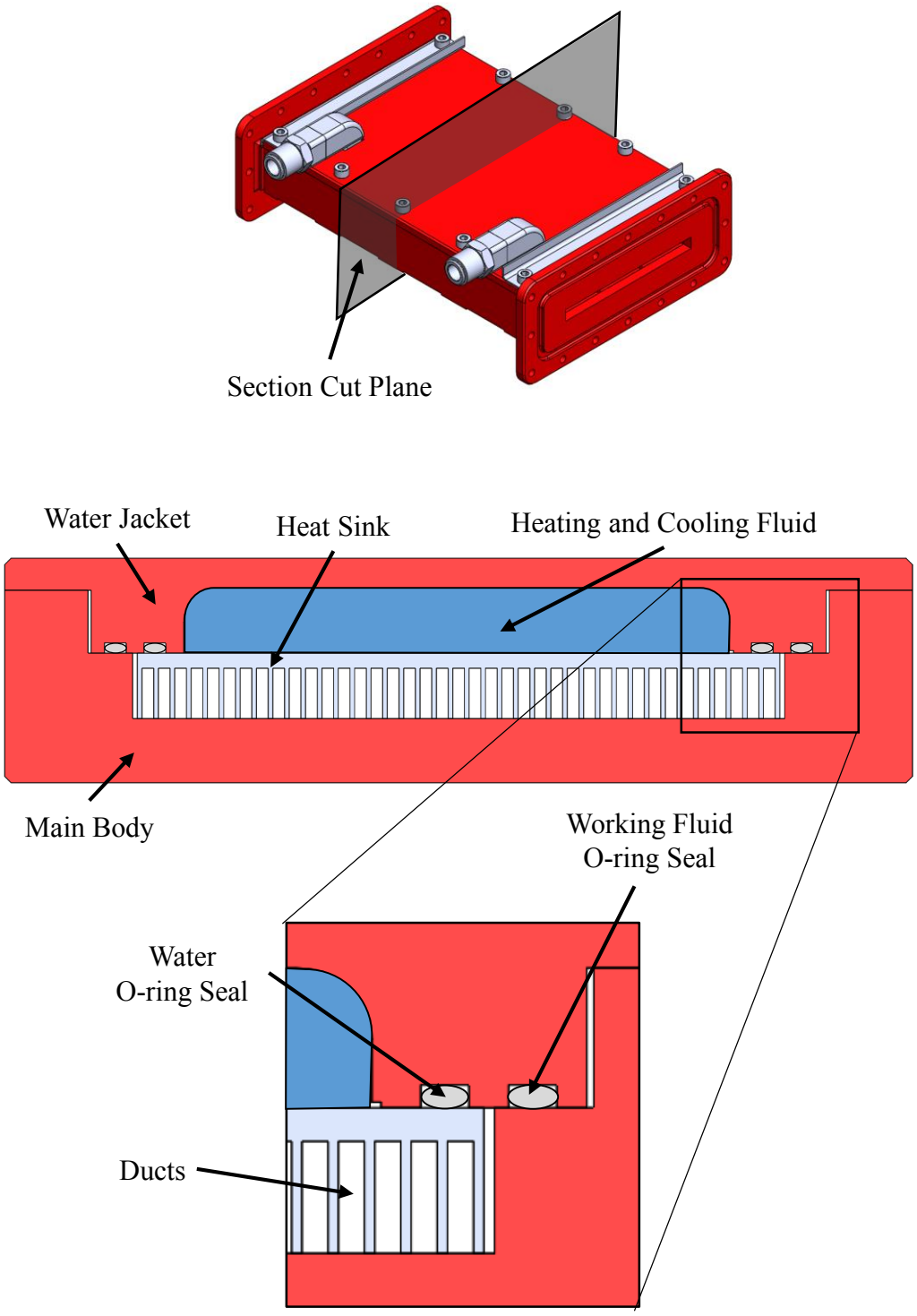


Figure 4.24 Section and detailed view of the solid model of the Mark 2's heat exchanger.

#### 4.4.1.4 Regenerator

The regenerator for the Mark 2 was designed to be modular so that several different regenerator types could be tested. The chosen regenerator materials included: a section of the same heat sink used in the heat exchangers, various densities of steel wool, and no regenerator at all as shown in Figure 4.25. To change the regenerator material a removable flange is used to provide access to the regenerator volume. The regenerator had two mounting flanges that were used to connect both of the heat exchangers together. To reduce the pressure drop through the regenerator, curved flow diverters were incorporated to direct the working fluid through the regenerator. The regenerator contained five DAQ ports to measure temperature or pressure, and a pressurization port used to check for leaks.

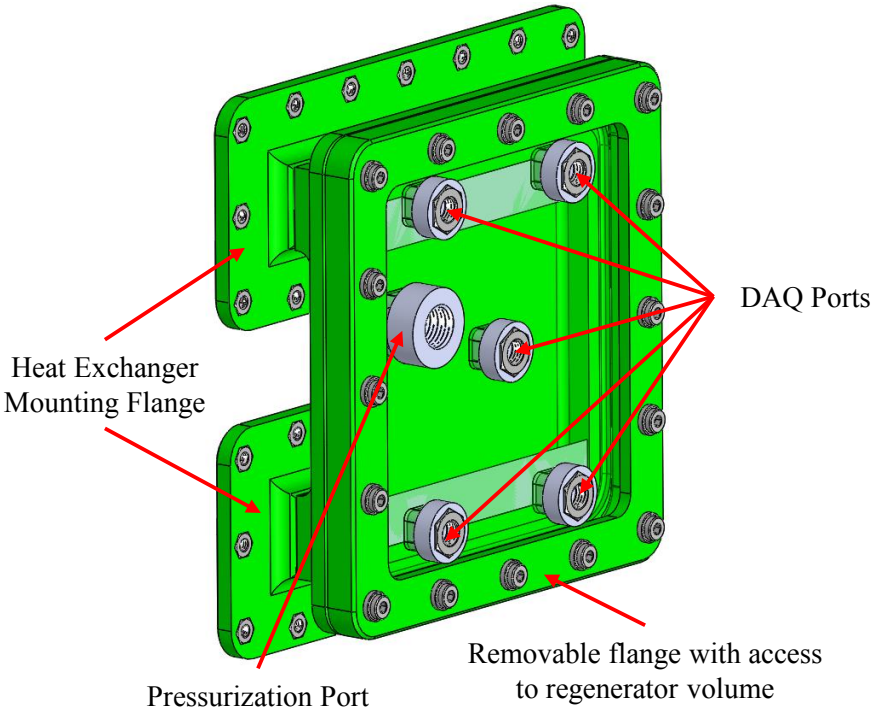


Figure 4.25 Solid model of the regenerator assembly.

#### 4.4.1.5 Drive Mechanism, and Flywheel

The drive mechanism used for both the displacer and power piston was a slider crank mechanism. The power piston had a slider crank system that could change the: crank arm length, connecting rod length, and phase angle relative to the displacer piston. Figure 4.26 displays the protractor crank arm component used to change the phase angle. The crank arm and connecting rod of the power piston are shown in Figure 4.27. The displacer piston system had a nonadjustable slider crank, which used a crosshead to connect the displacer piston connecting rod to the displacer piston rod as seen in Figure 4.28

Phase Angle Protractor

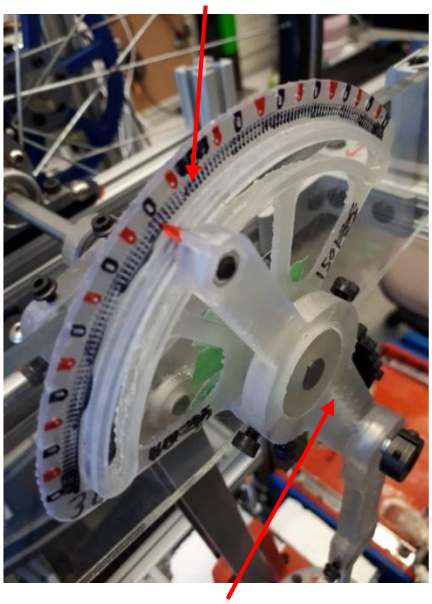

Power Piston Crank Arm

Figure 4.26 Image of the power piston crank arm's protractor that allowed phase angle to be changed.

Power Piston Crank Arm

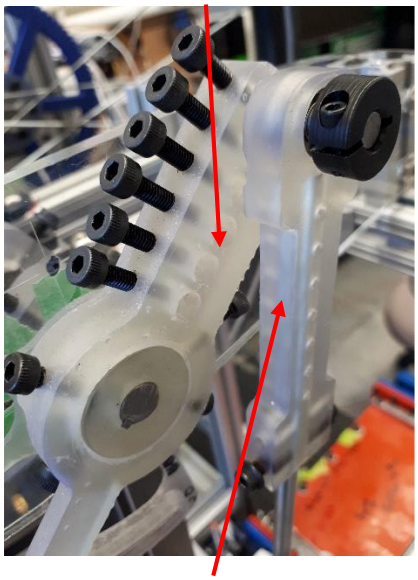

Power Piston Connecting Rod

Figure 4.27 Image of the power piston crank arm that allowed compression ratio to be changed.

In Figure 4.29, the original design of the flywheel for the Mark 2, a piece of water jet cut steel, is shown. This flywheel was designed so that the moment of inertia could be increased, and off weighting be applied by adding weighted section to it. It had a moment of inertia of 0.012 $kg/m^2$

A flywheel with significantly larger moment of inertia, estimated to be 0.142 $kg/m^2$ using SolidWorks, was used for the final configuration of the Mark 2. This flywheel was made from a

bicycle tire. It was chosen to drastically reduce the speed fluctuations of the Mark 2. The bicycle rim is shown at the beginning of this section in Figure 4.13.


Figure 4.28 Image of the displacer piston crosshead.

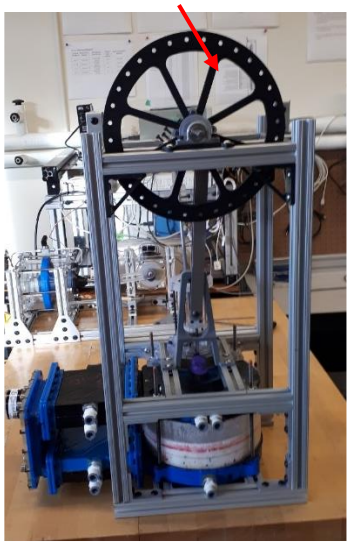


Figure 4.29 Image of the original flywheel used on the Mark 2.

#### 4.4.1.6 Frame

The main support frame of the Mark 2 was made of structural aluminum extrusion. It was used to secure the main components described above together. The framing allowed for quick assembly of the engine. Since the aluminum extrusion is a rail-based system, it allowed for alignment of shafts and bearing to be completed easily. The choice of using this framing was critical for later changes made to the engine (flywheel changing, and DAQ system addition).

#### 4.4.1.7 Instrumentation Locations

To measure the shaft power of the engine, the torque and engine speed were measured when a load was applied. A load was applied to the engine by hanging a mass on a belt hung on a load application pulley. When the engine was running, and therefore the load application pulley rotating, the hung mass would produce a frictional load between the belt and the pulley. A differential torque was measured with the torque sensor. Due to the small torques required to stall the engine, a gear reduction was applied to the power measurement system. This allowed larger

torques to be applied to the torque transducer, which reduced the uncertainty of the shaft power measurement. The final gear reduction was 5.55 using a 100-tooth gear and an 18-tooth gear. To determine the speed of the engine, a rotary encoder was used. The components that make up the power measurement system are showcased in Figure 4.30.

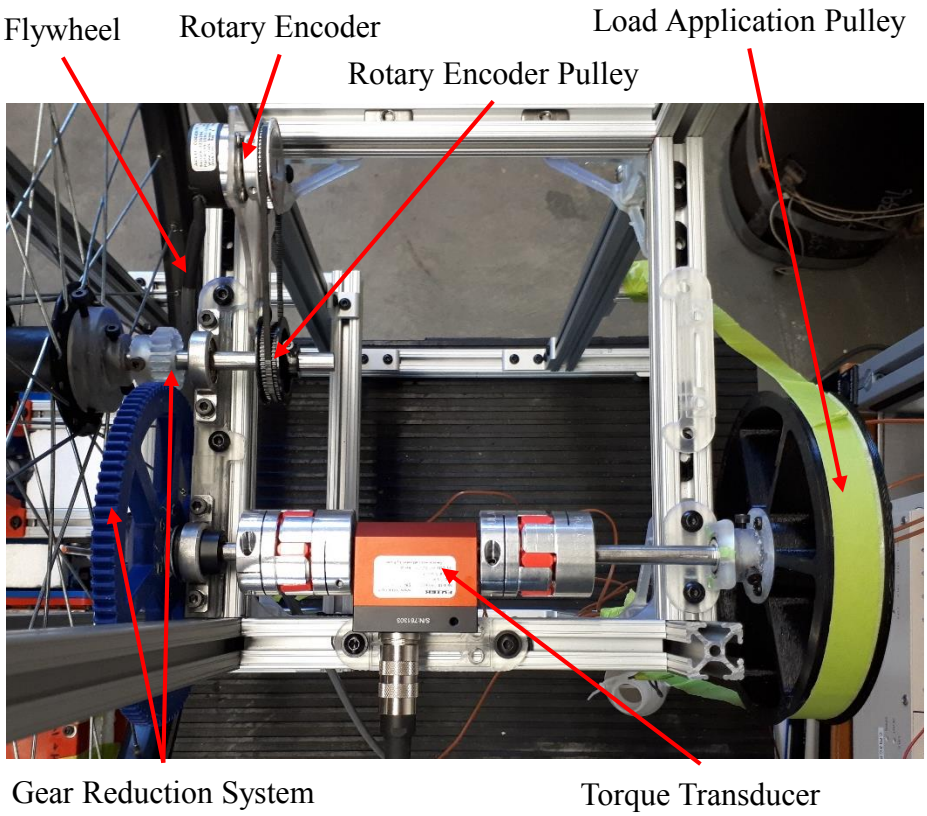


Figure 4.30 Image of the Mark 2's power measurement system.

The temperature of the working fluid was measured in four locations. Two of these locations were in the displacer cylinder to measure the temperature of the expansion and compression space. The temperature was also measured in the regenerator at the entrance/exit of each heat exchangers. Figure 4.32 show the four locations where the temperatures was measured. It also shows where the pressure measurements were taken. The water temperature at the inlet and outlet of each heat exchanger was measured. The RTDs were connected to the flow loop using tee fitting shown in Figure 4.32.

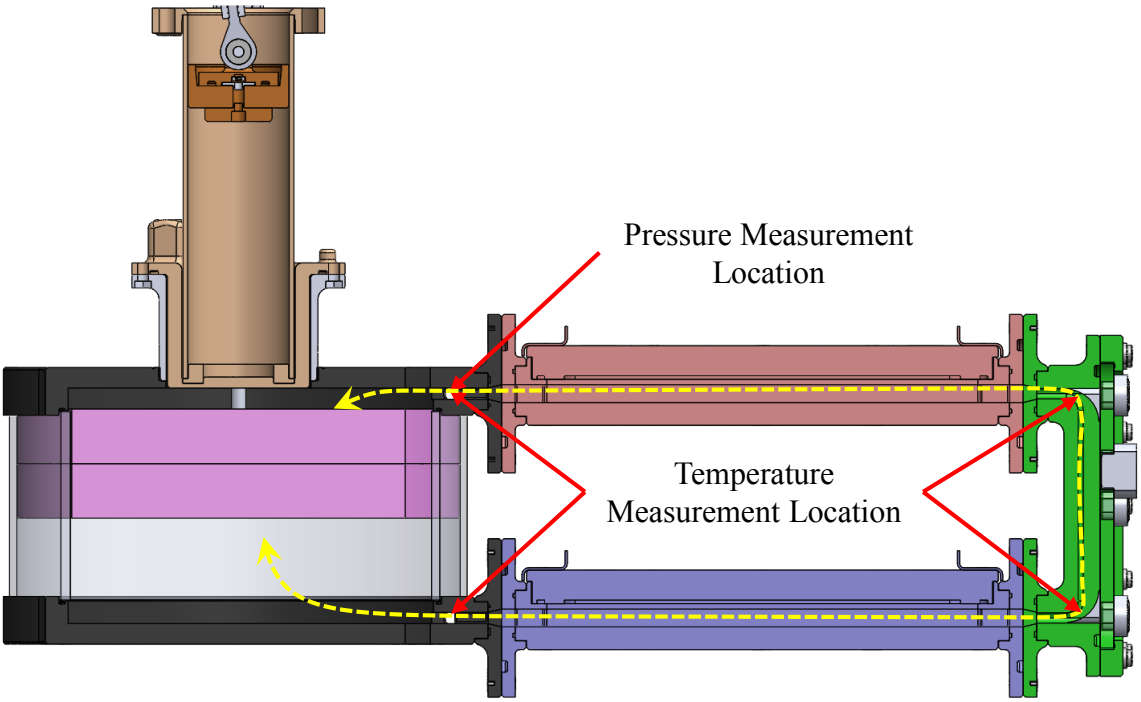


Figure 4.31 Section view of a solid model of the Mark 2 that showcases the four locations where the temperature of the working fluid was measured, and where the pressure of the work space was measured.

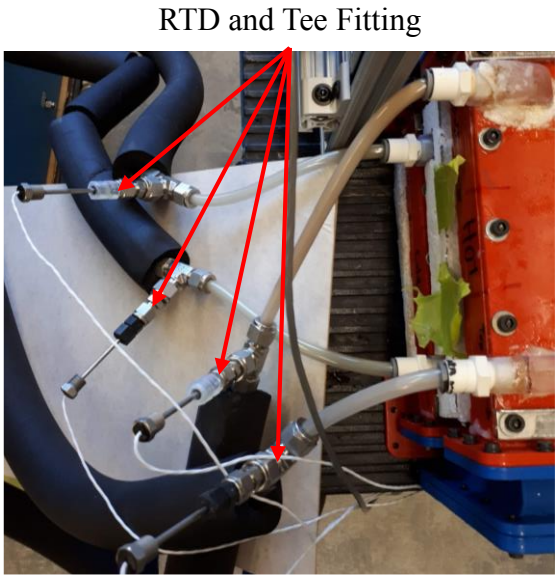


Figure 4.32 Image of the RTDs residing in their tee fittings.

#### 4.4.1.8 Component and Configuration Summary

Table 4.6 tabulates a summary of the dimensions and systems used by the final configuration of the Mark 2.

Table 4.6 Component summary of the Mark 2.

| Engine Name | Mark 2 |
|---|---|
| Engine Type | gamma |
| Drive Mechanism | Slider crank with crankshaft |
| Displacer Piston Dimensions | Bore = 0.1947 m<br>Stroke = 0.0535 m<br>Swept Volume= 0.00159 $m^3$ |
| Power Piston System Type | Piston-cylinder set |
| Power Piston Dimensions | Bore = 0.04445 m<br>Stroke = 0.127 m<br>Swept Volume= 0.000197 $m^3$ |
| Compression Ratio (Maximum) | 1.10 |
| Heat Exchanger Type | Extruded aluminum heat sink |
| Heat Exchanger Material | Aluminum |
| Heat Exchanger Volume | 0.000133 $m^3$ |
| Heat Exchanger Surface Area | 0.13 $m^2$ |
| Regenerator Volume | 0.000118 $m^3$ |
| Regenerator Material | Heat sink, steel wool, and none used |
| Flywheel Moment of Inertia | 0.142 kg*$m^2$ (Bicycle Wheel) |

The configurations of the Mark 2 tested are depicted in Table 4.7.

Table 4.7 Mark 2 configurations tested.

| Engine Configuration | Power Piston System | Heat Exchanger System | Flywheel | Able to run? |
|---|---|---|---|---|
| 1 | Rolling diaphragm | Flat Plate Duct | Waterjet Cut Metal | No |
| 2 | Piston O-ring | Flat Plate Duct | Waterjet Cut Metal | No |
| 3 | Graphite Piston Glass Cylinder | Flat Plate Duct | Waterjet Cut Metal | Yes, but not indefinitely |
| 4 | Graphite Piston Glass Cylinder | Aluminum Extrude Heat Sink | Waterjet Cut Metal | Yes |
| 5 | Graphite Piston Glass Cylinder | Aluminum Extrude Heat Sink | Bicycle Wheel | Yes |

### 4.4.2 Performance Evaluation of the Mark 2 Engine

The performance evaluation for the Mark 2 was based on: getting the engine to run and maximizing shaft power. After the engine was able to run, it was modified to increase the free running speed and reduce speed fluctuations. Finally, it was modified to optimize the shaft power by changing the compression ratio, phase angle, and regenerator used.

To determine maximum shaft power, the compression ratio and phase angle were varied. The compression ratio was varied to three different values: 1.097 (maximum compression ratio), 1.084 and 1.072 ± 0.007. For each compression ratio, six different phase angles were tested: 60°, 70°, 80°, 90°, 100°, and 110 ± 1°. The same load was applied to the Mark 2 for each combination of compression ratio and phase angle tested. The load used was chosen because it allowed for operation of the Mark 2 at all the desired test points.

Figure 4.33 shows the shaft power of the Mark 2 for each tested compression ratio and phase angle. For each combination of phase angle and compression ratio tested, a phase angle of 90 ± 1° always resulted in the maximum shaft power. The shaft power was seen to drop for both phase angles larger and smaller than 90 ± 1°. The maximum compression ratio of 1.097 ± 0.007 corresponded to the maximum shaft power for all phase angles tested. An upward trend in shaft power is seen for increasing compression ratio. A global maximum shaft power was not found for shaft power. This suggests that even larger compression ratios should be tested.

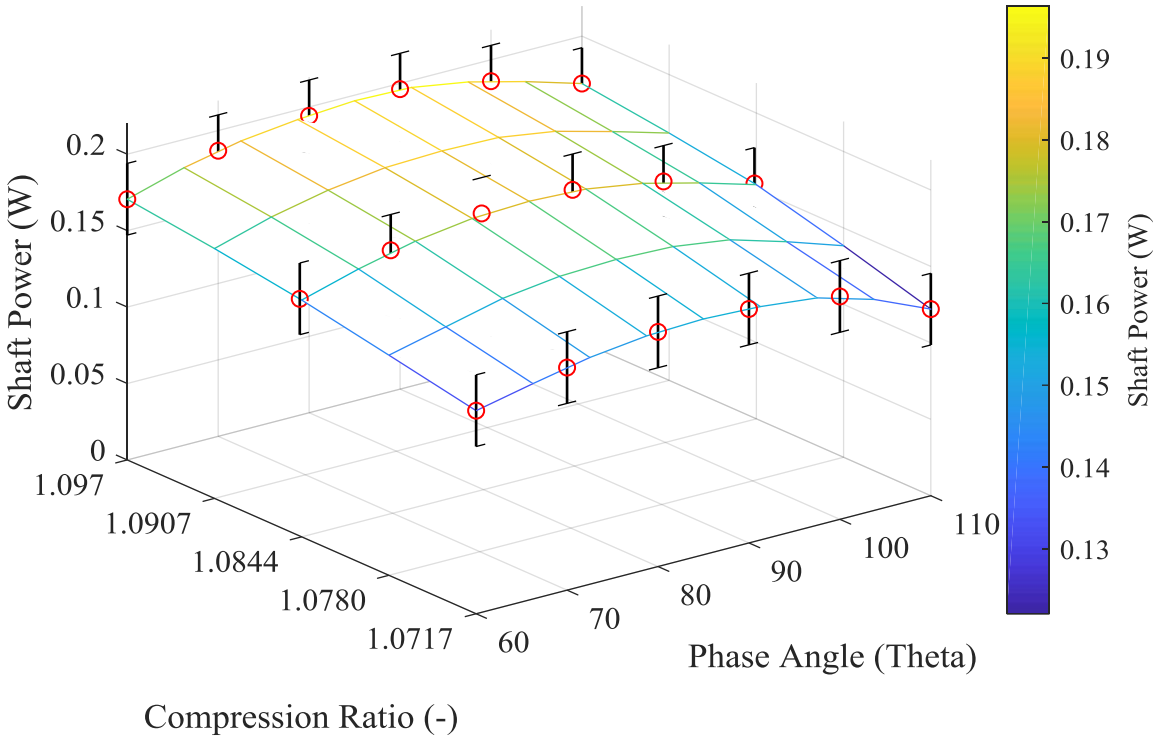


Figure 4.33 Shaft power of the Mark 2 for a constant load while the compression ratio and phase angle were varied.

Based on the shaft power relationship found from the investigation of changing the compression ratio and phase angle, further testing of the Mark 2 occurred at a phase angle of 90 ± 1° and a compression ratio of 1.097 ± 0.007. A load was applied to the Mark 2 and varied. The load was varied to produce a range of operating speeds of the Mark 2 and the corresponding shaft power was determined. The shaft power of the Mark 2 for a compression ratio of 1.097 ± 0.007 and a phase angle of 90° for various operating speeds is displayed in Figure 4.34. As the load was increased, the shaft power was found to increase while the operating speed decreased until the maximum shaft power occurred. After the engine was loaded more, the shaft power and the operating speed decreased. A local maximum shaft power of 0.26 ± 0.02 W at an operating speed of 27 ± 0.3 rpm was found.

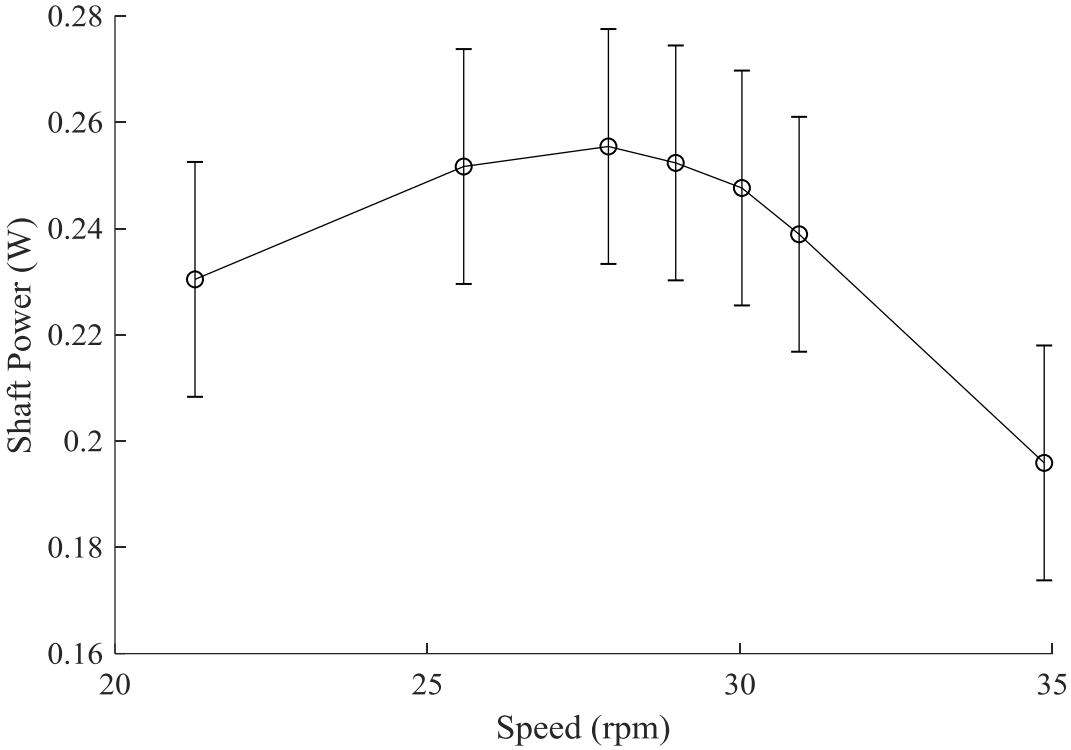

Figure 4.34 Shaft power of the Mark 2 for various speeds caused by the use of variable loads.

### 4.4.3 Lessons Learned

Many lessons were learned from the Mark 2. They were learned from the manufacturing process, trying to get it to run, and from trying to optimize the performance as described below.

#### 4.4.3.1 Manufacturing

- Direct acetone smoothing is better than acetone vapour smoothing. With direct acetone smoothing, acetone is applied directly to the ABS part and quickly melts the shell before it evaporates. With acetone vapor smoothing, acetone is allowed to evaporate into a vapor in a container containing the ABS. The acetone vapor slowly dissolves the shell and diffuses into the ABS. A problem arises if acetone is not given enough time to diffuse out of a part before the part is heated beyond acetone's boiling point 56 °C [94], or is close to the glass transition temperature of the ABS of 98 °C [83]. This causes the dissolved acetone in the ABS to boil and create bubbles that form due to the ABS being close to the glass transition temperature. This completely destroys the part as shown in the difference between Figure

4.35, an ABS part that has been acetone smoothed and not heated, and Figure 4.36 the same part heated before the acetone could full diffuse from the part.

Figure 4.35 Image of an ABS part that has been acetone vapor smoothed but not heated.

Figure 4.36 Image on an ABS part that has been acetone vapor smoothed and then heated up to 95 °C.

- Using a polyethylene sheet as a lip seal for the displacer piston allowed for engine operation. This provided a seal that was low friction. It provided a seal that allowed for the displacer piston to shuttle the working fluid through the heat exchangers without the working fluid bypassing the lip seal.
- Parts printed on the Form 2 became more brittle over time. UV light was used to cure the parts printed from the Form 2, so they would have the desired material properties. Additional UV light from fluorescent lights, or sunlight shining through the windows, caused the parts to become brittle and more prone to shattering when loaded rapidly in tension.
- The graphite piston could bind and become stuck in the glass cylinder.
    - Due to the very small tolerances associated with the piston-cylinder set, too much clamping force applied by the housing could cause the glass cylinder to deform and therefore cause the piston to bind.
    - The same problem could occur if the mounting frame, used to secure the graphite piston so it could be attached to the connecting rod, was also clamped too tight.

- The ball end joint used to connect the graphite piston to the connection rod was critical. It allowed for free movement of the connecting rod in one linear axis, along with rotation in two axes. This caused no moments to be directly applied to the graphite piston, which prevented the graphite piston from binding in the cylinder.

#### 4.4.3.2 Running

- The friction of the power piston system was the dominant engine loss until the graphite piston and glass cylinder was used.
- The engine could have too large of mass of working fluid inside it, depending on the location of the power piston when the engine was sealed. The extra mass would cause the mean cycle pressure to be greater than the buffer pressure, which results in more forced work. To counteract this the engine was sealed when the power piston was at half of its stroke.
- The engine could be sealed too well. When this happened, the mass of the working fluid could not change quick enough to amount that allowed for the engine to operate. This was combatted by be spinning the engine through a few revolutions until it could run on its own.
- PTFE bushings could provide a seal for the displacer piston rod that allowed for operation of the engine.

#### 4.4.3.3 Optimization

- Increasing the size of the flywheel decreased speed fluctuations and allowed the engine to continue operating at lower speeds.
- Implementing a regenerator, whether it being a section of the heat sink or steel wool, always caused the performance the Mark 2 to drop relative to the case with no regenerator. This could be caused by the increase pressure drop caused by the regenerator material.
- Operating at the maximum compression ratio possible produced the maximum shaft power.
- A peak compression ratio was never found due to the limitations of the power piston system. A power piston system that could produce larger compression ratio would be required to locate the peak.
- A phase angle of 90° produced the maximum shaft power.

## 4.5 Engine Description: EP-1

### 4.5.1 Engine Development and Description

The EP-1 is a gamma-type LTDSE. The design of the EP-1 was centered on finding a compression ratio and phase angle that would produce the maximum shaft power. The drive mechanism used allowed the phase angle and compression ratio to be easily changed. The majority of the EP-1's parts were made from metal. However, the parts that were 3D printed were made with the Form 2. The final configuration of the EP-1 is shown in Figure 4.37, and displays the main systems that will be described further in the following sections. A drawing package for the EP-1 is included in the Appendix E. Figure 4.38 displays the overall dimensions of the EP-1.

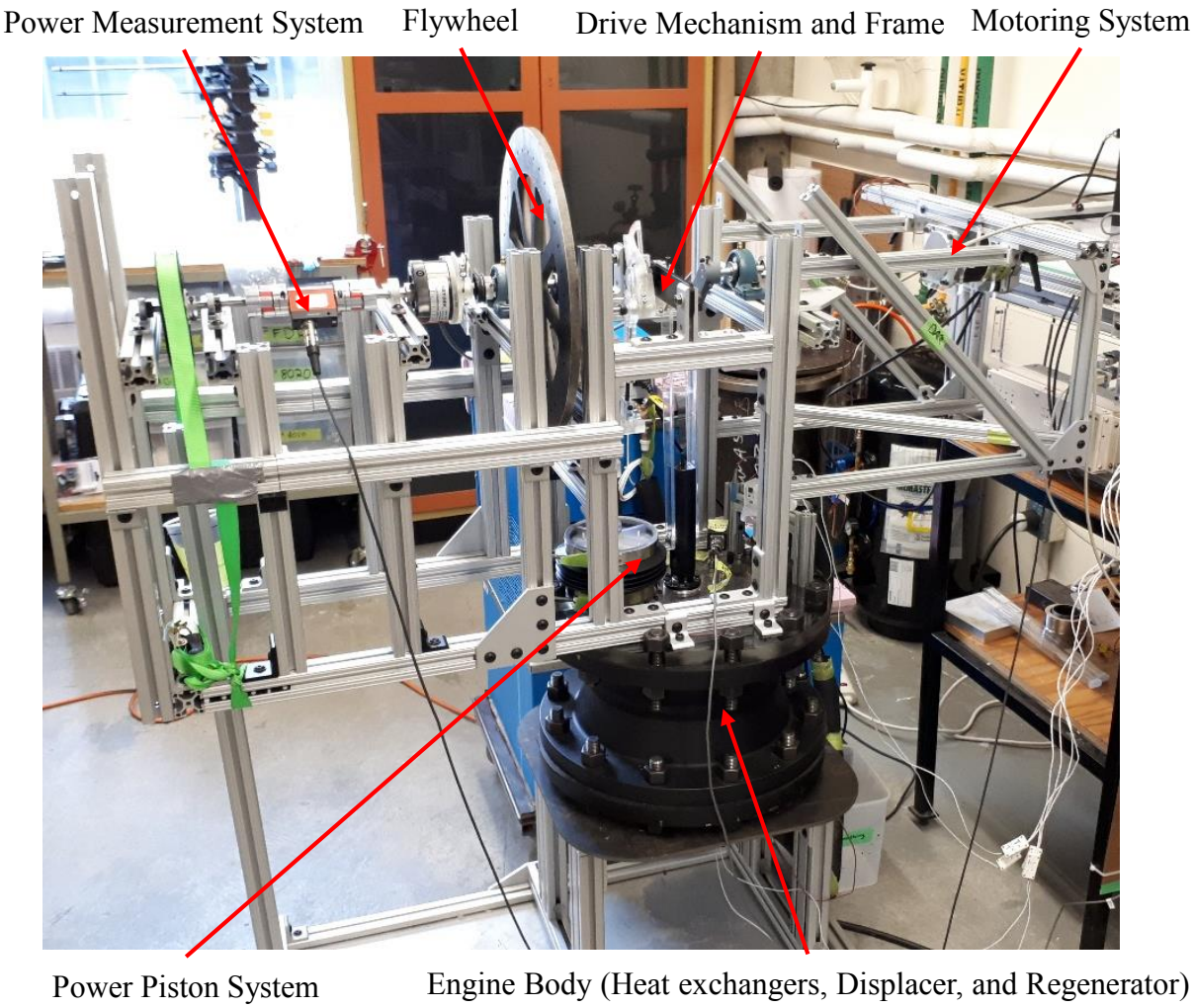


Figure 4.37 Image of the final configuration of the EP-1.

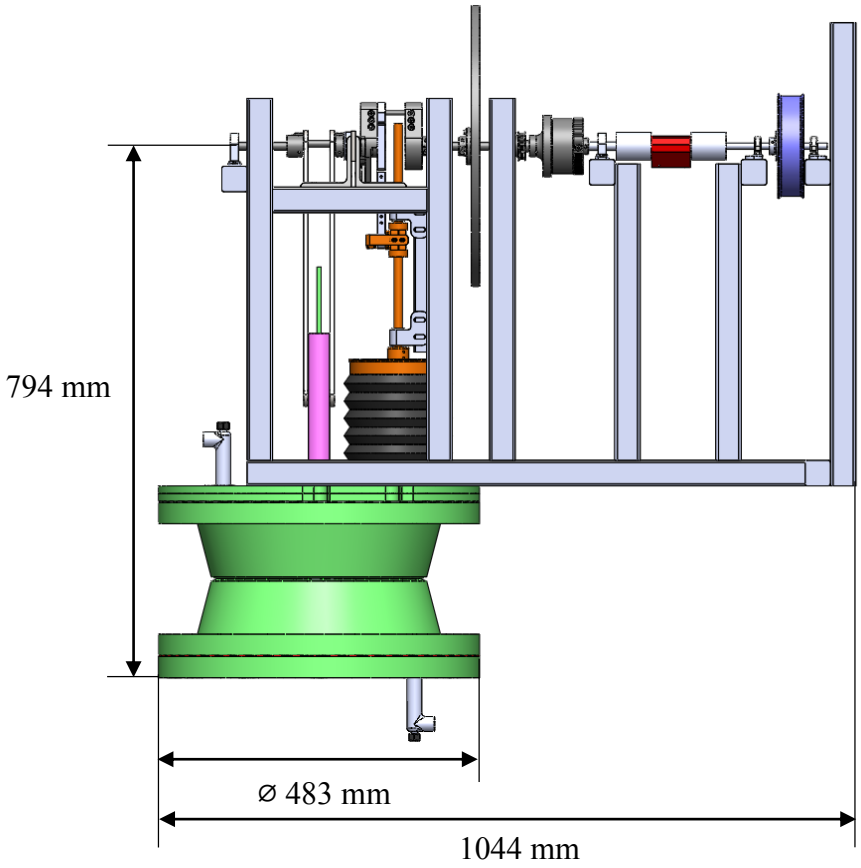


Figure 4.38 General dimensions of the EP-1.

#### 4.5.1.1 Power Piston System

Throughout its development, the EP-1 was able to successfully run with three different power piston system: a tapered bellows, a graphite piston-glass cylinder set, and a cylindrical bellows. Each power piston configuration was implemented for various reasons, as will be showcased below. A summary of the properties of each power piston system is presented in Table 4.8.

Table 4.8 Power piston systems used by the EP-1.

| Name | Stroke (m) | Bore (m) | Swept Volume ($m^3$) | Swept Volume (ml) | Maximum Compression Ratio (-) |
|---|---|---|---|---|---|
| Tapered bellows | 0.12 | - | 0.00056 | 560 | 1.06 |
| Graphite piston glass cylinder set | 0.127 | 0.044 | 0.000197 | 197 | 1.02 |
| Cylindrical bellows | 0.1 | 0.152 | 0.00183 | 1835 | 1.206 |

The first power piston system that allowed the EP-1 to run was the tapered bellows. The tapered bellows was chosen because it was still able to perform even if it was slightly misaligned. Internal support rings were used on the bellows so that it would not collapse when the working pressure was less than the buffer pressure. The bellows was made of neoprene rubber, and its material properties allowed it to operate between the temperature limits of the source and sink [95]. Figure 4.39(a) depicts how the bellows was secured to a piston and the engine body with hose clamps. The tapered bellows was replaced with the cylindrical bellows because of the need to go to larger compression ratios, and because it was difficult to determine the volume variations caused by the tapered bellows.

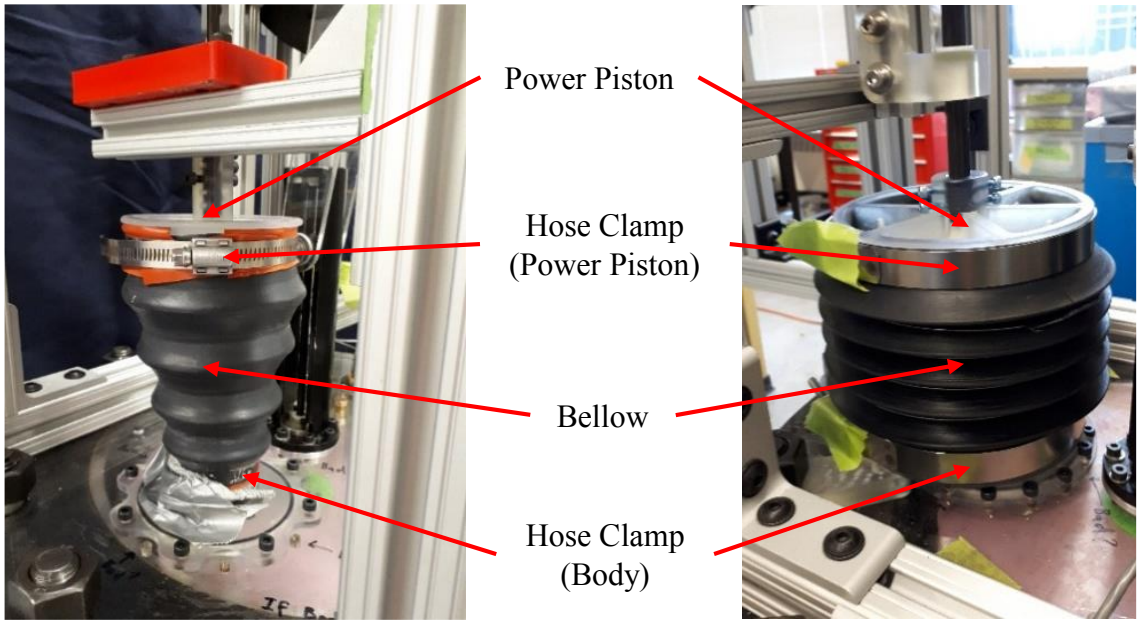


(a) (b)

Figure 4.39 Images of the two bellows used by the EP-1: (a) Tapered and (b) Cylindrical.

The precision glass cylinder and graphite piston set was used briefly to compare the performance between the EP-1 and Mark 2. It was only briefly used because it resulted in vary poor performance that was most likely caused by the very small compression ratio. This assembly used similar mounting methods to the Mark 2 displayed.

The cylindrical bellows was the final power piston system used on the EP-1. The cylindrical bellows was chosen because of the benefits seen from the tapered bellows. Most importantly, it

was chosen because it could produce a larger compression ratio than the tapered bellows with minimum modification required to the EP-1's drive mechanism and frame. Like the tapered bellows, the cylindrical bellows used internal support rings to prevent it from collapsing. External support rings were also used to prevent the internal support rings from moving, and to restrict the bellows from expanding in the radial direction. The bellows was secured to the power piston and the engine body with hose clamps as seen in Figure 4.39(b). The cylindrical bellows was made of nitrile rubber and was capable of operating between the required temperature limits of the thermal source and sink [95].

For the alternative power piston systems of the tapered and cylindrical bellows used by the EP-1, the effective piston cross sectional area could potentially vary. Therefore, internal and external support rings were implemented to help restrict the radial volume change of the bellows. After installation of the bellows, the peak of bellows' circumference was measured at the piston maximum and minimum volume. Since radial expansion and compression of the bellows was restricted, a linear volume change was assumed. The bore diameter provided in Table 4.8.

Table 4.8 is based off this assumption. The uncertainty in the instantaneous change in the bellows volume, 50 ml, was an estimated value based on the volume of the bellows folds at its minimum stroke position. This volume of these bellow folds were calculated using a solid model. The bellows folds when the bellows it at its minimum position is displayed in Figure 4.40.

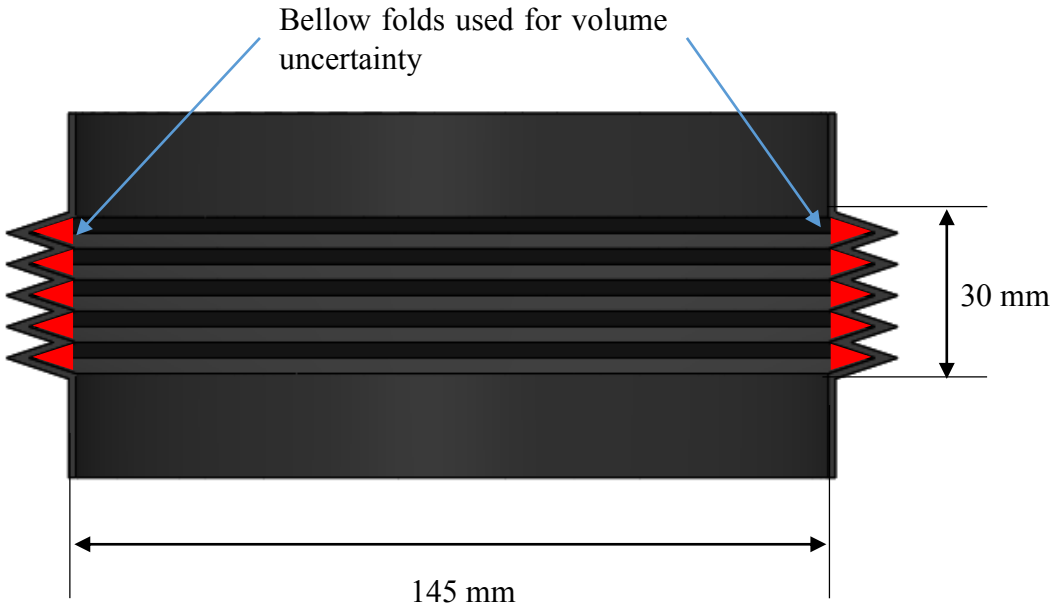


Figure 4.40 Cross sectional area of the bellows folds used to estimate the instantaneous uncertainty in the volume of the bellows.

#### 4.5.1.2 Displacer Piston System

The displacer piston system used for the EP-1 was a custom-made piston-cylinder set. Similar to the Mark 1, it consisted of a removable displacer cylinder that resided in the engine body. The displacer piston system has a bore diameter of 25.4cm, a stroke of 11.6cm, and a swept volume of 5880cm$^3$.

The EP-1 used the same displacer piston style as the Mark 1 and 2. The displacer piston was made of a 3D printed core to hold the displacer rod and 4 EPS discs as seen in Figure 4.41. The displacer piston had a thickness of 11.43cm. The displacer piston used a lip seal like the Mark 2; however, instead of one lip seal, the EP-1 used two. Figure 4.41 shows the locations of the lip seals at the interfaces of the EPS discs. Two lip seals were used because of the lack of concentricity of the displacer cylinder.

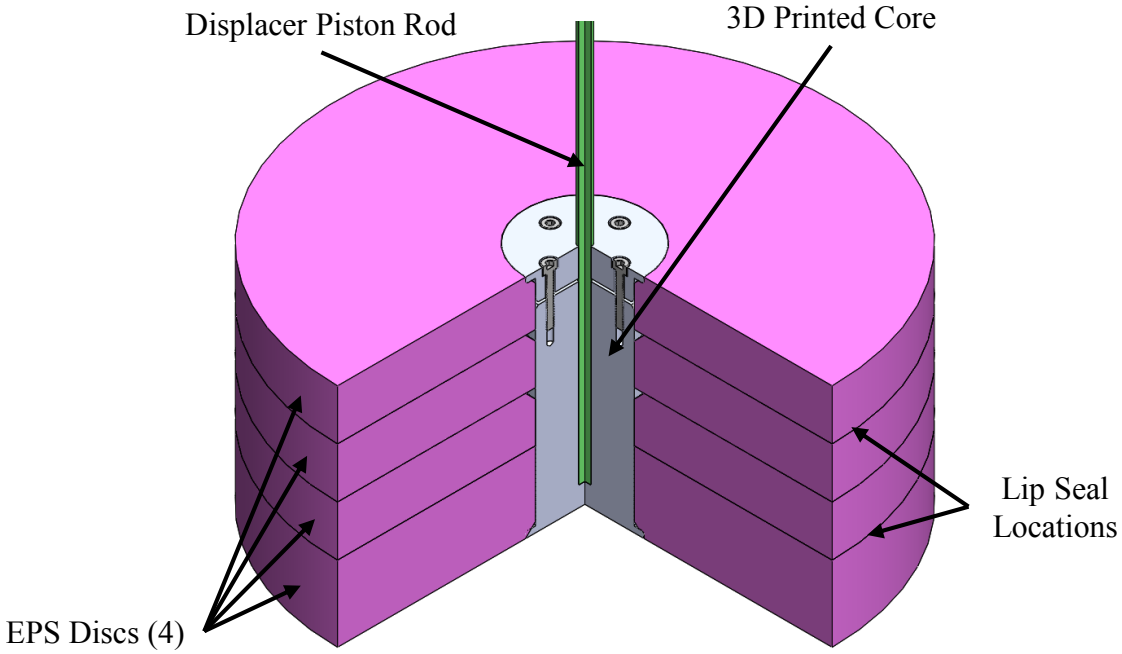


Figure 4.41 A section view of a solid model of the displacer piston of the EP-1.

#### 4.5.1.3 Engine End Caps

To create the work space, two end caps were used on the top and bottom of the engine body. The original end caps were both made of metal. However, the top cap was replaced with an acrylic end cap to reduce thermal losses as well as to allow the displacer piston to be visible. The bottom metal end cap was not changed. However, it did have a plastic ABS sheet placed on top of it. This plastic sheet acted as a barrier to prevent heat transfer between the working fluid and the metal end cap. The engine body was made of two pipe flanges welded together. Figure 4.42 shows the engine body and the two end caps, along with the other internal system of the EP-1.

Similar to the Mark 1, the displacer cylinder was a sleeve that was inserted into the engine body. The displacer cylinder consisted of three parts: two 25.4cm internal diameter pipes and a PC sleeve that was inserted into the pipes. The PC sleeve was used to create a constant smooth cylinder wall that the displacer piston's seal could interact with. It was also used to reduce the heat transfer between the working fluid and the metal pipes. The displacer cylinder was held concentrically inside the engine body by the heat exchangers that resided into the annulus created by the engine body and the displacer cylinder sleeve depicted in Figure 4.42. Like the Mark 1's displacer

cylinder, the EP-1's displacer cylinder sleeve rested on a plastic disc with feet. This provided a gap underneath the cylinder so that the working fluid would be able to travel through the annulus containing the heat exchangers and regenerator.

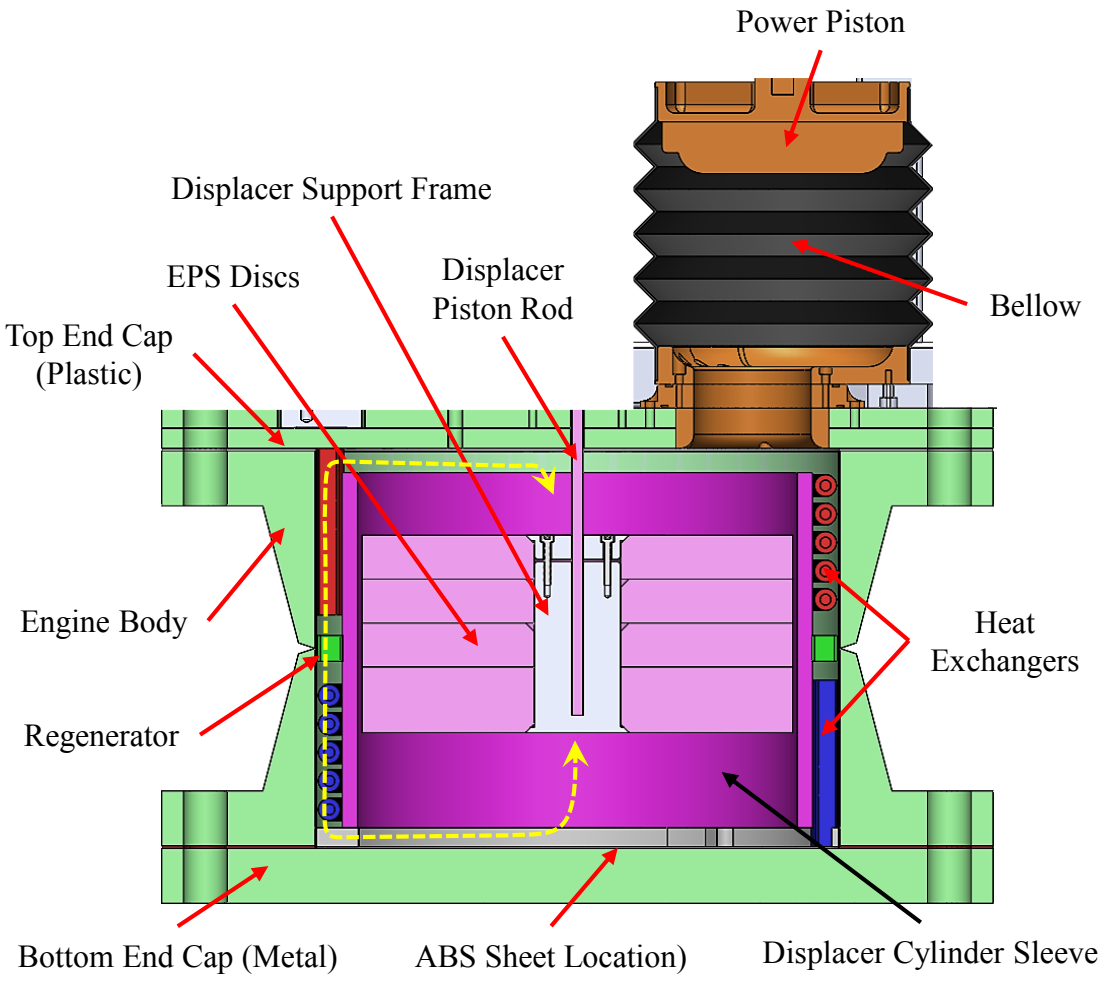


Figure 4.42 Section view of a solid model of the EP-1 showcasing its internal systems.

Figure 4.43 shows the PTFE linear bushing that the EP-1 used as a shaft seal for the displacer piston rod. As learned from the Mark 2, the bushing worked as a seal that had a very small friction loss associated with it while providing a seal that was more than adequate for the pressure swings that occurred inside the engine. The small amount that the displacer piston rod seal did leak allowed the engine to change the mass of the working fluid so forced work was minimized. The displacer rod was supported by the displacer tower as seen in Figure 4.44.

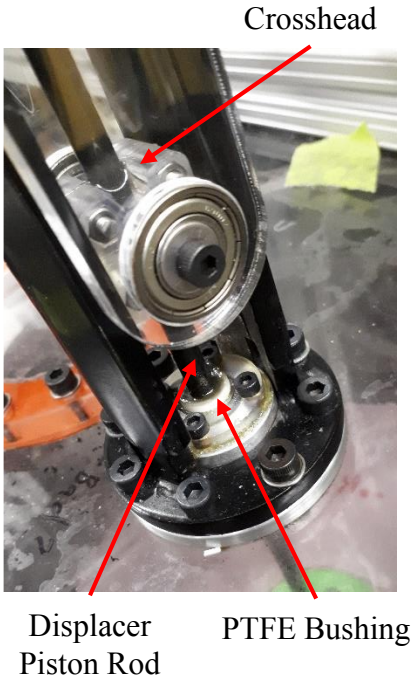


Figure 4.43 Image of the displacer piston rod.

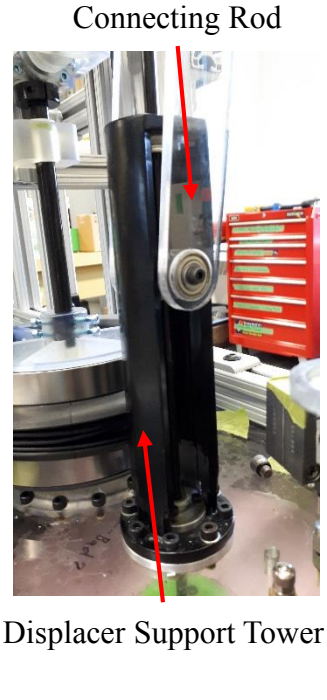


Figure 4.44 Image of the displacer support tower.

#### 4.5.1.4 Heat Exchangers

The heat exchangers for the EP-1 consisted of finned copper tubing that resided inside the annulus of the engine body. The two heat exchangers both had a surface area of 5530 $cm^2$. Five rings of finned copper tubing were linked together with a flow manifold, and each ring was spaced using support brackets as seen in Figure 4.45.

The fluid used to heat and cool the heat exchangers was distributed to the five rings through a manifold. The manifold was designed for each ring of tubing to experience the same flow rate of water. The connections on to the manifold used a 3D printed L-shape fitting that allowed an RTD to be placed inside to measure the temperature while allowing fluid to pass through.

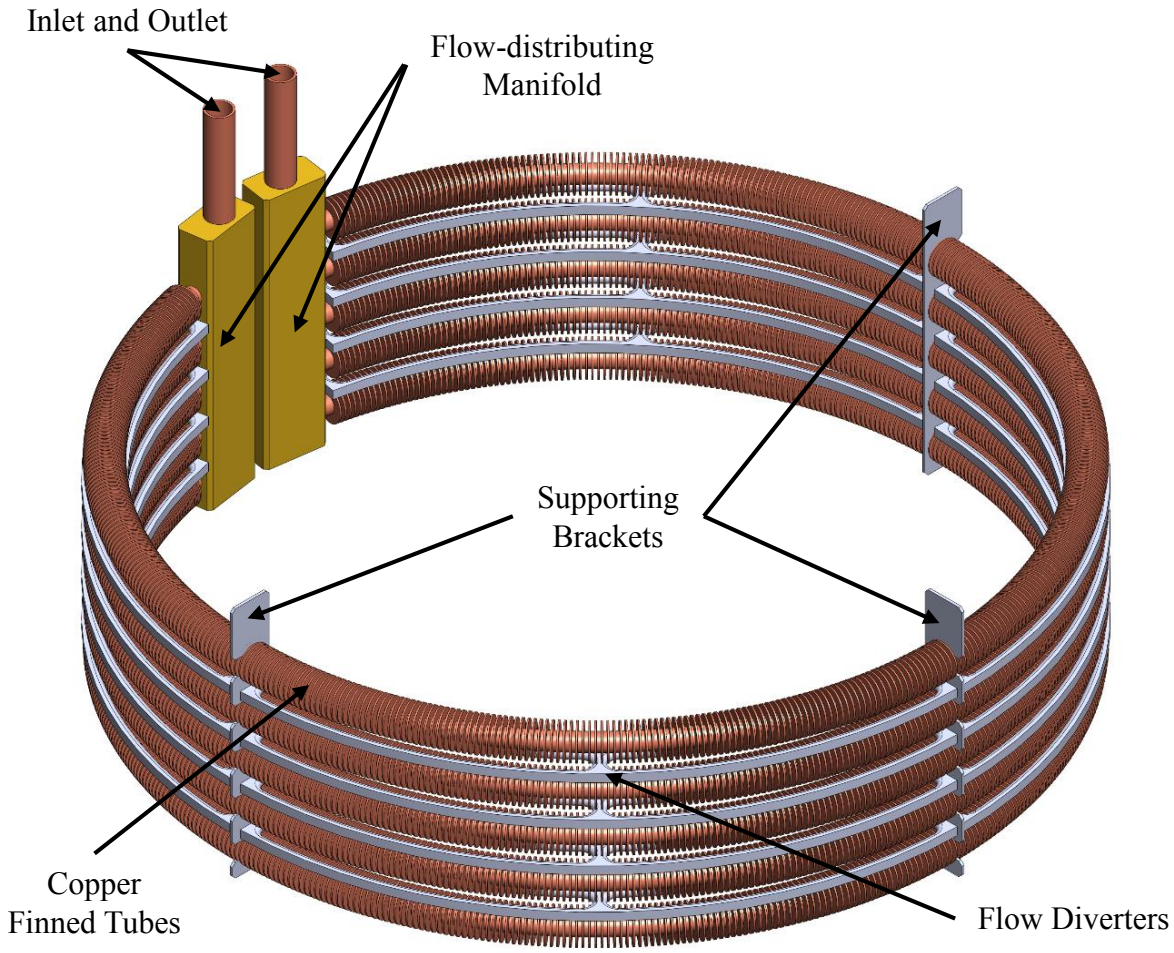


Figure 4.45 Solid model of the heat exchanger used for the EP-1.

Two modifications were made to the heat exchangers. To eliminate a flow path around the heat exchangers, and to reduce the dead volume of the heat exchangers, the gap between the two manifolds was filled with a solid material after installation. Flow diverters were installed to potentially alter the path the working fluid took through the heat exchangers. The cross-sectional view of the heat exchanger with and without the flow diverters is depicted in Figure 4.46.

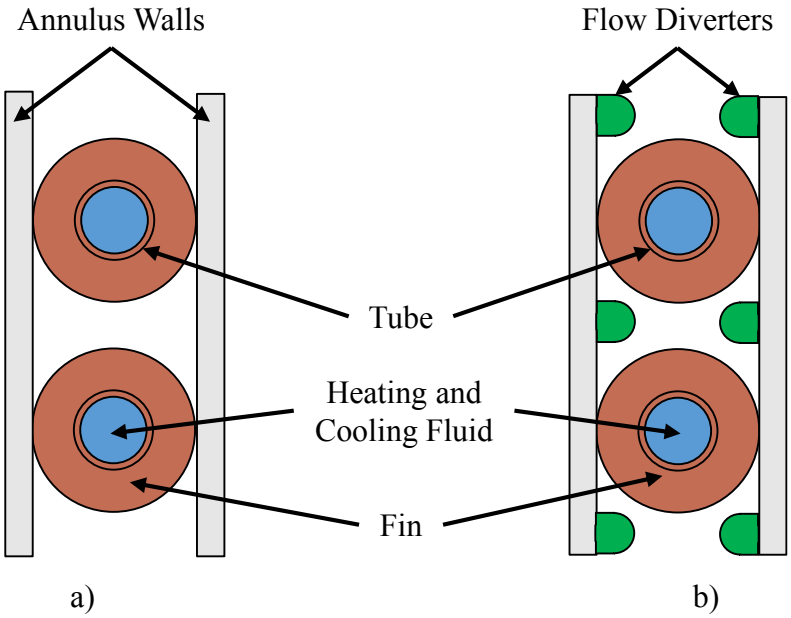


Figure 4.46 Section view of the finned copper tubing heat exchanger inside the EP-1 annulus (a) without (b) and with flow diverters.

#### 4.5.1.5 Regenerator

The regenerator volume resided between the two heat exchangers. The final configuration of the EP-1 used a slotted regenerator displayed in Figure 4.47. The slotted regenerator was used to reduce the dead volume of the engine, while having a possible low pressure drop associated with it.

Figure 4.47 Image of a section of the slotted regenerator used by the EP-1.

#### 4.5.1.6 Drive Mechanism

The drive mechanism for the EP-1 used a similar design to that of the Mark 2. The mechanism was designed so that the power piston stroke and phase angle could be changed easily. Both the power piston and displacer piston used a slider crank mechanism and a crosshead attachment to connect the connecting rod to the piston. The power piston crankshaft was connected directly to the crankshaft that had the flywheel so that torque did not need to be transferred through the displacer piston cranks arms when the engine was loaded. The displacer piston and power piston rod were supported at two locations with linear busing for optimal support because the crosshead connection method that was used.

Two sets of crank arms were used for the power piston of the EP-1. Each crank arm set had the ability to change the phase angle of the engine and the power piston stroke. The crank arm lengths and phase angles possible with each crank arm set are shown in Table 4.9. The phase angle chosen was aligned by eye and the uncertainty in the placement was determined to be 1°.

Table 4.9 Crank arm lengths and corresponding compression ratios for crank arms sets used.

| Crank Arm Set | Phase Angle | Crank Arm Lengths (mm) |
|---|---|---|
| A | 60° to 120° | 30<br>40<br>50 |
| B | 60° to 120° | 25<br>35<br>45 |

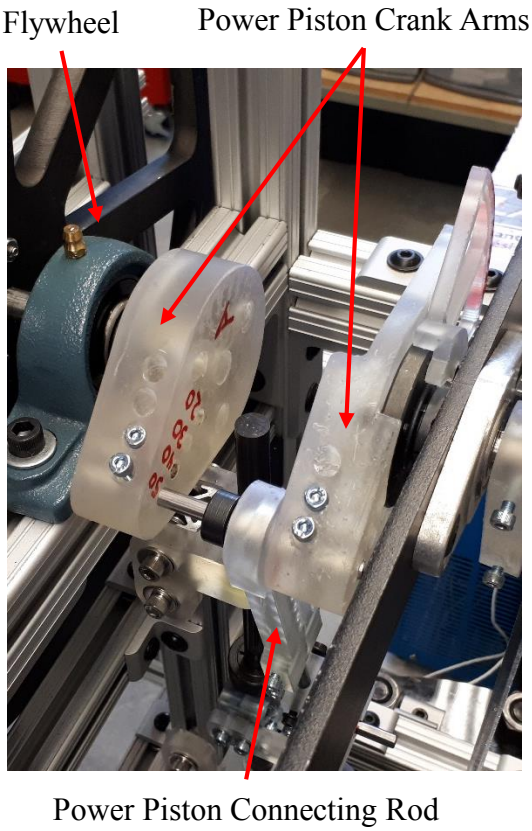


Figure 4.48 Image of the power piston crank arms and connecting rod used by the EP-1.

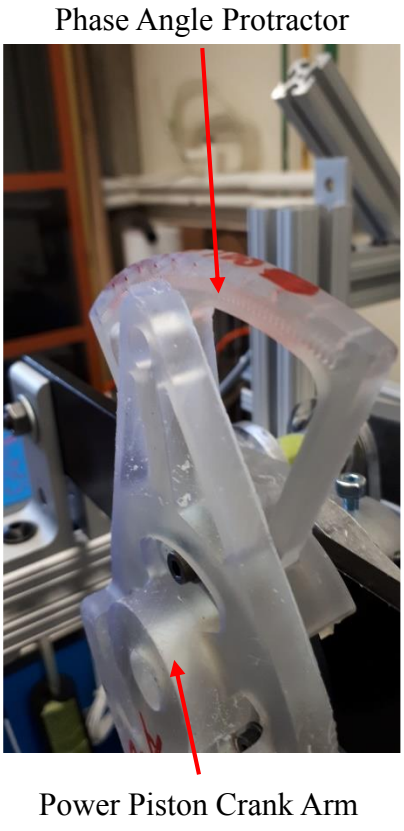


Figure 4.49 Image of phase angle adjustment method used by the EP-1.

#### 4.5.1.7 Frame

The EP-1 used structural aluminum extrusion framing like the Mark 2. It was chosen for the same reason as the Mark 2 summarized earlier.

#### 4.5.1.8 Instrumentation Locations

The shaft power measurement system was similar to the one used by the Mark 2. A load was applied to the engine by hanging a mass on a belt hung on a load application pulley. A differential torque was then measured with a torque transducer. To prevent damage to the torque transducer, a torque-limiting coupler was installed between the flywheel and torque transducer. No gear reduction system was used, and the torque transducer shaft was directly connected to the engine's shaft. The same rotary encoder system, with the rotary encoder, two pulleys, and timing belt, was used. The shaft power measurement system and its components are shown in Figure 4.50.

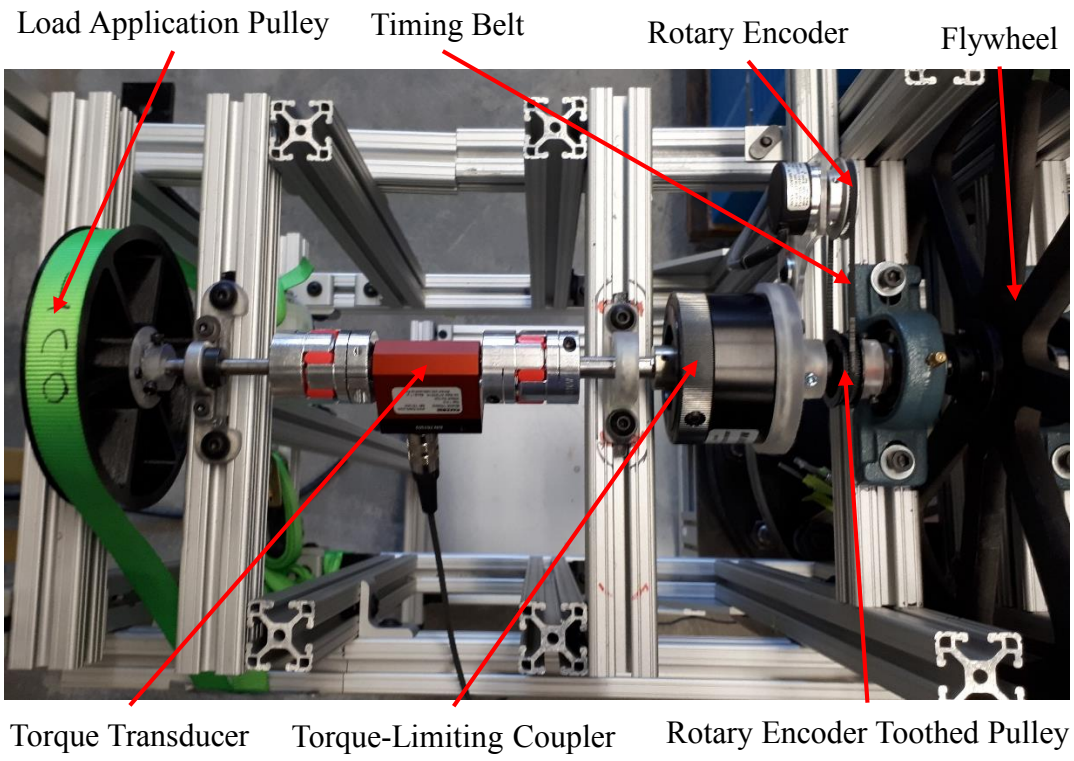


Figure 4.50 Image of the shaft power measurement system used by the EP-1.

The temperature was measured at two locations in the displacer cylinder. The locations corresponded to the entrance/exit of the thermal source and sink heat exchanger shown in Figure 4.51. These locations were chosen because the thermocouple resided in an area where the working fluid was moving and never stagnant. These locations were chosen as they were best thought to represent the temperature of the expansion and compression space respectively.

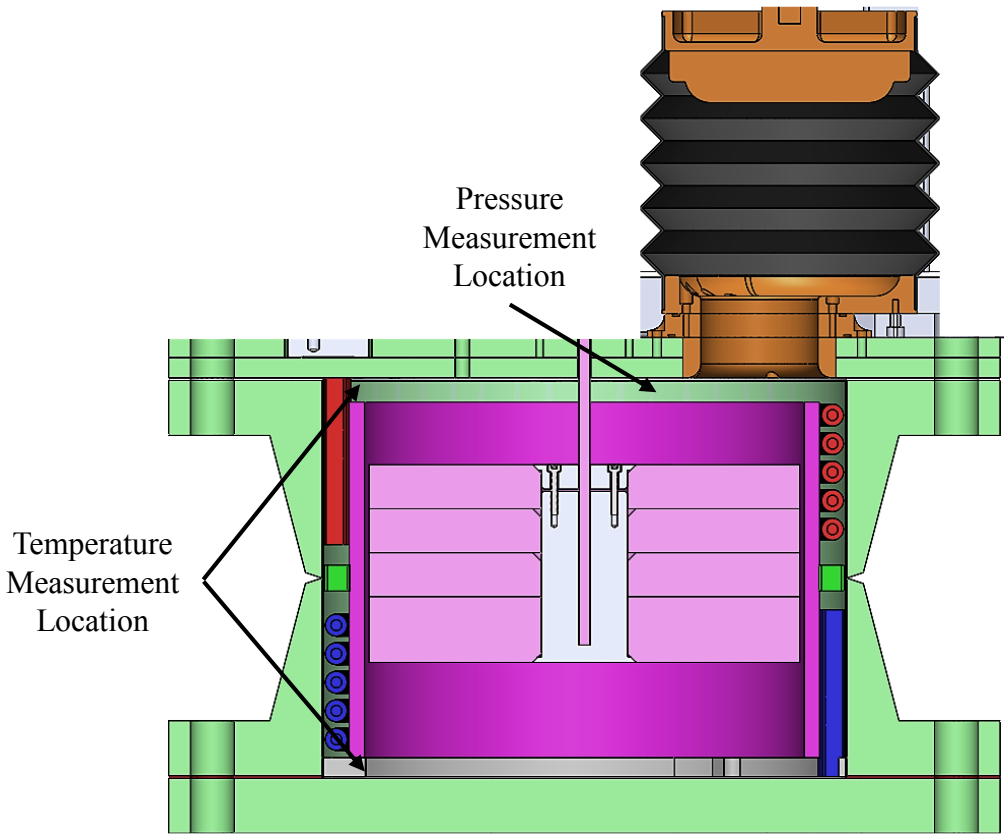


Figure 4.51 Section view of a solid model of the EP-1 that showcases the two locations where the temperature of the working fluid was measured.

The pressure transducer was located close to the power piston to make sure the pressure recorded was as close as possible to the actual pressure experienced by the power piston. This location is shown in Figure 4.51.

Finally, the temperature of the water was measured at the inlet and outlet of the heat exchangers. Instead of using tee fitting like the Mark 2, L-shape fitting were used. This allowed for the RTD

to be in more contact with the water and provided better measurement of the water's temperature. In Figure 4.52, the RTDs, L-shape fitting, and the depth of the RTD in the lee fitting is shown.

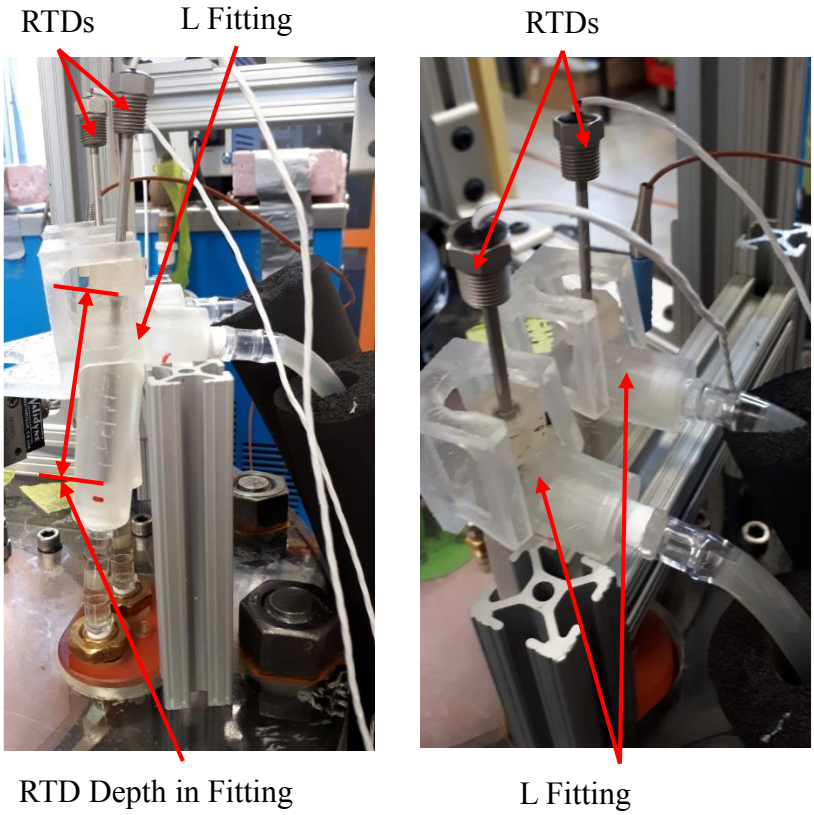


Figure 4.52 Images of the RTDs and L-shape fitting used to measure the temperature of the water used to heat and cool the Stirling engine.

#### 4.5.1.9 Component and Configuration Summary

A summary of the dimensions and systems used by the final configuration of the EP-1 is presented in Table 4.10.

Table 4.10 Component summary of the EP-1.

| | |
|---|---|
| Engine Name | EP-1 |
| Engine Name | gamma |
| Engine Type | Crankshaft |
| Drive Mechanism | Slider crank with crankshaft |
| Displacer Piston Dimensions | Bore = 0.254 m<br>Stroke = 0.116 m<br>Swept Volume= 0.00588 $m^3$ |
| Power Piston System Type | Bellows |
| Power Piston Dimensions | Bore = 0.152 m<br>Stroke = 0.1 m<br>Swept Volume= 0.00183 $m^3$ |
| Compression Ratio (Maximum) | 1.21 |
| Heat Exchanger Type | Finned tube bank |
| Heat Exchanger Material | Copper |
| Heat Exchanger Volume | 0.000714 $m^3$ |
| Heat Exchanger Surface Area | 0.553 $m^2$ |
| Regenerator Volume | 0.0000931 $m^3$ |
| Regenerator Material | Plastic Channels |
| Flywheel Moment of Inertia | 0.243 $kg*m^2$ |

A summary of all the different tested configurations of the EP-1 is presented in Table 4.11

Table 4.11 EP-1 configurations tested.

| Engine Configuration | Power Piston System | Heat Exchanger System | Regenerator | Able to run? |
|---|---|---|---|---|
| 1 | Rolling diaphragm | Finned Tube | - | No |
| 2 | Tapered Bellows | Finned Tube | - | Yes |
| 3 | Graphite Piston Glass Cylinder | Finned Tube | - | Yes |
| 4 | Cylindrical Bellows | Finned Tube | - | Yes |
| 5 | Cylindrical Bellows | Finned Tube with flow diverters | - | Yes |
| 6 | Cylindrical Bellows | Finned Tube with flow diverters | Slotted | Yes |

### 4.5.2 Performance Evaluation

The performance evaluation for the EP-1 was based on: getting the engine to run and maximizing shaft power. The results of the performance evaluation of the EP-1 is presented in the following chapter.

### 4.5.3 Lessons Learned

Like the Mark 1 and 2 before it, lessons were also learned from the EP-1. These lessons were learned from the manufacturing process and trying to get it to run as described below.

#### 4.5.3.1 Manufacturing

- The clear material used by Form 2 would creep at room temperature if a load was applied to it.
- Split rings were required to be strong and needed adhesives and securing methods that were able to withstand temperatures close to the thermal source temperature.

#### 4.5.3.2 Operation

- The engine was loaded by adding weights to a cup. This cup was connected to the belt that ran on the load application pulley. The friction between the belt and the pulley would impart a torque load on the engine. If the maximum load that the engine could run at was applied all at once, in its entirety, meaning all the weights were added into the cup at once, the engine would stall. However, if the weights were slowly added to the cup until the maximum load was reached, the engine would be able to run at this maximum load.

# Chapter 5 Shaft Power Optimization

This chapter provides the results of the optimization process for the EP-1 to produce the maximum shaft power. This optimization process involved changing the compression ratio, phase angle, heat exchangers locations, which working space, the expansion or compression space, the power piston connects to, and the applied torque load. After all the optimal parameters were found individually, the maximum shaft power of the EP-1 could be determined. The point of maximum shaft power of the EP-1 will then be used for a West number performance comparison of LTDSEs.

## 5.1 Constant Operating Parameters

Throughout all the tests described in the following sections, several operating parameters of the EP-1 were kept constant. These constant operating parameters are presented in Table 5.1. The temperature of the thermal source and sink were not varied. To achieve the maximum heat transfer rate possible by the heat exchangers, both water bath pumps were operated at that their maximum flow rate. Finally, the regenerator was used throughout all tests because it could not be removed without complete disassembly of the engine.

Table 5.1 Constant operating parameters across all tests.

| Parameter | Value and Unit |
|---|---|
| Thermal Source Temperature | 95 °C |
| Thermal Sink Temperature | 2 °C |
| Heated Flow Loop Mass Flow Rate | 0.0432 kg/s (maximum) |
| Regenerator | Plastic slotted regenerator. |

Table 5.2 tabulates the sampling time and frequency used for each group of DAQ instruments for all tests. The justification for the sampling frequency was provided in Chapter 3. Since the engines were running at steady state, the RTDs and thermocouples were only sampled for 10 seconds so that their average values could be determined. Group 3 was sampled for 20 seconds so that multiple engine cycles could be captured, and the average shaft torque and shaft power could be calculated as these two values are primarily used for the performance evaluation.

Table 5.2 Sampling time and frequency of DAQ instruments.

| Group # | DAQ Instruments | Sample Time (s) | Sample Frequency (Hz) |
|---|---|---|---|
| 1 | RTDs | 10 | 100 |
| 2 | Thermocouples | 10 | 5000 |
| 3 | Pressure Transducer<br>Rotary Encoder<br>Torque Sensor | 20 | 10000 |

## 5.2 Compression Ratio – Initial Tests

To determine what compression ratios should be further investigated, the shaft power was measured for various compression ratios, while different loads were applied to the engine. Table 5.3 tabulates the operating parameters used throughout these experiments. A phase angle of 90° was used. This was done because it resulted in the maximum indicated work, and it is the typical phase angle used for LTDSEs. Preliminary tests found having the heat exchanger on the top and the power piston connected to the expansion space resulted in better engine performance. Both the phase angle choice and heat exchanger position will be validated in later sections.

Table 5.3 Operating parameters used for initial compression ratio tests.

| Parameter | Value and Unit |
|---|---|
| Thermal Source Heat Exchanger Position | Top |
| Power Piston Position | Expansion Space |
| Compression Ratios | 1.103, 1.144, 1.165, 1.206 ± 0.006 |
| Phase Angle | 90 ± 1° |

To determine the free running speed of the engine, no load was applied. Depending on the compression ratio used, the heat transfer rate from the thermal source heat exchanger into the working fluid was sometimes greater than the heating capacity of the thermal source water bath. Therefore, to determine the free running speed, the engine was started and the temperature of the water at the inlet of the heat exchanger was allowed to drop until it reached 94 °C. At this temperature, the data was sampled. The process was used to determine the free running speed for all compression ratios tested.

When variable applied load tests were conducted, the maximum load was applied first. This was done by slowly adding weights into a cup that was connected to the belt that hung over the load application pulley. To test other loads, weights were removed from the cup. This process was repeated until the temperature of the inlet of the at the thermal source heat exchanger dropped below 94 °C. This was done so that the temperature difference of the thermal source and sink for each test stayed approximately constant.

Three compression ratios were initially tested: 1.103, 1.144, and 1.165. Figure 5.1 shows the operating speed of the engine for various applied loads. No error bars are shown because they

would be smaller than the marker size used. The average shaft torque was calculated by averaging the shaft torque for all the complete cycles captured. Since the sample time was 20 seconds for the torque sensor, the amount of engine cycles captured was equal to one third of the operating speed in revolutions per minute (rpm). The maximum torque applied to the engine for each compression ratio resulted in the minimum operating speed. The maximum compression ratio tested, 1.165, ran at the highest speed for the largest load applied. This compression ratio did not have the highest free running speed. This was unexpected and is investigated further in the following sections.

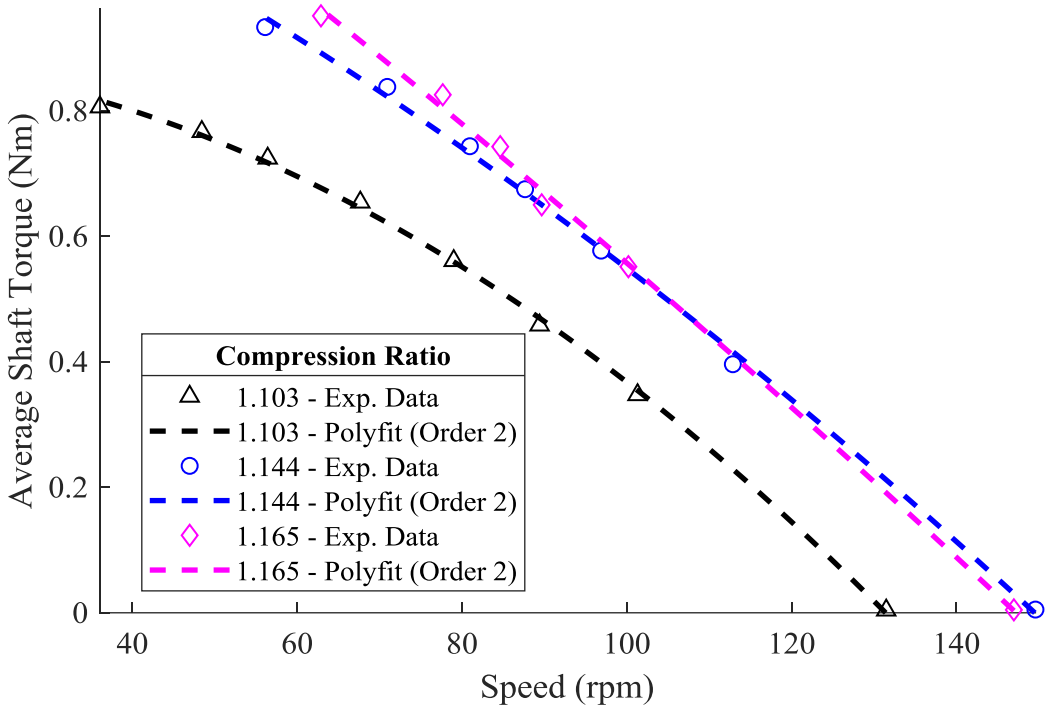


Figure 5.1 Average torque applied to the EP-1 and the resulting operating speed.

The shaft power and operating speed for the various applied torques is presented in Figure 5.2. Again, no error bars are shown because they would be smaller than the marker size. The shaft power was calculated from the average shaft torque and the average operating speed. For each compression ratio tested, the shaft power increases, reaches a maximum value, and then decreases as the operating speed decreases. This is caused by the shaft power being a function of both shaft torque and operating speed as discussed above. The point of maximum shaft torque does not correspond to the point of maximum power since the engine is running slower. The compression

ratio of 1.165 ± 0.006 produced the maximum shaft power of 6.72 ± 0.09 watts at an operating speed of 74.0± 0.3 rpm. A global maximum shaft power was not found and therefore larger compression ratios had to be tested.

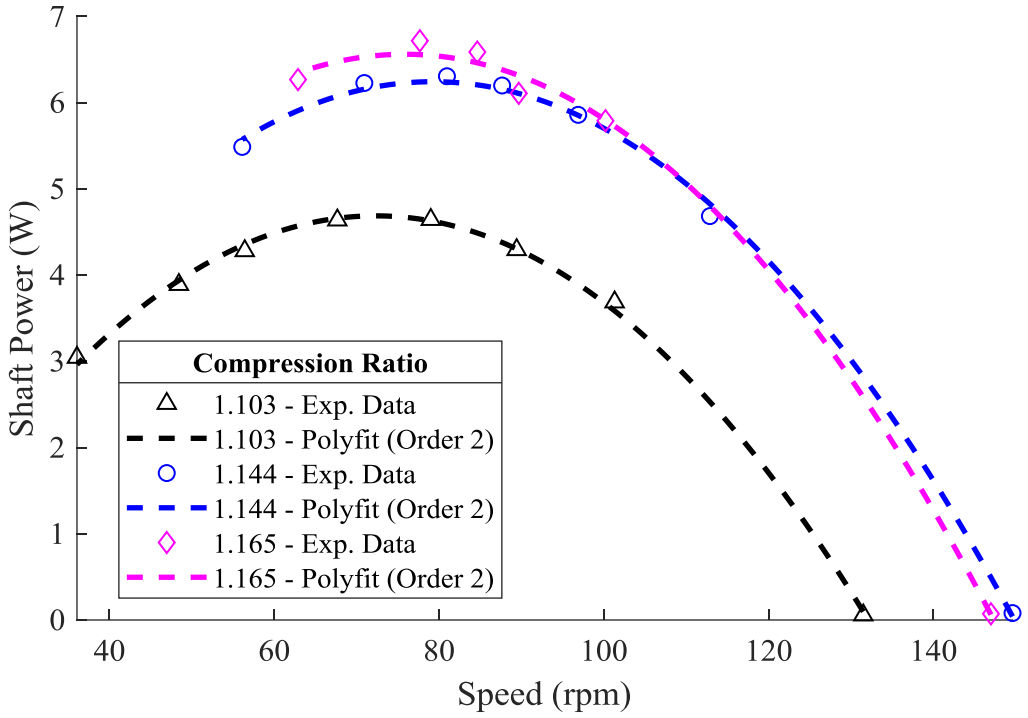


Figure 5.2 Shaft power of the EP-1 for various compression ratio and operating speeds with only internal split rings.

The maximum compression ratio, 1.206, could not be tested initially. This was because at any compression ratio higher than 1.165 the bellows stretched too much, and the internal split rings moved from their location in the bellow fold resulting in major deformation of the bellow. To combat this, larger diameter internal split rings were used, along with external split rings. After installation of the split rings, the compression ratio of 1.165 was retested to see the effects of the installation of the modified split rings. The maximum compression ratio, 1.206, was also tested.

Figure 5.3 showcases the applied torque and corresponding operating speed for the compression ratio of 1.165 before and after split ring modifications. For all tested points, an applied torque resulted in a slower operating speed after the split rings had been modified. This is most likely caused by the restriction of the bellow by the modified split rings producing a larger load for the

engine to overcome. A similar result of a decrease in the shaft power for the modified split rings is shown in Figure 5.4.

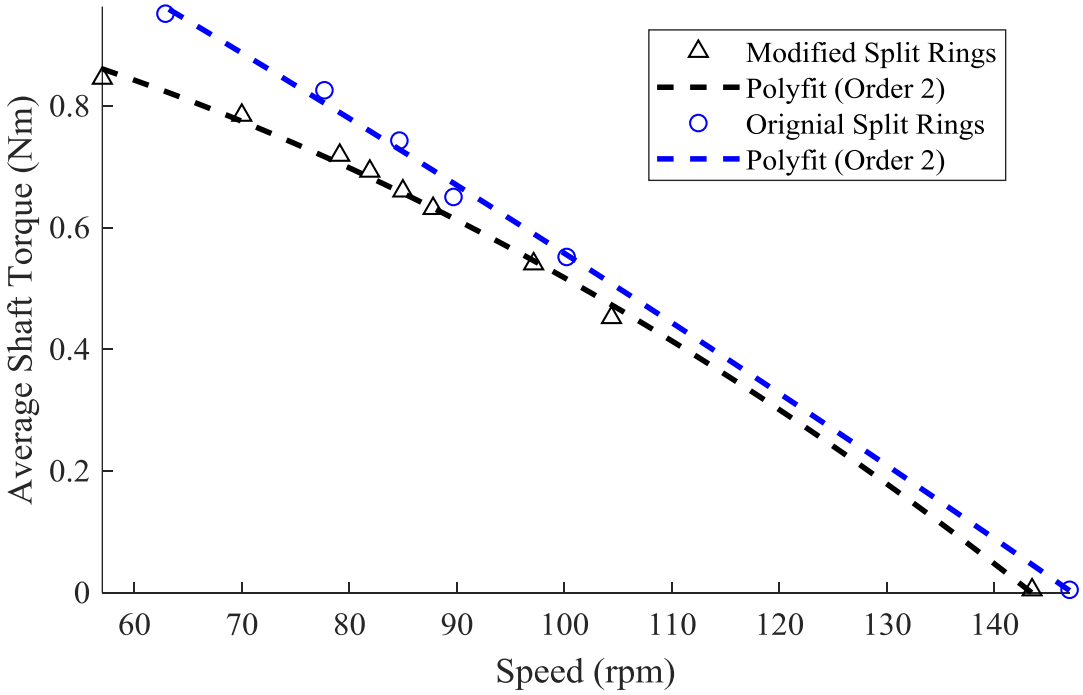


Figure 5.3 Applied torque and corresponding operating speed of the EP-1 for a compression ratio of 1.165 before and after split ring changes.

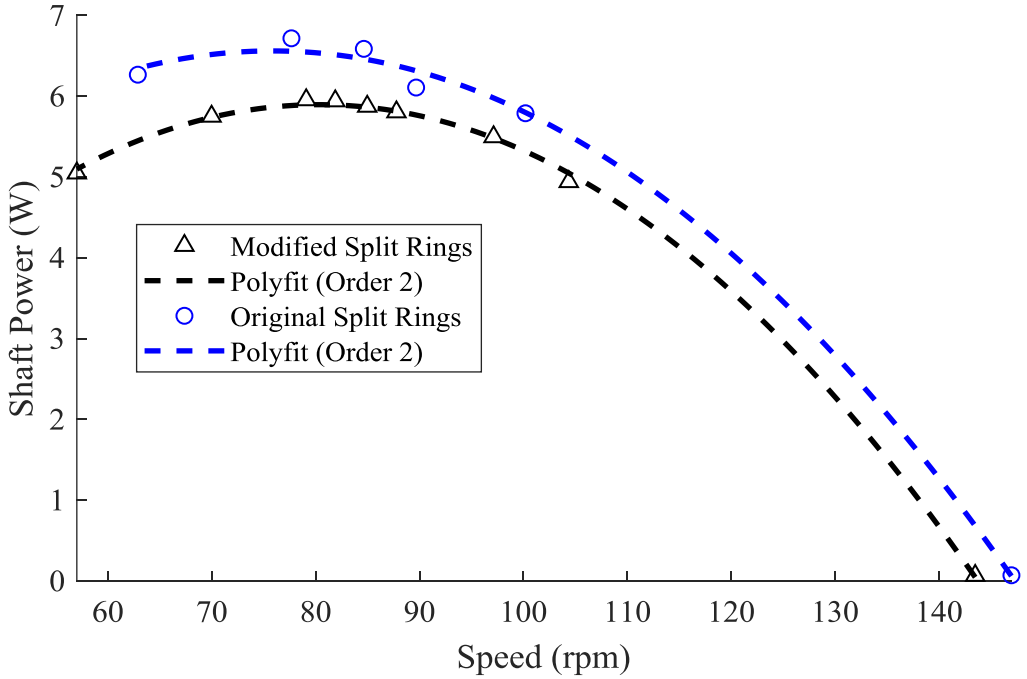


Figure 5.4 Shaft power and corresponding operating speed of the EP-1 for a compression ratio of 1.165 before and after split ring changes.

The operating speed for various applied torques when a compression ratio of 1.165 and 1.206 was used with the modified split rings is displayed in Figure 5.5. The same weights were used to provide an applied torque for both compression ratios but did not result in the same applied torques. This suggests the coefficient of kinetic friction in the loading mechanism is speed dependent. The larger compression ratio, 1.206, produced a slower free running speed. However, at larger torque values applied it had a higher operating speed. The modified split rings allowed the EP-1 to run at all compression ratios without the split rings becoming unaligned, but the engines performance was decreased relative to the original split rings

Limited data was sampled for the 1.206 compression ratio, for two reasons. The thermal source heat exchanger was only able to keep the inlet water temperature above 94 °C for operating speeds smaller than 85 rpm. This maximum operating speed, limited by the thermal source water bath, was much lower than previously tested compression ratios. Higher applied torque values were required to reduce the operating speed for the larger compression ratio. These higher applied torques were not initially tested because they were coming close to the end of the range of the torque measurement sensor. To go to higher applied torques, without risking damaging the torque sensor, a torque limiting coupler was installed.

The increased heating requirements of the engine at this compression ratio is most likely caused by the amplified cooling effect imparted on the working fluid produced by the larger volume change of the work space. West [22] refers to this as an adiabatic loss. Generally, for higher compression ratios this loss becomes larger. This is because of the larger pressure change caused by the larger compression ratio. The larger pressure change lead to a larger temperature change of the working fluid. The working fluid is cooled by the increase in the volume during the expansion stroke and heated by the decrease in the workspace volume during the compression stroke.

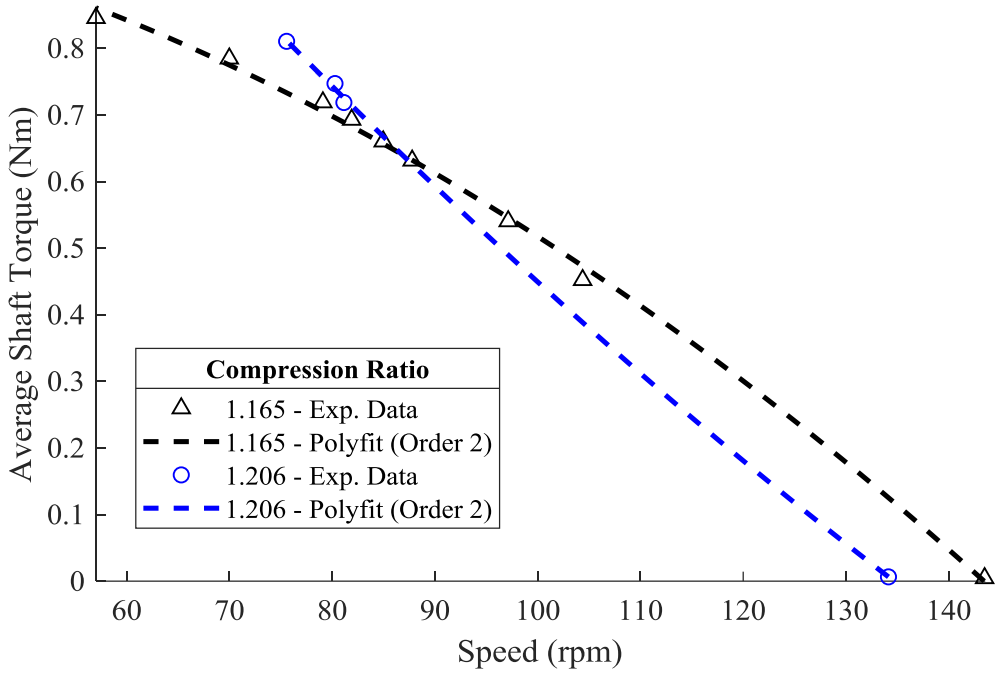


Figure 5.5 Average torque applied to the EP-1 and the resulting operating speed.

The shaft power for compression ratios of 1.165 and 1.206 for various applied torques with the modified split rings is presented in Figure 5.6. A maximum shaft power was not found for the maximum compression ratio tested. Therefore, higher applied loads were required.

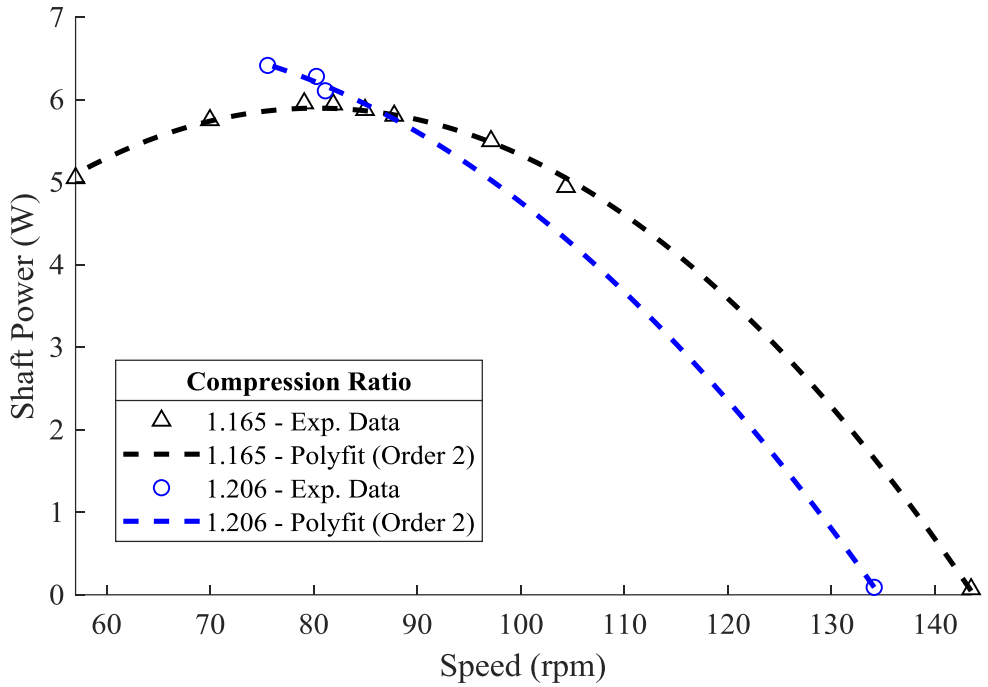


Figure 5.6 Shaft power of the EP-1 for various compression ratios and operating speeds with internal and external split rings.

Several lessons were learned from the initial compression ratio experiments. The thermal source water bath did not have a high enough heating capacity to keep up with the heat input required by the EP-1. The heat input rate required by the EP-1 was both dependent on the operating speed and the compression ratio used. The original split rings had to be modified so all compression ratios could be tested. These modifications decreased the performance of the engine. The torque required to find a maximum shaft power was close to the limit of the torque sensor. Therefore, a torque limiting coupler was installed to reduce the risk of damaging it. With all the lessons learned, the EP-1 was modified so that all compression ratios could be tested, and a maximum shaft power could be determined.

## 5.3 Compression Ratio – Optimization

The operating parameters used throughout the following tests are presented in Table 5.4. The operating parameters were chosen based on the initial testing completed.

Table 5.4 Operating parameters used for compression ratio optimization.

| Parameter | Value and Unit |
|---|---|
| Thermal Source Heat Exchanger Position | Top |
| Power Piston Position | Expansion Space |
| Compression Ratios | 1.144, 1.165, 1.186, and 1.206 ± 0.006 |
| Phase Angle | 90 ± 1° |

For the various torques applied, the corresponding operating speeds are presented in Figure 5.8. Not all operating points were tested for the minimum compression ratio of 1.114 because a component of the crankshaft came loose and stalled the engine during the experiment. Based on the data collected, it was found that the performance was worse than the other compression ratios tested, so the test was not repeated. As the compression ratio was increased, the free running speed decreased. For larger applied loads, the larger compression ratios had higher operating speeds. However, this was not the trend throughout all applied loads. As the applied load was decreased, the corresponding operating speed for the three largest compression ratios converged.

The cycle torque fluctuations for the maximum applied torque for a compression ratio of 1.206 is displayed in Figure 5.8. The torque fluctuations are found to leave the calibrated range of the sensor, 0 to 1 Nm. No higher torques were applied to the EP-1, to limit torque measurements outside the calibrated range and to limit applying torques in the over-torque protection range of the sensor. The torque fluctuations were found to consistently repeat every cycle.

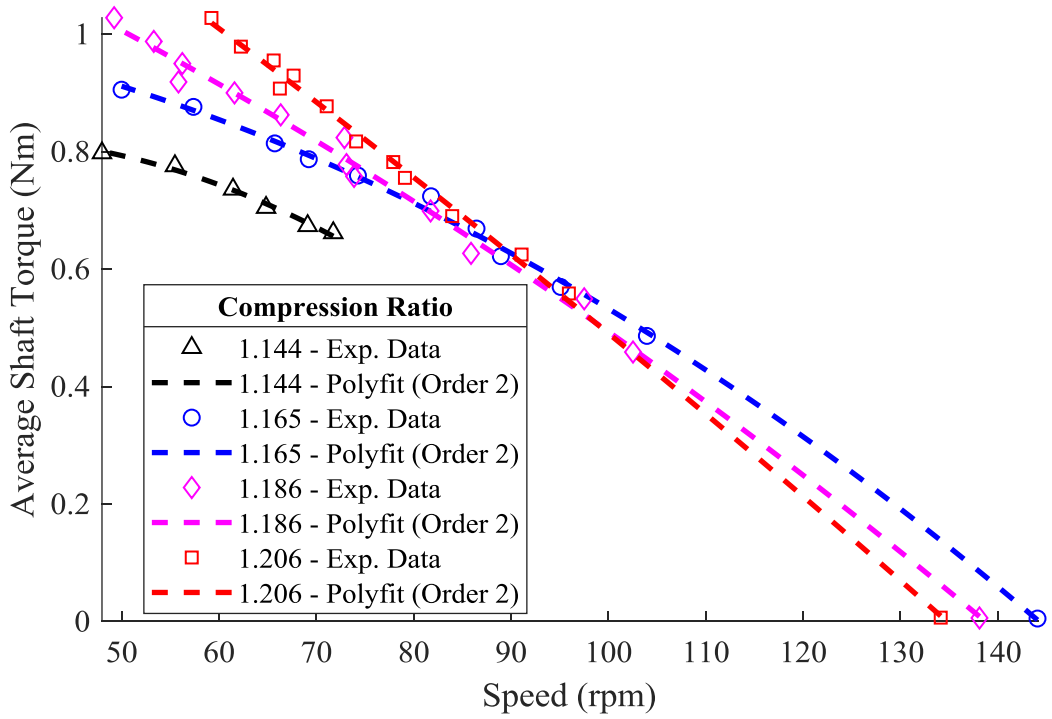


Figure 5.7 Applied torque and operating speeds of the EP-1 for various compression ratio.

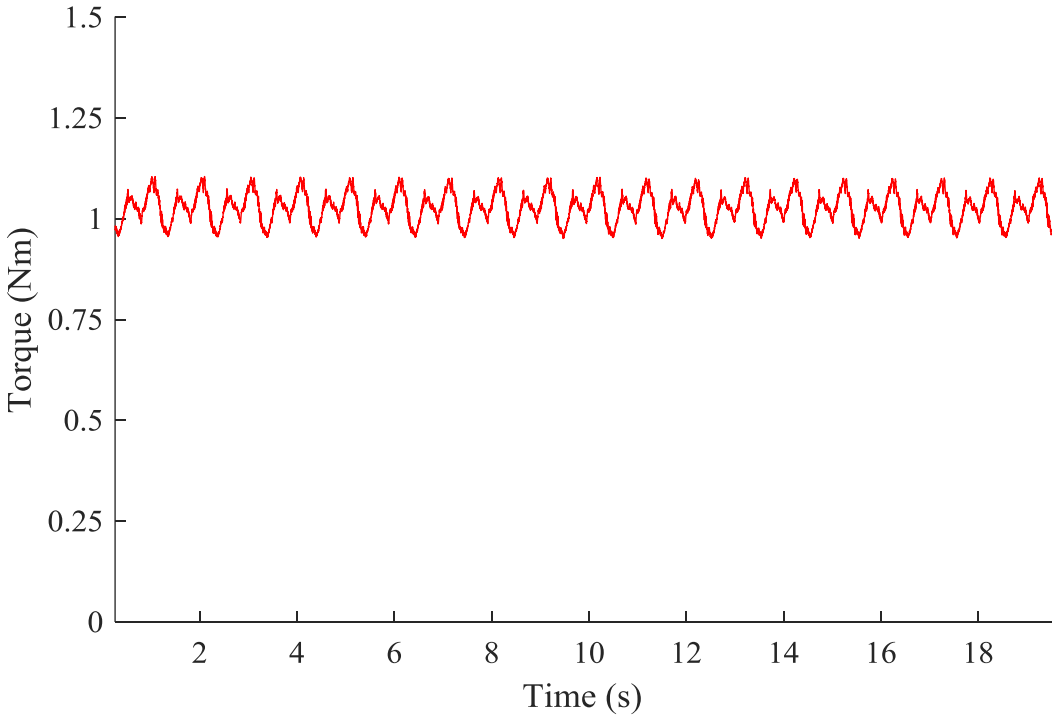


Figure 5.8 Torque fluctuations for the maximum applied load and a compression ratio of 1.206.

Figure 5.9 displays the shaft power and operating speed for the applied torques discussed above. The maximum compression ratio tested, 1.206, produced the maximum shaft power 6.58 ± 0.09 watts at an operating speed of 67.7± 0.3 rpm. The point occurred at approximately 50 % of the free running speed. A global maximum shaft power was not found, and it appears that the compression ratio could be increased even more to increase shaft power further.

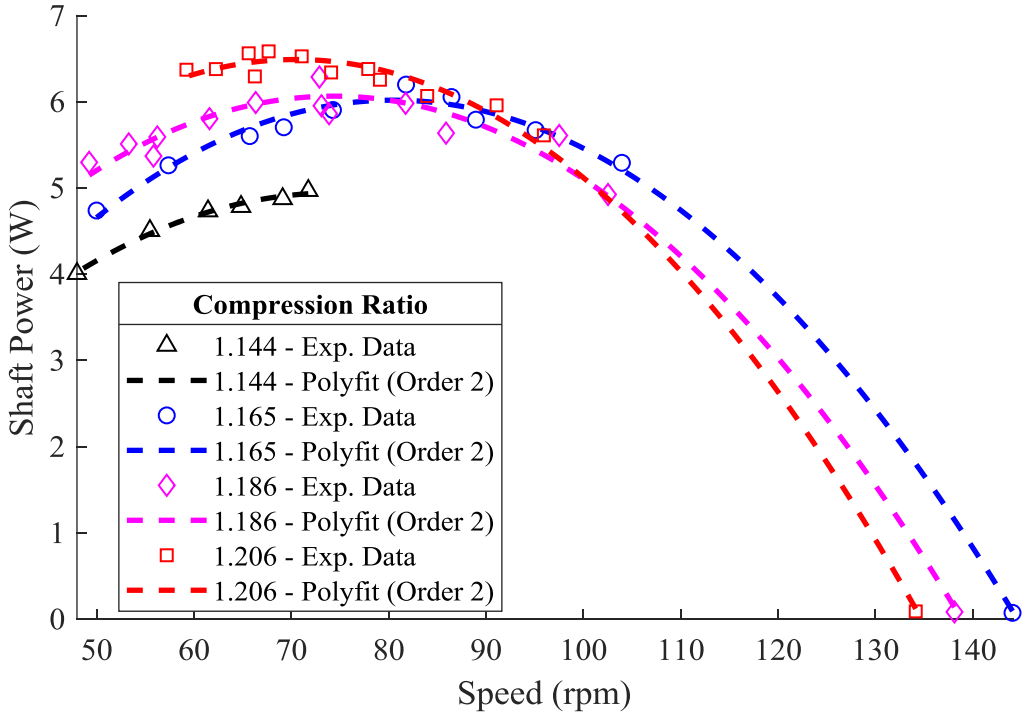


Figure 5.9 Shaft power of the EP-1 for various compression ratio and operating speeds.

A performance evaluation was completed for various compression ratios. A local maximum shaft power was found for the largest compression ratio possible with the power piston system. A global shaft power was not found and would require a power piston that could produce larger compression ratios. The maximum free running speed did not correspond to the compression ratio which produced the maximum shaft power. Therefore, the free running should not be used to estimate the compression ratio that could produce the maximum shaft power.

## 5.4 Phase Angle

To validate the choice of using a phase angle of 90° for the compression ratio optimization tests, the phase angle and applied loads were varied, and the shaft power was determined. Five different torque loads were applied to the EP-1 for one specific phase angle and the shaft power was measured. The phase angle was then changed, and the same loads were applied. The five loads were chosen based on two criteria: They had to cause the engine to run at a low enough speed so that the thermal source heat exchanger water inlet temperature did not drop below 94 °C, and they had to be a small enough that they could be tested at all the phase angles. The loads chosen were found by testing the EP-1 at the smallest phase angle of 60°. The phase angles tested, and the other operating parameters used, are tabulated in Table 5.5.

Table 5.5 Operating parameters used for phase angle optimization.

| Parameter | Value and Unit |
|---|---|
| Thermal Source Heat Exchanger Position | Top |
| Power Piston Position | Expansion Space |
| Compression Ratios | 1.206 ± 0.017 |
| Phase Angle | 60, 70, 75, 80, 85, 90, 100, 110 ± 1° |

The shaft power caused by the 5 different applied loads for each phase angle is shown in Figure 5.10. Expectedly, the phase angle of 90° produced the maximum shaft power. Unexpectedly, the shaft power did not necessarily decrease steadily for phase angle smaller or larger than 90°. A secondary peak was found for a phase angle of 70°. All the loads could not be tested for a phase angle of 110° as four of the loads caused the engine to stall. Phase angles greater than 90° performed significantly worse than phase angles less than 90°.

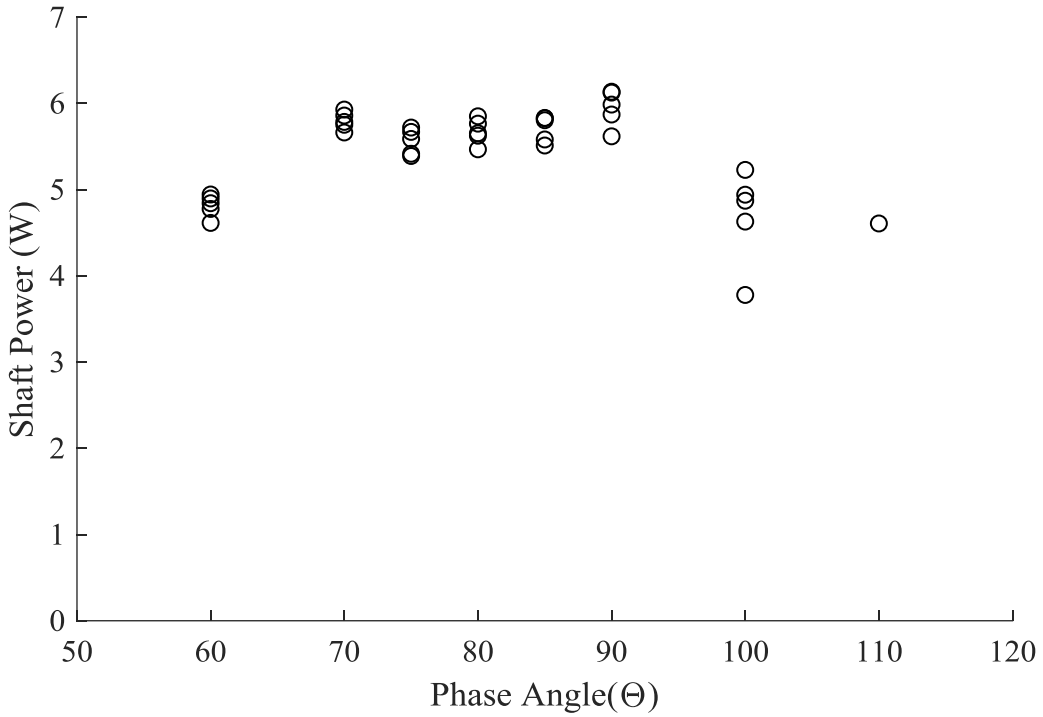


Figure 5.10 EP-1 shaft power at optimal compression ratio for same applied load at various phase angles.

## 5.5 Heat Exchanger Position

To validate the use of the hot heat exchanger on the top, which corresponds to the power piston connecting to the expansion space, tests were performed that varied the heat exchanger positions to find the influence on the shaft power. Depending on the location of the heat exchangers and which working space, the expansion or compression space, the power piston connects to, four configurations of the engine are possible. These configurations are listed in Table 5.6. The EP-1 is only able to be modified for configuration 1 and 2. This is because the power piston's location is fixed on the top of the EP-1's body. For the EP-1 to be modified so that configuration 3 and 4 could be tested, one of two modifications must be made. Either the power piston would have to have the ability to be removed and installed on the bottom of the EP-1's body, or the entire engine would have to be able to be flipped upside down.

Table 5.6 Possible configuration of the EP-1 based on the thermal source heat exchanger and power piston location.

| Power Piston Heat Exchanger Configuration | Thermal Source Heat Exchanger Position | Thermal Sink Heat Exchanger Position | Power Piston Working Space Connection |
|---|---|---|---|
| 1 | Top | Bottom | Expansion |
| 2 | Bottom | Top | Compression |
| 3 | Top | Bottom | Compression |
| 4 | Bottom | Top | Expansion |

The following tests use the operating parameters listed in Table 5.7. These tests were performed after the engine had been modified by a fellow researcher for testing a different configuration. Therefore, the results provided below cannot be directly compared to the phase angle and compression ratio tests discussed above. They instead act as a self-contained relative performance evaluation and validation for the use of a specific power piston heat exchanger configuration. The phase angle of 90° and a compression ratio of 1.206 were chosen because, as discussed above, they produced the maximum shaft power. When the location of the heat exchanger was changed, the rotation direction of the crank shaft had to be reversed for the engine to operate.

Table 5.7 Operating parameters used for power piston position optimization.

| Parameter | Value and Unit |
|---|---|
| Power Piston Heat Exchanger Configuration | 1 and 2 |
| Compression Ratios | 1.206 ± 0.017 |
| Phase Angle | 90 ± 1° |

Figure 5.11 shows the applied torque and the corresponding operating speed for both power piston heat exchanger configurations tested. The reduction in speed seen by configuration 2 for the same applied loads in configuration 1 could be caused by multiple factors. In configuration 2, the hot working fluid resided on the bottom of the engine, with the cold working fluid residing on the top. The buoyancy difference between the two fluids could have caused issues, with the hot fluid wanting to rise and the cold fluid wanting to fall. In configuration 1, the bellow was in contact with the hot working fluid which caused the bellow to heat up. This caused the bellow to become more flexible, and this could potentially have reduced the work required to move the bellow through one cycle. In contrast, when configuration 2 was tested, the bellow was in contact with the colder working fluid and therefore it became more rigid. This could have increased the work required to move the bellow throughout a complete cycle.

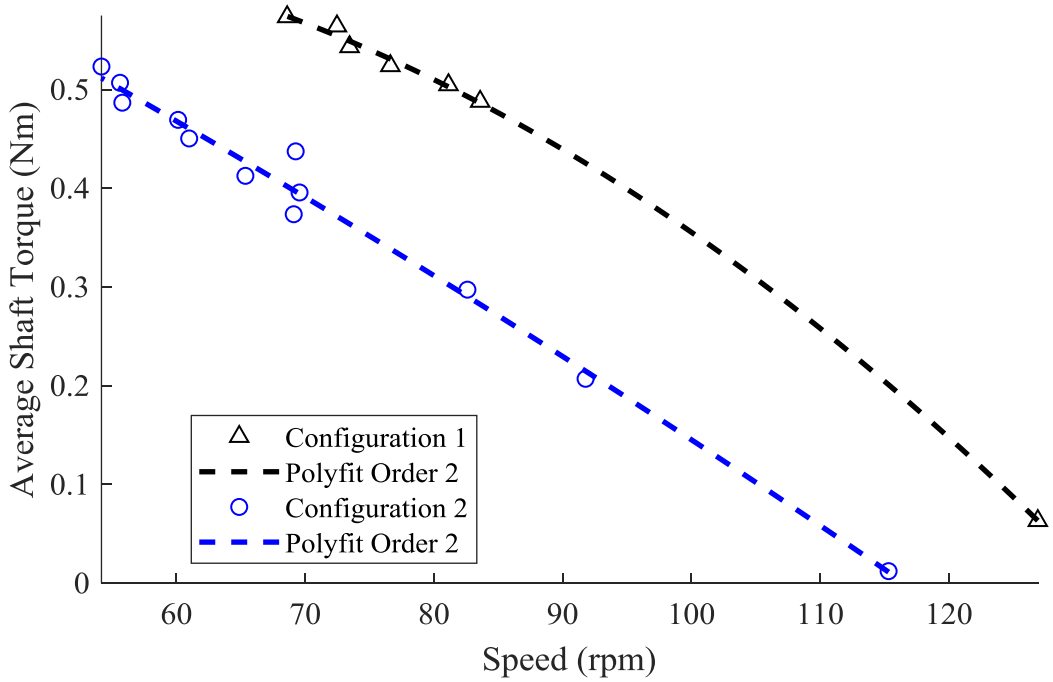


Figure 5.11 EP-1 shaft power at optimal compression ratio for same applied load at various phase angles.

The difference between the shaft power caused by the different power piston heat exchanger configurations is presented in Figure 5.12. Configuration 1 was found to produce a higher shaft power for all operating speeds when compared to configuration 2. The maximum shaft power of configuration 1 is less than the previously determined maximum shaft power when the same operating parameters were used for the compression ratio optimization tests. This may be caused by the modifications that were made to the engine between these tests and the compression ratio optimization tests. For this reason, these results should be taken as relative performance evaluation between the two configurations and not a comparison of shaft power before and after modifications were made to the engine.

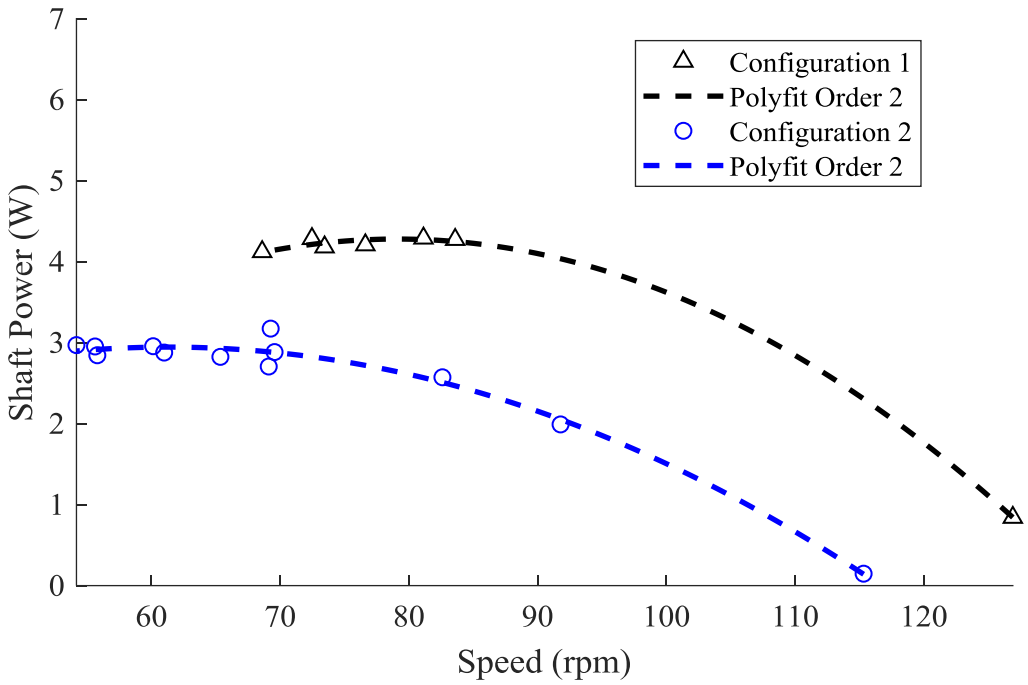


Figure 5.12 EP-1 shaft power at optimal compression ratio for same applied load at various phase angles.

The use of the specific configuration of the heat exchanger and power piston location was validated. The cause of the reduction in performance caused by the different configurations can only be speculated. To draw valid conclusions, tests that utilize all four configurations are required.

## 5.6 Maximum Shaft Power Configuration

Based on the validation provided by the phase angles and power piston heat exchanger configuration tests, the compression ratio optimization tests were used to determine the maximum shaft power possible with the modified split rings for the EP-1. The operating parameters of the configuration of the EP-1 that produced the maximum shaft power are tabulated in Table 5.8.

Table 5.8 Operating parameters for maximum shaft power.

| Parameter | Value and Unit |
|---|---|
| Thermal Source Heat Exchanger Position | Top |
| Power Piston Position | Expansion Space |
| Compression Ratios | 1.206 ± 0.017 |
| Phase Angle | 90 ± 1° |

The indicator diagram for the point of maximum shaft power produced is presented in Figure 5.13. The standard uncertainty in the volume and pressure is plotted at every 350$^{th}$ value. With the standard uncertainty applied, it can be seen how much the indicator diagram could vary. The figure also shows the mean cycle pressure is less than but very close to the buffer pressure.

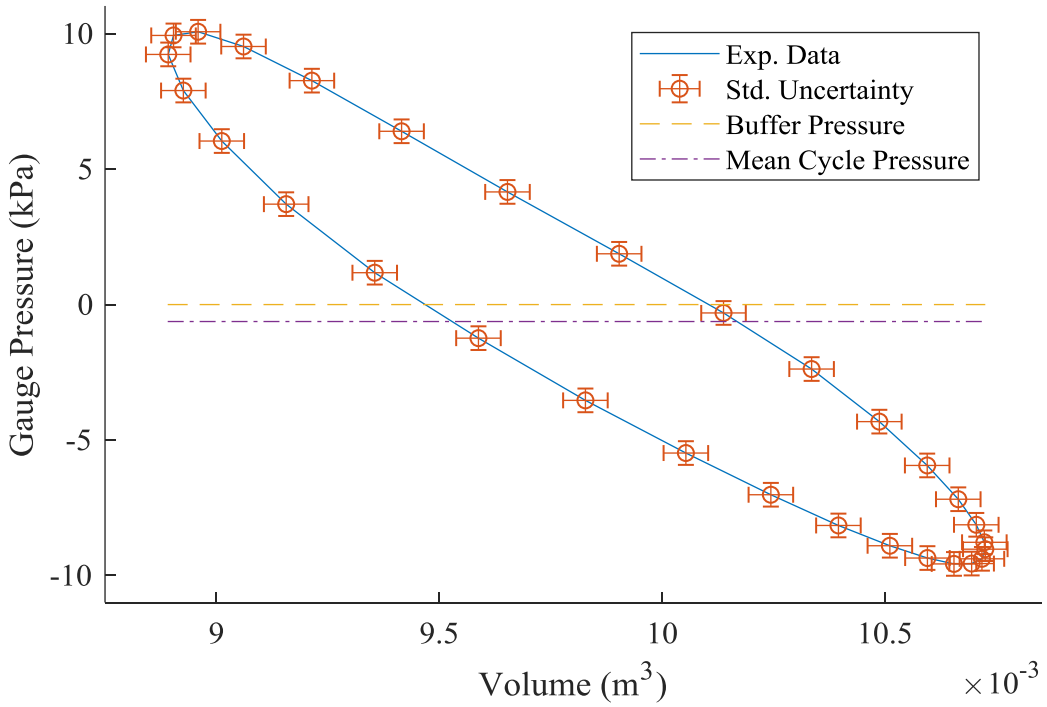


Figure 5.13 Plot of performance load curves for various compression ratios.

The outputs, excluding the shaft work, that are determined from the indicator diagram are presented in Table 5.6. Because of the standard uncertainty of the pressure and the volume, the standard uncertainty in the indicated work, forced work, and mechanism effectiveness is quite high. Therefore, the shaft power should be strictly used to evaluate the performance

Table 5.9 Values derived from the engine cycle and indicator diagram for various compression ratios.

| Indicated Work (J/cycle) | Forced Work (J/cycle) | Shaft Work (J/cycle) | Mechanism Effectiveness (-) |
|---|---|---|---|
| 9.3 ± 3.7 | 4.4 ± 0.5 | 5.83 ± 0.04 | 0.81 ± 0.20 |

The shaft power and operating speed loaded curve that produced the maximum shaft power is presented in Figure 5.14. The maximum shaft power of 6.58 ± 0.09 watts occurred at an operating speed of 67.7± 0.3 rpm. The point occurred at approximately 50 % of the free running speed.

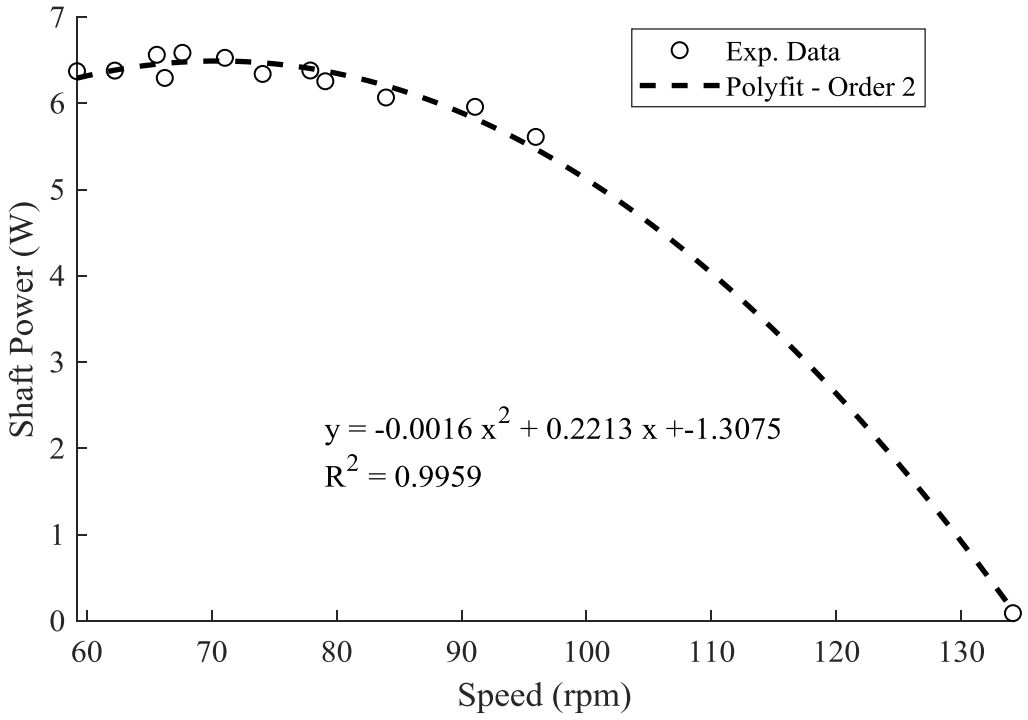


Figure 5.14 Shaft power of the EP-1 for its configuration that produced the maximum shaft power.

Figure 5.15 shows the thermal efficiency of the EP-1 for its maximum shaft power configuration. The thermal efficiency is found to increase for slower operating speeds. However due to the large uncertainty in the measurement, conclusions cannot be drawn. The large uncertainty is caused by the small temperature drop of the water across the inlet and outlet of the thermal source heat exchanger. The uncertainty in the thermal efficiency could be decreased by reducing the mass flow rate of water through the heat exchangers. The reduction in the mass flow would result in a larger temperature drop across the inlet and outlet. However, if the temperature leaving the thermal source heat exchanger was smaller, the heat transfer rate to the working fluid could also drop, which could reduce the shaft power of the engine. Therefore, since the goal was to optimize the shaft power and not thermal efficiency the water baths were operated at their maximum flow rate.

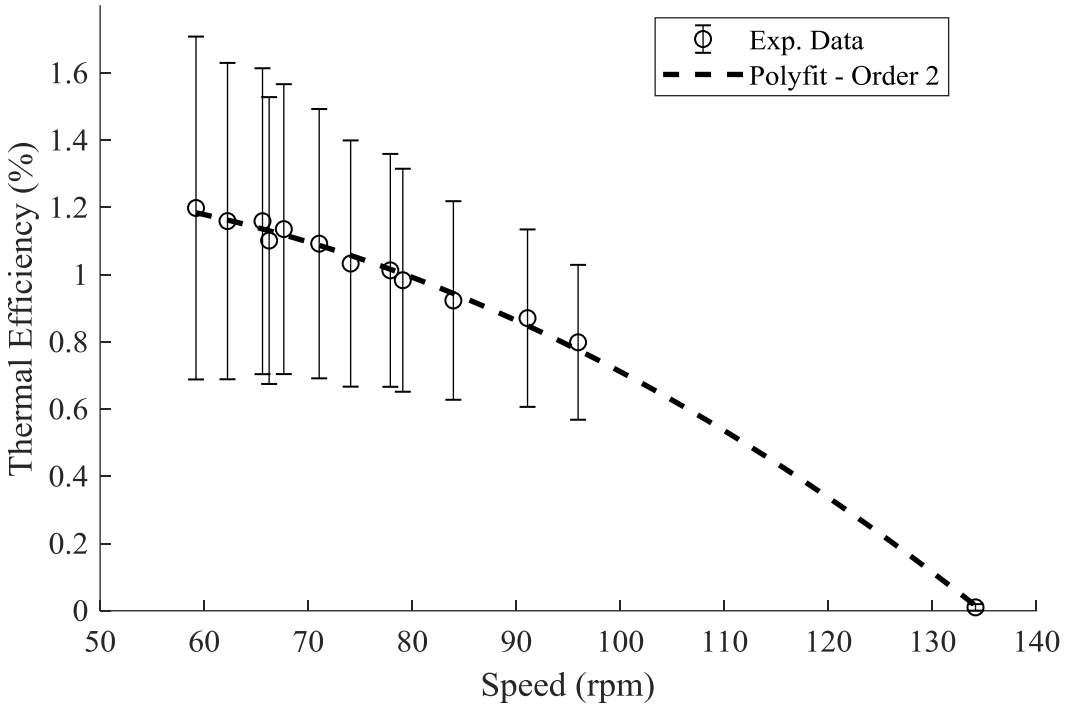


Figure 5.15 Thermal efficiency of the EP-1 for its configuration that produced the maximum shaft power.

## 5.7 Performance Comparison

The performance of the EP-1 was compared to other LTDSEs that used a temperature difference between the thermal source and sink of less than 150 °C. The West number was used for this comparison since the temperature difference used by each LTDSE was different.

In Table 5.10, the operating parameters used by the LTDSEs that were the manipulated variables used to optimize the shaft power of the EP-1 are presented. All the LTDSEs used a phase angle of 90° except the Ringbom. Ringbom Stirling engines do not have a constant phase angle since the displacer piston is not kinematically linked to the power piston. The power piston was connected to the compression space for all the engines except the ones presented in thesis and the Ringbom. The Ringbom power piston was connected to the half way point between the thermal source and sink flat plate heat exchangers. Only the Two Engine LTDSE and Mark 2 and EP-1 had the thermal source heat exchanger located on top.

Table 5.10 Operating parameters used to produce the maximum shaft power.

| Name and Reference | $CR_{exp}$ | Phase Angle (α) | Power Piston Location | Power Piston Connection | Thermal Source Heat Exchanger Location |
|---|---|---|---|---|---|
| Ringbom [41] | ≤ 1.214* | NA | Top | N/A | Bottom |
| 300 Watt [42], [47], [48] | 1.271 | 90 | Top | Compression | Bottom |
| Two Piston [43] | ≤ 1.140* | 90 | Top | Compression | Bottom |
| Two Engine [44] | ≤ 1.080* | 90 | Bottom | Compression | Top |
| Four Piston [45] | ≤ 1.181* | 90 | Top | Compression | Bottom |
| MDF Displacer [49] | 1.235 | 90 | Top | Compression | Bottom |
| EP-1 | 1.206 | 90 | Top | Expansion | Top |
| Mark 2 | 1.097 | 90 | Top | Expansion | Top |

* The compression ratio was calculated assuming the minimum engine volume was equal to the displacer piston swept volume, and the maximum equal to the summation of both pistons swept volume.

The operating parameters used to calculate the West number for each LTDSEs discussed above are presented in Table 5.11. All the engines were non-pressurized and utilized the atmosphere as the buffer pressure. However, the mean cycle pressure was not provided. Senft [96] used a mean cycle pressure of 1 bar, 98.7 kPa, for the calculation of the Beale number for non-pressurized engines. Therefore, if the mean cycle pressure was not provided, it was assumed to be 98.7 kPa.

Table 5.11 Operating parameters of experimental LTDSEs used to calculate the West number.

| Name and Reference | Source Temperature (°C) | Sink Temperature (°C) | Mean Cycle Pressure | Shaft Power (W) | Speed (rpm) | Power Piston Swept Volume ($m^3$) |
|---|---|---|---|---|---|---|
| Ringbom [41] | 90 | 10 | 98.7 kPa* | 0.69 | 113 | 0.00015 |
| 300 Watt [42], [47], [48] | 130 | 15 | 98.7 kPa* | 146 | 143 | 0.0251 |
| Two Piston [43] | 163 | 34 | 98.7 kPa* | 1.69 | 52.1 | 0.000894 |
| Two Engine [44] | 110 | 25 | 98.7 kPa* | 0.27 | 14 | 0.001168 |
| Four Piston [45] | 166 | 34 | 98.7 kPa* | 6.1 | 20 | 0.007392 |
| MDF Displacer[49] | 160 | 25 | 98.7 kPa* | 3.1 | 214 | 0.000154 |
| EP-1 | 95 | 2 | ≈ 92.5 kPa | 6.58 | 67.7 | 0.00184 |
| Mark 2 | 95 | 2 | ≈ 92.5 kPa | 0.26 | 27 | 0.000197 |

*Assumed be 1 bar, 98.7 kPa, for non-pressurized engines [97]

Other engines were also found that provided the required information for calculation of the West number, but they did not provide other operating parameters such as the compression ratio, phase angle, or power piston location. These gamma type LTDSEs and their operating parameters used to calculate the West number are tabulated in Table 5.12.

Table 5.12 Operating parameters of experimental LTDSEs used to calculate the West number.

| Name and Reference | Source Temperature (°C) | Sink Temperature (°C) | Mean Cycle Pressure | Shaft Power (W) | Speed (rpm) | Power Piston Swept Volume (m3) |
|---|---|---|---|---|---|---|
| ANL Engine [97] | 90 | 10 | 98.7 kPa | 0.7 | 100 | 0.00015 |
| Displacer – Standard [97] | 96 | 6 | 98.7 kPa | 0.642 | 105 | 0.00012 |
| Displacer – Regenerative [97] | 96 | 6 | 98.7 kPa | 1.05 | 123.78 | 0.00012 |
| L-27 [97] | 93 | 34 | 98.7 kPa | 0.252 | 270 | 0.000025 |

The calculated West numbers, sorted from lowest to highest, for each LTDSE, and the corresponding operation temperature difference of the thermal source and sink used, are provided in Table 5.13. A mean West number of 0.21 was calculated for LTDSEs. This is lower than the mean West number for HTDSE, 0.25. This could be caused by the smaller sample size of 12 used for the LTDSE West number compared to the 23 used by West [22] to calculate the mean West number for HTDSE. The Mark 2 produced a West number of 0.21 while the EP-1's West number was equal to 0.24. This means that the performance of the two engines is relatively average by LTDSE standard and worse than average by the HTDSE standard.

Table 5.13 West number sorted from lowest to highest and the corresponding temperature difference of the thermal source and sink for experimental LTDSEs.

| Name | Temperature Difference (°C) | West Number |
|---|---|---|
| Two Engine | 85 | 0.08 |
| Two Piston | 129 | 0.13 |
| Four Piston | 132 | 0.14 |
| 300 Watt | 90 | 0.20 |
| Ringbom | 80 | 0.20 |
| Mark 2 | 93 | 0.21 ± 0.02 |
| Displacer - Standard | 90 | 0.22 |
| ANL Engine | 80 | 0.23 |
| EP-1 | 93 | 0.238 ± 0.001 |
| L-27 | 59 | 0.26 |
| Displacer - Regenerative | 90 | 0.31 |
| MDF Displacer | 135 | 0.31 |

In Figure 5.16, the performance of experimental LTDSEs are compared to the EP-1 and Mark 2 using the West Number and the temperature difference of the thermal source and sink. It shows that having a high temperature difference doesn't necessarily result in a large West number.

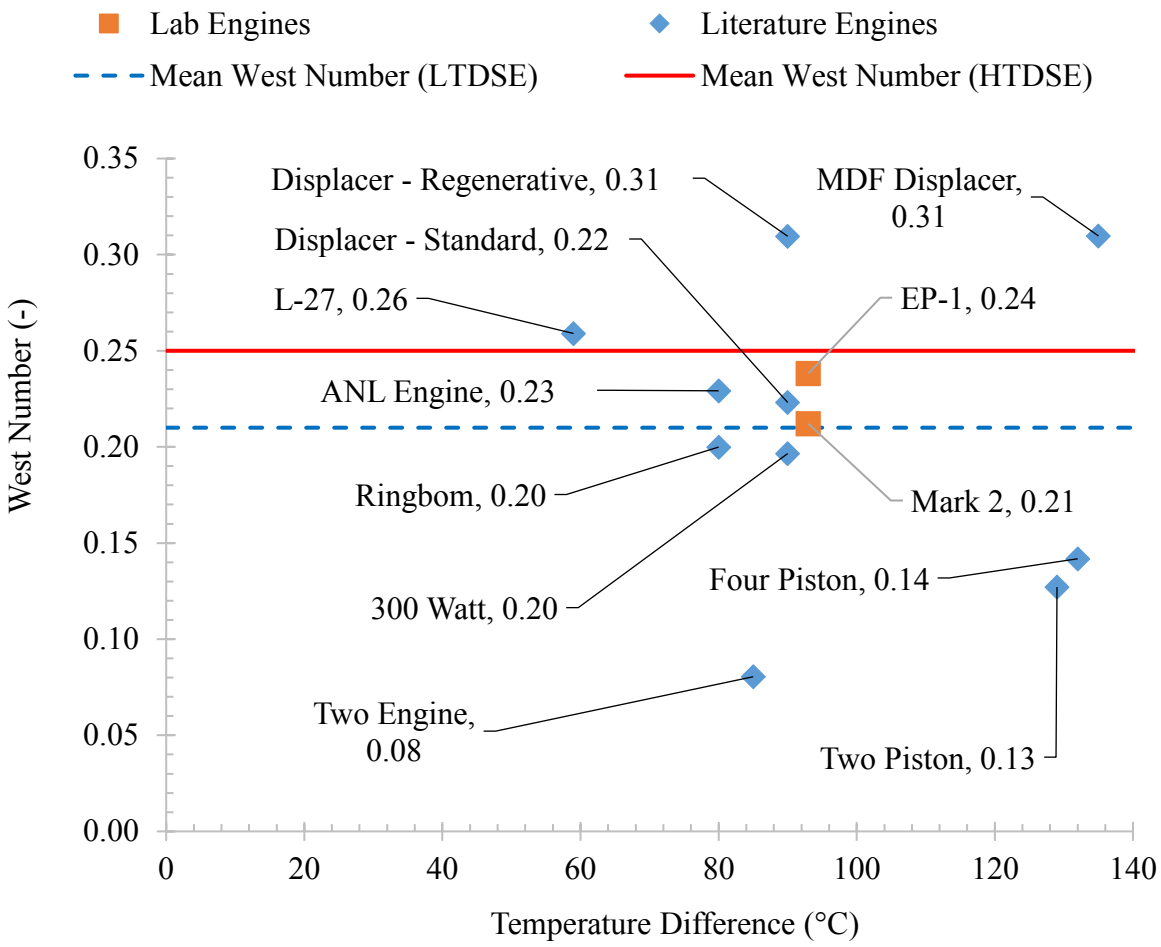


Figure 5.16 West number comparison of LTDSEs using a temperature difference less than 150 °C.

The maximum shaft power of the EP-1 was determined and was used to calculate the West number. It was then compared to the West number calculated for 12 different LTDSE. The EP-1's West number was found to be above average for LTDSE but below average for HTDSEs.

# Chapter 6 Compression Ratio Estimation

The validity of methods to determine the optimal compression ratio were investigated. Specifically, Kolin's compression ratio [29], Egas' ideal compression ratio [64], and Senft's optimum swept volume ratio [20] were compared against experimental results. A new method to determine the range of compression ratios that could result in the maximum shaft power for a LTDSEs is proposed based on the findings of this comparison and other finding found in the literature.

## 6.1 Kolin's Compression Ratio

Kolin's compression ratio was compared to the point of maximum shaft power for each of the four experimentally tested compression ratios. Kolin [29] stated that the compression ratio calculated using his method should be considered as an average value, and that the compression ratio should be varied according to the operating conditions used. Using Kolin's method with a temperature of the thermal source and sink of 95°C and 2 °C respectively, resulted in a calculated compression ratio of 1.085. Figure 6.1 compares this compression ratio to the four compression ratios tested and their corresponding point of maximum shaft power. Kolin's method resulted in a compression ratio that was smaller than the experimental compression ratios. Based on the decreasing maximum shaft power for smaller compression ratios, and that a compression ratio of 1 will not allow an engine to run, Kolin's method would result in compression ratio that would not result in the maximum shaft power. Based on the data presented, Kolin's method could act as a "lower bound" for compression ratios to be tested experimentally during a prototyping campaign.

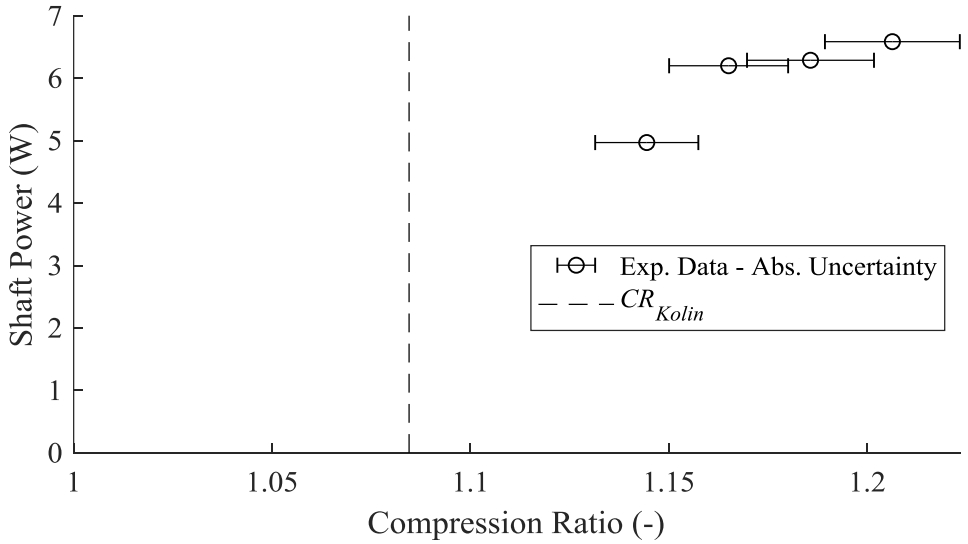


Figure 6.1 Comparison of Kolin's compression ratio to the points of maximum shaft power for various experimental compression ratios of the EP-1.

## 6.2 Egas' Ideal Compression Ratio

Two claims made by Egas [64] will be investigated. The first claim is that the ideal compression ratio proposed results in an optimum compression ratio that will extract the maximum work attainable. The second claim is that no engine should be designed with a compression ratio higher than the ideal compression ratio. Egas' ideal compression ratio is calculated from the temperature of the thermal source and sink. It could also be calculated using the average temperature of the working fluid in the expansions and compression space of an experimental engine. It can be calculated with these temperatures because of how the ideal compression ratio can be interpreted. For a gamma-type Stirling engine the ideal compression ratio represents a compression ratio where the displacer piston and power piston produce the same pressure change on the work space. The claims made by Egas will be tested by comparing the pressure change caused by the displacer piston only, to the pressure change caused power piston for various compression ratios. These results will then be compared to the shaft work determined from the compression ratio optimization tests in the previous chapter.

### 6.2.1 Displacer Piston

The cycle pressure change of the work space caused by the movement of the displacer piston only was determined. This was accomplished by removing the power piston, sealing the engine at constant volume, and then driving the displacer piston with an electric motor. The operating parameters used in the test are summarized in Table 6.1. Various operating speeds were tested to see if the pressure change caused by the displacer piston was dependent on speed. The operating speeds were chosen as they resulted in tests that did not cause the temperature of the water at the inlet of the thermal source heat exchanger to change throughout operation.

Table 6.1 Operating parameters used for displacer piston movement only tests.

| Parameter | Value and Unit |
|---|---|
| Thermal Source Heat Exchanger Position | Top |
| Compression Ratios | N/A |
| Operating Speeds | 20, 30, 40, 50, 60, 70, 80,90, and 100 rpm |

The pressure inside the work space throughout one cycle as a function of crank angle for the tested operating speeds is presented in Figure 6.2. The standard uncertainty in the 100-rpm test is shown for every 250$^{th}$ value. The figure shows that the difference in the workspace pressure for different operating speeds is quite small, and that the pressure profile does not significantly change for the tested operating speeds. It can be seen that the pressure change is not symmetric around the zero point, which may be caused by a preferential leak of the work space to the buffer space.

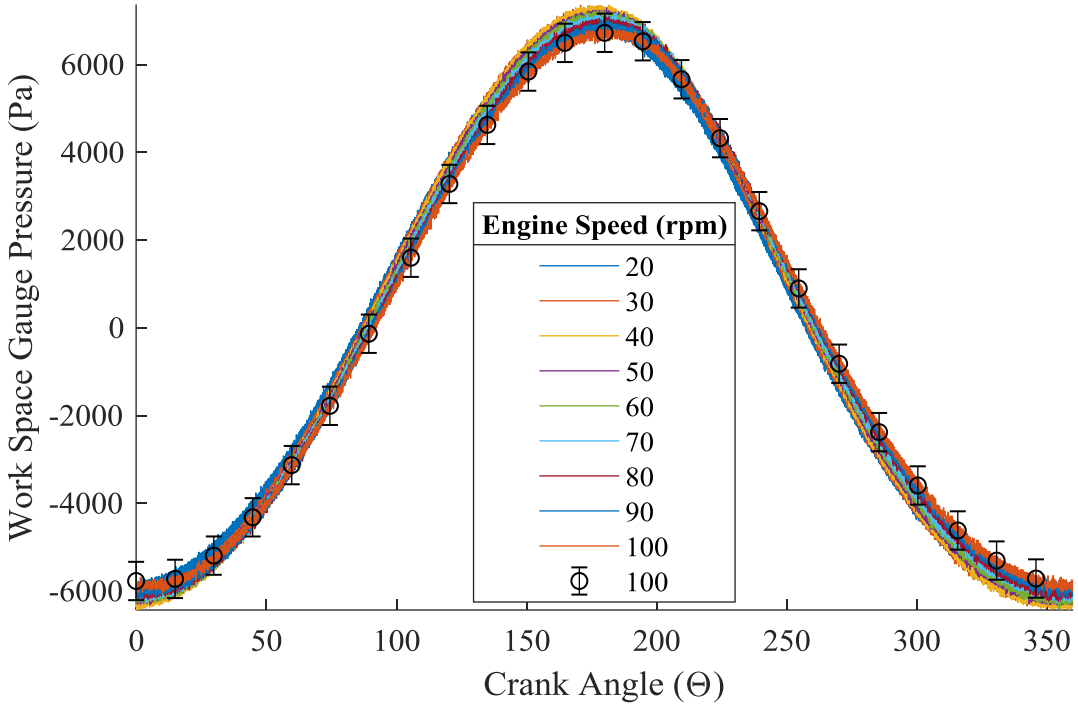


Figure 6.2 Gauge pressure of the work space over a complete cycle caused by the movement of the displacer piston for various controlled operating speeds.

To better visualize the data, presented in Figure 6.2 the pressure range of the workspace caused by the displacer piston motion for various speeds was calculated. The pressure range for one cycle was calculated by subtracting the maximum cycle pressure by the minimum cycle pressure. The pressure range was calculated for each cycle captured and then averaged. Figure 6.3 presents this data. It can be seen that the pressure range was dependent on speed but did not change significantly for the various speeds tested. The maximum pressure range occurred for a speed of 40 rpm but was not significantly larger than the pressure change at any other speeds. It was determined that

the pressure change of the workspace caused by the displacer piston only was approximately constant. Therefore, when comparing the pressure change caused by either piston, the operating speed should not matter.

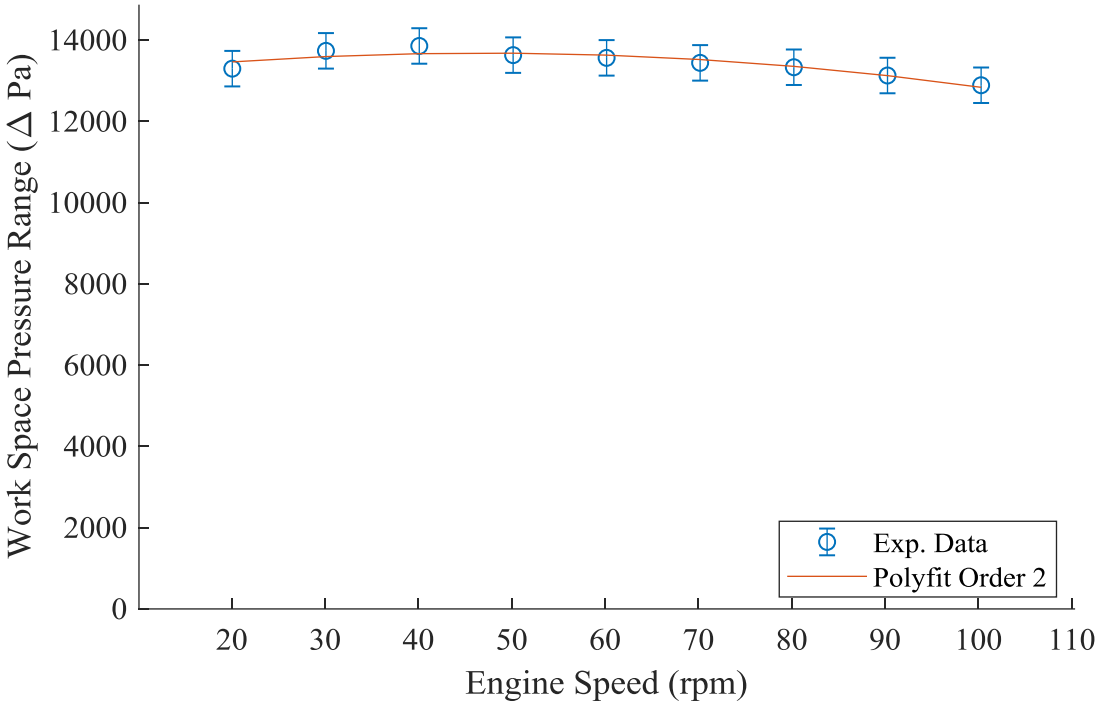


Figure 6.3 Range of the work space pressure caused by the movement of the displacer piston for various controlled operating speeds.

Since the pressure change of the workspace was seen to be relatively constant through various speeds the temperatures of the working fluid and the thermal source and sink for the same tests was investigated. The average temperature of the working fluid in the expansion and compression spaces, and the average temperature of the water at the inlet of both heat exchangers is presented in Figure 6.4. The average temperature in the expansion space and compression space is shown to be larger independent of speed. The average temperature of the compression space comes closer to equating the temperature of the thermal sink than the expansion space and the thermal source. This could be caused by the density change of the working fluid, with more heat being able to be transferred to the denser cold working fluid.

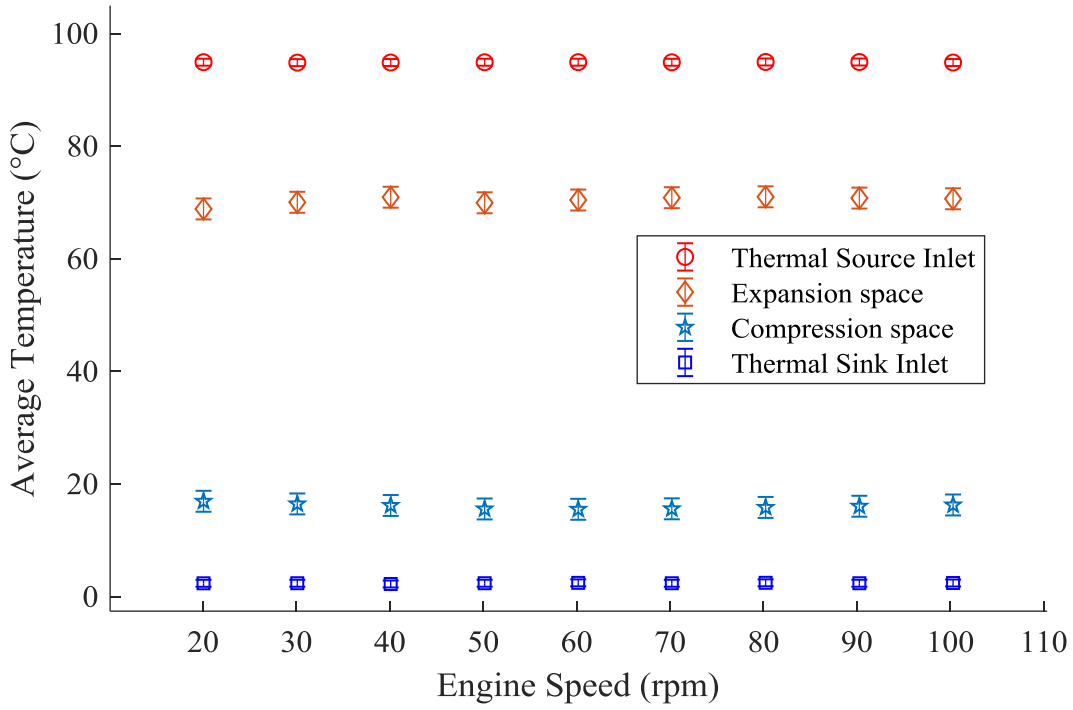


Figure 6.4 Average temperature of the working fluid in the expansion and compression space c, and the water of thermal source and sink heat exchanger at the inlet of the heat exchangers caused by displacer piston movement for various controlled operating speeds.

### 6.2.2 Power Piston

The cycle pressure change of the work space caused by the movement of the power piston only was determined so that it could be compared to pressure change caused by the displacer piston. This was accomplished by attaching the power piston, sealing the engine, and disconnecting the displacer piston from the crankshaft. The displacer piston was still contained within the working volume so that the minimum volume of the engine did not change. The water flow loop was disconnected from the heat exchangers, and then the power piston was driven with an electric motor. Table 6.2 tabulates the operating parameters used for the following tests. The power piston was only run at a speed of 30 rpm because the power requirement of moving the piston at high speeds was larger than the power output of the electric motor. To test the different compression ratios, the stroke length of the power piston was changed.

Table 6.2 Operating parameters used for power piston movement only test.

| Parameter | Value and Unit |
|---|---|
| Thermal Source Heat Exchanger Position | N/A |
| Compression Ratios | 1.144, 1.165, 1.186, and 1.206 |
| Operating Speeds | 30 rpm |

The pressure of the workspace through one complete cycle for various compression ratios is presented in Figure 6.5. The standard uncertainty of the pressure measurement is applied to every 750$^{th}$ value for the largest compression ratio tested. The pressure change caused by the displacer piston only for the 100-rpm test is also presented. The pressure change of the work space was found to increase for increasing compression ratio. The work space pressure change caused by the displacer piston for a speed of 100 rpm is shown to correspond very closely to the pressure change caused by the compression ratio of 1.144. If the ideal compression ratio is valid the compression ratios that produce a higher pressure change of the work space than the pressure change caused by the displacer piston only should result in less shaft work.

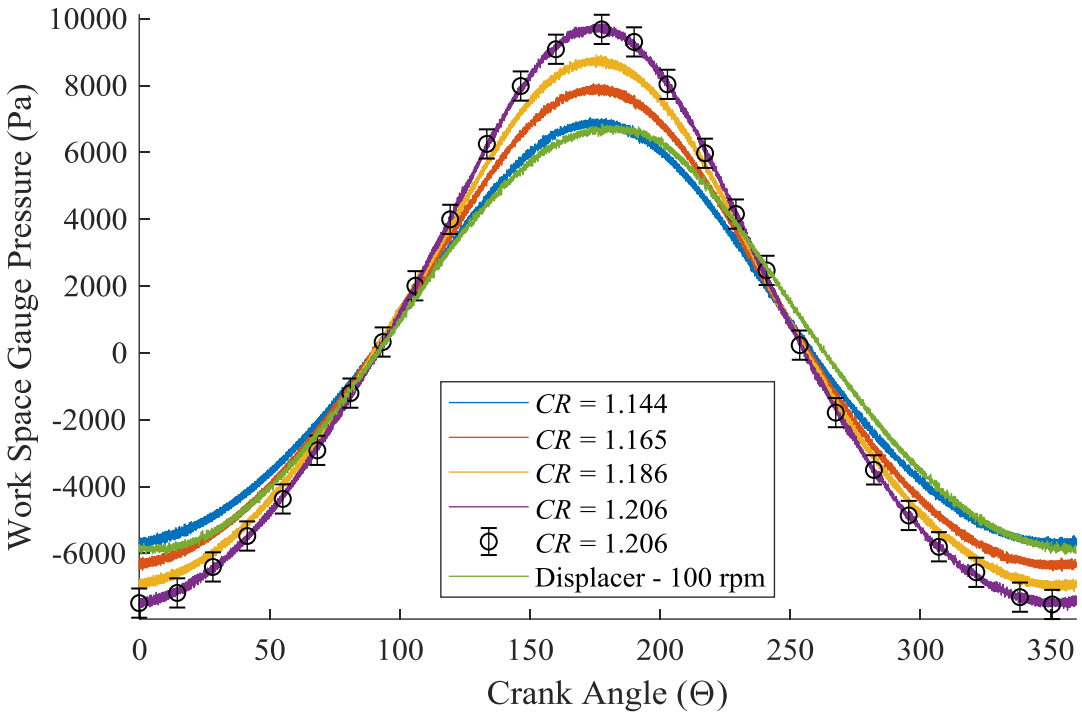


Figure 6.5 Gauge pressure of the work space over a complete cycle caused by the movement of the power piston for an operating speed of 30 rpm.

### 6.2.3 Discussion

The data required to check the validity of Egas' claims was determined. Based on the results in Chapter 5, it can be shown that the compression ratio that produces the maximum shaft power does not correspond to the one where the cycle pressure change caused by the displacer piston is equal to the cycle pressure change of the power piston. Contrary to Egas [64], having a compression ratio that is higher than the equal pressure change compression ratio is possible. This is because larger compression ratios result in larger indicated work. This larger indicated work can result in a corresponding higher shaft work at the expense of having to provide work into the system to combat the effects of an increase amount of forced work.

Figure 6.6 compares two calculated values for Egas' ideal compression ratios to the experimental compression ratios and corresponding maximum shaft powers of the EP-1. Egas' ideal compression ratio was calculated two ways. One way used the average temperature of the working fluid in the expansion and compression space of 67 °C and 21 °C, respectively. These temperatures were from the point of maximum shaft power using a compression ratio of 1.206. This method produced a compression ratio of 1.156. The other method used to calculate the ideal compression ratio used the temperature of the thermal source and sink of 95 °C and 2 °C respectfully and produced a compression ratio of 1.338. The ideal compression ratio calculated using the experimental gas temperatures is less than, but close to the experimental compression ratio that produced the maximum power. This method provides a better estimation than Kolin's method but is impractical. This is because it can only be used if the engine is already constructed and the temperatures of the working fluid are known. The ideal compression ratio calculated using the thermal source and sink is significantly higher than the tested compression ratios. The EP-1 was not tested at that high of a compression ratio as it was not possible with the power piston system. Based on the trend seen of the shaft power starting to level off for increasing compression ratios seen in Chapter 5, the ideal compression ratio should result in a smaller shaft power. This reduction is shaft power would be caused by the increase in the amount of forced work. Where Egas' ideal compression ratio calculated from the temperature of the thermal source and sink can be applied is as a theoretical "upper bound" for the compression ratio. This can be done because it is very difficult for the temperature of the working fluid to ever equate the temperature of the thermal source or sink.

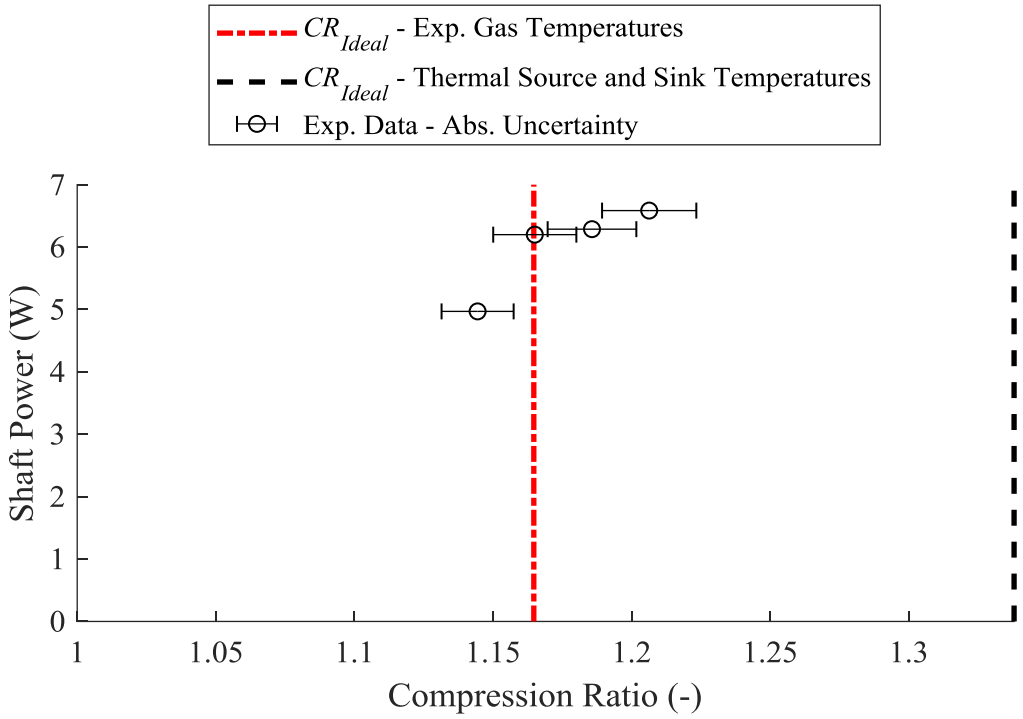


Figure 6.6 Comparison of Egas' ideal compression ratio the to the maximum shaft power points for various compression ratios of the EP-1.

## 6.3 Senft's Optimum Swept Volume Ratio

Senft's method to determine the optimum swept volume ratio was investigated. The validity of the method relies on how well the Schmidt model can predict the shape and size of the experimental indicator diagram. It also relies on how close the experimental parameters of the engine are to the assumptions made by the Schmidt model.

The two main assumptions of the Schmidt model that need be checked are the sinusoidal volume variations, and the heat transfer and temperature of the working fluid. The motion of the displacer and power piston are compared to sinusoidal motion in Figure 6.7. The instantaneous position of the pistons is nondimensionalized so that they can be compared. The motion of each piston was found to closely approximate sinusoidal motion, and therefore the assumption was assumed valid. In the Schmidt model, the working fluid immediately equates to the temperature of the thermal source or sink in the heat exchangers and expansion and compression spaces. Because of this, for the assumption to be valid, the temperature of the thermal source and sink used in the Schmidt analysis will be equal to the mean temperature of the working fluid in the expansion space and compression space, respectively.

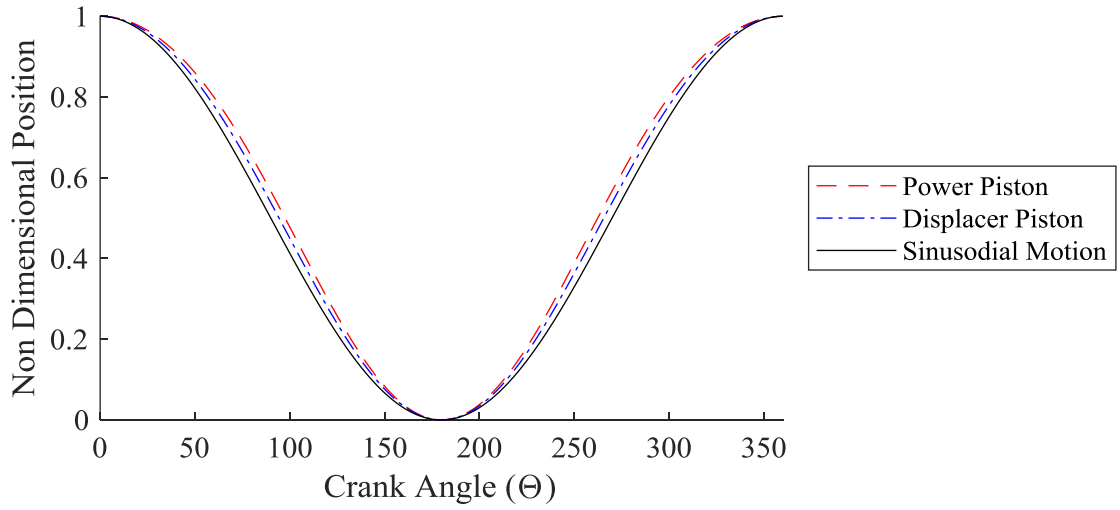


Figure 6.7 Comparison of the displacer and power piston motion so sinusoidal motion.

Figure 6.8 compares the indicator diagram produced by the EP-1 for its point of maximum shaft power to the indicator diagram produced by the Schmidt model. The Schmidt model used the

volumes of the EP-1, and the average temperature of the working fluid in the expansion and compression space of the engine. The experimental mean cycle pressure of the EP-1 was used to vary the mass in the Schmidt model until it had the same mean cycle pressure. The Schmidt model's indicator diagram produced a larger indicated work than the experimental diagram. This is caused by several factors. In the Schmidt model, the temperature of the working fluid in the compression and expansion space is constant, while the temperature varies in the experimental case. Also, the Schmidt model represents the maximum possible indicated work and neglects any thermodynamic losses that occur in actual Stirling engines. To better predict the indicator diagram, a higher order thermodynamic model that include transient heat transfer and thermodynamic losses could be used. However, all things considered, the indicator diagrams were found to have similar shapes which resulted in similar amounts of forced work.

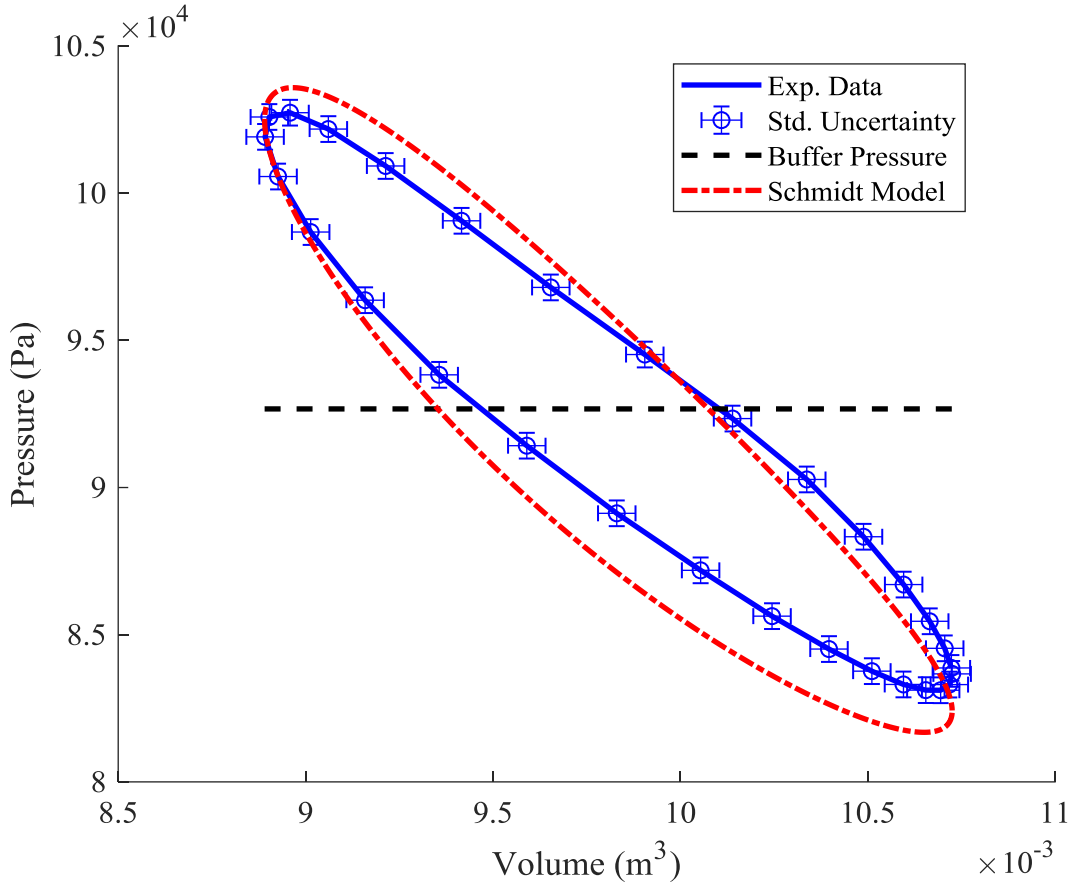


Figure 6.8 Comparison of the indicator diagrams between experimental data and the Schmidt model.

The values derived from the experimental and Schmidt indicator diagrams, and the fundamental efficiency theorem, are presented in Table 6.3. The experimental mechanism effectiveness was back-calculated from the experimental indicated work, forced work, and shaft work. This mechanism effectiveness was then used by the Schmidt model to determine the Schmidt shaft work. The large uncertainty in the indicated work produced a large uncertainty the experimental mechanism effectiveness. The indicated work produced by the Schmidt model is much larger that the experimental work most likely caused by the reasons discussed above. With this considered, Senft's method to determine the optimum swept volume ratio was used and assumed to produce results close to the experimental data.

Table 6.3 Values derived from the experimental and Schmidt indicator diagram.

| Method | Indicated Work (J/cycle) | Forced Work (J/cycle) | Shaft Work (J/cycle) | Mechanism Effectiveness (-) |
|---|---|---|---|---|
| Experimental | 9.3 ± 3.7 | 4.4 ± 0.5 | 5.83 ± 0.04 | 0.81 ± 0.20 |
| Schmidt | 12.4 | 4.7 | 8.3 ± 5.7 | 0.81 ± 0.20 |

Senft's method of varying the mechanism effectiveness and compression ratio is presented in Figure 6.9. The shaft work was determined by varying the compression ratio and the mechanism effectiveness using the model. A mechanism effectiveness of 0.75 produced a similar shaft work to the experimental shaft work. The mechanism effectiveness had a significant impact on the compression ratio that produced the maximum shaft work. For each mechanism effectiveness presented, a compression ratio that produces a maximum shaft work can be found. The Schmidt model is only able to predict the shaft work by using the indicated work, forced work, and mechanism effectiveness. Without the operating speed, the shaft power cannot be determined. Senft's method requires you to estimate the temperature of the working fluid in the expansion and compression space, the mean cycle pressure, and the engine volumes to produce results. Because of all the information required and the assumptions made by the Schmidt model, Senft's method only really provides an order of magnitude approximation of a Stirling engine's performance. The most important things to take away from Senft's method are the role of forced work, the requirement for high mechanism effectiveness to produce a high shaft work, and that a compression ratio that produces a peak shaft work should always be able to be found.

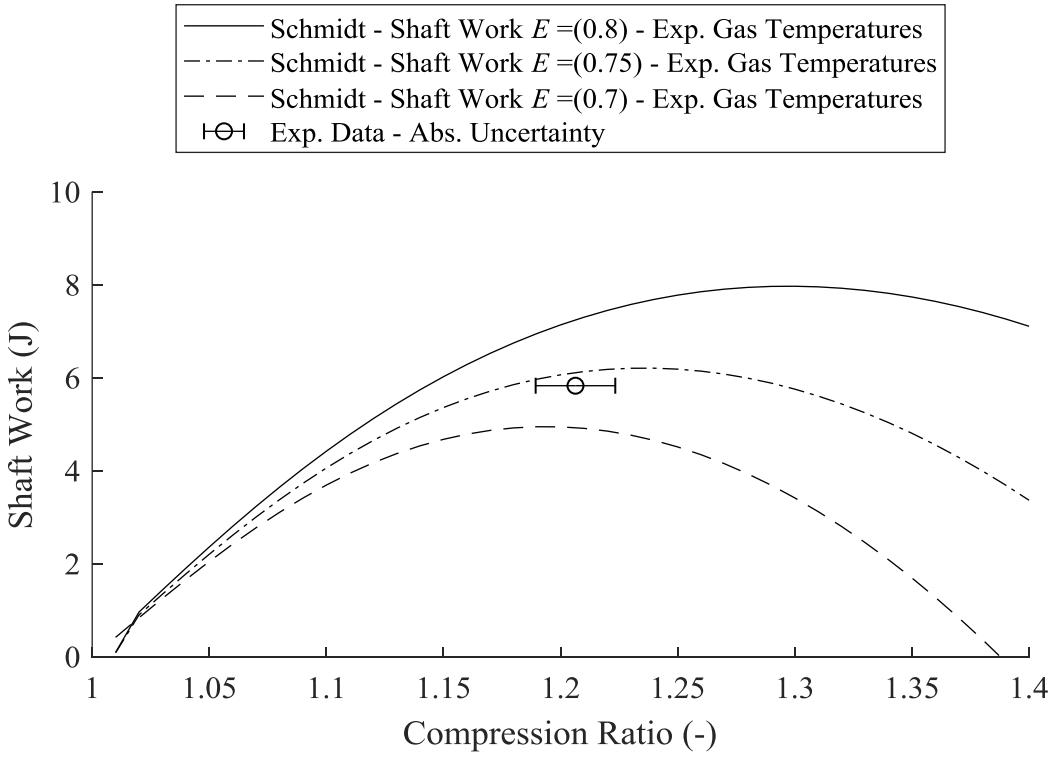


Figure 6.9 Comparison of Egas' ideal compression ratio the to the maximum shaft power points for various compression ratios of the EP-1.

## 6.4 Compression Ratio Range for Maximum Shaft Power

The following section presents a method that may be used to determine the potential range of compression ratios that should be investigated when trying to maximize shaft power for LTDSEs. This method proposes that the range of compression ratios to investigate should be bounded by Egas' ideal compression ratio as an upper bound and Kolin's compression ratio as a lower bound. The validity of this method is discussed and tested below.

The EP-1 and seven LTDSEs reviewed from the literature were chosen for this investigation. The literature engines' relevant parameters are summarized in Table 6.4. These engines were chosen as they were all LTDSEs that were proven to run and produce shaft power measurements. They also provided the thermal source and sink temperature, and either the experimental compression ratio, or the engine volumes required to approximate the experimental compression ratio. The thermal source and sink temperatures for each engine were used to calculate Kolin's compression ratio, and Egas' ideal compression ratio.

The Ringbom, Twin Piston, Two Engine, and the Four Piston LTDSEs did not provide the compression ratio and therefore it was estimated. This was done by using their displacer and power piston swept volume to calculate the minimum and maximum engine volume. This approach was used because all four engines used flat plate heat exchangers and therefore could be assumed to have a small amount of dead volume. The estimated compression ratio represents the maximum compression ratio possible for each engine.

The thermal sink temperature was not provided for the 10 Watt LTDSE. A thermal sink temperature of 15 °C was assumed. This was done because other LTDSEs at the same institute used 15 °C as the thermal sink temperature [48].

Table 6.4 Comparison of LTDSE's experimental and estimated compression ratios to Kolin's compression ratio and Egas' ideal compression ratio.

| Engine Name | Notes | $T_H$ | $T_C$ | $\Delta T$ | $CR_{ideal}$ | $CR_{Kolin}$ | $CR_{exp}$ | Ref |
|---|---|---|---|---|---|---|---|---|
| | | °C | °C | °C | | | | |
| Ringbom | LTD, Ringbom type, slider crank drive, PP = aluminum | 90 | 10 | 80 | 1.283 | 1.080 | ≤ 1.214* | [41] |
| 300 Watt | LTD, gamma-type, slider-crank drive and scotch yoke drive, PP = Piston (one-way seal) | 130 | 15 | 115 | 1.399 | 1.115 | 1.271 | [42], [47], [48] |
| 10 Watt | LTD, gamma-type, slider crank drive | 130 | 15 | 115 | 1.399 | 1.115 | 1.224 | [50] |
| Twin Piston | LTD, gamma-type, slider crank drive, PP = Steel (x2) | 163 | 34 | 129 | 1.420 | 1.129 | ≤ 1.140* | [43] |
| Two Engine | LTD, dual engine gamma-type, slider crank drive, PP = aluminum | 110 | 25 | 85 | 1.285 | 1.085 | ≤ 1.080* | [44] |
| Four Piston | LTD, gamma-type, slider crank drive, PP = Steel (×4) | 166 | 34 | 132 | 1.430 | 1.132 | ≤ 1.181* | [45] |
| MDF Displacer | LTD, gamma-type, slider crank drive, PP = aluminum | 160 | 25 | 135 | 1.453 | 1.135 | 1.235 | [49] |

* The compression ratio was calculated assuming the minimum engine volume was equal to the displacer piston swept volume, and the maximum equal to the summation of both pistons swept volume.

** A thermal sink temperature was not provided, therefore, a thermal sink temperature of 15 °C was assumed due to similar tests performed on other LTDSE at the same institute [48]

Figure 6.10 depicts where the experimental and estimated compression ratio is relative to the ideal compression ratio as an upper bound, and Kolin's compression ratio as a lower bound for each engine. This figure shows that all the engine's experimental or estimated compression ratios fall within the proposed range.

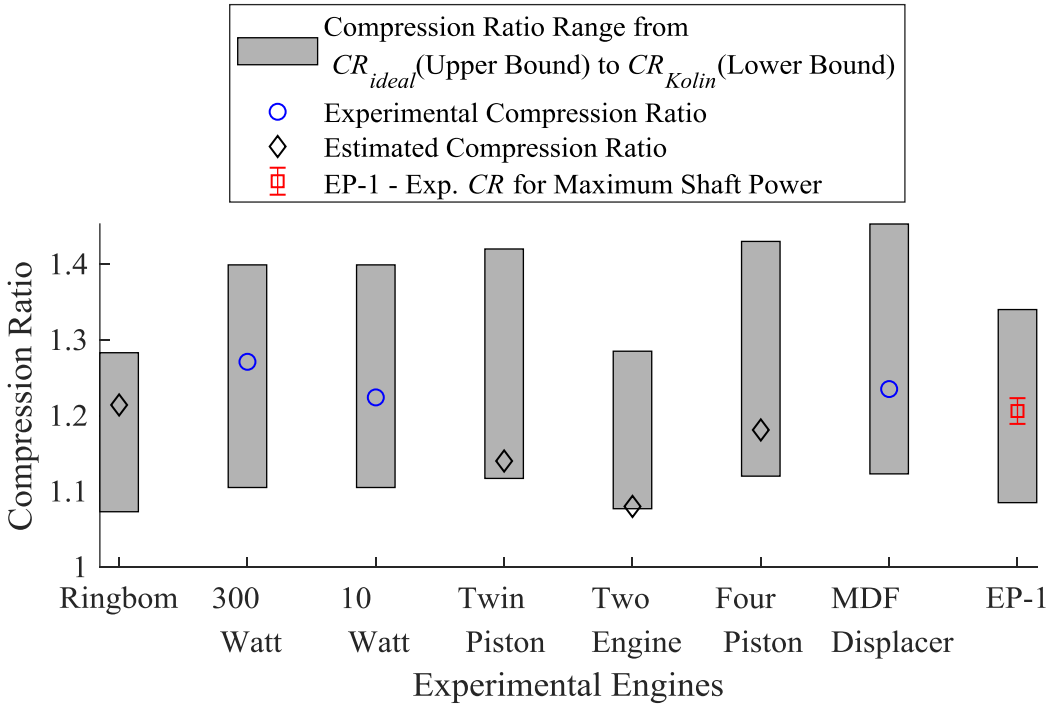


Figure 6.10 LTDSEs estimated and experimental compression ratios as compared to the Egas' ideal compression ratio and Kolin's compression ratio.

The 10 Watt LTDSE had its experimental compression ratio varied for three different thermal source temperatures—130 °C, 110 °C and 80 °C [50]. These tests were similar to the compression ratio optimization tests performed by the EP-1. The various compression ratios tested for each temperature difference and which one produced the maximum shaft power for both the EP-1 and the 10 Watt is presented in Figure 6.11. For the 10 Watt, nearly all of the tested compression ratios fell within the proposed bounds. The compression ratio that produced the maximum shaft power resided near the mean value of the two methods for the three thermal source temperatures tested for the 10-Watt engine. However, as discussed above, the thermal sink temperature was not provided and the thermal sink temperature of 15 °C was assumed based on that use by other LTDSEs in the same facility [48]. Similar results were seen with the EP-1 with all the compression

ratios tested falling within the proposed range. Unlike the 10-Watt engine, a compression ratio was not found that produced a global maximum shaft power.

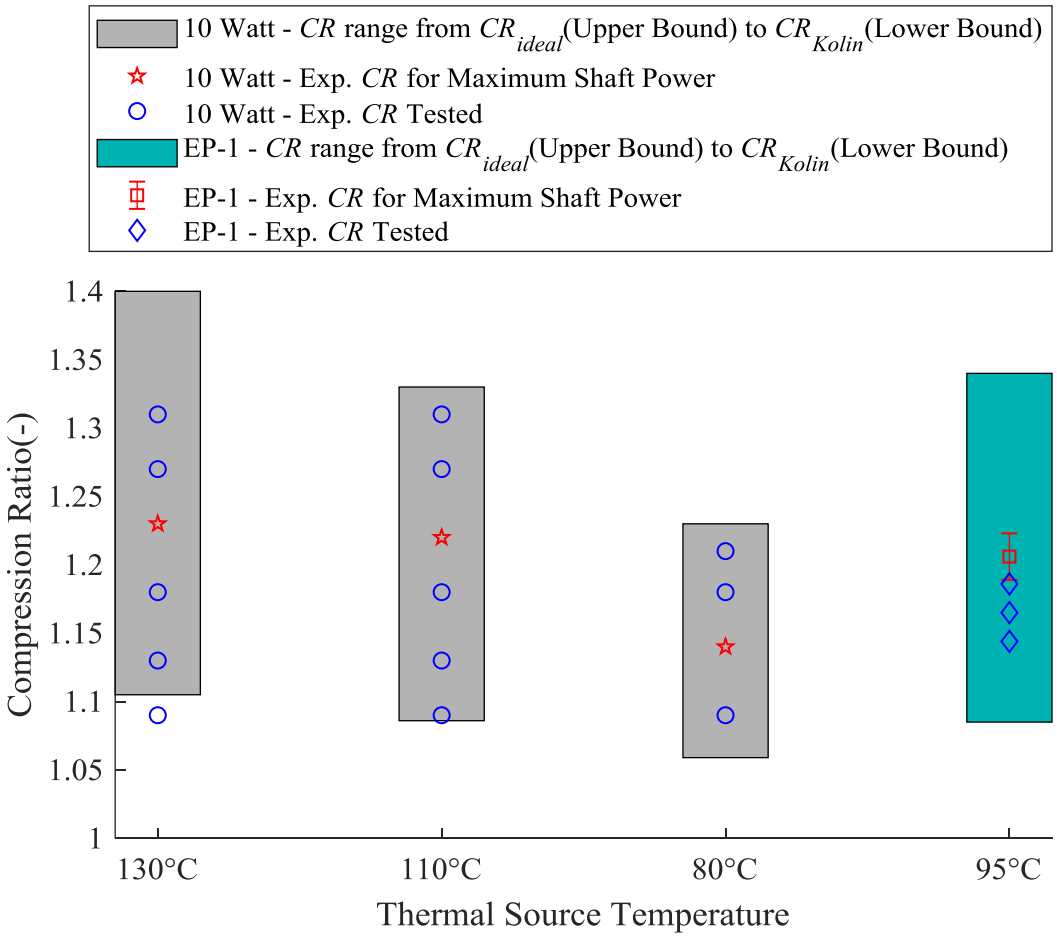


Figure 6.11 Predicted maximum shaft work based on the Schmidt model by varying compression ratio and mechanism effectiveness.

The range of compression ratios to investigate when trying to find the maximum shaft power for LTDSEs was proposed. The compression ratio range that was produced by the Egas' ideal compression ratio acting as an upper bound and Kolin's compression ratio acting as a lower bound. It was found that the majority of the LTDSEs used had their experimental or estimated compression ratio fall within this range. The compression ratio optimization tests performed by the 10 Watt and the EP-1 found that the compression ratio that produced the maximum shaft power resided close 50% percentile between the upper and the lower bound. Therefore, the shaft power compression ratio, $CR_{SP}$, can be proposed based on the ratio of the temperature of the thermal

source and sink as shown in Equation 6.1. This compression ratio is for LTDSEs that use air as a working fluid with a buffer pressure equal to atmospheric pressure. The coefficients of the equation were calculated to produce the mean value between Egas' ideal compression ratio and Kolin's compression ratio. Like Kolin's compression ratio, the shaft power compression ratio should be considered as an average value with adjustments made depending on the specific operating conditions. To further validate this method, more data is required. This would require compression ratio optimization tests to be performed for more LTDSEs.

$$CR_{SP} = 0.624\frac{T_H}{T_C} + 0.376 \qquad 6.1$$

Figure 6.12 presents Kolin's compression ratio as a lower bound, Egas' ideal compression ratio as an upper bound, and the proposed shaft power compression ratio falling in-between them. These methods are compared to the experimental and estimated compression ratio for the LTDSEs discussed above. The experimental and estimated compression ratios are found to fall above and below the proposed shaft power compression ratio line.

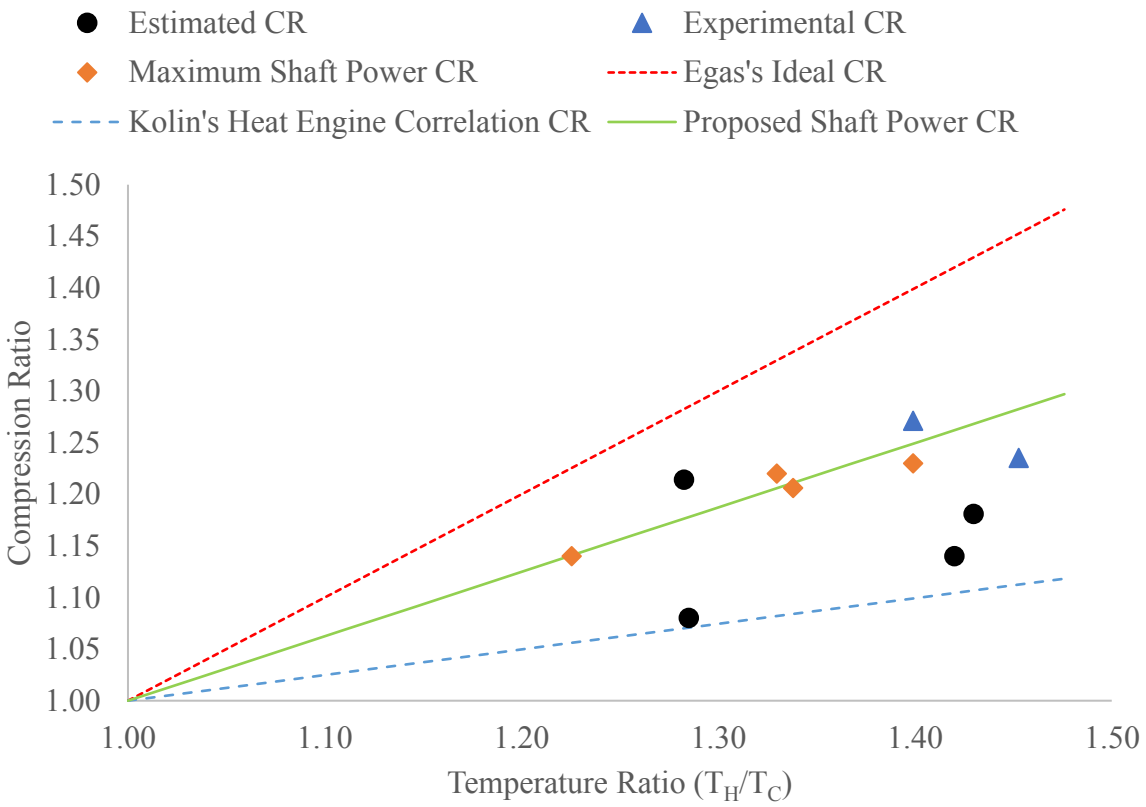


Figure 6.12 Compression ratio estimation methods compared to experimental and estimated compression ratio of LTDSEs.

# Chapter 7 Conclusion and Future Work

The investigations conducted in this thesis had three main goals. The first goal was to determine the operating parameter of a LTDSE, the EP-1, which would produce the maximum shaft power. Using the configuration and operating parameters that produced the maximum shaft power, the West number could be calculated. The second goal was to calculate the average West number for LTDSE and see how it compared to the West number calculated for HTDSEs. The final goal was to try and validate the methods used to estimate the compression ratio used for a Stirling engine.

The compression ratio, phase angle, and heat exchanger and power piston location were varied to determine the maximum shaft power for the EP-1. The compression ratios tested were 1.144, 1.165, 1.186, and 1.206 ± 0.006. The maximum compression ratio possible with the bellows power piston system, 1.206 ± 0.017, resulted in the maximum local shaft power. To find the global maximum shaft power, a power piston system that could produce higher compression ratios would be required. The phase angles used throughout testing were 60, 70, 75, 80, 85, 90, 100, 110 ± 1°. A phase angle of 90° was used to produce the local maximum shaft power as expected. However, unexpectedly, a secondary peak in the shaft power was observed for a phase angle of 70°. Only two of the possible four configurations of the heat exchanger and power piston location were tested. Having the thermal source heat exchanger located on top of the thermal sink heat exchanger with the power piston connected to the expansion space was used to yield the local maximum shaft power. The local maximum shaft power found was 6.58 ± 0.09 Watts and occurred at an operating speed of 67.7± 0.3 rpm.

The mean West number for LTDSEs was calculated to be of 0.21. This value was calculated using the data from 12 different experimental engines. It was found to be smaller but close to the value of the mean West number for HTDSEs of 0.25. The mean West number for HTDSEs is based off data from 23 different experimental HTDSES. Since the two values are so close it suggests that the West number can be used to compare the performance of Stirling engine that run off of any temperature difference. To

Three models used to estimate the compression ratio of a Stirling engine were investigated. Two of the models, Kolin's compression ratio and Egas' ideal compression ratio only required the temperature of the thermal source and sink used. The other model, Senft's optimum swept volume

ratio, required several additional operating parameters to be known. Kolin's method under predicted the compression ratio for maximum shaft power, while Egas' method over predicted it. When using the experimental temperature of the working fluid in the compression and expansion space with Egas' method, a compression ratio was produced that was an under prediction, but significantly closer the compression ratio for maximum shaft power. Senft's method was used with the EP-1 operating parameters. It produced an indicator diagram that resulted in a larger amount of indicated work when compared to the experimental indicator diagram. It required estimation of the mechanism effectiveness to calculate the shaft work, which resulted in a larger uncertainty in the shaft work. Senft's method required several operating parameters but did the best job of providing a range of compression ratios to use.

The experimental and estimated compression ratios for various LTDSEs were compared. All the compression ratios were found to fall within a range bounded by Egas' ideal compression ratio as an upper bound, and Kolin's compression ratio as a lower bound. Based on this, a model was proposed to estimate the compression ratio that could produce the maximum shaft power for a LTDSE. The model could be used for LTDSE that operate with a temperature difference less than 150 °C, a working fluid of air, and a constant buffer pressure equal to atmospheric pressure. The compression ratio produced by the model should be considered an average value and the compression ratio should be varied based on the specific operating conditions and parameters. The model may require further validation from compression ratio optimization tests of more LTDSEs.

Future work could include:

1. Using a method to better determine the minimum volume of the EP-1, and the instantaneous volume of the bellows used by the EP-1, so that the uncertainty in the compression ratio and the indicator diagram can be reduced.
2. Varying the thermal source heat exchanger position and the power piston work space connection location of the EP-1 to determine the performance of each configuration.
3. Performance testing of the EP-1 at temperature differences that are lower than the one tested in this thesis, so that the shaft power compression ratio and mean West number for LTDSEs can be further validated.
4. The testing of larger power piston systems, and therefore the ability for the use of larger compression ratios, so that the compression ratio that produces the global maximum shaft

power for a temperature of the thermal source of 95 °C and the thermal sink of 2 °C can be found.

# References


[1] International Energy Agency, “Global Energy & CO2 Status Report 2017,” 2018.

[2] IPCC, “Global Warming of 1.5 °C,” 2018.

[3] U.S. Energy Information Administration, “International Energy Outlook 2018,” 2018.

[4] U.S. Energy Information Administration, “Capacity Factors for Utility Scale Generators Not Primarily Using Fossil Fuels, January 2013-August 2018,” 2018. [Online]. Available: https://www.eia.gov/electricity/monthly/epm_table_grapher.php?t=epmt_6_07_b. [Accessed: 23-Nov-2018].

[5] U.S. Energy Information Administration, “Capacity Factors for Utility Scale Generators Primarily Using Fossil Fuels, January 2013-August 2018,” 2018. [Online]. Available: https://www.eia.gov/electricity/monthly/epm_table_grapher.php?t=epmt_6_07_a. [Accessed: 23-Nov-2018].

[6] R. Fares, “Renewable Energy Intermittency Explained: Challenges, Solutions, and Opportunities,” 2015. [Online]. Available: https://blogs.scientificamerican.com/plugged-in/renewable-energy-intermittency-explained-challenges-solutions-and-opportunities/. [Accessed: 31-Oct-2018].

[7] Government of Alberta, “Phasing out coal pollution.” [Online]. Available: https://www.alberta.ca/climate-coal-electricity.aspx.

[8] J. Banks and N. B. Harris, “Geothermal Potential of Foreland Basins: A Case Study from the Western Canadian Sedimentary Basin,” *Geothermics*, vol. 76, pp. 74–92, 2018.

[9] R. Ward, “Albertans may face $8B bill for orphan wells unless rules change, lawyer says,” 2017. [Online]. Available: https://www.cbc.ca/news/canada/calgary/orphan-wells-alberta-energy-minister-redwater-1.4420929. [Accessed: 31-Oct-2018].

[10] CMC, AITF, and AIHA, “Community Integrated Energy Mapping Feasibility Study In Alberta’s Industrial Heartland And Strathcona Industrial Area.” 2014.

[11] D. Layzell and K. Manfred, “It’s time to put an end to Alberta’s energy waste,” 2015. [Online]. Available: https://www.theglobeandmail.com/opinion/its-time-to-put-an-end-to-albertas-energy-waste/article26061509/. [Accessed: 31-Oct-2018].

[12] Electratherm, “4200 Specification Sheet,” 2018.

[13] Gentherm, “Thermoelectric Generators (TEGs).” [Online]. Available: http://www.genthermglobalpower.com/products/thermoelectric-generators-tegs. [Accessed: 11-Dec-2018].

[14] Cool Energy Inc., “ThermoHeart 25 kWe High Performance Stirling Engine,” 2016. [Online]. Available: https://www.ohio.edu/mechanical/stirling/engines/ThermoHeart.pdf. [Accessed: 31-Dec-2018].

[15] C. P. Speer, “Modifications to Reduce the Minimum Thermal Source Temperature of the ST05G-CNC Stirling Engine,” University of Alberta, 2018.

[16] T. C. Harman, T. C. Harman, P. J. Taylor, M. P. Walsh, and B. E. Laforge, “Quantum Dot Superlattice Thermoelectric Materials and Devices,” *Science (80-. ).*, vol. 297, pp. 2229–2232, 2002.

[17] Government of Canada, “Canadian Climate Normals 1981-2010 Station Data,” 2018. [Online]. Available: http://climate.weather.gc.ca/climate_normals/results_1981_2010_e.html?stnID=1865&autofwd=1. [Accessed: 31-Oct-2018].

[18] I. Urieli and B. David, *Stirling Cycle Engine Analysis*. Adam Hilger Ltd, 1984.

[19] G. T. Reader and C. Hooper, *Stirling Engines*. E. & F.N. SPon, 1983.

[20] J. R. Senft, *Mechanical Efficiency of Heat Engines*. CAmbridge University Press, 2007.

[21] G. Walker and J. R. Senft, *Free Piston Stirling Engines*. Springer Berlin Heidelberg, 1985.

[22] C. D. West, *Principles and applications of Stirling engines*. 1986.

[23] K. Wang, S. R. Sanders, S. Dubey, F. Hoong, and F. Duan, “Stirling Cycle Engines for

Recovering Low and Moderate Temperature Heat: A Review," *Renew. Sustain. Energy Rev.*, vol. 62, pp. 89–108, 2016.

[24] H. Karabulut, M. Okur, and A. O. Ozdemir, "Performance prediction of a Martini type of Stirling engine," *Energy Convers. Manag.*, vol. 179, no. August 2018, pp. 1–12, 2019.

[25] C. D. West, *Liquid Piston Stirling Engines*. Van Nostrand Reinhold Company Inc, 1983.

[26] H. Hachem, R. Gheith, F. Aloui, and S. Ben Nasrallah, "Technological challenges and optimization efforts of the Stirling machine: A review," *Energy Convers. Manag.*, vol. 171, no. March, pp. 1365–1387, 2018.

[27] J. A. C. Kentfield, "The Thermodynamics of Stirling Engines Revisited: the Relative Merits of Hot Zone or Cold Zone Work Extraction," *SAE Technical Papers*. 1992.

[28] G. Walker, *Stirling-cycle Machines*. Oxford University Press, 1973.

[29] I. Kolin, *Stirling Motor - History - Theory - Pratice*. 1991.

[30] D. Rajkovic and M. Golub, "Technical and Economic Possibilities of Using Low Temperature Geothermal Sources in Croatia," *Proc. 17th Int. Min. Congr. Exhib.*, pp. 615–620, 2001.

[31] A. Scheyhing, "Assessment of Low Temperature Electricity Production with Focus on Geothermal Energy," Chalmers University of Technology, 2012.

[32] Z. S. H. Abu-Hamatteh, K. Al-Zughoul, and S. Al-Jufout, "Potential Geothermal Energy Utilization in Jordan: Possible Electrical Power Generation," *Int. J. Therm. Environ. Eng.*, vol. 3, no. 1, pp. 9–14, 2010.

[33] I. Kolin, S. Koscak-kolin, M. Golub, and P. Engineering, "Geothermal Electricity Production By Means Ofthe Low Temperature Difference Stirling Engine," *World Geotherm. Congr. 2000*, pp. 3199–3203, 2000.

[34] R. B. Peterson, "Thermocompression engine cycle with isothermal expansion," *Energy Sources*, vol. 20, no. 3, pp. 199–208, 1998.

[35] C. Alimonti, D. Berardi, D. Bocchetti, and E. Soldo, “Coupling of Energy Conversion Systems and Wellbore Heat Exchanger in a Depleted Oil Well,” *Geotherm. Energy*, vol. 4, no. 1, 2016.

[36] M. Janowski, “Alternative Ways of Utilising Geothermal Energy by Means of a Module Based on the Stirling Engine for Electricity Production,” in *World Geothermal Congress*, 2015, no. April, p. 5.

[37] M. J. Dadi, I. M. Molvi, and A. V Mehta, “The Most Efficient Waste Heat Recovery Device: A Gamma Type Stirling Engine,” *Int. J. Adv. Eng. Technol.*, vol. 3, no. I, pp. 189–195, 2012.

[38] D. A. N. Scarpete, K. Uzuneanu, and N. Badea, “Stirling Engine in Residential Systems Based on Renewable Energy,” *Adv. Energy Planning, Environ. Educ. Renew. Energy Sources*, pp. 124–129, 2010.

[39] S. M. A. Sufian, K. A. Sagar, M. A. Ullah, and D. Baidya, “Harvesting Electrical Power From Waste Heat Using Stirling Engine,” *Proc. 9th Int. Forum Strateg. Technol.*, pp. 343–346, 2014.

[40] Cool Energy, “ThermoHeart 25 kW e High Performance Stirling Engine,” 2016.

[41] J. R. Senft, “A Low Temperature Difference Ringbom Stirling Demonstration Engine,” 1984, pp. 1929–1934.

[42] S. Iwamoto, F. Toda, K. Hirata, M. Takeuchi, and T. Yamamoto, “Comparison of Low and High Temperature Differential Stirling Engines,” pp. 29–38, 1997.

[43] B. Kongtragool and S. Wongwises, “Performance of a Twin Power Piston Low Temperature Differential Stirling Engine Powered by a Solar Simulator,” *Sol. Energy*, vol. 81, no. 7, pp. 884–895, 2007.

[44] A. R. Tavakolpour, A. Zomorodian, and A. Akbar Golneshan, “Simulation, Construction and Testing of a Two-cylinder Solar Stirling Engine Powered by a Flat-plate Solar Collector Without Regenerator,” *Renew. Energy*, vol. 33, no. 1, pp. 77–87, 2008.

[45] B. Kongtragool and S. Wongwises, “A Four Power-piston Low-temperature Differential Stirling Engine Using Simulated Solar Energy as a Heat Source,” *Sol. Energy*, vol. 82, no. 6, pp. 493–500, 2008.

[46] ReviverSoft, .“MAT File Extension.” [Online]. Available: https://www.reviversoft.com/file-extensions/mat. [Accessed: 18-Dec-2018].

[47] Dynamics of Machinery Laboratory, “Structure of 300 W class low temperature difference Stirling engine.” [Online]. Available: http://www.bekkoame.ne.jp/~khirata/academic/kiriki/yama1/300strct.html. [Accessed: 05-Oct-2018].

[48] Dynamics of Machinery Laboratory, “Performance of 300 W class low temperature difference Stirling engine.” [Online]. Available: http://www.bekkoame.ne.jp/~khirata/academic/kiriki/yama1/300pfrm.html. [Accessed: 05-Oct-2018].

[49] C. Çinar, F. Aksoy, and D. Erol, “The Effect of Displacer Material on the Performance of a Low Temperature Differential Stirling Engine,” *Int. J. Energy Res.*, vol. 36, no. 8, pp. 911–917, 2012.

[50] Dynamics of Machinery Laboratory, “10 W Class Low Temperature Difference Stirling Engine,” 1998. [Online]. Available: http://www.bekkoame.ne.jp/~khirata/academic/kiriki/10wse/index.html. [Accessed: 02-Nov-2018].

[51] L. Lemaire, “Miniaturized Stirling Engines for Waste Heat Recovery,” McGill University, 2012.

[52] G. Aragón-González, M. Cano-Blanco, A. Canales-Palma, and A. León-Galicia, “Developing and Testing Low Cost LTD Stirling Engines,” *Rev. Mex. Física*, vol. 59, no. 1, pp. 199–203, 2013.

[53] S. Kwankaomeng, B. Silpsakoolsook, J. Wongsa-ngam, and R. Norruang, “Design of an Ultra-Low Temperature Differential Stirling Engine,” in *Proc. 5th International*

*Conference on Mechanical Engineering*, 2014, no. December.

[54] Y. Kato, "Indicated diagrams of low temperature differential Stirling engines with channel-shaped heat exchangers," *Renew. Energy*, vol. 103, pp. 30–37, 2017.

[55] Y. Kato, "Indicated diagrams of a low temperature differential Stirling engine using flat plates as heat exchangers," *Renew. Energy*, vol. 85, 2016.

[56] R. Li, L. Grosu, and D. Queiros-Condé, "Losses effect on the performance of a Gamma type Stirling engine," *Energy Convers. Manag.*, vol. 114, pp. 28–37, 2016.

[57] B. Kongtragool and S. Wongwises, "Testing of a low-temperature differential stirling engine by using actual solar energy," *Int. J. Green Energy*, vol. 5, no. 6, pp. 491–507, 2008.

[58] N. Boutammachte and J. Knorr, "Field-test of a Solar Low Delta-T Stirling Engine," *Sol. Energy*, vol. 86, no. 6, pp. 1849–1856, 2012.

[59] H. El Hassani, N. Boutammachte, and M. Hannaoui, "Study of Some Power Influencing Parameters of a Solar Low Temperature Stirling Engine," *Eur. J. Sustain. Dev.*, vol. 3, no. 2, pp. 109–118, 2014.

[60] H. Jokar and A. R. Tavakolpour-Saleh, "A Novel Solar-powered Active Low Temperature Differential Stirling Pump," *Renew. Energy*, vol. 81, pp. 319–337, 2015.

[61] G. Walker, "Elementary Design Guidelines for Stirling Engines," in *Proc. 14th Intersociety Energy Conversion Engineering Conference*, 1979.

[62] J. R. Senft, "A Simple Derivation of the Generalized Beale Number," in *Proc. 17th Energy Conversion Engineering Conference*, 1982, pp. 1652–1655.

[63] W. R. Martini, "Stirling Engine Design Manual," 1983.

[64] J. Egas, "Stirling Engine Configuration Selection," *Energies*, vol. 11, no. 584, pp. 1–23, 2018.

[65] Alberta Health Services, "Thermometer Calibration," 2011. [Online]. Available: https://www.albertahealthservices.ca/assets/wf/eph/wf-eh-thermometer-calibration.pdf.

[Accessed: 16-Nov-2018].

[66] M. Chaplin, “Water Phase Diagram,” 2000. [Online]. Available: http://www1.lsbu.ac.uk/water/water_phase_diagram.html. [Accessed: 28-Nov-2018].

[67] Omega Engineering, “Revised Thermocouple Reference Tables - Type T.”

[68] Dynapar, “The Driving Force: Magnetic versus Optical Encoder Engines.” [Online]. Available: https://www.dynapar.com/technology/optical-encoders/. [Accessed: 08-Dec-2018].

[69] A. . Wheeler and A. R. Ganji, *Introduction to Engineering Experimentation*, 3rd ed. New Jersey Pearson Higher Education, 2004.

[70] Validyne Engineering, “Resolution and Frequency Response in Pressure Transducers.” [Online]. Available: http://www.validyne.com/blog/resolution-and-frequency-response-in-pressure-transducers/. [Accessed: 05-Dec-2018].

[71] Futek, “Rotary Torque Sensor – Non-Contact Shaft-to-Shaft Model TRS600 - Specfication Sheet.”

[72] W. Cleghorn and D. Nikolai, *Mechanics of Machines*. Oxford University Press, 2015.

[73] J. R. Senft, “Optimum Stirling engine geometry,” *Int. J. Energy Res.*, vol. 26, no. 12, pp. 1087–1101, 2002.

[74] R. Gordon, M. Pickering, and D. Bisson, “Uncertainty Analysis by the ‘Worst Case’ Method,” *J. Chem. Educ.*, vol. 61, no. 9, pp. 780–781, 1984.

[75] N. I. of S. and Technology, “Propagation of Error Considerations.” [Online]. Available: https://www.itl.nist.gov/div898/handbook/mpc/section5/mpc55.htm. [Accessed: 10-Dec-2018].

[76] LibreTexts, “Propagation of Error,” 2018. [Online]. Available: https://chem.libretexts.org/Textbook_Maps/Analytical_Chemistry/Supplemental_Modules_(Analytical_Chemistry)/Quantifying_Nature/Significant_Digits/Propagation_of_Error. [Accessed: 10-Dec-2018].

[77] B. Ridder, “Worst-Case Propagation of Uncertainty,” 2014. [Online]. Available: https://www.mathworks.com/matlabcentral/fileexchange/48139-worst-case-propagation-of-uncertainty. [Accessed: 10-Dec-2018].

[78] Weatherstats, “Station Pressure - Hourly data for Edmonton.” [Online]. Available: https://edmonton.weatherstats.ca/charts/pressure_station-hourly.html. [Accessed: 02-Dec-2018].

[79] B. Redwood, S. Filemon, and B. Garret, *The 3D Printing Handbook*. 3D Hubs B.V., 2017.

[80] B. Redwood, S. Filemon, and B. Garret, *The 3D Printing Handbook*. 3D Hubs B.V.

[81] Ultimaker, “Ultimaker 2+ Specifications.” [Online]. Available: https://ultimaker.com/en/products/ultimaker-2-plus/specifications. [Accessed: 13-Nov-2018].

[82] Formlabs, “Form 2 Tech Specs.” [Online]. Available: https://formlabs.com/3d-printers/form-2/tech-specs/. [Accessed: 15-Nov-2018].

[83] MatWeb, “Deflection Temperature Testing of Plastics.” [Online]. Available: http://www.matweb.com/reference/deflection-temperature.aspx. [Accessed: 16-Nov-2018].

[84] MatWeb, “Tensile Property Testing of Plastics.” [Online]. Available: http://www.matweb.com/reference/tensilestrength.aspx. [Accessed: 16-Nov-2018].

[85] FormLabs, “Materials Data Sheet,” pp. 76–77, 2014.

[86] SD3D, “Technical Data Sheet.”

[87] MatWeb, “Aluminum, Al.” [Online]. Available: http://www.matweb.com/search/datasheet.aspx?bassnum=AMEAL00&ckck=1. [Accessed: 30-Nov-2018].

[88] MatWeb, “Copper, Cu; Annealed.” [Online]. Available: http://www.matweb.com/search/datasheet_print.aspx?matguid=9aebe83845c04c1db5126fada6f76f7e. [Accessed: 30-Nov-2018].

[89] D. Conner, “3D Printed Stirling Engine,” 2012. [Online]. Available: http://www.solarheatengines.com/2012/10/29/3d-printed-stirling-engine/. [Accessed: 05-Nov-2018].

[90] Direct Plastic, “Acetal or Delrin – Does it Really Matter Which One You Use?,” 2013. [Online]. Available: https://www.directplastics.co.uk/about_plastics/why-choose-acetal-or-delrin. [Accessed: 20-Nov-2018].

[91] Polymer Properties Database, “POLYSTYRENES.” [Online]. Available: https://polymerdatabase.com/polymer classes/Polystyrene type.html. [Accessed: 13-Nov-2018].

[92] A. Ross, *Making Stirling Engines*. 1993.

[93] Airport Corp, “Cylinder Seal Table.” [Online]. Available: https://airpot.com/wp-content/uploads/1970/01/Cylinder-Seal-Table.png. [Accessed: 14-Nov-2018].

[94] Pub Chem, “Acetone.” [Online]. Available: https://pubchem.ncbi.nlm.nih.gov/compound/acetone#section=Odor. [Accessed: 19-Nov-2018].

[95] J.J. Short Associates Inc, “Temperature Capabilities of Elastomers.” [Online]. Available: http://www.jjshort.com/Rubber-Properties.php. [Accessed: 23-Nov-2018].

[96] J. R. Senft, *Ringbom Stirling Engines*. Oxford University Press, 1993.

[97] B. Kongtragool and S. Wongwises, “Investigation on power output of the gamma-configuration low temperature differential Stirling engines,” *Renew. Energy*, vol. 30, no. 3, pp. 465–476, 2004.

[98] National Instruments, “SCXI-1600 User Manual,” 2004.

[99] National Instruments, “NI 9217 - Datasheet,” 2016.

[100] Validyne Engineering, “DP15 - Specification Sheet.”

[101] National Instruments, “NI USB-6211 - Device Specifcations,” pp. 1–14, 2016.

[102] Druck, “DPI 603 - Specification Sheet.”

[103] Encoder Products Company, “Model 15S - Incremental Shaft Encoder - Specfication Sheet,” 2014.

[104] Ohaus Corporation, “Ohaus Scale Bases - Instruction Manual,” 1999.

# Appendix A: Uncertainty Analysis - Instruments

This section contains tables that list the sources of errors, specifications, and the calculated standard uncertainty for the measurement instruments.

## A.1 Thermocouple

Table A.1 Thermocouple specifications.

| | |
|---|---|
| **Measurement Type:** | Working Fluid Temperature |
| **Measurement Device:** | TTSS-116E-6, Omega Engineering Inc. |
| **Maximum Range:** | -200 to 350 °C |
| **Full Scale:** | 550 °C |
| **Standard Uncertainty:** | ± 1.9 °C |

Table A.2 Sources of error for thermocouple system.

| Error | Error Type | Uncertainty Contribution | Comments |
|---|---|---|---|
| Manufacturer Accuracy | Systematic | 1 °C | Greater of 1.0 °C or 0.75% Above 0 °C Reference: [67] |
| DAQ Module Accuracy (SCXI-1600) | Systematic | 1.56 °C | Absolute Accuracy at Full Scale (mV) @ 0.05V = 0.061 Reference: [98] |
| Calibration | Systematic | 0.1 °C | Resolution of Mercury Thermometer Model No. ERTCO -1005-3s |
| Spatial Variation | Systematic | - | Sensing tip size is small (⌀ = 0.7mm) |
| Time Constant | Systematic | - | Ignored by taking average of measurement values at steady state |
| Noise and Quantization | Random | - | Included in DAQ Module Accuracy |

## A.2 RTD

Table A.3 RTD specifications.

| | |
|---|---|
| **Measurement Type:** | Water Temperature |
| **Measurement Device:** | RTD-810, Omega Engineering Inc. |
| **Maximum Range:** | -200 to 750 °C |
| **Full Scale:** | 950 °C |
| **Standard Uncertainty:** | ± 0.62 °C |

Table A.4 Sources of error for RTD system.

| Error | Error Type | Uncertainty Contribution | Comments |
|---|---|---|---|
| Manufacturer Accuracy | Systematic | 0.35 °C | Class A: ± 0.35 °C @ 100 °C Reference: [98] |
| DAQ Module Accuracy (NI-9217) | Systematic | 0.5 °C | Maximum (-40 to 70 °C) = 0.5 °C Reference: [99] |
| Calibration | Systematic | 0.1 °C | Resolution of Mercury Thermometer Model No. ERTCO -1005-3s |
| Spatial Variation | Systematic | - | Majority of sensing mass resides inside water |
| Time Constant | Systematic | - | Ignored by taking average of measurement values at steady state |
| Noise and Quantization | Random | - | Included in DAQ Module Accuracy |

## A.3 Pressure Transducer

Table A.5 Pressure transducer specifications.

| | |
|---|---|
| **Measurement Type:** | Work Space Pressure |
| **Measurement Device:** | Validyne DP15-50, Validyne Engineering |
| **Maximum Range:** | -86.18 to 86.18 kPa |
| **Full Scale:** | 172.37 kPa |
| **Standard Uncertainty:** | ± 0.44 kPa |

Table A.6 Sources of error for pressure transducer system.

| Error | Error Type | Uncertainty Contribution | Comments |
|---|---|---|---|
| Manufacturer Accuracy | Systematic | 0.43 kPa | ± 0.25% FS<br>Reference: [100] |
| DAQ Module Accuracy (NI USB-6211) | Systematic | 0.02 kPa | Absolute Accuracy at Full Scale (μV) @ 10V = 2690<br>Reference: [101] |
| Calibration | Systematic | 0.07 kPa | Resolution of Calibration Device<br>Reference: [102] |
| Spatial Variation | Systematic | - | Ignored because pressure measurement area is small |
| Time Constant | Systematic | - | Ignored by taking average of measurement values at steady state |
| Noise and Quantization | Random | - | Included in DAQ Module Accuracy |

## A.4 Torque Sensor

Table A.7 Torque sensor specifications.

| | |
|---|---|
| **Measurement Type:** | Torque |
| **Measurement Device:** | TRS600, Futek Advanced Sensor Technology Inc. |
| **Maximum Range:** | -1 to 1 Nm |
| **Full Scale:** | 2 Nm |
| **Standard Uncertainty:** | ± 0.006 Nm |

Table A.8 Sources of error for torque sensor system.

| Error | Error Type | Uncertainty Contribution | Comments |
|---|---|---|---|
| Manufacturer Accuracy and Calibration | Systematic | 0.004 Nm | Nonlinearity: ± 0.2% of RO Reference: [71] |
| Manufacturer Accuracy and Calibration | Systematic | 0.002 Nm | Hysteresis: ±0.1% of RO Reference: [71] |
| Manufacturer Accuracy and Calibration | Systematic | 0.004 Nm | Nonrepeatability: ±0.2% of RO Reference: [71] |
| DAQ Module Accuracy (NI USB-6211) | Systematic | 0.000282 Nm | Absolute Accuracy at Full Scale (μV) @ 5V = 1410 Reference: [101] |
| Spatial Variation | Systematic | - | N/A |
| Time Constant | Systematic | - | Ignored by taking average of output |
| Noise and Quantization | Random | - | Included in DAQ Module Accuracy |

## A.5 Rotary Encoder

Table A.9 Rotary encoder specifications.

| | |
|---|---|
| **Measurement Type:** | Angle |
| **Measurement Device:** | 15S-19M1-0500NV1ROC-F03-S1, Encoder Products Company |
| **Maximum Range:** | Unlimited Rotation |
| **Full Scale:** | Unlimited Rotation |
| **Standard Uncertainty:** | ± 1° |

Table A.10 Sources of error for rotary encoder system.

| Error | Error Type | Uncertainty Contribution | Comments |
|---|---|---|---|
| Manufacturer Accuracy | Systematic | 0.017° | Within 0.017° mechanical or 1 arc-minute from true position. Reference: [103] |
| Manufacturer Accuracy | Systematic | 1° | Comm. Accuracy: 1° mechanical Reference: [103] |
| DAQ Module Accuracy (NI USB-6211) | Systematic | - | Ignored due to only looking for 5-volt peaks or 0 V troughs, not specific voltage values. |
| Spatial Variation | Systematic | - | N/A |
| Time Constant | Systematic | - | Ignored because data is sampled at a much higher rate than the Nyquist frequency, and rotation speed is significantly slower than maximum speed of 8000rpm |
| Noise and Quantization | Random | - | Ignored due to only looking for 5-volt peaks or 0 V troughs |

## A.6 Weight Scale

Table A.11 Weight scale specifications.

| | |
|---|---|
| **Measurement Type:** | Mass |
| **Measurement Device:** | Ohaus B50AS |
| **Maximum Range:** | 0 to 50 kg |
| **Full Scale:** | 50 kg |
| **Standard Uncertainty:** | ± 0.017 kg |

Table A.12 Sources of error for weight scale system.

| Error | Error Type | Uncertainty Contribution | Comments |
|---|---|---|---|
| Manufacturer Accuracy | Systematic | 0.005 kg | Readability: 0.005kg Reference: [104] |
| Manufacturer Accuracy | Systematic | 0.005 kg | Repeatability: ±0.01% Reference: [104] |
| Manufacturer Accuracy | Systematic | 0.015 kg | Linearity: ±0.03% Reference: [104] |
| Spatial Variation | Systematic | - | Included in standard error from multiple measurements |
| Time Constant | Systematic | - | Ignored by taking average of measurement values at steady state |
| Noise and Quantization | Random | - | Included in standard error from multiple measurements |

# Appendix B: Uncertainty Analysis – Output Variables

This section contains the equations, propagation of uncertainty, sample calculations and standard uncertainty for the output variables.

## B.1 Change in Mass

Table B.1 Equations and sample calculation for the propagation of uncertainty of change in mass.

| **Output Variable:** | Change in Mass ($\Delta m_w$) |
|---|---|
| **Equation:** | $\Delta m_w = m_f - m_i$ |
| **Propagation of Uncertainty Equation:** | $\sigma_{\Delta m_w} = \sqrt{\sigma_{m_f}^2 + \sigma_{m_i}^2}$ |
| **Value:** | 1.319 kg |
| **Standard Uncertainty:** | ±0.024 kg |

Table B.2 Input values and standard uncertainty used to calculate change in mass.

| **Input Variable** | **Value** | **Standard Uncertainty** | **Uncertainty Notes** |
|---|---|---|---|
| Initial Mass ($m_i$) | 0.732 kg | 0.017 kg | Weight Scale |
| Final Mass ($m_f$) | 2.051 kg | 0.017 kg | Weight Scale |

## B.2 Mass Flow Rate

Table B.3 Equation and sample calculation for the propagation of uncertainty of mass flow rate.

| **Output Variable:** | Mass flow rate ($\dot{m}_w$) |
|---|---|
| **Equation:** | $\dot{m}_w = \frac{\Delta m_w}{t}$ |
| **Propagation of Uncertainty Equation:** | $\sigma_{\dot{m}_w} = \dot{m}_w \sqrt{\left(\frac{\sigma_{\Delta m_w}}{\Delta m_w}\right)^2 + \left(\frac{\sigma_t}{t}\right)^2}$ |
| **Value:** | 0.0432 kg/s |
| **Standard Uncertainty:** | ±0.0008 kg/s |

Table B.4 Input values and standard uncertainty used to calculate mass flow rate.

| **Input Variable** | **Value** | **Standard Uncertainty** | **Uncertainty Notes** |
|---|---|---|---|
| Change in Mass ($\Delta m_w$) | 1.296 kg | 0.024 kg | Propagation |
| Time (t) | 30.02 s | 0.2 s | Reaction Time, Stop Watch |

## B.3 RTD – Change in Temperature

Table B.5 Equations and sample calculation for the propagation of uncertainty of the change in temperature the water in the flow loop.

| **Output Variable:** | Change in Temperature ($\Delta T_{RTD}$) |
|---|---|
| **Equation:** | $\Delta T_{RTD} = T_{hxi} - T_{hxo}$ |
| **Propagation of Uncertainty Equation:** | $\sigma_{\Delta T_{RTD}} = \sqrt{\sigma_{T_{hxi}}^2 + \sigma_{T_{hxo}}^2}$ |
| **Value:** | 2.94 °C |
| **Standard Uncertainty:** | ±0.88 °C |

Table B.6 Input values and standard uncertainty used to calculate the change in temperature the water in the flow loop.

| **Input Variable** | **Value** | **Standard Uncertainty** | **Uncertainty Notes** |
|---|---|---|---|
| Temperature In ($T_{hxi}$) | 95.24 °C | 0.62 °C | RTD |
| Temperature Out ($T_{hxo}$) | 89.74 °C | 0.62 °C | RTD |

## B.4 Rate of Heat Transfer into the System

Table B.7 Equations and sample calculation for the propagation of uncertainty of the rate of heat transfer into the system.

| **Output Variable:** | Rate of heat transfer into system ($\dot{Q}_{in}$) |
|---|---|
| **Equation:** | $\dot{Q_{in}} = \dot{m}_w \times c_p \times \Delta T_{RTD}$ |
| **Propagation of Uncertainty Equation:** | $\sigma_{\dot{Q_{in}}} = \dot{Q_{in}} \sqrt{\left(\frac{\sigma_{c_p}}{c_p}\right)^2 + \left(\frac{\sigma_{\dot{m}_w}}{\dot{m}_w}\right)^2 + \left(\frac{\sigma_{\Delta T_{RTD}}}{\Delta T_{RTD}}\right)^2}$ |
| **Value:** | 532 W |
| **Standard Uncertainty:** | ±160 W |

Table B.8 Input values and standard uncertainty used to calculate the rate of heat transfer into the system.

| **Input Variable** | **Value** | **Standard Uncertainty** | **Uncertainty Notes** |
|---|---|---|---|
| Mass Flow Rate ($\dot{m}_w$) | 0.0431 kg/s | 0.0008 kg/s | Propagation |
| Specific Heat Capacity ($c_p$) | 4200 J/kg*K | 36 J/kg*K | Range Difference (100 °C to 0 °C) |
| Temperature Difference ($\Delta T_{RTD}$) | 2.94 °C | 0.88 | Propagation |

## B.5 Frequency

Table B.9 Equations and sample calculation for the propagation of uncertainty of the engine operating frequency.

| **Output Variable:** | Engine Frequency ($f$) |
|---|---|
| **Equation:** | $f = \frac{\Delta\theta}{t_p}$ |
| **Propagation of Uncertainty Equation:** | $\sigma_f = f\sqrt{\left(\frac{\sigma_{\Delta\theta}}{\Delta\theta}\right)^2 + \left(\frac{\sigma_{t_p}}{t_p}\right)^2}$ |
| **Value:** | 2 Hz |
| **Standard Uncertainty:** | ±0.005 Hz |

Table B.10 Input values and standard uncertainty used to calculate the engine operating frequency.

| **Input Variable** | **Value** | **Standard Uncertainty** | **Uncertainty Notes** |
|---|---|---|---|
| Cycle ($\Delta\theta$) | 1 | 0.0055 | Since the rotary encoder has an uncertainty of 1° then the determination of a cycle can be off by (362/360)-1 = 0.0055 of a cycle. |
| Engine Period ($t_p$) | 0.5 | 0.0002 | The time uncertainty is based off the sampling frequency 10000hz |

## B.6 Shaft Power

Table B.11 Equations and sample calculation for the propagation of uncertainty of the shaft power.

| **Output Variable:** | Shaft Power ($P_{Shaft}$) |
|---|---|
| **Equation:** | $P_{shaft} = W_{shaft} * f$ |
| **Propagation of Uncertainty Equation:** | $\sigma_{P_{Shaft}} = P_{shaft}\sqrt{\left(\frac{\sigma_{W_{shaft}}}{W_{shaft}}\right)^2 + \left(\frac{\sigma_f}{f}\right)^2}$ |
| **Value:** | 3.14 W |
| **Standard Uncertainty:** | ±0.07 W |

Table B.12 Input values and standard uncertainty used to calculate the shaft power.

| **Input Variable** | **Value** | **Standard Uncertainty** | **Uncertainty Notes** |
|---|---|---|---|
| Shaft Work ($W_{shaft}$) | 6.28 | 0.04 | Torque Error * 2π |
| Engine Frequency ($f$) | 0.5 | 0.011 | Propagation |

## B.7 Thermal Efficiency

Table B.13 Equations and sample calculation for the propagation of uncertainty of the thermal efficiency.

| **Output Variable:** | Thermal Efficiency ($n_{th}$) |
|---|---|
| **Equation:** | $n_{th} = \frac{P_{shaft}}{\dot{Q}_{in}}$ |
| **Propagation of Uncertainty Equation:** | $\sigma_{n_{th}} = n_{th}\sqrt{\left(\frac{\sigma_{\dot{Q}_{in}}}{\dot{Q}_{in}}\right)^2 + \left(\frac{\sigma_{P_{shaft}}}{P_{shaft}}\right)^2}$ |
| **Value:** | 1.24 % |
| **Standard Uncertainty:** | ±0.37 % |

Table B.14 Input values and standard uncertainty used to calculate the thermal efficiency

| **Input Variable** | **Value** | **Standard Uncertainty** | **Uncertainty Notes** |
|---|---|---|---|
| Heat Rate In ($\dot{Q}_{in}$) | 532 | 160 | Propagation |
| Shaft Power ($P_{shaft}$) | 6.58 | 0.072 | Propagation |

# Appendix C: Specification Sheets

## C.1 Torque Sensor – Calibration Sheets

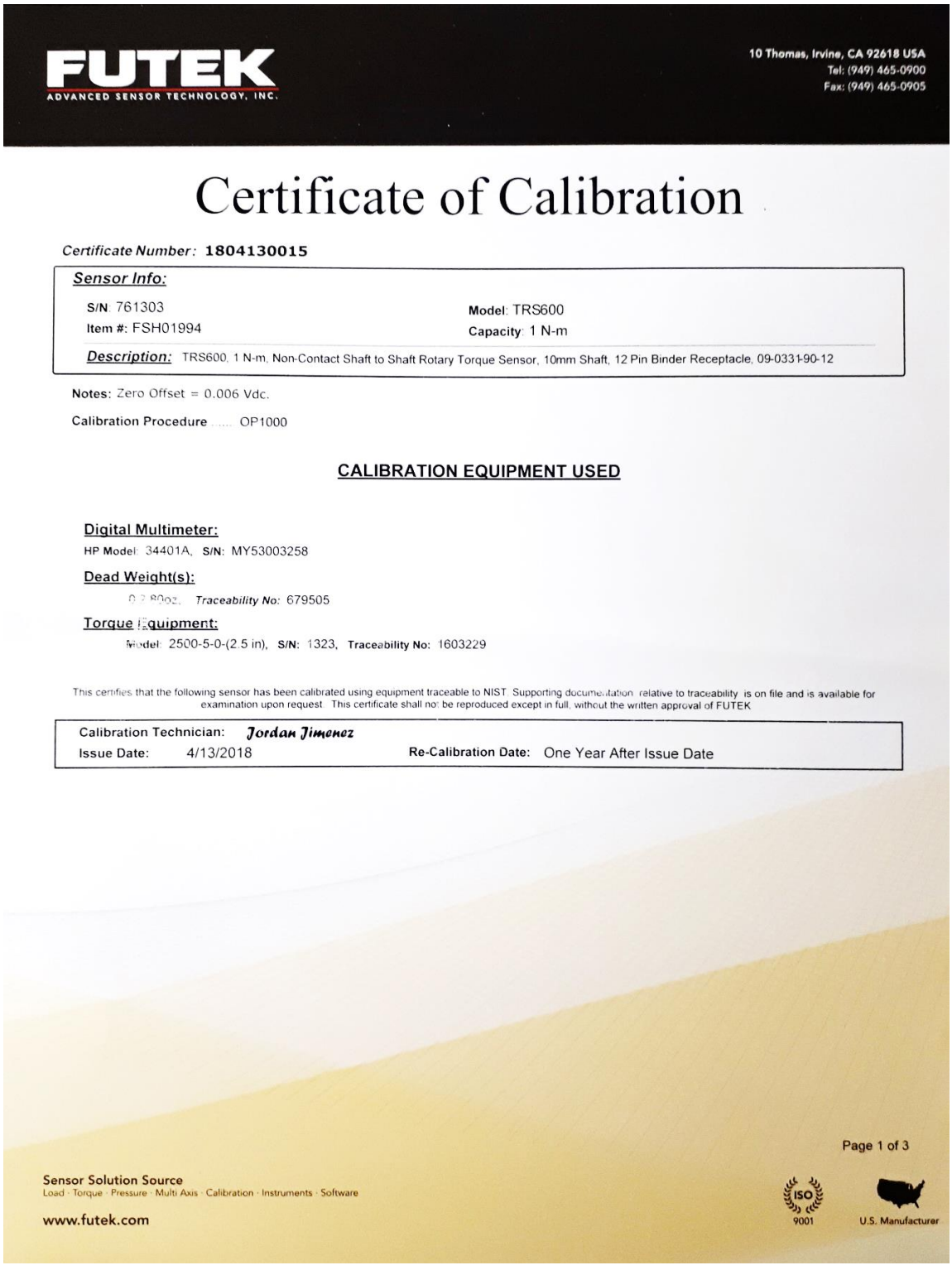

FUTEK
ADVANCED SENSOR TECHNOLOGY, INC.

10 Thomas, Irvine, CA 92618 USA
Tel: (949) 465-0900
Fax: (949) 465-0905

Certificate of Calibration

*Certificate Number:* **1804130015**

***Sensor Info:***

**S/N**: 761303 **Model**: TRS600
**Item #**: FSH01994 **Capacity**: 1 N-m

***Description:*** TRS600, 1 N-m, Non-Contact Shaft to Shaft Rotary Torque Sensor, 10mm Shaft, 12 Pin Binder Receptacle, 09-0331-90-12

**Notes:** Zero Offset = 0.006 Vdc.

**Calibration Procedure** ..... OP1000

**CALIBRATION EQUIPMENT USED**

**Digital Multimeter:**
**HP Model**: 34401A, **S/N**: MY53003258

**Dead Weight(s):**
0.2.80oz. *Traceability No:* 679505

**Torque Equipment:**
Model: 2500-5-0-(2.5 in), **S/N**: 1323, **Traceability No**: 1603229

This certifies that the following sensor has been calibrated using equipment traceable to NIST. Supporting documentation relative to traceability is on file and is available for examination upon request. This certificate shall not be reproduced except in full, without the written approval of FUTEK.

**Calibration Technician:** Jordan Jimenez
**Issue Date:** 4/13/2018 **Re-Calibration Date:** One Year After Issue Date

Page 1 of 3

Sensor Solution Source
Load · Torque · Pressure · Multi Axis · Calibration · Instruments · Software
www.futek.com

ISO 9001
U.S. Manufacturer

FUTEK
ADVANCED SENSOR TECHNOLOGY, INC.

10 Thomas, Irvine, CA 92618 USA
Tel: (949) 465-0900
Fax: (949) 465-0905

*Certificate Number:* **1804130015**

***Single Channel Item***

## *CALIBRATION DATA*

Test Temp: 70 °F (21 °C) Relative Humidity: 51 % Excitation: 20.01 Vdc

### *TorqueCW*

| Load (N-m) | Output (Vdc) | Non-Lin. Error (% R.O.) |
|---|---|---|
| 0.0000 | 0.000 | 0.000 |
| 0.1412 | 0.703 | -0.052 |
| 0.2825 | 1.410 | -0.033 |
| 0.4237 | 2.116 | -0.025 |
| 0.5649 | 2.821 | -0.036 |
| 1.0010 | 5.002 | 0.000 |
| 0.0000 | 0.001 | |

### *TorqueCCW*

| Load (N-m) | Output (Vdc) | Non-Lin. Error (% R.O.) |
|---|---|---|
| 0.0000 | 0.000 | 0.000 |
| 0.1412 | -0.706 | -0.006 |
| 0.2825 | -1.411 | -0.041 |
| 0.4237 | -2.117 | -0.047 |
| 0.5649 | -2.824 | -0.033 |
| 1.0010 | -5.007 | 0.000 |
| 0.0000 | -0.008 | |

FUTEK
ADVANCED SENSOR TECHNOLOGY, INC.

10 Thomas, Irvine, CA 92618 USA
Tel: (949) 465-0900
Fax: (949) 465-0905

*Certificate Number:* **1804130015**

*Single Channel Item*

## *SHUNT CALIBRATION*

| Direction | Shunt Value (KΩ) | Shunt Connection | Output Value (Vdc) | Equivalent Load (N-m) |
|---|---|---|---|---|
| TorqueCW | Internal | Pin A to K | 5.003 | 1.0012 |
| TorqueCCW | Internal | Pin A to K | 5.003 | 1.0002 |

# C.2 Mercury Barometer – Calibration Sheets

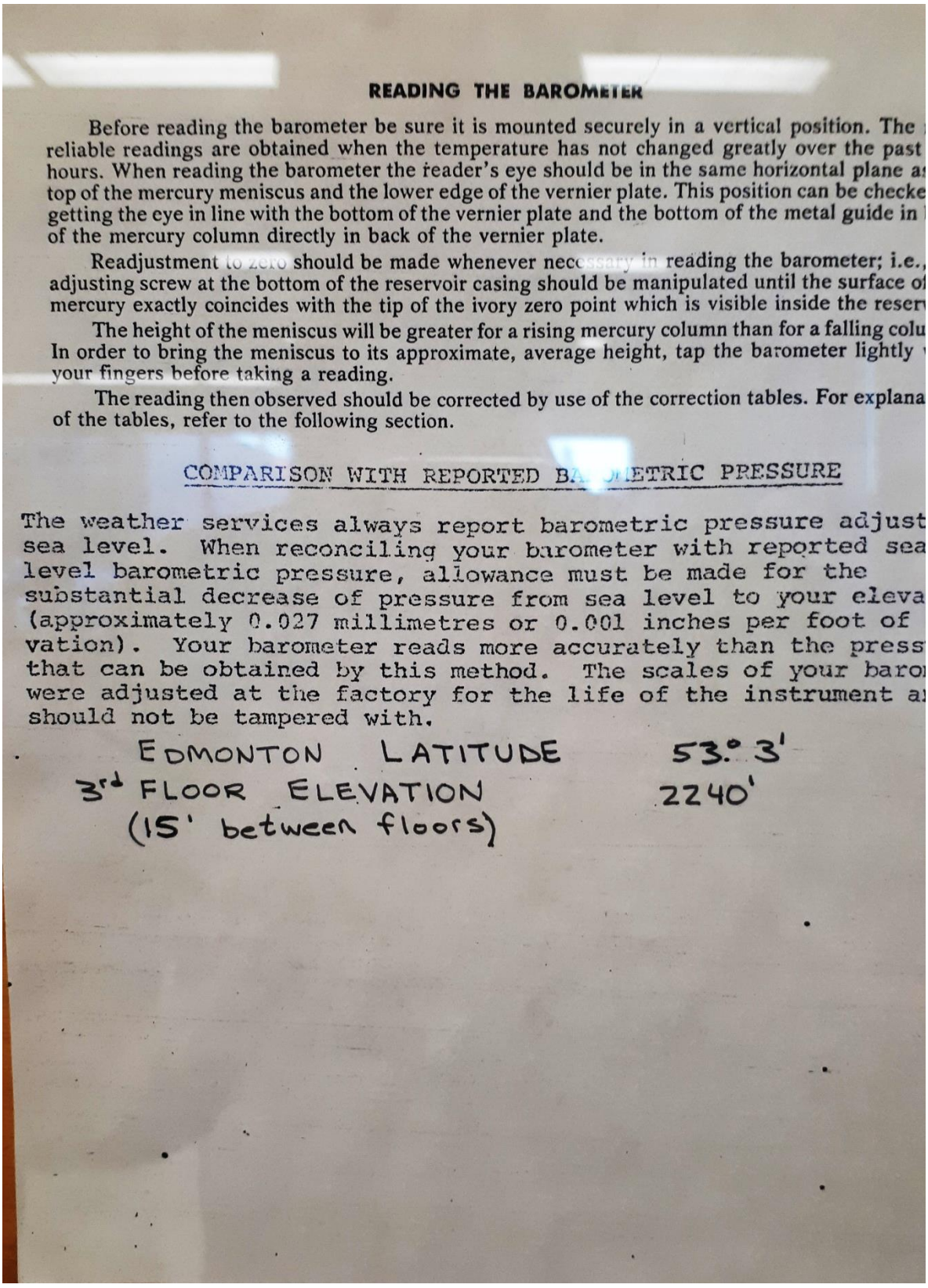

**READING THE BAROMETER**

Before reading the barometer be sure it is mounted securely in a vertical position. The reliable readings are obtained when the temperature has not changed greatly over the past hours. When reading the barometer the reader's eye should be in the same horizontal plane a top of the mercury meniscus and the lower edge of the vernier plate. This position can be checke getting the eye in line with the bottom of the vernier plate and the bottom of the metal guide in of the mercury column directly in back of the vernier plate.

Readjustment to zero should be made whenever necessary in reading the barometer; i.e., adjusting screw at the bottom of the reservoir casing should be manipulated until the surface o mercury exactly coincides with the tip of the ivory zero point which is visible inside the reser

The height of the meniscus will be greater for a rising mercury column than for a falling colu In order to bring the meniscus to its approximate, average height, tap the barometer lightly your fingers before taking a reading.

The reading then observed should be corrected by use of the correction tables. For explana of the tables, refer to the following section.

COMPARISON WITH REPORTED BAROMETRIC PRESSURE

The weather services always report barometric pressure adjust sea level. When reconciling your barometer with reported sea level barometric pressure, allowance must be made for the substantial decrease of pressure from sea level to your eleva (approximately 0.027 millimetres or 0.001 inches per foot of vation). Your barometer reads more accurately than the press that can be obtained by this method. The scales of your baro were adjusted at the factory for the life of the instrument a should not be tampered with.

EDMONTON LATITUDE 53.° 3'

3rd FLOOR ELEVATION 2240'

(15' between floors)

## Table 2. TEMPERATURE CORRECTION, Metric Units

To reduce the reading of the barometer to standard temperature

| Temperature C | Observed Reading of the Barometer in Millimetres or Millibars | | | | | | | | | | | | |
|---|---|---|---|---|---|---|---|---|---|---|---|---|---|
| | 540 | 560 | 580 | 600 | 620 | 640 | 660 | 680 | 700 | 720 | 740 | 760 | 780 |
| | ALL CORRECTIONS SUBTRACTIVE | | | | | | | | | | | | |
| 0 | 0.00 | 0.00 | 0.00 | 0.00 | 0.00 | 0.00 | 0.00 | 0.00 | 0.00 | 0.00 | 0.00 | 0.00 | 0.00 |
| 1 | .09 | .09 | .09 | .10 | .10 | .10 | .11 | .11 | .11 | .12 | .12 | .12 | .13 |
| 2 | .18 | .18 | .19 | .20 | .20 | .21 | .22 | .22 | .23 | .24 | .24 | .25 | .25 |
| 3 | .26 | .27 | .28 | .29 | .30 | .31 | .32 | .33 | .34 | .35 | .36 | .37 | .38 |
| 4 | .35 | .37 | .38 | .39 | .40 | .42 | .43 | .44 | .46 | .47 | .48 | .50 | .51 |
| 5 | 0.44 | 0.46 | 0.47 | 0.49 | 0.51 | 0.52 | 0.54 | 0.56 | 0.57 | 0.59 | 0.60 | 0.62 | 0.64 |
| 6 | .53 | .55 | .57 | .59 | .61 | .63 | .65 | .67 | .69 | .71 | .72 | .74 | .76 |
| 7 | .62 | .64 | .66 | .69 | .71 | .73 | .75 | .78 | .80 | .82 | .85 | .87 | .89 |
| 8 | .70 | .73 | .76 | .78 | .81 | .84 | .86 | .89 | .91 | .94 | .97 | .99 | 1.02 |
| 9 | .79 | .82 | .85 | .88 | .91 | .94 | .97 | 1.00 | 1.03 | 1.06 | 1.09 | 1.12 | 1.15 |
| 10 | 0.88 | 0.91 | 0.95 | 0.98 | 1.01 | 1.04 | 1.08 | 1.11 | 1.14 | 1.17 | 1.21 | 1.24 | 1.27 |
| 11 | .97 | 1.00 | 1.04 | 1.08 | 1.11 | 1.15 | 1.18 | 1.22 | 1.26 | 1.29 | 1.33 | 1.36 | 1.40 |
| 12 | 1.06 | 1.10 | 1.13 | 1.17 | 1.21 | 1.25 | 1.29 | 1.33 | 1.37 | 1.41 | 1.45 | 1.49 | 1.53 |
| 13 | 1.14 | 1.19 | 1.23 | 1.27 | 1.31 | 1.36 | 1.40 | 1.44 | 1.48 | 1.53 | 1.57 | 1.61 | 1.65 |
| 14 | 1.23 | 1.28 | 1.32 | 1.37 | 1.41 | 1.46 | 1.51 | 1.55 | 1.60 | 1.64 | 1.69 | 1.73 | 1.78 |
| 15 | 1.32 | 1.37 | 1.42 | 1.47 | 1.52 | 1.56 | 1.61 | 1.66 | 1.71 | 1.76 | 1.81 | 1.86 | 1.91 |
| 16 | 1.41 | 1.46 | 1.51 | 1.56 | 1.62 | 1.67 | 1.72 | 1.77 | 1.82 | 1.88 | 1.93 | 1.98 | 2.03 |
| 17 | 1.50 | 1.55 | 1.61 | 1.66 | 1.72 | 1.77 | 1.83 | 1.88 | 1.94 | 1.99 | 2.05 | 2.10 | 2.16 |
| 18 | 1.58 | 1.64 | 1.70 | 1.76 | 1.82 | 1.88 | 1.93 | 1.99 | 2.05 | 2.11 | 2.17 | 2.23 | 2.29 |
| 19 | 1.67 | 1.73 | 1.79 | 1.86 | 1.92 | 1.98 | 2.04 | 2.10 | 2.17 | 2.23 | 2.29 | 2.35 | 2.41 |
| 20 | 1.76 | 1.82 | 1.89 | 1.95 | 2.02 | 2.08 | 2.15 | 2.21 | 2.28 | 2.34 | 2.41 | 2.47 | 2.54 |
| 21 | 1.85 | 1.91 | 1.98 | 2.05 | 2.12 | 2.19 | 2.26 | 2.32 | 2.39 | 2.46 | 2.53 | 2.60 | 2.67 |
| 22 | 1.93 | 2.01 | 2.08 | 2.15 | 2.22 | 2.29 | 2.36 | 2.43 | 2.51 | 2.58 | 2.65 | 2.72 | 2.79 |
| 23 | 2.02 | 2.10 | 2.17 | 2.25 | 2.32 | 2.40 | 2.47 | 2.54 | 2.62 | 2.69 | 2.77 | 2.84 | 2.92 |
| 24 | 2.11 | 2.19 | 2.26 | 2.34 | 2.42 | 2.50 | 2.58 | 2.66 | 2.73 | 2.81 | 2.89 | 2.97 | 3.05 |
| 25 | 2.20 | 2.28 | 2.36 | 2.44 | 2.52 | 2.60 | 2.68 | 2.77 | 2.85 | 2.93 | 3.01 | 3.09 | 3.17 |
| 26 | 2.28 | 2.37 | 2.45 | 2.54 | 2.62 | 2.71 | 2.79 | 2.88 | 2.96 | 3.04 | 3.13 | 3.21 | 3.30 |
| 27 | 2.37 | 2.46 | 2.55 | 2.63 | 2.72 | 2.81 | 2.90 | 2.99 | 3.07 | 3.16 | 3.25 | 3.34 | 3.42 |
| 28 | 2.46 | 2.55 | 2.64 | 2.73 | 2.82 | 2.91 | 3.00 | 3.10 | 3.19 | 3.28 | 3.37 | 3.46 | 3.55 |
| 29 | 2.55 | 2.64 | 2.73 | 2.83 | 2.92 | 3.02 | 3.11 | 3.21 | 3.30 | 3.39 | 3.49 | 3.58 | 3.68 |
| 30 | 2.63 | 2.73 | 2.83 | 2.93 | 3.02 | 3.12 | 3.22 | 3.32 | 3.41 | 3.51 | 3.61 | 3.71 | 3.80 |
| 31 | 2.72 | 2.82 | 2.92 | 3.02 | 3.12 | 3.22 | 3.32 | 3.43 | 3.53 | 3.63 | 3.73 | 3.83 | 3.93 |
| 32 | 2.81 | 2.91 | 3.02 | 3.12 | 3.22 | 3.33 | 3.43 | 3.54 | 3.64 | 3.74 | 3.85 | 3.95 | 4.05 |
| 33 | 2.89 | 3.00 | 3.11 | 3.22 | 3.32 | 3.43 | 3.54 | 3.64 | 3.75 | 3.86 | 3.97 | 4.07 | 4.18 |
| 34 | 2.98 | 3.09 | 3.20 | 3.31 | 3.42 | 3.53 | 3.64 | 3.75 | 3.87 | 3.98 | 4.09 | 4.20 | 4.31 |

## Table 2 Continued. TEMPERATURE CORRECTION, Metric Units

To reduce the reading of the barometer to standard temperature

| Tempera-ture C | Observed Reading of the Barometer in Millimetres or Millibars | | | | | | | | | | | | |
|---|---|---|---|---|---|---|---|---|---|---|---|---|---|
| | 800 | 820 | 840 | 860 | 880 | 900 | 920 | 940 | 960 | 980 | 1000 | 1020 | 1040 |
| | ALL CORRECTIONS SUBTRACTIVE | | | | | | | | | | | | |
| 0 | 0.00 | 0.00 | 0.00 | 0.00 | 0.00 | 0.00 | 0.00 | 0.00 | 0.00 | 0.00 | 0.00 | 0.00 | 0.00 |
| 1 | .13 | .13 | .14 | .14 | .14 | .15 | .15 | .15 | .16 | .16 | .16 | .17 | .17 |
| 2 | .26 | .27 | .27 | .28 | .29 | .29 | .30 | .31 | .31 | .32 | .33 | .33 | .34 |
| 3 | .39 | .40 | .41 | .42 | .43 | .44 | .45 | .46 | .47 | .48 | .49 | .50 | .51 |
| 4 | .52 | .54 | .55 | .56 | .57 | .59 | .60 | .61 | .63 | .64 | .65 | .67 | .68 |
| 5 | 0.65 | 0.67 | 0.69 | 0.70 | 0.72 | 0.73 | 0.75 | 0.77 | 0.78 | 0.80 | 0.82 | 0.83 | 0.85 |
| 6 | .78 | .80 | .82 | .84 | .86 | .88 | .90 | .92 | .94 | .96 | .98 | 1.00 | 1.02 |
| 7 | .91 | .94 | .96 | .98 | 1.01 | 1.03 | 1.05 | 1.07 | 1.10 | 1.12 | 1.14 | 1.17 | 1.19 |
| 8 | 1.04 | 1.07 | 1.10 | 1.12 | 1.15 | 1.17 | 1.20 | 1.23 | 1.25 | 1.28 | 1.31 | 1.33 | 1.36 |
| 9 | 1.17 | 1.20 | 1.23 | 1.26 | 1.29 | 1.32 | 1.35 | 1.38 | 1.41 | 1.44 | 1.47 | 1.50 | 1.53 |
| 10 | 1.30 | 1.34 | 1.37 | 1.40 | 1.44 | 1.47 | 1.50 | 1.53 | 1.57 | 1.60 | 1.63 | 1.66 | 1.70 |
| 11 | 1.44 | 1.47 | 1.51 | 1.54 | 1.58 | 1.61 | 1.65 | 1.69 | 1.72 | 1.76 | 1.79 | 1.83 | 1.87 |
| 12 | 1.57 | 1.60 | 1.64 | 1.68 | 1.72 | 1.76 | 1.80 | 1.84 | 1.88 | 1.92 | 1.96 | 2.00 | 2.03 |
| 13 | 1.70 | 1.74 | 1.78 | 1.82 | 1.86 | 1.91 | 1.95 | 1.99 | 2.03 | 2.08 | 2.12 | 2.16 | 2.20 |
| 14 | 1.83 | 1.87 | 1.92 | 1.96 | 2.01 | 2.05 | 2.10 | 2.14 | 2.19 | 2.24 | 2.28 | 2.33 | 2.37 |
| 15 | 1.96 | 2.00 | 2.05 | 2.10 | 2.15 | 2.20 | 2.25 | 2.30 | 2.35 | 2.40 | 2.44 | 2.49 | 2.54 |
| 16 | 2.09 | 2.14 | 2.19 | 2.24 | 2.29 | 2.35 | 2.40 | 2.45 | 2.50 | 2.55 | 2.61 | 2.66 | 2.71 |
| 17 | 2.22 | 2.27 | 2.33 | 2.38 | 2.44 | 2.49 | 2.55 | 2.60 | 2.66 | 2.71 | 2.77 | 2.82 | 2.88 |
| 18 | 2.35 | 2.40 | 2.46 | 2.52 | 2.58 | 2.64 | 2.70 | 2.76 | 2.81 | 2.87 | 2.93 | 2.99 | 3.05 |
| 19 | 2.48 | 2.54 | 2.60 | 2.66 | 2.72 | 2.78 | 2.85 | 2.91 | 2.97 | 3.03 | 3.09 | 3.16 | 3.22 |
| 20 | 2.60 | 2.67 | 2.74 | 2.80 | 2.87 | 2.93 | 3.00 | 3.06 | 3.13 | 3.19 | 3.26 | 3.32 | 3.39 |
| 21 | 2.73 | 2.80 | 2.87 | 2.94 | 3.01 | 3.08 | 3.14 | 3.21 | 3.28 | 3.35 | 3.42 | 3.49 | 3.56 |
| 22 | 2.86 | 2.94 | 3.01 | 3.08 | 3.15 | 3.22 | 3.29 | 3.37 | 3.44 | 3.51 | 3.58 | 3.65 | 3.72 |
| 23 | 2.99 | 3.07 | 3.14 | 3.22 | 3.29 | 3.37 | 3.44 | 3.52 | 3.59 | 3.67 | 3.74 | 3.82 | 3.89 |
| 24 | 3.12 | 3.20 | 3.28 | 3.36 | 3.44 | 3.51 | 3.59 | 3.67 | 3.75 | 3.83 | 3.90 | 3.98 | 4.06 |
| 25 | 3.25 | 3.33 | 3.42 | 3.50 | 3.58 | 3.66 | 3.74 | 3.82 | 3.90 | 3.99 | 4.07 | 4.15 | 4.23 |
| 26 | 3.38 | 3.47 | 3.55 | 3.64 | 3.72 | 3.81 | 3.89 | 3.97 | 4.06 | 4.14 | 4.23 | 4.31 | 4.40 |
| 27 | 3.51 | 3.60 | 3.69 | 3.78 | 3.86 | 3.95 | 4.04 | 4.13 | 4.21 | 4.30 | 4.39 | 4.48 | 4.57 |
| 28 | 3.64 | 3.73 | 3.82 | 3.91 | 4.01 | 4.10 | 4.19 | 4.28 | 4.37 | 4.46 | 4.55 | 4.64 | 4.73 |
| 29 | 3.77 | 3.87 | 3.96 | 4.05 | 4.15 | 4.24 | 4.34 | 4.43 | 4.53 | 4.62 | 4.71 | 4.81 | 4.90 |
| 30 | 3.90 | 4.00 | 4.10 | 4.19 | 4.29 | 4.39 | 4.49 | 4.58 | 4.68 | 4.78 | 4.88 | 4.97 | 5.07 |
| 31 | 4.03 | 4.13 | 4.23 | 4.33 | 4.43 | 4.53 | 4.63 | 4.73 | 4.84 | 4.94 | 5.04 | 5.14 | 5.24 |
| 32 | 4.16 | 4.26 | 4.37 | 4.47 | 4.57 | 4.68 | 4.78 | 4.89 | 4.99 | 5.09 | 5.20 | 5.30 | 5.41 |
| 33 | 4.29 | 4.40 | 4.50 | 4.61 | 4.72 | 4.82 | 4.93 | 5.04 | 5.15 | 5.25 | 5.36 | 5.47 | 5.57 |
| 34 | 4.42 | 4.53 | 4.64 | 4.75 | 4.86 | 4.97 | 5.08 | 5.19 | 5.30 | 5.41 | 5.52 | 5.63 | 5.74 |

## Table 3. GRAVITY CORRECTION

To reduce the reading of the barometer to standard gravity

| Latitude N or S | Height of the mercury column: Inches 26 | 27 | 28 | 29 | 30 | Millimetres 680 | 700 | 720 | 740 | 760 | 780 | Millibars 900 | 950 | 1000 | 1050 |
|---|---|---|---|---|---|---|---|---|---|---|---|---|---|---|---|
| | LATITUDE 0° TO 45° THE CORRECTION IS TO BE SUBTRACTED | | | | | | | | | | | | | | |
| | LATITUDE 46° TO 90° THE CORRECTION IS TO BE ADDED | | | | | | | | | | | | | | |
| 90° | +.067 | +.070 | +.073 | +.075 | +.078 | +1.76 | +1.82 | +1.8 | | 1.97 | +2.02 | +2.33 | +2.46 | +2.59 | +2.72 |
| 88 | .067 | .070 | .072 | .075 | .078 | 1.76 | 1.81 | 1.86 | 1.9 | 1.97 | 2.02 | 2.33 | 2.46 | 2.59 | 2.72 |
| 86 | .067 | .069 | .072 | .074 | .077 | 1.75 | 1.80 | 1.85 | 1.90 | 1.95 | 2.00 | 2.31 | 2.44 | 2.57 | 2.70 |
| 84 | .066 | .068 | .071 | .074 | .076 | 1.72 | 1.77 | 1.83 | 1.88 | 1.93 | 1.98 | 2.28 | 2.41 | 2.54 | 2.66 |
| 82 | .065 | .067 | .070 | .072 | .075 | 1.69 | 1.74 | 1.79 | 1.84 | 1.89 | 1.94 | 2.24 | 2.37 | 2.49 | 2.62 |
| 80 | +.063 | +.066 | +.068 | +.071 | +.073 | +1.65 | +1.70 | +1.75 | +1.80 | +1.85 | +1.90 | +2.19 | +2.31 | +2.43 | +2.56 |
| 78 | .061 | .064 | .066 | .069 | .071 | 1.61 | 1.65 | 1.70 | 1.75 | 1.80 | 1.84 | 2.13 | 2.25 | 2.36 | 2.48 |
| 76 | .059 | .062 | .064 | .066 | .068 | 1.55 | 1.60 | 1.64 | 1.69 | 1.74 | 1.78 | 2.05 | 2.17 | 2.28 | 2.40 |
| 74 | .057 | .059 | .061 | .064 | .066 | 1.49 | 1.53 | 1.58 | 1.62 | 1.66 | 1.71 | 1.97 | 2.08 | 2.19 | 2.30 |
| 72 | .054 | .056 | .058 | .061 | .063 | 1.42 | 1.46 | 1.50 | 1.54 | 1.59 | 1.63 | 1.88 | 1.98 | 2.09 | 2.19 |
| 70 | +.051 | +.053 | +.055 | +.057 | +.059 | +1.34 | +1.38 | +1.42 | +1.46 | +1.50 | +1.54 | +1.78 | +1.87 | +1.97 | +2.07 |
| 68 | .048 | .050 | .052 | .054 | .056 | 1.26 | 1.30 | 1.33 | 1.37 | 1.41 | 1.44 | 1.67 | 1.76 | 1.85 | 1.94 |
| 66 | .045 | .046 | .048 | .050 | .052 | 1.17 | 1.20 | 1.24 | 1.27 | 1.31 | 1.34 | 1.55 | 1.63 | 1.72 | 1.80 |
| 64 | .041 | .043 | .044 | .046 | .047 | 1.07 | 1.10 | 1.13 | 1.17 | 1.20 | 1.23 | 1.42 | 1.50 | 1.58 | 1.65 |
| 62 | .037 | .039 | .040 | .041 | .043 | 0.97 | 1.00 | 1.03 | 1.06 | 1.08 | 1.11 | 1.28 | 1.36 | 1.43 | 1.50 |
| 60 | +.033 | +.034 | +.036 | +.037 | +.038 | +0.86 | +0.89 | +0.91 | +0.94 | +0.97 | +0.99 | +1.14 | +1.21 | +1.27 | +1.33 |
| 58 | .029 | .030 | .031 | .032 | .033 | 0.75 | 0.78 | 0.80 | 0.82 | 0.84 | 0.86 | 1.00 | 1.05 | 1.11 | 1.16 |
| 56 | .024 | .025 | .026 | .027 | .028 | 0.64 | 0.66 | 0.68 | 0.69 | 0.71 | 0.73 | 0.84 | 0.89 | 0.94 | 0.99 |
| 54 | .020 | .021 | .021 | .022 | .023 | 0.52 | 0.54 | 0.55 | 0.57 | 0.58 | 0.60 | 0.69 | 0.73 | 0.77 | 0.80 |
| 52 | .015 | .016 | .016 | .017 | .018 | 0.40 | 0.41 | 0.42 | 0.44 | 0.45 | 0.46 | 0.53 | 0.56 | 0.59 | 0.62 |
| 50 | +.011 | +.011 | +.011 | +.012 | +.012 | +0.28 | +0.29 | +0.29 | +0.30 | +0.31 | +0.32 | +0.37 | +0.39 | +0.41 | +0.43 |
| 48 | .006 | .006 | .006 | .007 | .007 | 0.15 | 0.16 | 0.16 | 0.17 | 0.17 | 0.18 | 0.20 | 0.21 | 0.23 | 0.24 |
| 46 | +.001 | +.001 | +.001 | +.001 | +.001 | +0.03 | +0.03 | +0.03 | +0.03 | +0.03 | +0.03 | +0.04 | +0.04 | +0.04 | +0.04 |
| 45 | −.001 | −.001 | −.001 | −.001 | −.001 | −0.03 | −0.03 | −0.04 | −0.04 | −0.04 | −0.04 | −0.04 | −0.05 | −0.05 | −0.05 |
| 44 | .004 | .004 | .004 | .004 | .004 | 0.10 | 0.10 | 0.10 | 0.11 | 0.11 | 0.11 | 0.13 | 0.13 | 0.14 | 0.15 |
| 42 | .008 | .009 | .009 | .009 | .010 | 0.22 | 0.23 | 0.23 | 0.24 | 0.25 | 0.25 | 0.29 | 0.31 | 0.33 | 0.34 |
| 40 | −.013 | −.014 | −.014 | −.015 | −.015 | −0.35 | −0.36 | −0.37 | −0.38 | −0.39 | −0.40 | −0.46 | −0.48 | −0.51 | −0.53 |
| 38 | .018 | .019 | .019 | .020 | .021 | 0.47 | 0.48 | 0.50 | 0.51 | 0.52 | 0.54 | 0.62 | 0.65 | 0.69 | 0.72 |
| 36 | .022 | .023 | .024 | .025 | .026 | 0.59 | 0.61 | 0.62 | 0.64 | 0.66 | 0.67 | 0.78 | 0.82 | 0.86 | 0.91 |
| 34 | .027 | .028 | .029 | .030 | .031 | 0.71 | 0.73 | 0.75 | 0.77 | 0.79 | 0.81 | 0.93 | 0.99 | 1.04 | 1.09 |
| 32 | .031 | .033 | .034 | .035 | .036 | 0.82 | 0.84 | 0.87 | 0.89 | 0.92 | 0.94 | 1.08 | 1.14 | 1.20 | 1.27 |
| 30 | −.036 | −.037 | −.038 | −.040 | −.041 | −0.93 | −0.96 | −0.98 | −1.01 | −1.04 | −1.07 | −1.23 | −1.30 | −1.37 | −1.44 |
| 28 | .040 | .041 | .043 | .044 | .046 | 1.04 | 1.07 | 1.10 | 1.13 | 1.16 | 1.19 | 1.37 | 1.45 | 1.52 | 1.60 |
| 26 | .043 | .045 | .047 | .048 | .050 | 1.14 | 1.17 | 1.20 | 1.24 | 1.27 | 1.30 | 1.50 | 1.59 | 1.67 | 1.75 |
| 24 | .047 | .049 | .051 | .053 | .054 | 1.23 | 1.27 | 1.30 | 1.34 | 1.38 | 1.41 | 1.63 | 1.72 | 1.81 | 1.90 |
| 22 | .051 | .052 | .054 | .056 | .058 | 1.32 | 1.36 | 1.40 | 1.44 | 1.48 | 1.52 | 1.75 | 1.85 | 1.94 | 2.04 |
| 20 | −.054 | −.056 | −.058 | −.060 | −.062 | −1.41 | −1.45 | −1.49 | −1.53 | −1.57 | −1.61 | −1.86 | −1.96 | −2.07 | −2.17 |
| 18 | .057 | .059 | .061 | .063 | .065 | 1.48 | 1.53 | 1.57 | 1.61 | 1.66 | 1.70 | 1.96 | 2.07 | 2.18 | 2.29 |
| 16 | .059 | .062 | .064 | .066 | .068 | 1.55 | 1.60 | 1.64 | 1.69 | 1.73 | 1.78 | 2.05 | 2.17 | 2.28 | 2.40 |
| 14 | .062 | .064 | .066 | .069 | .071 | 1.61 | 1.66 | 1.71 | 1.76 | 1.80 | 1.85 | 2.14 | 2.26 | 2.37 | 2.49 |
| 12 | .064 | .066 | .069 | .071 | .074 | 1.67 | 1.72 | 1.77 | 1.82 | 1.87 | 1.91 | 2.21 | 2.33 | 2.45 | 2.58 |
| 10 | −.066 | −.068 | −.071 | −.073 | −.076 | −1.72 | −1.77 | −1.82 | −1.87 | −1.92 | −1.97 | −2.27 | −2.40 | −2.52 | −2.65 |
| 8 | .067 | .070 | .072 | .075 | .077 | 1.75 | 1.81 | 1.86 | 1.91 | 1.96 | 2.01 | 2.32 | 2.45 | 2.58 | 2.71 |
| 6 | .068 | .071 | .073 | .076 | .079 | 1.78 | 1.84 | 1.89 | 1.94 | 1.99 | 2.05 | 2.36 | 2.49 | 2.62 | 2.76 |
| 4 | .069 | .072 | .074 | .077 | .080 | 1.81 | 1.86 | 1.91 | 1.97 | 2.02 | 2.07 | 2.39 | 2.52 | 2.66 | 2.79 |
| 2 | .070 | .072 | .075 | .078 | .080 | 1.82 | 1.87 | 1.93 | 1.98 | 2.03 | 2.09 | 2.41 | 2.54 | 2.67 | 2.81 |
| 0 | −.070 | −.072 | −.075 | −.078 | −.080 | −1.82 | −1.88 | −1.93 | −1.98 | −2.04 | −2.09 | −2.41 | −2.55 | −2.68 | −2.82 |

Tables 1 thru 3 are condensed from the "Smithsonian Meteorological Tables", Sixth Revised Edition 1949, Fifth Reprint 1971; and are corrected for consistancy with the recommendations contained in the "International Meteorological Tables", World Meteorological Organization, 1966, with amendments thru July 1973.

# Appendix D: Schmidt Model

The code showcased below combines the Schmidt model and the fundamental efficiency theorem to predict the shaft work.

```
function
[W_ind,FW,W_shaft,P_shaft,P_cycle,Vtotal]=Schmidt_Forced_Work(Temp_Hot_Disp_A
vg,Temp_Cold_Disp_Avg,Crank_Arm_Val,Phase_Angle,Period,Pres_Atmo,MCP,Mech_E)
%% Schmidt Analysis and Forced Work

% Written by Connor Speer, November 2016
% Forced Work modifications - September 2017
%
% This script calculates the pressure, heat transfer rates, work done, and
% efficiency of a Stirling engine using the Schmidt analysis equations
% which may be found in Appendix A of "Stirling Cycle Engine Analysis" by
% Urieli and Berchowitz. The equation set summary is on page 46.
%
% The Schmidt analysis uses the Isothermal model and assumes sinusoidal
% volume variations to obtain closed form solutions.
%
% With pressure functions from the isothermal model, the forced work
% analysis determines the forced work in the cycle and deducts it from the
% indicated work with the mechanical effectiveness.
%
% See Senft Pg 17 for a definition of forced work.

%% Define Working Gas Properties
R = 287; % Specific ideal gas constant of working gas [J/kg K]

%% Imported Engine Variables
TH = 273.15+Temp_Hot_Disp_Avg;     % Hot side gas temperature in [K].
TC = 273.15+Temp_Cold_Disp_Avg;     % Cold side gas temperature in [K].

Phase_Ang=Phase_Angle;       % Phase Angle (Theta)
f = 1/Period;                % Operating Frequency [cycles/s]

%% Define Engine Variables (EP-1)

Pp_cal= 2*Crank_Arm_Val/1000; % Power Piston Crank Arm Length [m]

V_max = 0.001834674; % Maximum Power Piston Volume [m^3]
S_max = 100/1000; % Maximum Stroke Position [m]

Vswp = V_max/S_max*Pp_cal; % Piston swept volume in [m^3].

Dd = 0.254;  % Displacer diameter in [m].
Sd = 0.116;  % Displacer stroke in [m].

Vswd = (pi/4)*(Dd^2)*(Sd); % Displacer swept volume in [m^3].
```

```
V_min = 0.008890682; % Minimum Engine Volume [m^3]
Vd = 0.003012875; % Engine Dead Volume [m^3]

% Phase angle of the expansion space volume variations relative to
% the compression space volume variations.
alpha = ((Phase_Ang)/180)*pi; %[rad]

Pfill = MCP; % Engine fill pressure [Pa]

E = Mech_E; % Mechanism effectiveness

%%%%%%%%%%%%%%%%%%%%%%%%%%%%%%%%%%%%%%%%%%%%%%%%%%%%%%%%%%%%%%%%%%%%%%%%%%%%%%%
% Buffer Pressure

P_buffer_min = Pres_Atmo;
P_buffer_max = Pres_Atmo;

%% Cycle Indicator Diagram
% This can be calculated using any model you like. Experimental data could
% also be used.

% Gamma Schmidt Analysis - Written by Jason Michaud, June 2016
% Modified by Connor Speer, November 2016
%
% This script calculates the pressure, heat transfer rates, work done, and
% efficiency of a Gamma Stirling engine using the Schmidt analysis
% equations which may be found in Appendix C of "Mechanical Efficiency of
% Heat Engines" by James R. Senft.
%
% The Schmidt analysis uses the Isothermal model and assumes sinusoidal
% volume variations to obtain closed form solutions.

% Constant Calculations
tao = TC/TH; % Temperature ratio
kappa = Vswp/Vswd; % Ratio of piston swept volume to displacer swept volume
chi = Vd/Vswd; % Dead volume ratio

% Senft Volume calculations
theta = (1:1:360)*(pi/180); % Define crank angle as zero when compression
space volume is maximum.
Ve = (Vswd*0.5)*(1+cos(theta+alpha)); % Expansion space volume in [m^3].
Vc = Vswd-Ve+(Vswp*0.5*(1+cos(theta))); % Compression space volume in [m^3].
Vtotal = Ve + Vc + Vd;

% Senft Pressure calculations
M = (Pfill*(V_min+Vswp))/(R*(TH+TC)/2);% Mass of gas in the engine [kg].
Y = 1 + tao + kappa + ((4*chi*tao)/(1+tao));
A = kappa - ((1-tao)*cos(alpha));
B = (1-tao)*sin(alpha);
phi = acos(A/(sqrt((A^2) + (B^2))));
X = sqrt((A^2) + (B^2));

% Calculation of the pressures.
Pmean = (2*M*R*TC)/(Vswd*sqrt((Y^2)-(X^2))); % Mean pressure in [Pa].
```

```
%% Change the mass of the working fluid to get the correct mean cycle
pressure
Pdif = Pfill - Pmean;

if Pdif >=0
    pns = 1;
else
    pns=-1;
end

mass_res=0.00000001;

while Pdif > 1

M=pns*mass_res+M;
    % M = (Pfill*(Vd+Vswp+Vswd))/(R*((TH+TC)/2));% Mass of gas in the engine
[kg].
Y = 1 + tao + kappa + ((4*chi*tao)/(1+tao));
A = kappa - ((1-tao)*cos(alpha));
B = (1-tao)*sin(alpha);
phi = acos(A/(sqrt((A^2) + (B^2))));
X = sqrt((A^2) + (B^2));

% Calculation of the pressures.
Pmean = (2*M*R*TC)/(Vswd*sqrt((Y^2)-(X^2))); % Mean pressure in [Pa].
Pmax = (2*M*R*TC)/(Vswd*(Y - X)); % Maximum cycle pressure in [Pa].
Pmin = (2*M*R*TC)/(Vswd*(Y + X)); % Minimum cycle pressure in [Pa].

Pdif = Pfill - Pmean;

end

P_cycle = (Pmean*sqrt((Y^2)-(X^2))./(Y + (X*cos(theta - phi)));

% Calculation of heat and work.
W = (pi*(1-tao)*(Vswd+Vswp)*Pmean*kappa*sin(alpha))/((kappa+1)*(sqrt((Y^2)-
(X^2))+Y));

% Calculate Indicated Work by Integrating the Indicator Diagram
W_ind = polyarea(Vtotal,P_cycle);

%Function buffer pressure for cycle volume
P_buffer=Pres_Atmo;

%%%%%%%%%%%%%%%%%%%%%%%%%%%%%%%%%%%%%%%%%%%%%%%%%%%%%%%%%%%%%%%%%%%%%%%%%%%
% Determine the Volume Ranges Where Forced Work Occurs
%%%%%%%%%%%%%%%%%%%%%%%%%%%%%%%%%%%%%%%%%%%%%%%%%%%%%%%%%%%%%%%%%%%%%%%%%%%

% Calculate the difference b/w cycle and buffer pressure at each point

P_diff = P_cycle - P_buffer;

LEN = length(Vtotal);
```

```
dV = zeros(1,LEN);
dV(2:LEN-1) = (Vtotal(3:LEN)-Vtotal(1:LEN-2));
dV(1) = (Vtotal(2)-Vtotal(LEN));
dV(LEN) = (Vtotal(1)-Vtotal(LEN-1));
dV = dV/2;

FW = 0;

% Use DEFINITION of Forced work and Rienmann Sums to find final FW
for i = 1:length(dV)
    if (sign(dV(i)) ~= sign(P_diff(i))) % If they are of opposite sign
        FW = FW + abs(P_diff(i)*dV(i));
    end
end

W_shaft = (E*W_ind) - (((1/E) - E)*FW); %Shaft Work

P_shaft = (W_shaft*f); % Power output in [W].
end
```

# Appendix E: Drawing Packages

This section contains the drawing packages for the Mark 1, Mark 2 and the EP-1.

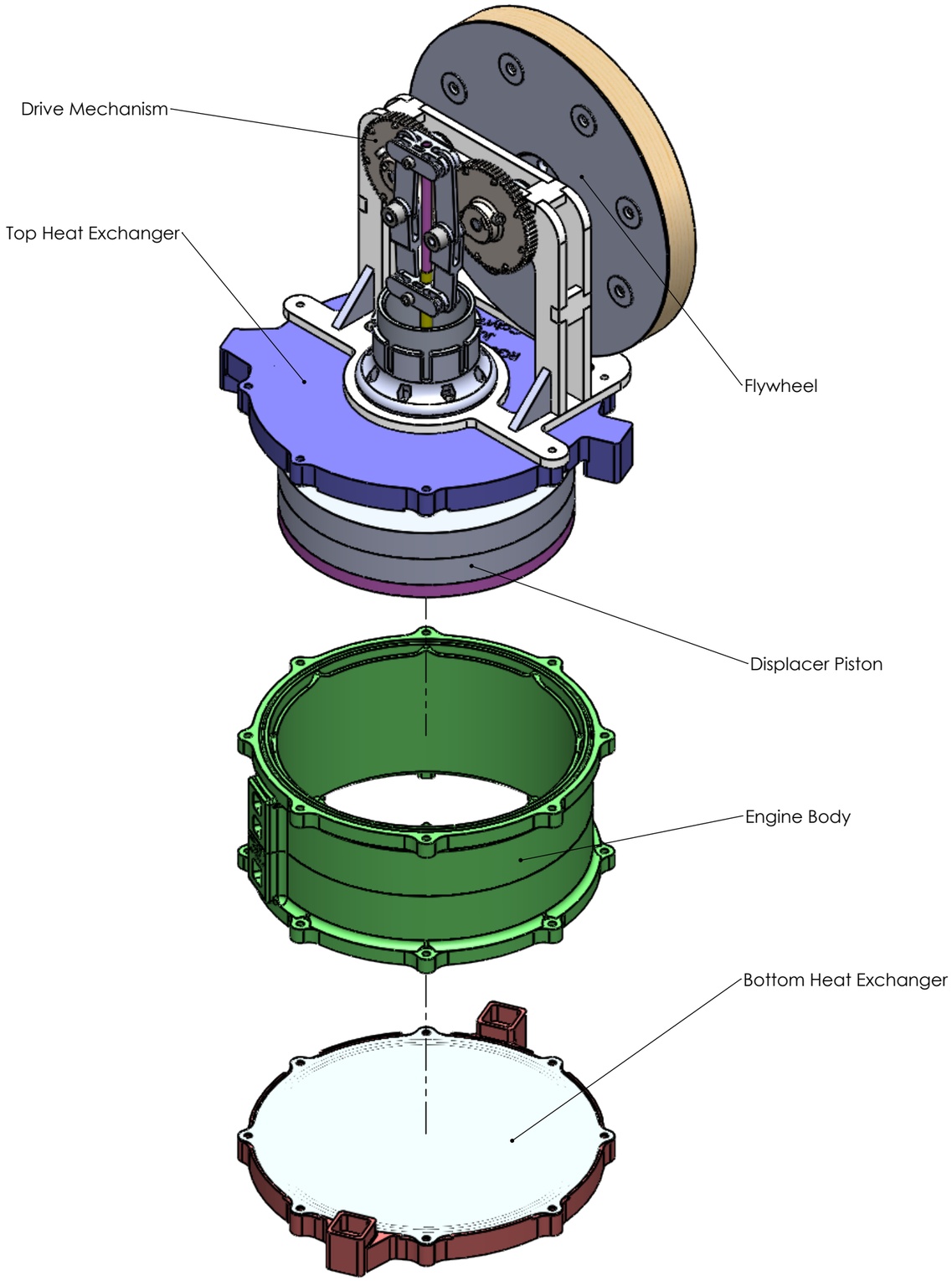


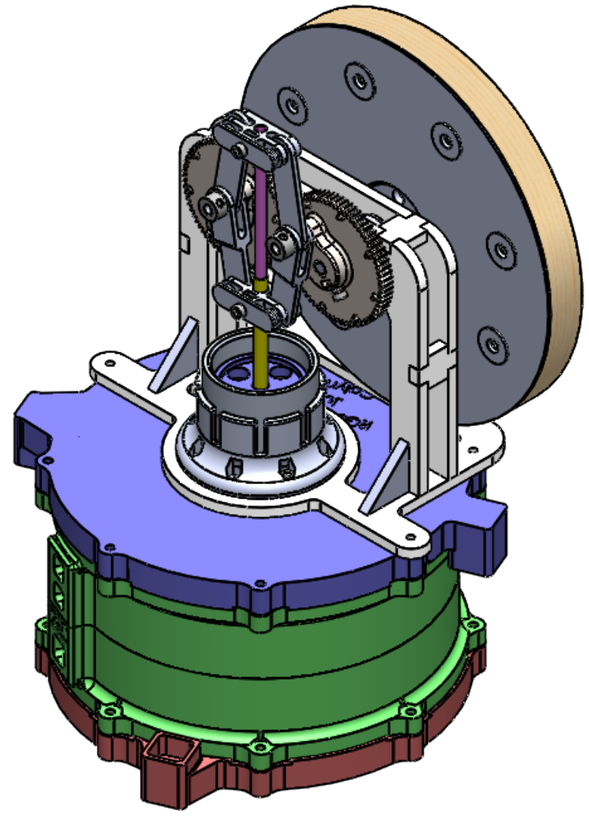

| | | | |
|---|---|---|---|
| **Nobes Lab** | UNLESS OTHERWISE SPECIFIED: | | NAME |
| Contact: | DIMENSIONS ARE IN MM<br>TOLERANCES:<br>ANGULAR: ± 0.5°<br>.X = ± 0.25<br>.XX = ± 0.05 | DRAWN BY | Calynn Stumpf |
| Email: | | SMB | Calynn Stumpf |
| Phone: | | CHECKED BY | |
| Comments: | SURFACE FINISH µm 0.6 | **Speed Code** | |
| | MATERIAL: N/A | **MecE Job #** | |
| | | File Name: | A - Assembly - RGS |
| | Lab Location: | calynn<br>Monday, December 31, 2018 4:48:20 PM<br>Tuesday, July 05, 2016 12:43:24 PM | |
| | DO NOT SCALE DRAWING | | |

The Department of Mechanical Engineering
UNIVERSITY OF ALBERTA

TITLE: Mark 1

| SIZE | Project: | REV |
|---|---|---|
| B | MSc | |

SCALE: 1:3 | Mass: 4410.63 | SHEET 1 OF 3

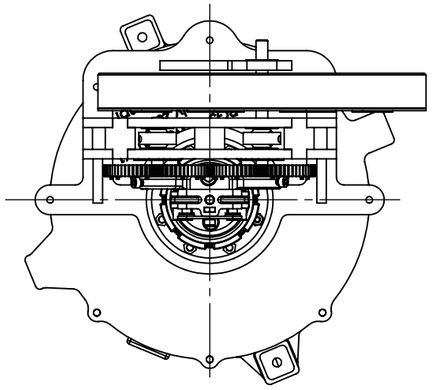

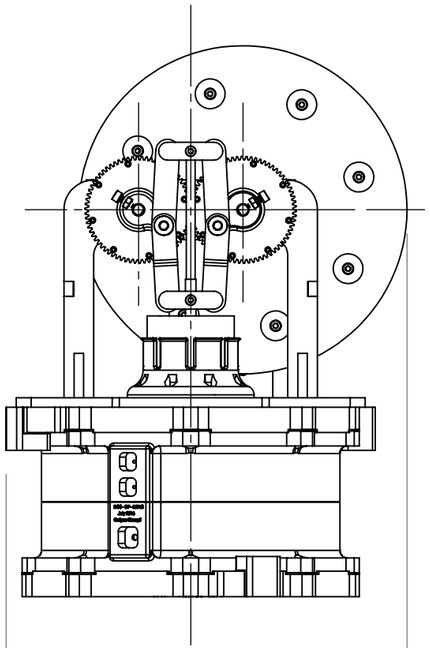


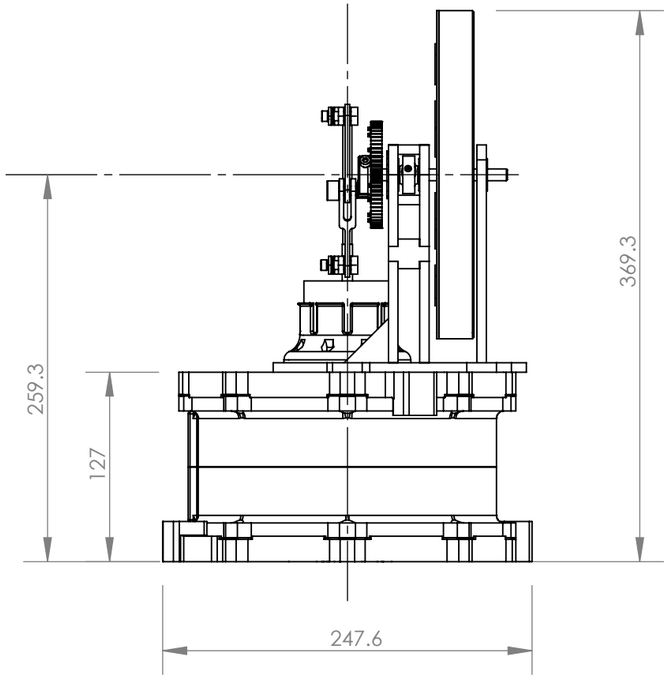


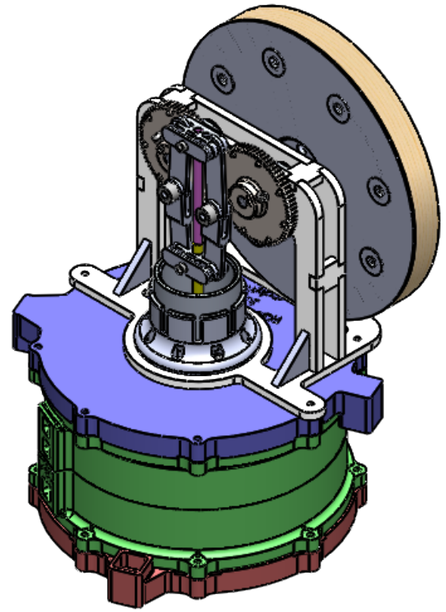

| | | | |
|---|---|---|---|
| **Nobes Lab** | UNLESS OTHERWISE SPECIFIED: | | NAME |
| Contact: | DIMENSIONS ARE IN MM<br>TOLERANCES:<br>ANGULAR: ± 0.5°<br>.X = ± 0.25<br>.XX = ± 0.05 | DRAWN BY | Calynn Stumpf |
| Email: | | SMB | Calynn Stumpf |
| Phone: | | CHECKED BY | |
| Comments: | SURFACE FINISH 0.6 µm | **Speed Code** | |
| | MATERIAL: N/A | **MecE Job #** | |
| | | File Name: | A - Assembly - RGS |
| | Lab Location: | calynn<br>Monday, December 31, 2018 4:48:20 PM<br>Tuesday, July 05, 2016 12:43:24 PM | |
| | DO NOT SCALE DRAWING | | |

The Department of Mechanical Engineering
UNIVERSITY OF ALBERTA

TITLE: Mark 1

| SIZE | Project: | REV |
|---|---|---|
| B | MSc | |

SCALE: 1:4 | Mass: 4410.63 | SHEET 2 OF 3

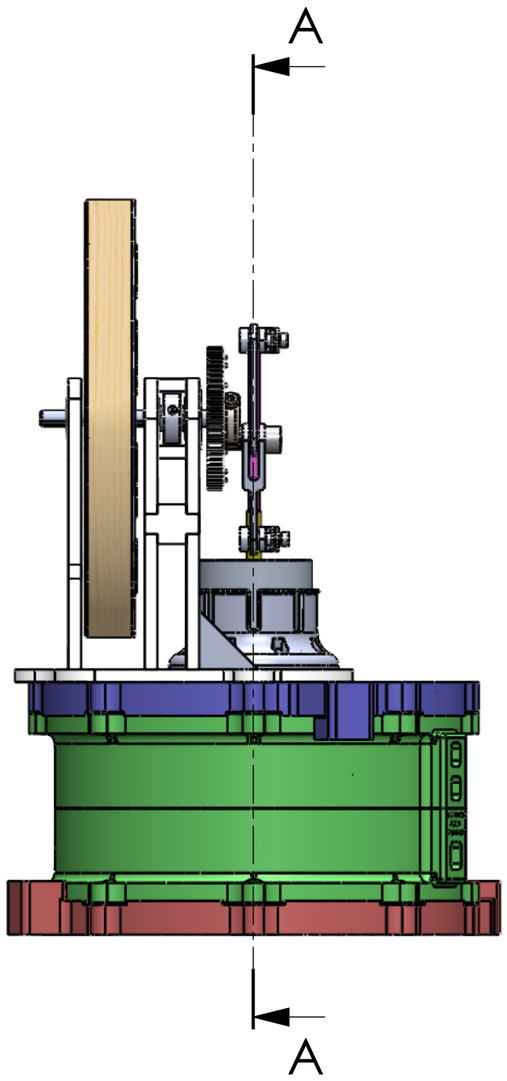


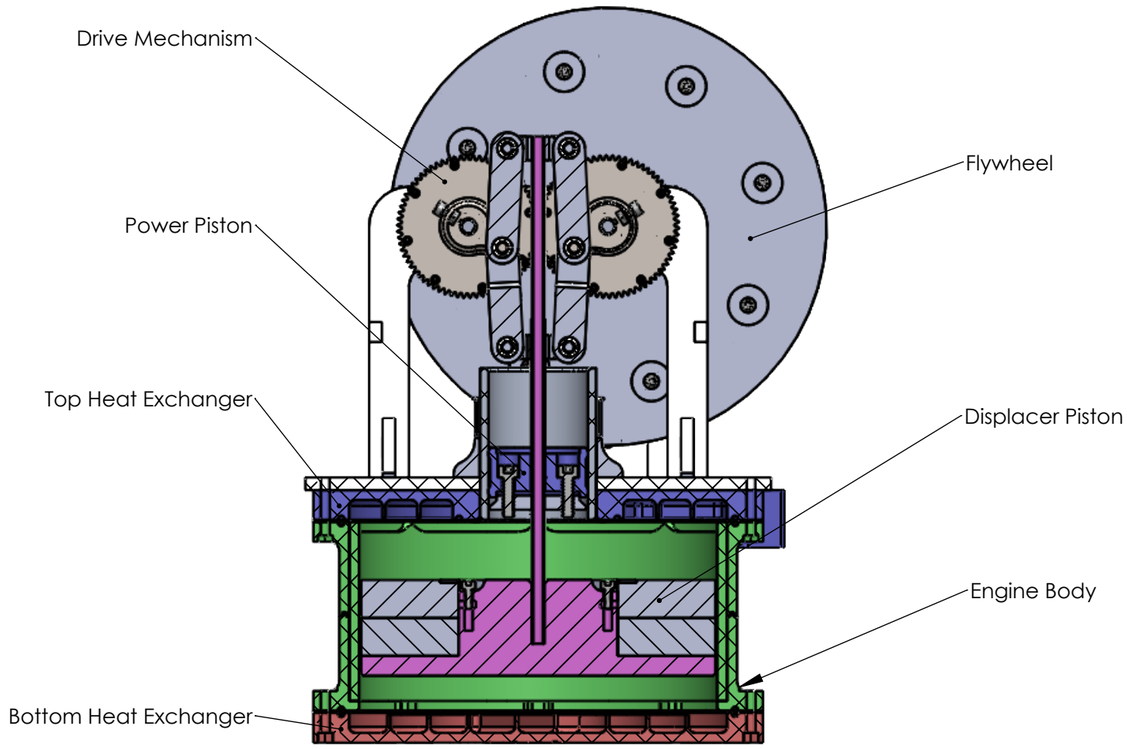


SECTION A-A

| | | | |
|---|---|---|---|
| **Nobes Lab** | UNLESS OTHERWISE SPECIFIED: | | NAME |
| Contact: | DIMENSIONS ARE IN MM<br>TOLERANCES:<br>ANGULAR: ± 0.5°<br>.X = ± 0.25<br>.XX = ± 0.05 | DRAWN BY | Calynn Stumpf |
| Email: | | SMB | Calynn Stumpf |
| Phone: | | CHECKED BY | |
| Comments: | SURFACE FINISH µm 0.6 | **Speed Code** | |
| | MATERIAL: N/A | **MecE Job #** | |
| | | File Name: | A - Assembly - RGS |
| | Lab Location: | calynn<br>Monday, December 31, 2018 4:48:20 PM<br>Tuesday, July 05, 2016 12:43:24 PM | |
| | DO NOT SCALE DRAWING | | |

The Department of Mechanical Engineering
UNIVERSITY OF ALBERTA

TITLE: Mark 1

| SIZE | Project: | REV |
|---|---|---|
| B | MSc | |

SCALE: 1:3 | Mass: 4410.63 | SHEET 3 OF 3

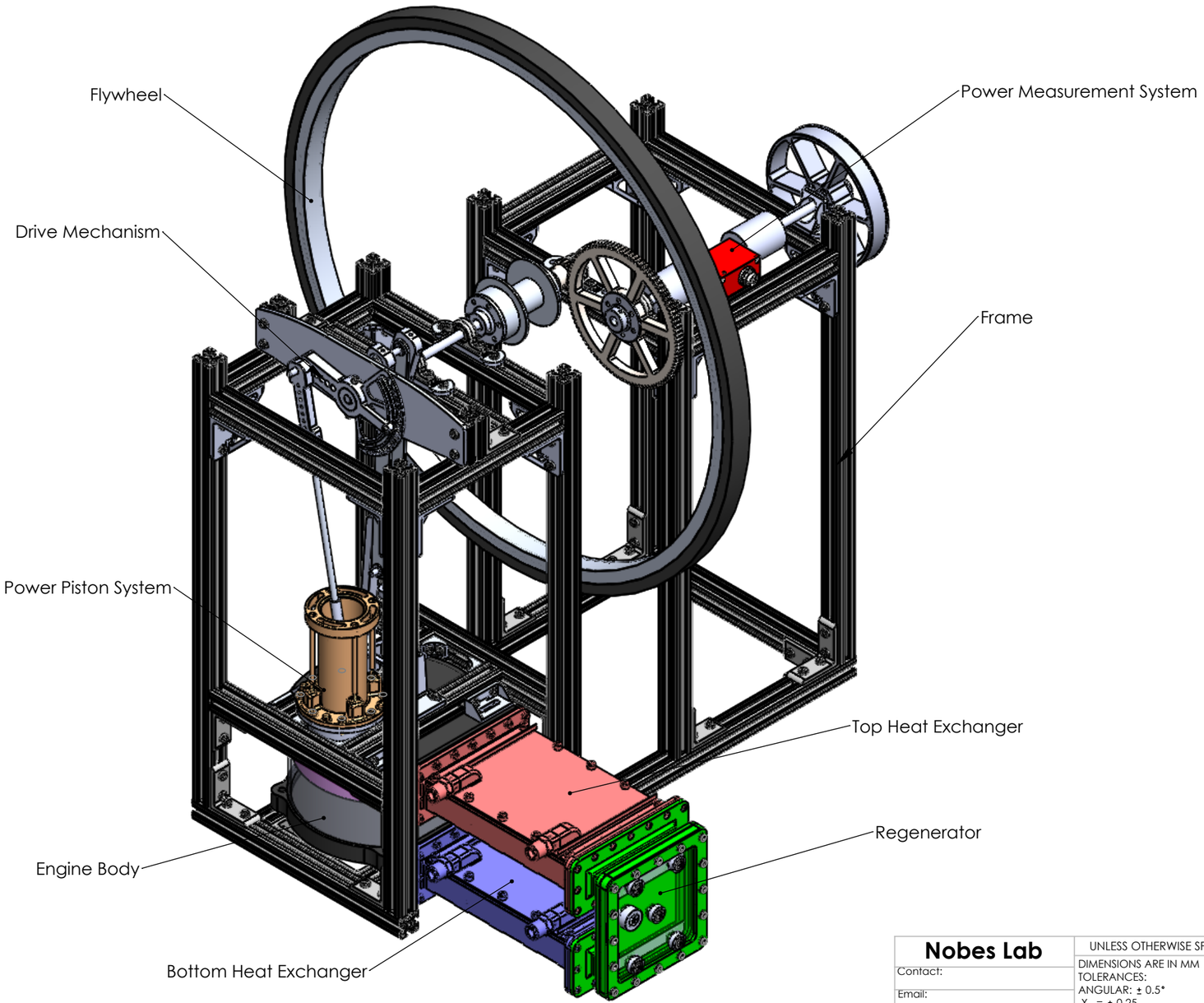


| | | | |
|---|---|---|---|
| **Nobes Lab** | UNLESS OTHERWISE SPECIFIED: | | NAME |
| Contact: | DIMENSIONS ARE IN MM<br>TOLERANCES:<br>ANGULAR: ± 0.5°<br>.X = ± 0.25<br>.XX = ± 0.05 | DRAWN BY | Calynn Stumpf |
| Email: | | SMB | Calynn Stumpf |
| Phone: | | CHECKED BY | |
| Comments: | SURFACE FINISH µm 0.6 | **Speed Code** | |
| | MATERIAL: N/A | **MecE Job #** | |
| | | File Name: | A - Assembly - Engine |
| | Lab Location: | calynn<br>Monday, December 31, 2018 5:12:05 PM<br>Tuesday, January 17, 2017 2:06:04 PM | |
| | DO NOT SCALE DRAWING | | |

The Department of Mechanical Engineering
UNIVERSITY OF ALBERTA

TITLE: Mark 2

| SIZE | Project: | REV |
|---|---|---|
| B | MSc | |

| SCALE: 1:5 | Mass: 4439.76 | SHEET 1 OF 4 |
|---|---|---|

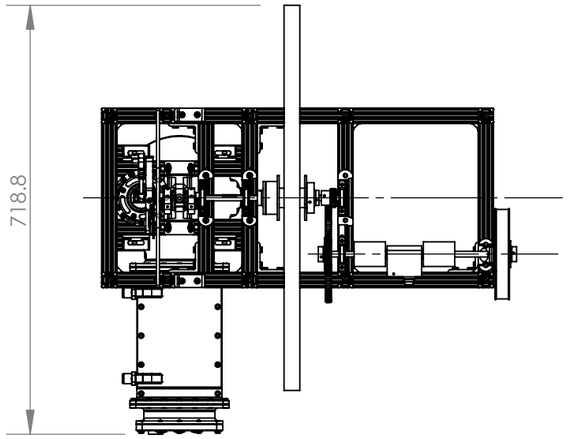


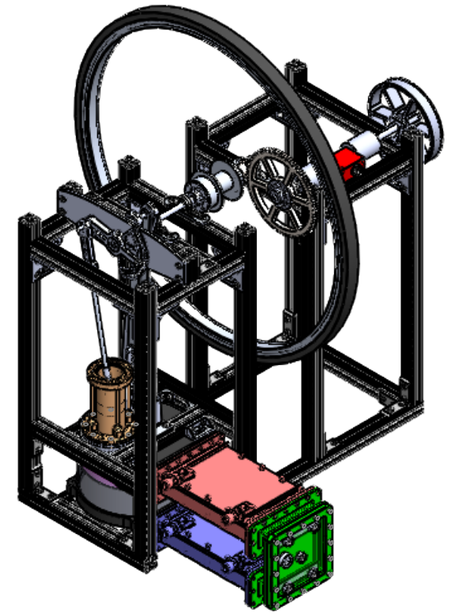

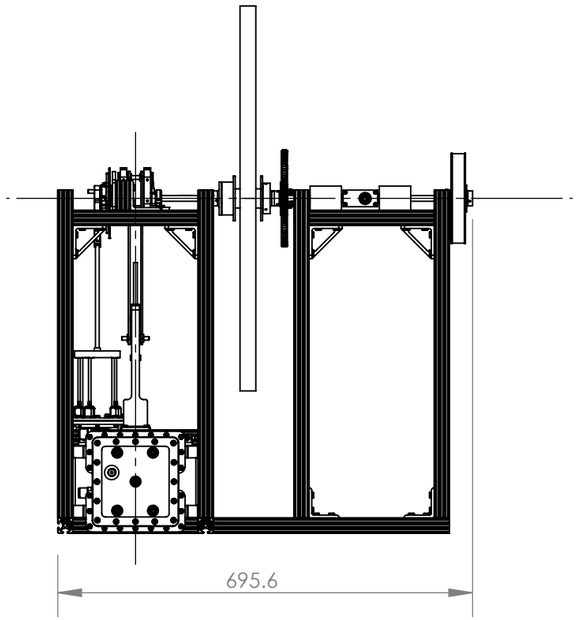


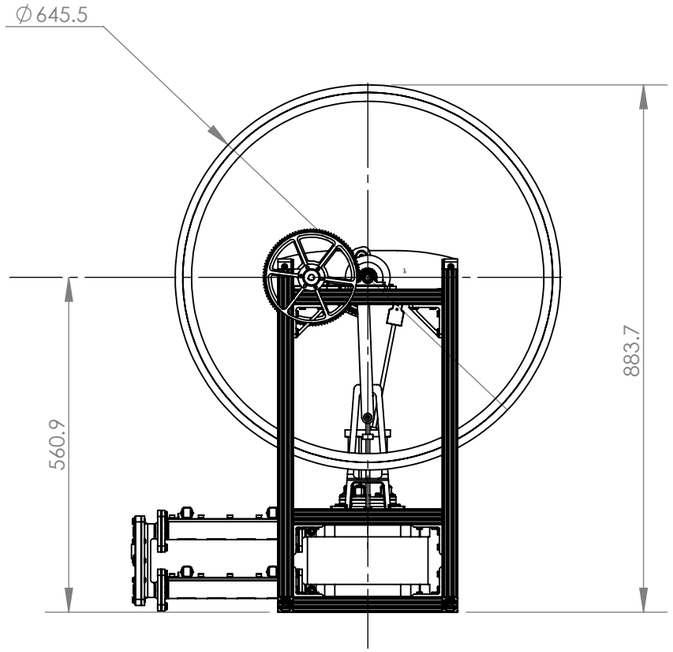


| | | | |
|---|---|---|---|
| **Nobes Lab** | UNLESS OTHERWISE SPECIFIED: | | NAME |
| Contact: | DIMENSIONS ARE IN MM<br>TOLERANCES:<br>ANGULAR: ± 0.5°<br>.X = ± 0.25<br>.XX = ± 0.05 | DRAWN BY | Calynn Stumpf |
| Email: | | SMB | Calynn Stumpf |
| Phone: | | CHECKED BY | |
| Comments: | SURFACE FINISH µm 0.6 | **Speed Code** | |
| | MATERIAL: N/A | **MecE Job #** | |
| | | File Name: | A - Assembly - Engine |
| | Lab Location: | calynn | |
| | DO NOT SCALE DRAWING | Monday, December 31, 2018 5:12:05 PM<br>Tuesday, January 17, 2017 2:06:04 PM | |

The Department of Mechanical Engineering
UNIVERSITY OF ALBERTA

TITLE: Mark 2

| SIZE | Project: | REV |
|---|---|---|
| B | MSc | |

| SCALE: 1:10 | Mass: 4439.76 | SHEET 2 OF 4 |
|---|---|---|

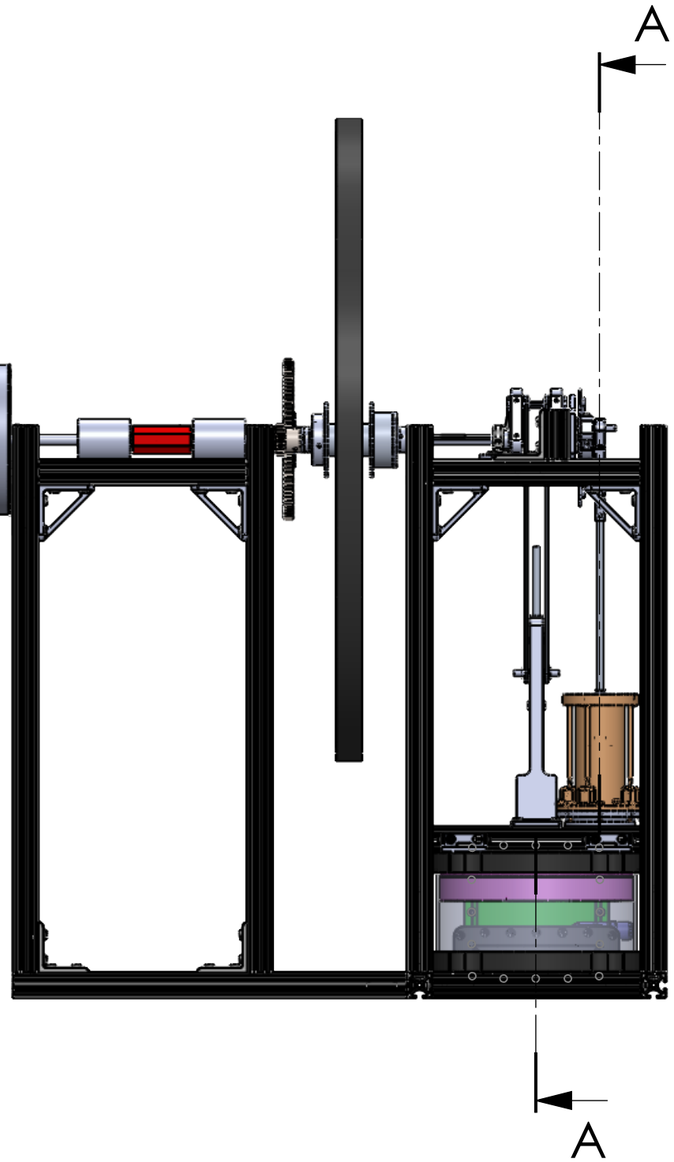


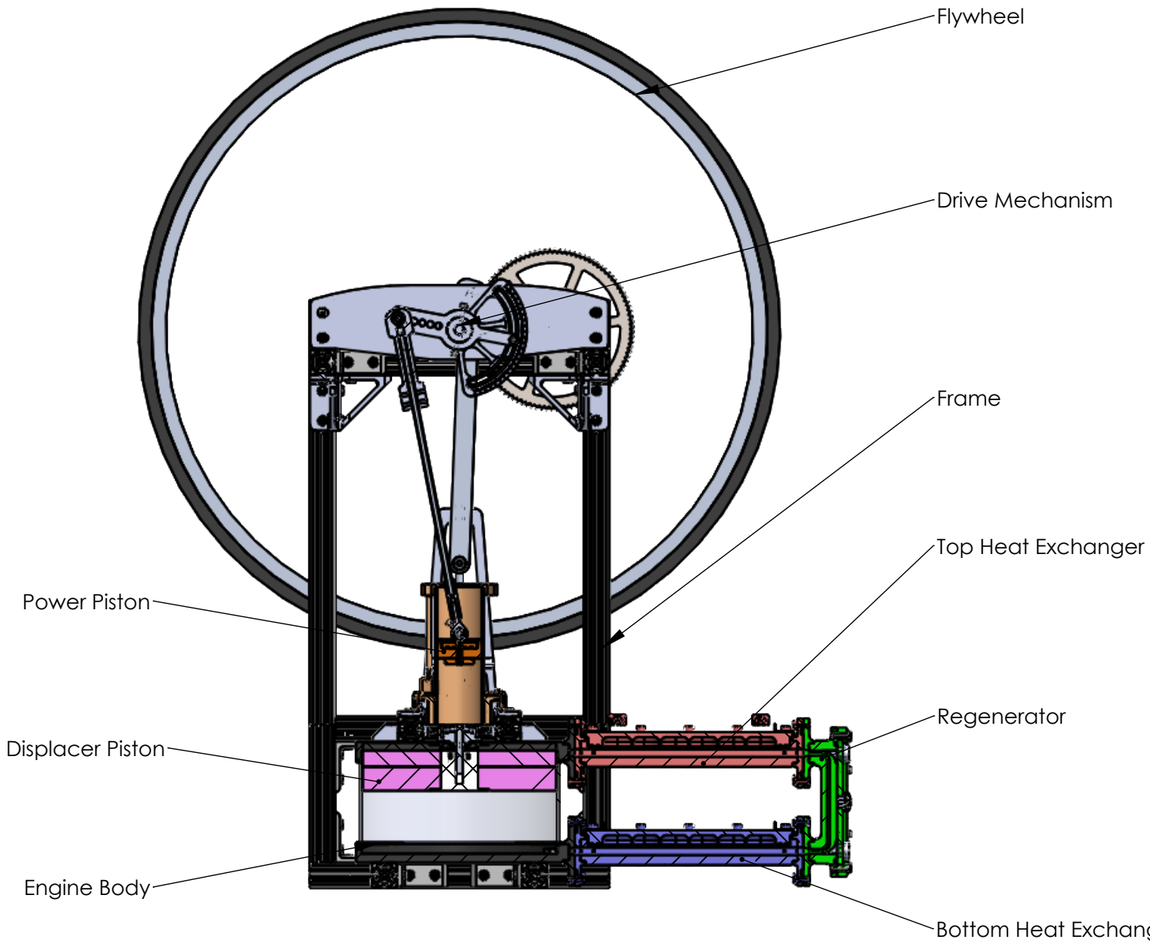


SECTION A-A

| | | | |
|---|---|---|---|
| **Nobes Lab** | UNLESS OTHERWISE SPECIFIED: | | NAME |
| Contact: | DIMENSIONS ARE IN MM<br>TOLERANCES:<br>ANGULAR: ± 0.5°<br>.X = ± 0.25<br>.XX = ± 0.05 | DRAWN BY | Calynn Stumpf |
| Email: | | SMB | Calynn Stumpf |
| Phone: | | CHECKED BY | |
| Comments: | SURFACE FINISH µm 0.6 | **Speed Code** | |
| | MATERIAL: N/A | **MecE Job #** | |
| | | File Name: | A - Assembly - Engine |
| | Lab Location: | calynn<br>Monday, December 31, 2018 5:12:05 PM<br>Tuesday, January 17, 2017 2:06:04 PM | |
| | DO NOT SCALE DRAWING | | |

The Department of Mechanical Engineering
UNIVERSITY OF ALBERTA

TITLE: Mark 2

| SIZE | Project: | REV |
|---|---|---|
| B | MSc | |

SCALE: 1:6 | Mass: 4439.76 | SHEET 3 OF 4

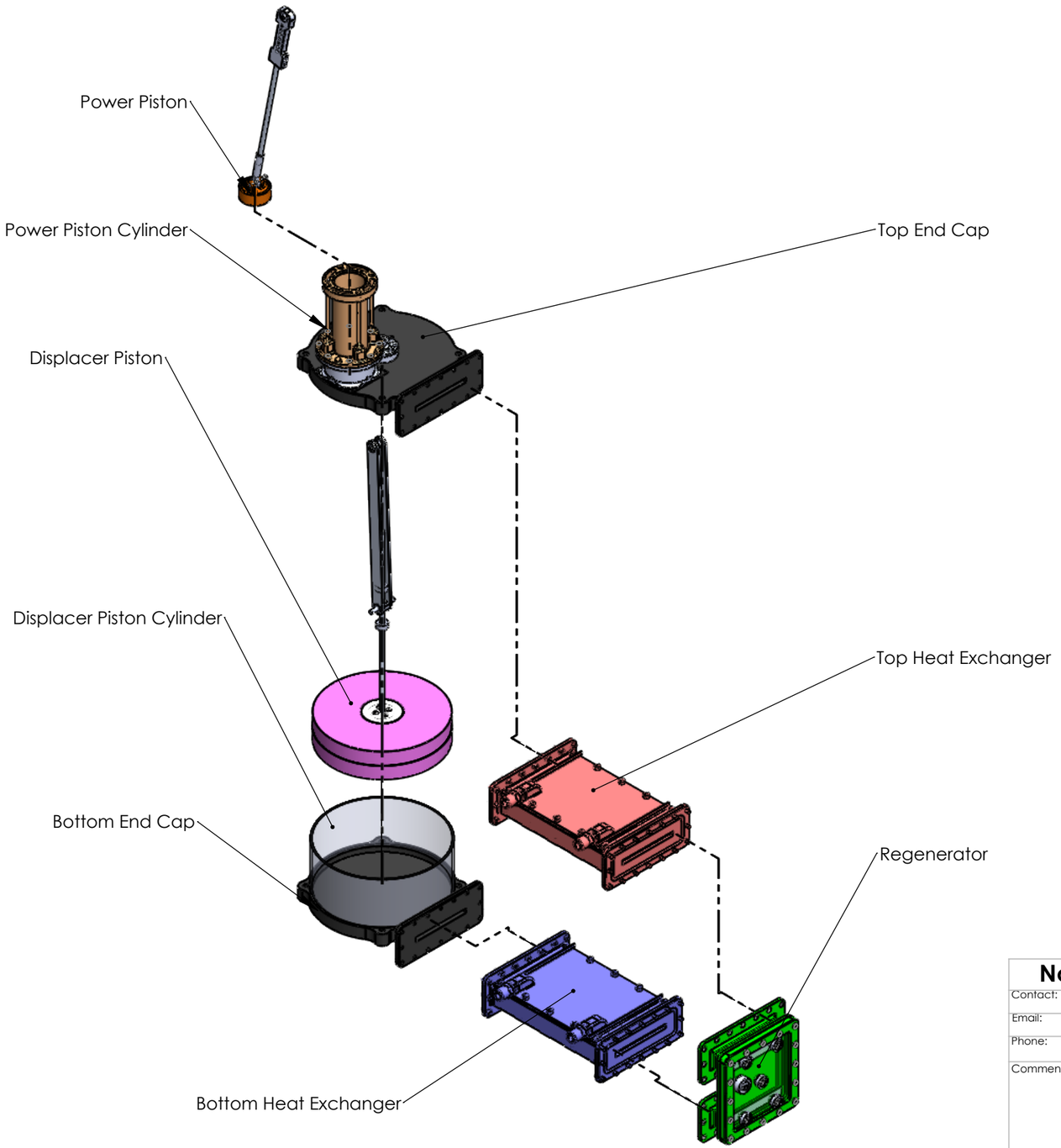


| | | | |
|---|---|---|---|
| **Nobes Lab** | UNLESS OTHERWISE SPECIFIED: | | NAME |
| Contact: | DIMENSIONS ARE IN MM | DRAWN BY | Calynn Stumpf |
| Email: | TOLERANCES: ANGULAR: ± 0.5° .X = ± 0.25 .XX = ± 0.05 | SMB | Calynn Stumpf |
| Phone: | | CHECKED BY | |
| Comments: | SURFACE FINISH µm 0.6 | **Speed Code** | |
| | MATERIAL: N/A | **MecE Job #** | |
| | | File Name: | A - Assembly - Engine |
| | Lab Location: | calynn | |
| | DO NOT SCALE DRAWING | Monday, December 31, 2018 5:12:05 PM<br>Tuesday, January 17, 2017 2:06:04 PM | |

The Department of Mechanical Engineering
UNIVERSITY OF ALBERTA

TITLE: Mark 2

| SIZE | Project: | REV |
|---|---|---|
| B | MSc | |

SCALE: 1:7 | Mass: 4439.76 | SHEET 4 OF 4

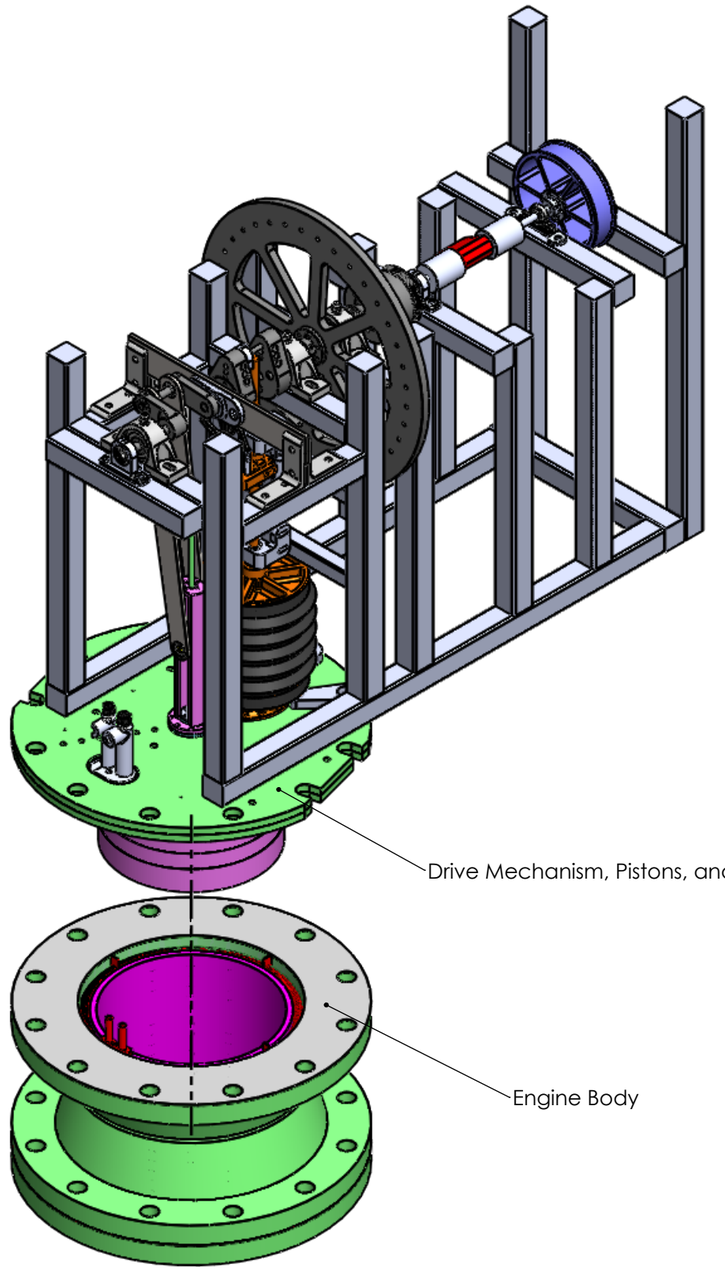


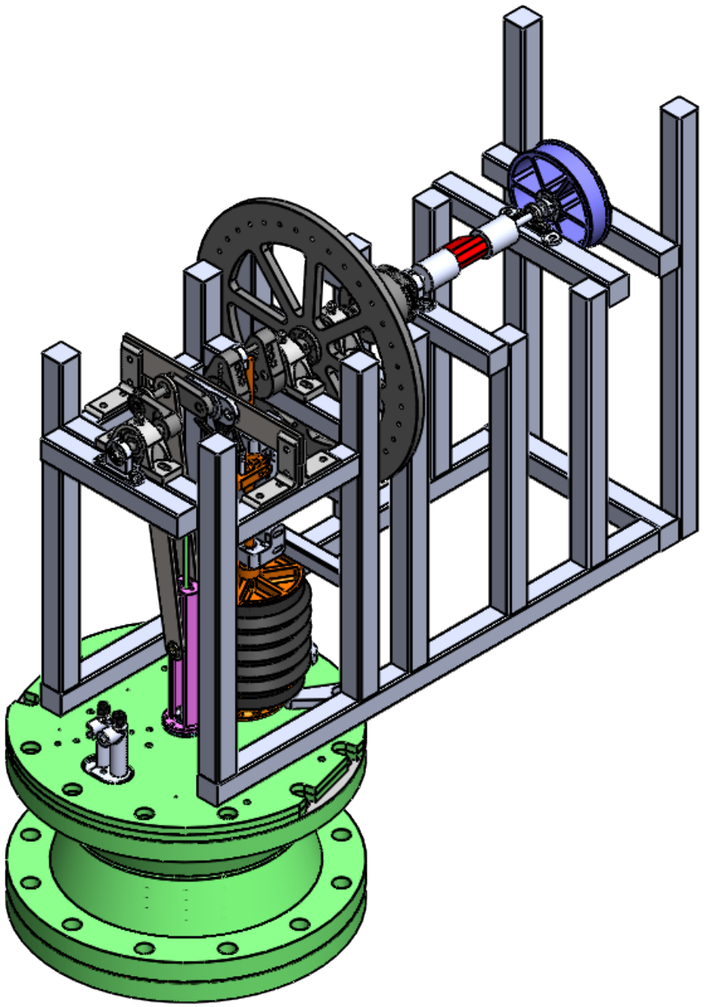

| | | | |
|---|---|---|---|
| **Nobes Lab** | UNLESS OTHERWISE SPECIFIED: | | NAME |
| Contact: | DIMENSIONS ARE IN MM<br>TOLERANCES:<br>ANGULAR: ± 0.5°<br>.X = ± 0.25<br>.XX = ± 0.05 | DRAWN BY | Calynn Stumpf |
| Email: | | SMB | Calynn Stumpf |
| Phone: | | CHECKED BY | |
| Comments: | SURFACE FINISH µm 0.6 | **Speed Code** | |
| | MATERIAL: N/A | **MecE Job #** | |
| | | File Name: | 00-PRESIDENT_OVERALL_ASM_V2 |
| | Lab Location: | calynn<br>Sunday, December 30, 2018 5:25:18 PM<br>Wednesday, May 10, 2017 9:27:27 AM | |
| | DO NOT SCALE DRAWING | | |

The Department of Mechanical Engineering
UNIVERSITY OF ALBERTA

TITLE:

# EP-1

| SIZE | Project: | REV |
|---|---|---|
| B | MSc | |

SCALE: 1:8 | Mass: 177418.03 | SHEET 1 OF 4

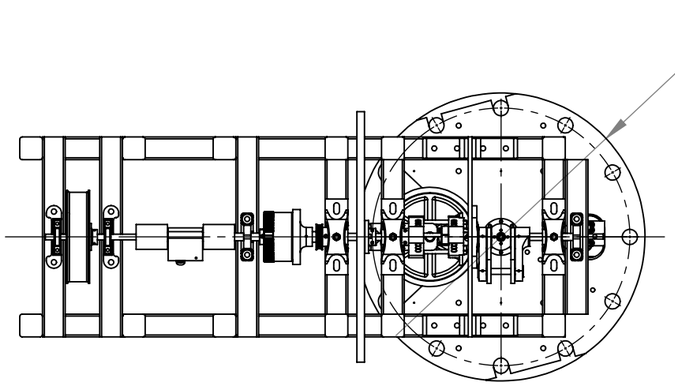


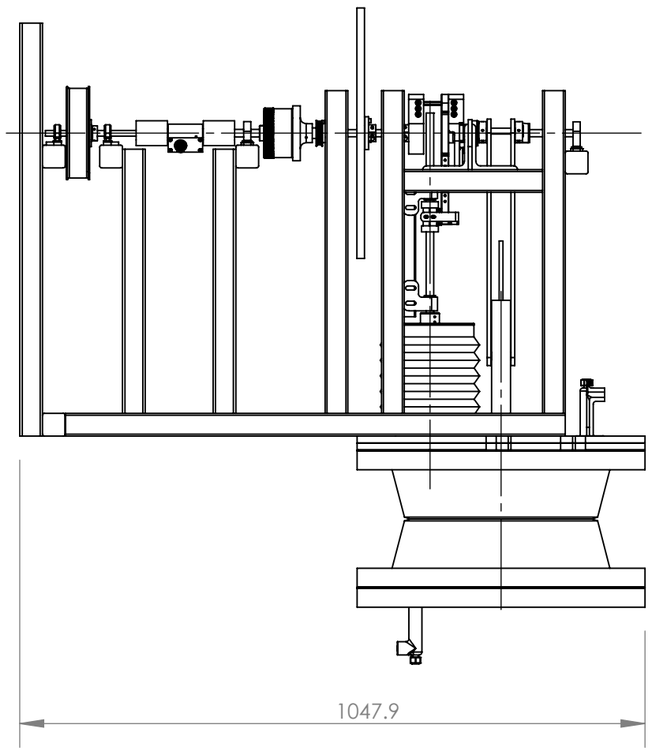


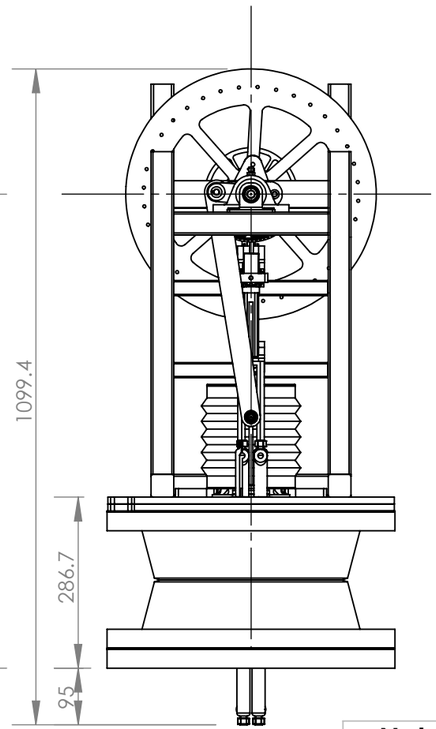

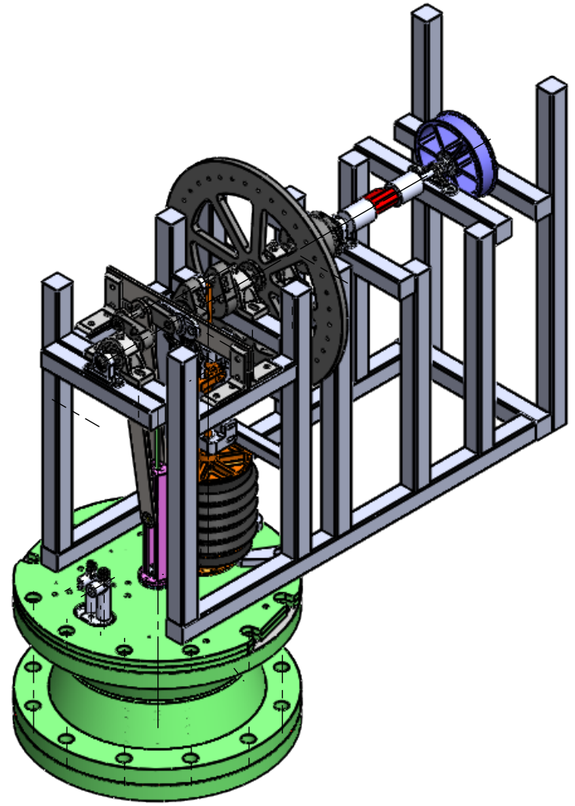

| | |
|---|---|
| **Nobes Lab** | |
| Contact: | |
| Email: | |
| Phone: | |
| Comments: | |
| UNLESS OTHERWISE SPECIFIED: | |
| DIMENSIONS ARE IN MM | |
| TOLERANCES: | |
| ANGULAR: ± 0.5° | |
| .X = ± 0.25 | |
| .XX = ± 0.05 | |
| SURFACE FINISH µm | 0.6 |
| MATERIAL: | N/A |
| Lab Location: | |
| DO NOT SCALE DRAWING | |
| | NAME |
| DRAWN BY | Calynn Stumpf |
| SMB | Calynn Stumpf |
| CHECKED BY | |
| **Speed Code** | |
| **MecE Job #** | |
| File Name: | 00-PRESIDENT_OVERALL_ASM_V2 |
| calynn | |
| Sunday, December 30, 2018 5:25:18 PM | |
| Wednesday, May 10, 2017 9:27:27 AM | |

The Department of Mechanical Engineering
UNIVERSITY OF ALBERTA

TITLE:

# EP-1

| | | | |
|---|---|---|---|
| SIZE **B** | Project: MSc | | REV |
| SCALE: 1:10 | Mass: 177418.03 | SHEET 2 OF 4 | |

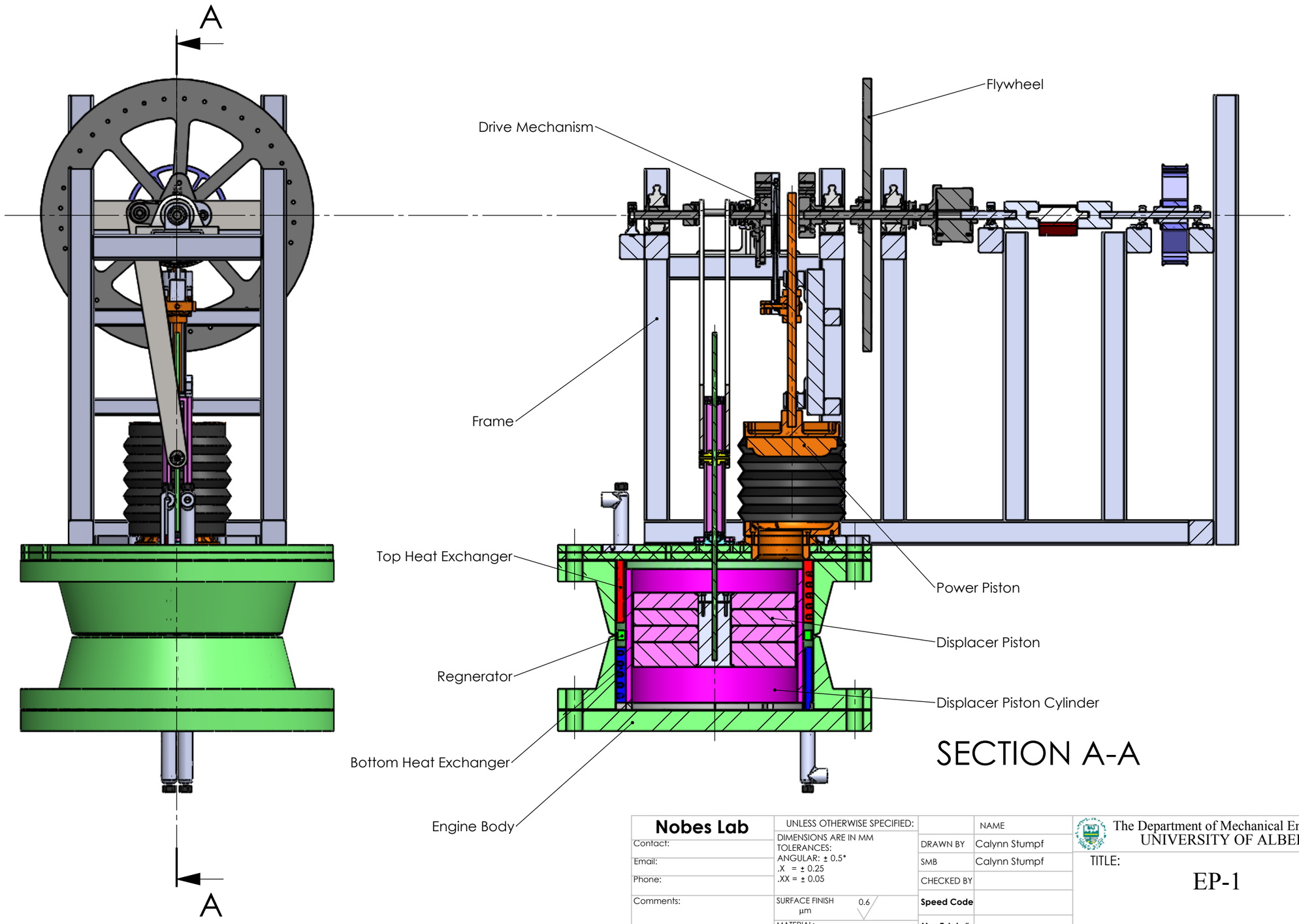


SECTION A-A

| | | | |
|---|---|---|---|
| **Nobes Lab** | UNLESS OTHERWISE SPECIFIED: | | NAME |
| Contact: | DIMENSIONS ARE IN MM<br>TOLERANCES:<br>ANGULAR: ± 0.5°<br>.X = ± 0.25<br>.XX = ± 0.05 | DRAWN BY | Calynn Stumpf |
| Email: | | SMB | Calynn Stumpf |
| Phone: | | CHECKED BY | |
| Comments: | SURFACE FINISH µm 0.6 | **Speed Code** | |
| | MATERIAL: N/A | **MecE Job #** | |
| | | File Name: | 00-PRESIDENT_OVERALL_ASM_V2 |
| | Lab Location: | calynn<br>Sunday, December 30, 2018 5:25:18 PM<br>Wednesday, May 10, 2017 9:27:27 AM | |
| | DO NOT SCALE DRAWING | | |

The Department of Mechanical Engineering
UNIVERSITY OF ALBERTA

TITLE: EP-1

| SIZE | Project: | REV |
|---|---|---|
| B | MSc | |

SCALE: 1:6 | Mass: 177418.03 | SHEET 3 OF 4

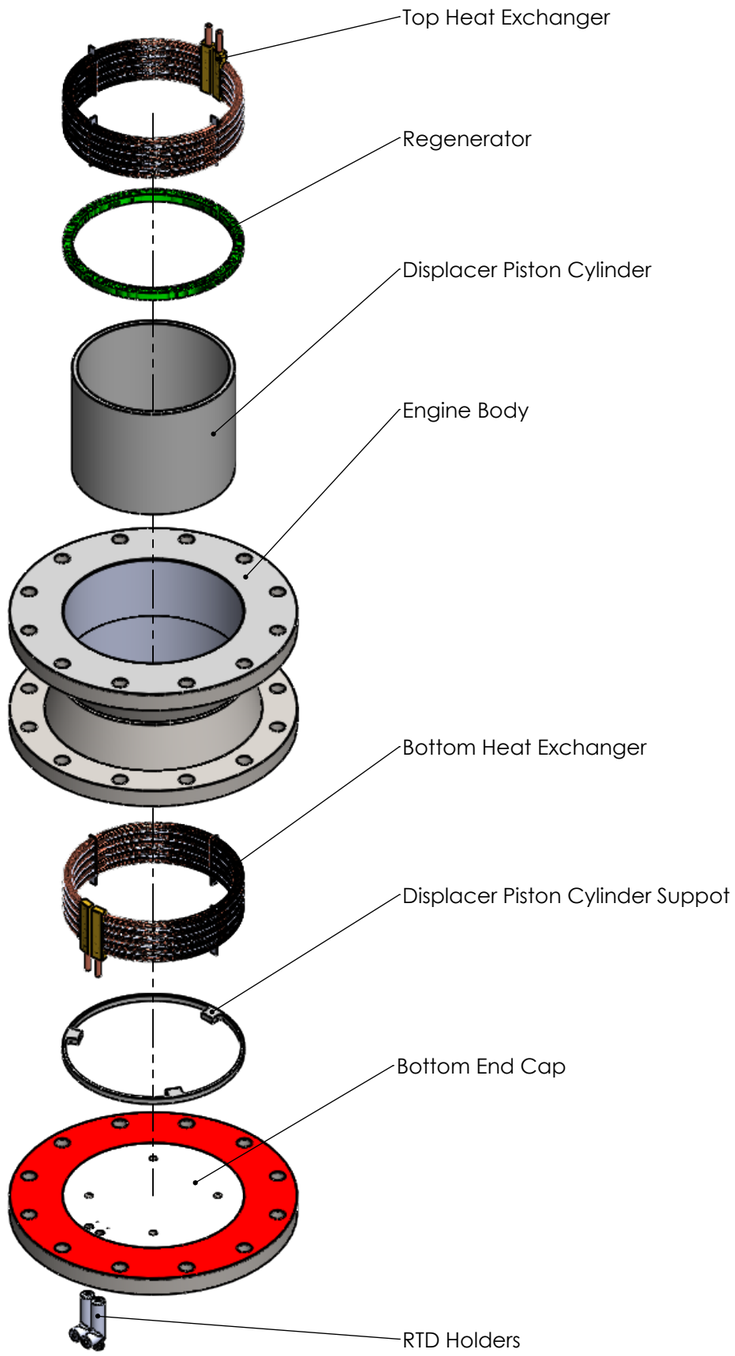


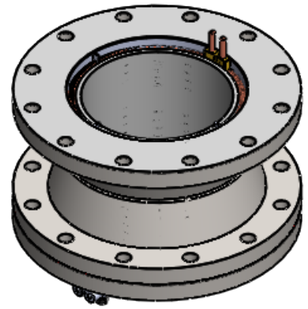

| | | | |
|---|---|---|---|
| **Nobes Lab** | UNLESS OTHERWISE SPECIFIED: | | NAME |
| Contact: | DIMENSIONS ARE IN MM<br>TOLERANCES:<br>ANGULAR: ± 0.5°<br>.X = ± 0.25<br>.XX = ± 0.05 | DRAWN BY | Calynn Stumpf |
| Email: | | SMB | Calynn Stumpf |
| Phone: | | CHECKED BY | |
| Comments: | SURFACE FINISH µm 0.6 | **Speed Code** | |
| | MATERIAL: VARIOUS | **MecE Job #** | |
| | | File Name: | 1-0-00-DISP-CYL-ASM |
| | Lab Location: | calynn<br>Sunday, December 30, 2018 4:59:57 PM<br>Tuesday, May 09, 2017 3:22:29 PM | |
| | DO NOT SCALE DRAWING | | |

The Department of Mechanical Engineering
UNIVERSITY OF ALBERTA

TITLE:
# Engine Body Assembly

| SIZE | Project: | REV |
|---|---|---|
| B | MSc | |
| SCALE: 1:10 | Mass: | SHEET 4 OF 4 |